Determination of the gluon polarization in the nucleon

Determination of the gluon polarization in the nucleon

ACADEMISCH PROEFSCHRIFT

ter verkrijging van de graad van doctor
aan de Universiteit van Amsterdam
op gezag van de Rector Magnificus
prof.mr. P.F. van der Heijden
ten overstaan van
een door het college voor promoties ingestelde commissie,
in het openbaar te verdedigen
in de Aula der Universiteit
op dinsdag 20 december 2005, te 10:00 uur

door

Vanessa Mexner

geboren te Münster, Duitsland

Promotor: Prof. dr. G. van der Steenhoven
Co-promotor: Dr. Ir. W.H.A. Hesselink

Faculteit der Natuurwetenschappen, Wiskunde en Informatica

ISBN 90 6464 481 0

The work described in this thesis is part of the research programme of the *Nationaal Instituut voor Kernfysica en Hoge-Energie Fysica* (NIKHEF) in Amsterdam, the Netherlands. The author was financially supported by the *Stichting voor Fundamenteel Onderzoek der Materie* (FOM).

Contents

Chapter 1

Introduction

Studying the fundamental constituents of matter and their interactions forms the main focus of high-energy physics. This thesis addresses the role of one such constituent, the gluon, in the substructure of the nucleon. In particular, the gluon contribution to the nucleon spin is determined, based on data taken by the HERMES experiment at DESY.

By the 1960s high-energy physicists had discovered a multitude of hadrons, which could be grouped into multiplets based on properties such as mass, charge and spin. This classification posed the question whether these many hadrons could be described as composite systems of more fundamental objects. In 1964 Gell-Mann and Zweig proposed a model containing three fundamental entities called quarks (and their corresponding antiquarks[1]), whose bound states were assumed to correspond to the observed hadrons. While this model was based on theoretical considerations, experimental evidence on the substructure of nucleons was provided in the late 1960s by the first deep-inelastic lepton-nucleon scattering (DIS) experiments at SLAC. In 1968 Feynman and Bjørken interpreted the SLAC results by assuming the existence of point-like spin-$\frac{1}{2}$ constituents inside the nucleon called partons. The partons of Feynman and Bjørken were later identified with the quarks of Gell-Mann and Zweig and both concepts merged into the Quark-Parton-Model (QPM).

The QPM provided a more fundamental interpretation of the structure functions, which had originally been introduced as a phenomenological description of electron scattering experiments involving hadrons. So far, these parametrizations had only been empirically determined, while now the structure functions could be decomposed into charge-weighted sums of the parton distribution functions (PDFs). However, subsequent deep-inelastic scattering measurements of the structure functions in the early 1970s showed that only approximately 50% of the nucleon momentum was carried by the quarks, implying the existence of other carriers of momentum. Furthermore, the Bjørken scaling of the structure functions (i.e. their independence of the momentum transfer from the lepton to the nucleon), as predicted by the QPM, was found to be violated.

[1] The term quarks is often used as collectively referring to both quarks and antiquarks.

Both these experimental observations could be accommodated by Quantum Chromodynamics (QCD), the theory developed in the mid 1970s to describe the strong interaction. In QCD the spin-$\frac{1}{2}$ quarks interact via the exchange of spin-1 gluons. The missing nucleon momentum could now be attributed to the gluons. Also the scaling violations could be explained by taking into account interactions between the partons, - quarks and gluons -, which were beyond the scope of the simple QPM. QCD and especially the concept of gluons received even more experimental support when in 1979 at DESY the first three-jet events were seen in e^+e^- collisions, explicable by the existence of gluons. The lowest order approximation of QCD reproduces the intuitive picture of the QPM, which therefore in many situations retains its descriptive importance.

Despite its more fundamental character QCD does not allow the computation of the structure functions, and in turn the parton distribution functions, from first principles. Instead, precision measurements of the structure functions are needed to extract the PDFs via QCD fits to the data. The gluon distribution function has in these QCD fits been indirectly deduced from the observed scaling violations of the structure functions. Direct measurements of the gluon distribution can be performed by isolating those processes in which a gluon from the nucleon is involved in the hard scattering. This has successfully been done by selecting e.g. jets with large transverse momentum or charmed hadrons, in DIS as well as hadron collision experiments.

The formalism as described so far has not taken into account spin-dependent quantities. In the same way as the discovery of the nucleon substructure allowed the decomposition of the nucleon momentum into its constituent parton momenta, a similar relation should hold for the spin, another fundamental property of matter. In principle, the nucleon spin S can receive contributions from the intrinsic quark and gluon spins, $\Delta\Sigma$ and ΔG, as well as from their orbital angular momenta, L_q and L_G,[2]

$$S = \frac{1}{2} = \frac{1}{2}\Delta\Sigma + \Delta G + L_q + L_G \ . \tag{1.1}$$

In complete analogy to the spin-independent structure functions and parton distribution functions, spin-dependent counterparts can be defined, which are again not calculable from first principles in QCD, but need to be accessed experimentally. Such spin-dependent functions are often referred to as polarized since they occur in the description of polarized scattering processes; spin-independent is often replaced by unpolarized.

In the simple QPM one could naively assume that the nucleon spin is carried only by the three valence quarks. However, in 1987 EMC, the first polarized DIS experiment at CERN, concluded from measurements of the polarized structure function that $\Delta\Sigma$ is small. A second generation of polarized DIS experiments at SLAC and CERN increased the precision of these measurements and found the quark contribution to the nucleon spin to be about 30%. Just as for the nucleon momentum, also for the nucleon spin the contributions from gluons (and possibly orbital angular momentum) must therefore be considered important.

[2]The individual contributions to the sum are scale and scheme dependent.

From the observed scaling violations of the polarized structure functions the polarized gluon distribution can be indirectly inferred. Since all polarized DIS experiments so far have utilized fixed targets, the kinematic range of the measured polarized structure functions is rather limited. Therefore the polarized gluon distribution extracted indirectly from these fits is hardly constrained. Direct measurements are thus needed to determine it more accurately. As in the unpolarized case, this requires isolating scattering processes with the gluon in the initial state, which in DIS experiments can most promisingly be done by detecting charmed hadrons or jets with large transverse momentum.

HERMES at DESY belongs to a third generation of polarized DIS experiments designed not only for precise inclusive measurements of the polarized structure functions but especially for semi-inclusive measurements in order to study the flavour decomposition of the quark spin content of the nucleon. The experiment utilizes the polarized lepton beam of the HERA ring and a polarized gas target internal to the ring. To detect the produced hadrons in coincidence with the scattered lepton, a large acceptance spectrometer with good particle identification is used. This experimental setup also allows to attempt a direct measurement of the gluon polarization. As the HERMES centre-of-mass energy is only just above the threshold for the production of pairs of charmed quarks, this channel proved not to deliver enough events for a significant measurement. The available energy is also too small to produce high-p_T jets. However, one can instead consider high-p_T hadrons or hadron pairs.

In this thesis two analyses are reported, referred to as single high-p_T hadron electroproduction and high-p_T hadron pair photoproduction. Both analyses are based on double spin asymmetries measured at HERMES. Since selecting events with high-p_T hadrons does not suffice to completely isolate processes with a gluon in the initial state, involved Monte Carlo (MC) simulations are required to determine the contributions of the different (signal and background) processes to the measured asymmetries. This is achieved with the most recent version of PYTHIA MC, tuned to HERMES energies. Having decomposed the measured asymmetries in terms of several contributing processes, the gluon polarization can be extracted. This procedure introduces an unavoidable model dependence of the results. However, an estimate of the size of this model dependence can be given by performing a variety of studies. Such model dependent systematic uncertainties are inherent to the present kinematic regime. Nevertheless, the HERMES experiment is able to make a significant contribution to further constraining the polarized gluon distribution, and consequently to the understanding of the nucleon spin structure.

Chapter 2 contains a review of the theoretical framework relevant for the analysis presented in this thesis. Chapter 3 describes the HERMES experimental setup with its various components: polarized beam, polarized target, luminosity monitor, spectrometer and Lambda Wheels (silicon detector). Chapter 4 covers the formalism of the data analysis, including all tools required to extract double spin asymmetries. Chapter 5 focusses on the formalism for the extraction of the gluon polarization from measured asymmetries by means of Monte Carlo simulations. Chapter 6 presents the results for single high-p_T hadron electroproduction, while chapter 7 is dedicated to the results for high-p_T hadron pair photoproduction. Both these analysis chapters include an extraction of the gluon polarization, together with studies to evaluate the model dependent systematic uncertainties. Chapter 8 summarizes the results for the gluon polarization of the two previous chapters, discusses their consistency, and compares the results to existing data as well as to theoretical calculations.

Chapter 2

Theoretical framework

Deep-inelastic lepton nucleon scattering has since the 1960s proven to be a powerful probe of the nucleon's internal structure, but some important questions still remain unanswered, in particular concerning spin-dependent observables. Current experimental results addressing this topic cannot be understood without some theoretical concepts used in the description of deep-inelastic scattering. This chapter therefore treats some of these aspect which are of particular relevance to the analysis presented later in this thesis.
A convenient set of variables has become standard to describe the DIS kinematics (section 2.1). The inclusive DIS cross sections and cross section asymmetries can be related to the commonly used unpolarized and polarized structure functions (section 2.2). Many aspects of these structure functions are captured in the framework of the so-called Quark-Parton-Model (QPM), which allows to express them in terms of the parton distribution functions (section 2.3). The naive QPM has been superceded by QCD, comprising a full description of both the quarks and the gluons as well as their interactions (section 2.4). After the hard interaction, the quarks and gluons form the hadrons which can be observed in semi-inclusive measurements (section 2.5) While the quark distributions have been determined with rather high accuracy, the gluon distribution, in particular in its polarized version, is so far much less constrained but currently receives a lot of attention as evidenced by several ongoing efforts to measure the gluon polarization indirectly as well as directly (section 2.6).

2.1 Deep-inelastic scattering kinematics

As opposed to elastic lepton-nucleon scattering where the nucleon recoils but stays intact, in deep-inelastic lepton-nucleon scattering (DIS) the energy involved in the process is so large that the nucleon breaks apart. In this way the lepton serves to probe the substructure of the nucleon. In most DIS experiments a charged point-like lepton[1] l scatters off a nucleon N to an outgoing lepton l' leaving a hadronic final state X as

$$l + N \rightarrow l' + X \ . \tag{2.1}$$

[1] Experiments which employ (anti)neutrino beams will not be discussed here.

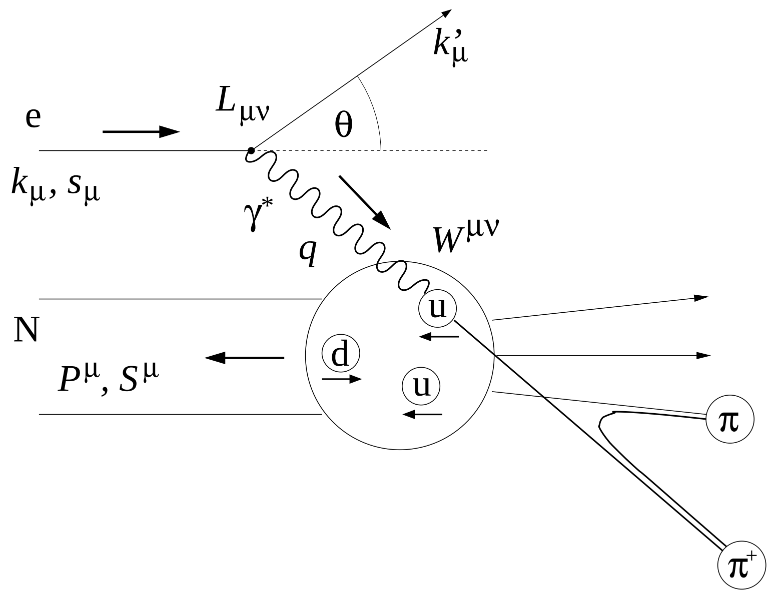

Figure 2.1: *Diagram of the polarized deep-inelastic scattering process in the single photon exchange approximation. The arrows indicate the spin of the particles.*

In lowest order pertubation theory this interaction is described as the exchange of a neutral boson (γ or Z^0) between the charged lepton and the charged constituents inside the nucleon. At HERMES Z^0-exchange can be neglected as the energy transfer in HERMES ($\sqrt{s} \sim 7$ GeV in the centre of mass system) is well below the mass of the neutral weak boson ($m_{Z^0} = 91$ GeV) where this contribution would become significant. Therefore, the dominant process is single photon exchange. This process is depicted in Fig. 2.1. The incident lepton l is characterized by its four-momentum[2] k_μ and its spin s_μ, while the four-momentum of the outgoing lepton l' is denoted as k'_μ, and its spin four-vector s'_μ. The four-vector q_μ represents the momentum of the exchanged virtual photon which can, due to its virtuality, be either longitudinally or transversely polarized. Contrary to virtual photons, real photons have zero mass and are therefore always longitudinally polarized.[3]

The four-momentum for the target nucleon is described by P_μ and its spin by S_μ. In fixed target experiments the laboratory frame is identical to the nucleon rest frame, $P_\mu = (M, \vec{0})$ with M the nucleon mass. In this frame the incoming lepton l scatters at an angle θ into the outgoing state l' and, since the energies of the incident and scattered leptons (E,E') are much larger than their mass (m), the latter can be neglected.

The scattering process can be characterized by the following quantities:

[2]The four-vectors are here indicated by an index μ, which in the following is often suppressed.

[3]Note that a longitudinally polarized photon, with its spin parallel or antiparallel to its momentum, is often named a transverse photon (reflecting the fact that in classical electrodynamics the propagation vector of the photon is perpendicular to the E and B fields), while a transversely polarized photon, with its spin oriented perpendicular to the direction of motion, is often called a longitudinal photon, as used throughout this thesis.

- The negative four-momentum squared of the virtual photon, expressed as

$$Q^2 \equiv -q^2 = (k-k')^2 \stackrel{lab}{=} 4EE'sin^2\frac{\theta}{2} \ . \tag{2.2}$$

The quantity Q^2 is positive and represents a measure of the spatial scale a virtual photon with wavelength $\lambda = \frac{1}{|\vec{q}|}$ can resolve.
- The energy of the virtual photon, transferred in the reaction,

$$\nu \equiv \frac{P \cdot q}{M} \stackrel{lab}{=} E - E' \ . \tag{2.3}$$

- The squared invariant mass of the hadrons in the final state which carry away the transferred momentum and energy,

$$W^2 \equiv (P+q)^2 \stackrel{lab}{=} M^2 + 2M\nu - Q^2 \ . \tag{2.4}$$

The kinematics of the process can also be expressed in terms of two dimensionless variables, the Bjørken variable

$$x \equiv \frac{-q^2}{2P \cdot q} \stackrel{lab}{=} \frac{Q^2}{2M\nu} \ , \tag{2.5}$$

and the fractional energy-transfer from the lepton to the nucleon

$$y \equiv \frac{P \cdot q}{P \cdot k} \stackrel{lab}{=} \frac{\nu}{E} \ . \tag{2.6}$$

The Bjørken variable x can be viewed as a measure for the inelasticity of the scattering process. Its kinematically allowed range is $0 \leq x \leq 1$. The limit $x = 1$ corresponds to elastic scattering with $W^2 = M^2$, while for inelastic scattering $W^2 > M^2$ and therefore $x < 1$. The deep-inelastic scattering region is usually defined by $Q^2 > 1$ GeV^2 and $W^2 > 4$ GeV^2. More details on DIS kinematics can be found e.g. in [1, 2, 3].
All the variables defined in Eqs. (2.2) to (2.6) are Lorentz-invariant. For a fixed target experiment these variables can be calculated from the kinematics of the outgoing lepton. In a so-called *inclusive* measurement only the outgoing lepton l' is detected, and the corresponding cross section for this process depends on two independent variables, which can either be chosen as (E',θ), or alternatively, for example, as (x,Q^2).

In a *semi-inclusive* measurement one or more particles of the hadronic final state X are detected in addition to the scattered lepton l'. The four-momentum of a hadron is denoted by $p_h = (E_h, \vec{p}_h)$. These hadrons can be characterized by their fractional energy (relative to the virtual photon)

$$z \equiv \frac{P \cdot p_h}{P \cdot q} \stackrel{lab}{=} \frac{E_h}{\nu} \ , \tag{2.7}$$

their transverse momentum (again relative to the virtual photon)

$$p_T \equiv \frac{|\vec{p}_h \times \vec{q}|}{|\vec{q}|} \ , \tag{2.8}$$

and their azimuthal angle ϕ_h (relative to the scattering plane). Integrating over the azimuthal angle, as it is often done, the semi-inclusive cross section then depends, in addition to the inclusive variables mentioned above, on two extra quantities per hadron, which can be chosen as (z,p_T).

2.2 Deep-inelastic scattering cross sections

This section deals with the deep-inelastic scattering cross section, introducing first the general formalism and averaging over the spin, and later focussing on the spin-dependent case. The topic has been covered in much detail e.g. in [4, 5, 6, 7, 8, 9].

The inclusive DIS cross section, calculated for the single photon exchange as depicted in the Feynman diagram of Fig. 2.1, can be written as the product of the leptonic tensor $L_{\mu\nu}$ and the hadronic tensor $W^{\mu\nu}$ [4, 5]. The differential cross section to detect the scattered lepton in the solid angle $d\Omega$ and in the energy range $(E', E' + dE')$ in the laboratory frame can be expressed as

$$\frac{d^2\sigma}{dE'd\Omega} = \frac{\alpha^2}{2MQ^4}\frac{E'}{E}L_{\mu\nu}W^{\mu\nu} \ , \tag{2.9}$$

with α the fine structure constant. The leptonic tensor $L_{\mu\nu}$ describes the emission of a virtual photon by a lepton and is calculable in Quantum Electrodynamics, while the hadronic tensor $W^{\mu\nu}$ contains information on the structure of the nucleon as probed by the virtual photon.

The leptonic tensor, after summation over the spin s' of the final state lepton, can be split into a symmetric (S) and an antisymmetric (A) part under μ, ν interchange (parity transformation) according to

$$L_{\mu\nu}(k, s; k') = \sum_{s'} L_{\mu\nu}(k, s; k', s') = L^{(S)}_{\mu\nu}(k; k') + iL^{(A)}_{\mu\nu}(k, s; k') \ . \tag{2.10}$$

The symmetric part is spin-independent, while the antisymmetric part on the contrary, depends on the spin s of the incident lepton. Unlike the lepton tensor, the hadronic tensor cannot be perturbatively derived from first principles[4] but serves to parametrize the unknown nucleon structure probed by the photon. This tensor depends only on q,P, and S and can, by imposing parity and current conservation as well as time-reversal invariance, also be decomposed into a symmetric and an antisymmetric part. The symmetric part is again spin-independent, while the antisymmetric part depends on the nucleon spin,

$$W_{\mu\nu}(q; P, S) = W^{(S)}_{\mu\nu}(q; P) + iW^{(A)}_{\mu\nu}(q; P, S) \ . \tag{2.11}$$

The symmetric part can be written in terms of two spin-independent *inelastic form factors*, W_1 and W_2, while the antisymmetric part can be written in terms of two spin-dependent ones, G_1 and G_2,

$$\begin{aligned} \frac{1}{2M}W^{(S)}_{\mu\nu}(q; P) &= \left(-g_{\mu\nu} + \frac{q_\mu q_\nu}{q^2}\right) W_1(P\cdot q, q^2) \\ &+ \left[\left(P_\mu - \frac{P\cdot q}{q^2}q_\mu\right)\left(P_\nu - \frac{P\cdot q}{q^2}q_\nu\right)\right]\frac{W_2(P\cdot q, q^2)}{M^2} \ , \end{aligned} \tag{2.12}$$

[4]In the future lattice QCD calculations might provide a direct (non-perturbative) theoretical access to the hadronic tensor.

$$\begin{aligned}\frac{1}{2M}W^{(A)}_{\mu\nu}(q;P,S) &= \epsilon_{\mu\nu\alpha\beta}q^{\alpha}\{MS^{\beta}G_1(P\cdot q,q^2) \\ &\quad + \left[(P\cdot q)S^{\beta}-(S\cdot q)P^{\beta}\right]\frac{G_2(P\cdot q,q^2)}{M}\}\ .\end{aligned} \tag{2.13}$$

According to standard notation, $g_{\mu\nu}$ is the metric tensor and $\epsilon_{\mu\nu\alpha\beta}$ the totally antisymmetric Levi-Civita tensor with $\epsilon_{0123}=+1$.
The inelastic form factors W_1,W_2,G_1 and G_2 are Lorentz-invariant scalars and depend on two independent Lorentz-invariant scalar combinations of P and q, which can, alternatively to $(P\cdot q, q^2)$, also be chosen as (x, Q^2). They can be rewritten in terms of four dimensionless structure functions, two spin-independent ones, F_1,F_2, and two spin-dependent, g_1,g_2 (in the following often named unpolarized and polarized structure functions), as

$$F_1(x,Q^2)\equiv MW_1(P\cdot q,q^2)\ ,\quad g_1(x,Q^2)\equiv\tfrac{(P\cdot q)^2}{\nu}G_1(P\cdot q,q^2)\ , \tag{2.14}$$
$$F_2(x,Q^2)\equiv \nu W_2(P\cdot q,q^2)\ ,\quad g_2(x,Q^2)\equiv\nu(P\cdot q)G_2(P\cdot q,q^2)\ . \tag{2.15}$$

In the energy regime where the contribution of the Z_0-exchange cannot be neglected ($Q^2\geq m_{Z_O}$) the most general form of the hadronic tensor includes one more unpolarized structure function, namely F_3, and three more polarized structure functions, namely g_3,g_4 and g_5.
Using the symmetric and antisymmetric parts of the leptonic and hadronic tensors in Eq. (2.9) one obtains for the cross section

$$\frac{d^2\sigma}{dE'd\Omega}=\frac{\alpha^2}{2MQ^4}\frac{E'}{E}\left[L^{(S)}_{\mu\nu}W^{\mu\nu(S)}-L^{(A)}_{\mu\nu}W^{\mu\nu(A)}\right]\ . \tag{2.16}$$

Since the electromagnetic interaction conserves parity, only terms with like symmetry contribute to the cross section. The spin-independent term in the cross section is accounted for by the symmetric parts of the leptonic and hadronic tensors. The spin-dependent term is given by the antisymmetric parts of the leptonic and hadronic tensors and will only contain non-zero contributions if both the lepton and the nucleon polarization are non-zero. Only if both the lepton and the nucleon are polarized can the spin-dependent structure functions be measured (hence the alternative terminology *polarized* structure functions).

2.2.1 The unpolarized cross section

The spin-independent DIS cross section for the scattering of unpolarized leptons off unpolarized nucleons (in this thesis often named unpolarized DIS cross section) can be derived from Eq. (2.16) by averaging over the spins in the initial state, and summing over the spins in the final state [4]. In this case only the symmetric parts of the leptonic and hadronic tensors contribute,

$$\frac{d^2\sigma^{unpol}}{dE'd\Omega}(k,P;k')=\frac{\alpha^2}{2MQ^4}\frac{E'}{E}L^{(S)}_{\mu\nu}(k;k')W^{\mu\nu(S)}(q;P)\ . \tag{2.17}$$

Inserting explicit expressions for the symmetric part of the leptonic and hadronic tensors, one obtains the unpolarized cross section [5, 6] expressed in terms of the unpolarized structure functions F_1 and F_2 according to

$$\frac{d^2\sigma^{unpol}}{dE'd\Omega} = \underbrace{\frac{4\alpha^2 E'^2}{Q^4} cos^2\left(\frac{\theta}{2}\right)}_{\sigma_{Mott}} \left[\frac{2}{M}F_1(x,Q^2)\tan^2\left(\frac{\theta}{2}\right) + \frac{1}{\nu}F_2(x,Q^2)\right] \; . \tag{2.18}$$

The factor σ_{Mott} is the Mott cross section which describes the elastic scattering of a relativistic point-like spin-1/2 electron off a point-like spinless nucleus. Thus the unpolarized structure functions parameterize the deviation of the observed DIS cross section from the Mott cross section.

The DIS process can also be viewed as the absorption of a virtual photon by the nucleon, with the charged lepton as the source of the virtual photon. In this view the DIS cross section can be split into two parts: the virtual photon flux (the probability for photon emission by the charged lepton) and the virtual photon-nucleon absorption cross section. Factorizing into the fluxes Γ_T and Γ_L of transverse or longitudinal virtual photons and the photon-nucleon absorption cross sections $\sigma_T(x,Q^2)$ and $\sigma_L(x,Q^2)$ for transverse or longitudinal virtual photons, one obtains for the lepton-nucleon cross section

$$\frac{d^2\sigma^{unpol}}{dxdQ^2} = \Gamma_T(x,Q^2)\sigma_T(x,Q^2) + \Gamma_L(x,Q^2)\sigma_L(x,Q^2) = \Gamma_T\sigma_T(1+\epsilon R) \; , \tag{2.19}$$

where the ratios $R = \sigma_L/\sigma_T$ and $\epsilon = \Gamma_L/\Gamma_T$ have been introduced. Since neither the flux nor the virtual photon-nucleon cross section but only their product are observables, there exist different definitions for the flux. In the so-called Hand convention [10] the flux is defined a:

$$\Gamma_T = \frac{\alpha(1-x)}{2\pi^2 Q^2 \nu}\left[y^2\left(1-\frac{2m_e^2}{Q^2}\right) + \frac{2}{1+\gamma^2}\left(1-y-\frac{Q^2}{4E^2}\right)\right] \; , \tag{2.20}$$

and the virtual photon polarization as

$$\epsilon = \left[1 + \frac{1}{2}\left(1-\frac{2m_e^2}{Q^2}\right)\frac{y^2+\frac{Q^2}{E^2}}{1-y-\frac{Q^2}{4E^2}}\right]^{-1} \; , \tag{2.21}$$

with $\gamma^2 = Q^2/\nu^2$.
Comparing the expression for the unpolarized lepton-nucleon cross section in terms of the photon-nucleon absorption cross sections, Eq. (2.19), with the expression in terms of the unpolarized structure functions, Eq. (2.18), the ratio R of the photon-nucleon absorption cross sections can be related to the unpolarized structure functions as

$$R(x,Q^2) = \frac{\sigma_L(x,Q^2)}{\sigma_T(x,Q^2)} = \frac{(1+\gamma^2)F_2(x,Q^2) - 2xF_1(x,Q^2)}{2xF_1(x,Q^2)} \; . \tag{2.22}$$

An overview of experimental data and parametrizations available for R is given e.g. in [11]. Using Eq. (2.22) for the relation between R and the structure functions F_1 and F_2,

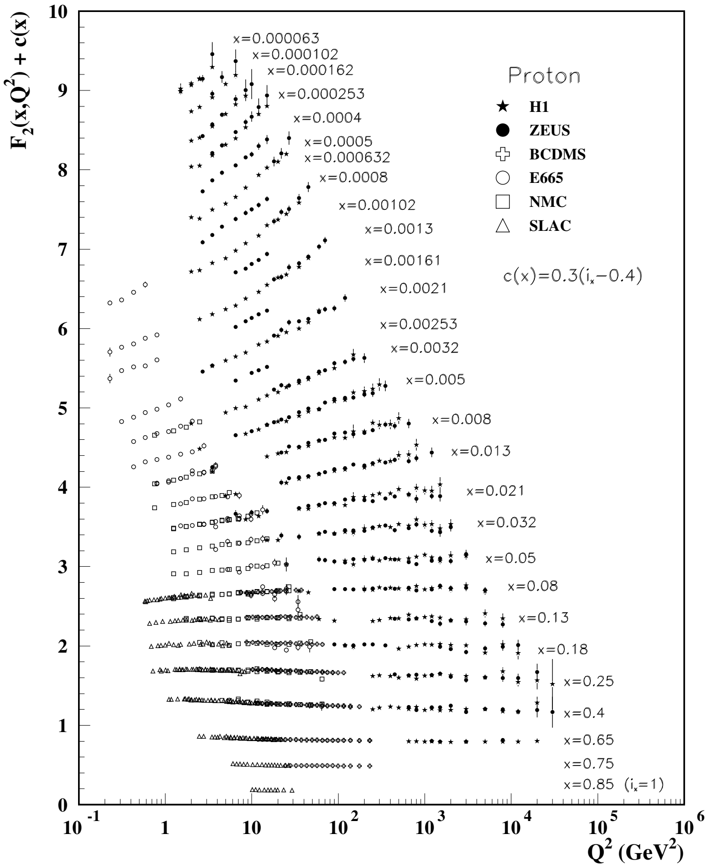

Figure 2.2: *Presently existing data of the unpolarized proton structure function $F_2^p(x,Q^2)$. The plot is taken from [12].*

the unpolarized cross section from Eq. (2.18) can be rewritten as

$$\frac{d^2\sigma^{unpol}}{dxdQ^2} = \frac{4\pi\alpha^2}{xQ^4}\left[1 - y - \frac{Q^2}{4E^2} + \frac{(1+\gamma^2)}{(1+R(x,Q^2))}\frac{(y^2+\frac{Q^2}{E^2})}{2}\right]F_2(x,Q^2)\ , \qquad (2.23)$$

where the differential cross section $\frac{d^2\sigma}{dE'd\Omega}$ has been changed into the differential cross section $\frac{d^2\sigma}{dxdQ^2}$. The structure functions F_2 for proton and deuteron, F_2^p and F_2^d, have been measured over a wide kinematic range in x and Q^2 by various fixed target experiments at SLAC and CERN. Collider experiments at DESY have extended the data set for F_2^p to very low values of x. Presently existing data for F_2^p are shown in Fig. 2.2.

2.2.2 The polarized cross section

If Eq. (2.16) is not averaged over the spins in the initial state, i.e. if the incident lepton beam and the target are polarized, the spin-dependent cross section for scattering of

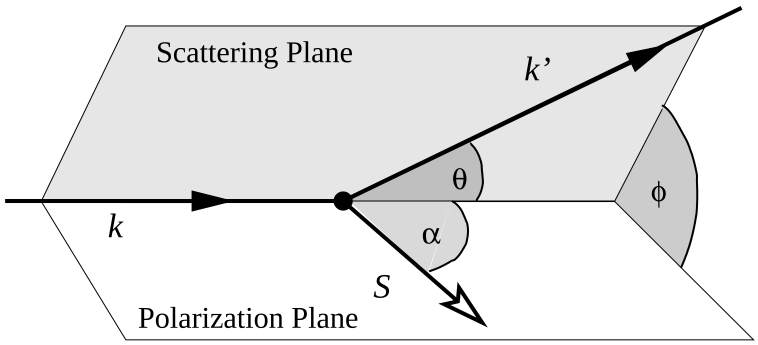

Figure 2.3: *Definitions of angles and planes relevant to describe polarized deep-inelastic scattering processes.*

polarized leptons off polarized nucleons (in this thesis often named polarized cross section) depends on the antisymmetric parts of the leptonic and hadronic tensors. The polarized structure functions g_1 and g_2 can be accessed by isolating the antisymmetric parts of the cross section. This can be achieved by taking the difference of the cross sections with opposite target spin orientations S and $-S$ with respect to the incident lepton spin and summing over the spins of the scattered lepton in the final state [5],

$$\sum_{s'}\left[\frac{d^2\sigma}{dE'd\Omega}(k,s,P,-S;k',s') - \frac{d^2\sigma}{dE'd\Omega}(k,s,P,S;k',s')\right] =$$

$$\frac{\alpha^2}{2MQ^4}\frac{E'}{E}L^{(A)}_{\mu\nu}(k,s;k')W^{\mu\nu(A)}(q;P,S)\ . \tag{2.24}$$

For a longitudinally polarized lepton, i.e. a lepton with spin along the direction of motion, denoted by $\rightarrow$, this cross section difference [5] is given by

$$\frac{d^2\sigma^{\rightarrow,-S}}{dE'd\Omega} - \frac{d^2\sigma^{\rightarrow,S}}{dE'd\Omega} =$$

$$\frac{4\alpha^2}{M\nu Q^2}\frac{E'}{E}\left[(E\cos\alpha + E'\cos\psi)g_1 + \frac{2EE'}{\nu}(\cos\psi - \cos\alpha)g_2\right]\ , \tag{2.25}$$

where $\cos\psi = \sin\theta\sin\alpha\cos\Phi + \cos\theta\cos\alpha$. The angles are defined as shown in Fig. 2.3. The angle α is fixed by the nucleon spin direction $\vec{S}$ and the momentum of the incident lepton $\vec{k}$; θ denotes the angle of the momentum of the scattered lepton $\vec{k'}$ with respect to the momentum of the incident lepton $\vec{k}$. The scattering plane, determined by the momenta of the incident and scattered lepton $\vec{k}$ and $\vec{k'}$, and the polarization plane, given by the momentum of the incident lepton $\vec{k}$ and the nucleon spin direction $\vec{S}$, define the angle Φ. The angle ψ is the one between the momentum of the scattered lepton $\vec{k'}$ and the nucleon spin direction $\vec{S}$.

Two configurations for the angle α are especially interesting, namely $\alpha = 0$ and $\alpha = \pi/2$. In the first case the nucleon spin is aligned parallel ($\Rightarrow$) or antiparallel ($\Leftarrow$) to the spin of the incident lepton ($\cos\psi = \cos\theta$). In the second case the nucleon spin is oriented

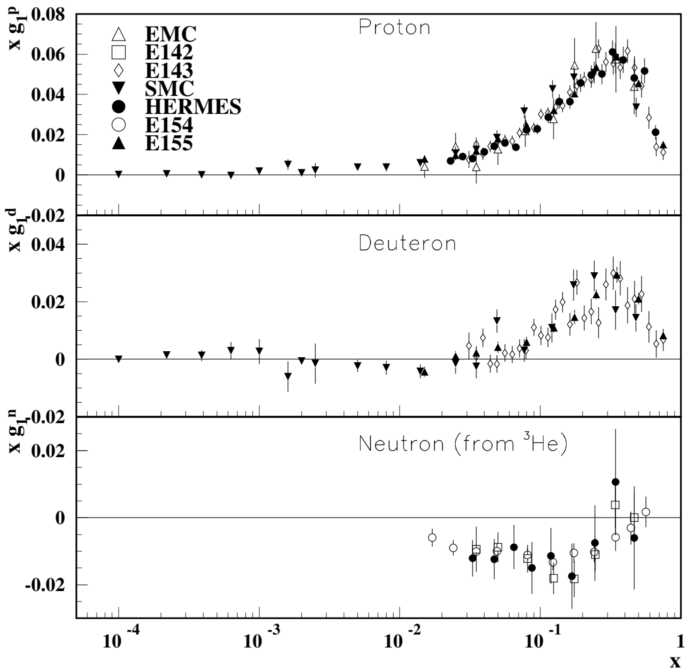

Figure 2.4: *Presently existing data of the polarized structure function* $xg_1(x, Q^2)$ *for proton, deuteron and neutron. The plot is taken from [12].*

transversely (up $\Uparrow$ and down $\Downarrow$) with respect to the spin of the incident lepton ($\cos\psi = \sin\theta\cos\Phi$). The two corresponding cross section differences [4] then simplify to

$$\frac{d^2\sigma^{\overleftarrow{\Rightarrow}}}{dE'd\Omega} - \frac{d^2\sigma^{\overrightarrow{\Rightarrow}}}{dE'd\Omega} = \frac{4\alpha^2}{M\nu Q^2}\frac{E'}{E}\left[(E + E'\cos\theta)g_1 - \frac{Q^2}{\nu}g_2\right] , \tag{2.26}$$

$$\frac{d^2\sigma^{\rightarrow\Uparrow}}{dE'd\Omega} - \frac{d^2\sigma^{\rightarrow\Downarrow}}{dE'd\Omega} = \frac{4\alpha^2}{M\nu Q^2}\frac{E'^2\sin\theta\cos\Phi}{E}\left[g_1 + \frac{2E}{\nu}g_2\right] . \tag{2.27}$$

The former cross section is largely determined by g_1 since the contribution from g_2 is suppressed by a factor $Q^2/E\nu = 2M\nu x/E\nu \approx M/E$ ($E \gg M$). The latter cross section strongly depends on g_2 as $2E/\nu > 1$. Measurements of the structure function g_1 were performed by various fixed target experiments at SLAC, CERN and DESY. Fig. 2.4 shows presently existing data for g_1^p, g_1^d, and g_1^n.

2.2.3 Cross section asymmetries

In principle the polarized structure functions g_1 and g_2 can be determined by a measurement of the two cross section differences for longitudinally and transversely polarized targets discussed in the previous subsection. However, the precision needed for measuring absolute cross sections is experimentally difficult to reach. Therefore, one rather measures cross section asymmetries, as in an asymmetry measurement (spin-independent) systematic instrumental effects largely cancel. The longitudinal and transverse double spin asymmetries $A_{\|}$ and $A_{\perp}$ are defined as

$$A_{\|} \equiv \frac{\sigma^{\rightleftarrows} - \sigma^{\rightrightarrows}}{\sigma^{\rightleftarrows} + \sigma^{\rightrightarrows}} \ , \quad A_{\perp} \equiv \frac{\sigma^{\rightarrow\Downarrow} - \sigma^{\rightarrow\Uparrow}}{\sigma^{\rightarrow\Downarrow} + \sigma^{\rightarrow\Uparrow}} \ . \tag{2.28}$$

Here σ is the shorthand notation for the differential cross sections $\frac{d^2\sigma}{dE'd\Omega}$ from Eqs. (2.26) and (2.27). The double spin asymmetry $A_{\|}$ can also be written in terms of the polarized and unpolarized cross sections

$$\Delta\sigma = \frac{1}{2}(\sigma^{\rightleftarrows} - \sigma^{\rightrightarrows}) \ , \quad \sigma_0 = \frac{1}{2}(\sigma^{\rightleftarrows} + \sigma^{\rightrightarrows}) \ , \tag{2.29}$$

yielding

$$A_{\|} = \frac{\Delta\sigma}{\sigma_0} \ . \tag{2.30}$$

As discussed for the unpolarized cross section in section 2.2.1, also the polarized cross section can be expressed in terms of virtual photon-nucleon absorption cross sections. One defines the two asymmetries A_1 and A_2 as

$$A_1 \equiv \frac{\sigma^T_{\frac{1}{2}} - \sigma^T_{\frac{3}{2}}}{\sigma^T_{\frac{1}{2}} + \sigma^T_{\frac{3}{2}}} \ , \quad A_2 \equiv \frac{2\sigma^{LT}_{\frac{1}{2}}}{\sigma^T_{\frac{1}{2}} + \sigma^T_{\frac{3}{2}}} \ . \tag{2.31}$$

Here σ is the shorthand notation for the differential virtual photon-nucleon absorption cross sections. The subscripts $\frac{1}{2}$ and $\frac{3}{2}$ represent the projection of the total angular momentum of the virtual photon-nucleon system along the momentum of the photon. The superscripts T and L denote the polarization of the virtual photon. Accordingly, $\sigma^T_{\frac{1}{2}}$ and $\sigma^T_{\frac{3}{2}}$ define the differential cross sections for the absorption of a transverse photon with the spin antiparallel and parallel to the nucleon spin (in the following named virtual photon-nucleon absorption cross section). The term $\sigma^{LT}_{\frac{1}{2}}$ arises from the interference of transverse and longitudinal photon-nucleon absorption amplitudes. The list of virtual photon-nucleon absorption cross sections is completed by $\sigma^L_{\frac{1}{2}}$, which denotes the differential cross section for the absorption of a longitudinal virtual photon. Those cross sections can be rewritten to obtain the cross sections σ_L and σ_T for the absorption of longitudinal and transverse virtual photons already introduced in section 2.2.1,

$$\sigma_L \equiv \sigma^L_{\frac{1}{2}} \ , \tag{2.32}$$

$$\sigma_T \equiv \frac{1}{2}\left(\sigma^T_{\frac{1}{2}} + \sigma^T_{\frac{3}{2}}\right) \ . \tag{2.33}$$

The relation between A_1 and A_2 and the experimental double spin asymmetries $A_{\|}$ and $A_{\perp}$ is given by

$$A_{\|} = D(A_1 + \eta A_2) \ , \tag{2.34}$$

$$A_\perp = D(\xi A_2 - \frac{\eta}{\xi}A_1) , \tag{2.35}$$

where η and ξ are purely kinematical factors. The so-called depolarization factor D is the effective polarization of the virtual photon. It describes the degree of depolarization in the spin transfer from the initial lepton to the virtual photon and depends on kinematic factors and the cross section ratio $R = \sigma_L/\sigma_T$, and is given by

$$D \equiv \frac{y\left[\left(1+\frac{\gamma^2 y}{2}\right)(2-y) - \frac{2y^2 m_e^2}{Q^2}\right]}{y^2\left(1-\frac{2y^2 m_e^2}{Q^2}\right)(1+\gamma^2) + 2(1+R)\left(1-y-\frac{Q^2}{4E^2}\right)} . \tag{2.36}$$

It can be shown that the virtual photon-nucleon absorption cross section asymmetries A_1 and A_2 are related to the structure functions, defined above, by

$$A_1 = \frac{g_1 - \gamma^2 g_2}{F_1} , \quad A_2 = \frac{\gamma(g_1+g_2)}{F_1} , \tag{2.37}$$

where again $\gamma^2 = Q^2/\nu^2$.
Combining Eqs. (2.37) and (2.34) one can express the double spin asymmetry $A_{||}$ in terms of the structure functions g_1, g_2 and F_1,

$$A_{||} = D\frac{g_1(1+\eta\gamma) + g_2(\eta\gamma - \gamma^2)}{F_1} . \tag{2.38}$$

The contribution of g_2 in this equation is suppressed by the kinematic factors $\eta\gamma$ and γ^2, which are small in the HERMES kinematic range. Neglecting the contribution of g_2 altogether Eq. (2.38) simplifies to

$$A_{||} \approx D(1+\eta\gamma)\frac{g_1}{F_1} . \tag{2.39}$$

Taking F_1 from unpolarized cross section measurements this relation allows to approximately extract g_1 from a measurement of $A_{||}$.

In analogy to section 2.2.1, where the unpolarized lepton-nucleon cross section was written in terms of the fluxes Γ_T and Γ_L of transverse or longitudinal virtual photons from unpolarized leptons and the virtual photon-nucleon absorption cross sections $\sigma_T(x, Q^2)$ and $\sigma_L(x, Q^2)$ for transverse or longitudinal virtual photons by unpolarized nucleons, also $A_{||}$ can now be expressed in this formalism as

$$A_{||} = \frac{\Delta\sigma^{ep}}{\sigma_0^{ep}} = D\frac{\Delta\sigma_T^{\gamma^* p}}{\sigma_T^{\gamma^* p}} . \tag{2.40}$$

Here the superscripts ep and $\gamma^* p$ have been added to the cross sections to clarify the transition from lepton-nucleon cross sections to virtual photon-nucleon absorption cross sections. The cross section difference for the absorption of longitudinal virtual photons by polarized nucleons $\Delta\sigma_L$ vanishes and the interference term σ_{LT} is neglected, while σ_L is contained in D, the depolarization factor as given in Eq. (2.36). This factor can be written as

$$D = \frac{\Delta\Gamma_T}{\Gamma_T + R\Gamma_L} , \tag{2.41}$$

where Γ_T and Γ_L are the previously defined fluxes, while $\Delta\Gamma_T$ is just a notation for all kinematic terms of the nominator (The notation $\Delta\Gamma_T$ is chosen since it collects the kinematic terms associated with $\Delta\sigma$). With this notations one gets

$$A_{\|} = \frac{\Delta\sigma^{ep}}{\sigma_0^{ep}} = \frac{\Delta\Gamma_T \Delta\sigma_T^{\gamma^* p}}{\Gamma_T \sigma_T^{\gamma^* p} + \Gamma_L \sigma_L^{\gamma^* p}} \ . \tag{2.42}$$

2.3 The quark parton model

The DIS experiments at SLAC in the late 1960s and early 1970s showed that the unpolarized structure function F_2 becomes approximately independent of Q^2 for large momentum transfer Q^2 and large hadronic invariant mass W [13]. This confirmed Bjørken's prediction [14] that

$$\lim_{Q^2,\nu\to\infty} F_{1,2}(x, Q^2) = F_{1,2}(x) \ . \tag{2.43}$$

This phenomenon is called Bjørken scaling. This scaling property is a key aspect of the parton model as developed by Bjørken [15] and Feynman [16]. In this model, deep-inelastic lepton-nucleon scattering at high enough energies is interpreted as the incoherent elastic scattering of the lepton off free point-like spin-$\frac{1}{2}$ charged nucleon constituents, called partons. These partons were later recognized as the quarks which Gell-Mann and Zweig had proposed in 1964 to form bound states, accounting for the global properties of all hadrons at low energies. The combination of these ideas has since been widely known as the Quark Parton Model (QPM).

The QPM can be formulated in the so-called Breit frame. In this frame the nucleon moves with very high momentum in the negative z-direction so that the parton and nucleon masses as well as the parton momenta transverse to the direction of motion can be neglected. The struck parton recoils with its original momentum reversed. As the structure functions are Lorentz invariant their description in the Breit frame is valid in any other frame as well. The scattering can be viewed in the Breit frame as the absorption of a virtual photon by one of the collinearly moving partons inside the nucleon. The struck quark carries a fraction of the total momentum of the nucleon $p_q = \xi P$. After the absorption the parton is again on-shell so that its four-momentum vanishes,

$$(\xi P + q)^2 = \xi^2 P^2 + 2\xi P q - Q^2 = 0 \ . \tag{2.44}$$

In the scaling limit where Q^2 is very large the term $\xi^2 P^2$ is negligible and $\xi = Q^2/2M\nu$ which is equivalent to the definition of Bjørken-x in section 2.1. In the QPM the Bjørken-x variable can thus be interpreted as the fractional momentum of the nucleon carried by the struck quark. The DIS process is then the incoherent sum of elastic scattering off the free partons carrying a momentum fraction x of the nucleon momentum.

In the QPM the nucleon can be described by the parton distribution functions $q_f(x)$ which give the probability to find a quark of flavour f and fractional momentum x in the nucleon. Using the notations $q_f^{\overset{\rightarrow}{\Rightarrow}}(x)$ and $q_f^{\overset{\leftarrow}{\Rightarrow}}(x)$ for the probabilities to find a quark of flavour f with momentum fraction x and spin parallel or antiparallel, respectively, to the nucleon spin, one can construct combinations of these probabilities defining the spin-independent and spin-dependent parton distribution functions as

$$q_f(x) = q_f^{\overset{\rightarrow}{\rightarrow}}(x) + q_f^{\overset{\rightarrow}{\leftarrow}}(x) \;, \tag{2.45}$$

$$\Delta q_f(x) = q_f^{\overset{\rightarrow}{\rightarrow}}(x) - q_f^{\overset{\rightarrow}{\leftarrow}}(x) \;. \tag{2.46}$$

In this equations $q_f(x)$ represents the distribution of the partons averaged over the spin degrees of freedom, while $\Delta q_f(x)$ is given by the difference of the distributions of the partons with different helicity states within the nucleon.

The unpolarized structure functions are then obtained from the unpolarized parton distribution functions by taking the charge-weighted sums over the quark flavours f and integrating over the momentum fractions ξ as

$$F_1(x) = \frac{1}{2}\sum_f \int_0^1 d\xi e_f^2 q_f(\xi)\delta(\xi - x) = \frac{1}{2}\sum_f e_f^2 q_f(x) \;, \tag{2.47}$$

$$F_2(x) = \sum_f \int_0^1 d\xi \xi e_f^2 q_f(\xi)\delta(\xi - x) = \sum_f x e_f^2 q_f(x) \;. \tag{2.48}$$

Similarly, the polarized structure functions can be expressed as the charged weighted sums of the polarized parton distribution functions as

$$g_1(x) = \frac{1}{2}\sum_f e_f^2 (q_f^{\overset{\rightarrow}{\rightarrow}}(x) - q_f^{\overset{\rightarrow}{\leftarrow}}(x)) = \frac{1}{2}\sum_f e_f^2 \Delta q_f(x) \;, \tag{2.49}$$

$$g_2(x) = 0 \;. \tag{2.50}$$

The sums run over all quark flavours f (including antiquarks) in the nucleon and e_f is the charge of the quark with flavour f. Because of the large masses of c, b and t quarks, in practice only the three lightest flavours contribute to the structure functions, i.e. the sums are reduced to run only over flavours u, d, s and their corresponding antiquarks.
Eqs. (2.47) and (2.48) for the unpolarized structure functions satisfy the so-called Callan-Gross relation [17]

$$F_2(x) = 2xF_1(x) \;. \tag{2.51}$$

This relation is in agreement with Eq. (2.22), relating R, F_1 and F_2, in the Bjørken limit $Q^2 \to \infty$ and $\nu \to \infty$ (and hence $\gamma \to 0$). If one assumes the spin-$\frac{1}{2}$ nature of the quarks the longitudinal photon-nucleon absorption cross section σ_L vanishes in this limit. This is a consequence of helicity conservation at the virtual photon-quark vertex. As the parton recoils in the Breit frame its spin also has to be flipped in order to conserve the helicity of the parton. This is not possible by the absorption of a longitudinal virtual photon which has spin z-component 0. Thus $\sigma_L \to 0$ and therefore $R \to 0$. If instead one assumes spin-0 partons, the relation reads quite differently. In this case, transverse photons cannot couple to the (spin-0) partons because of helicity conservation. Thus $\sigma_T \to 0$, therefore $R \to \infty$ and $2xF_1(x)/F_2(x) = 0$. This is clearly excluded by the results from early DIS experiments performed at SLAC [13], which yielded data close to $2xF_1/F_2 \simeq 1$, thus proving the spin-1/2 nature of quarks.

In the QPM the polarized structure function g_1 is sensitive to the polarized parton distributions in the nucleon. Because the nucleon constituents are spin-$\frac{1}{2}$ partons the spin-1 transverse photon has to be absorbed by partons with both momentum and spin pointing opposite to momentum and spin of the photon (photon and parton helicities are equal) in order to obtain a recoiling spin-$\frac{1}{2}$ parton in the final state with flipped spin which is needed to conserve helicity in the Breit frame. The cross section $\sigma^T_{1/2}$ ($\sigma^T_{3/2}$) to absorb a virtual photon by a nucleon with the same helicity (opposite helicity) is then proportional to $q^{\rightrightarrows}$ ($q^{\rightleftarrows}$), the parton distribution function for partons with spin parallel (antiparallel) to the nucleon. Here q represents the sum over all flavours. The structure function g_1 is proportional to the difference of the two cross sections, $\sigma^T_{1/2} - \sigma^T_{3/2}$. In the QPM, the partons move collinearly to the nucleon, and the structure function g_2 has no interpretation and vanishes because it is related to the transverse degrees of freedom of the quarks in the nucleon not included in this model.

The parton distribution functions $q_f(x)$ are normalized so that certain sum rules are fulfilled. For the proton the uud quark content has to be reproduced by integrating over the unpolarized parton distribution functions, (with the shorthand notation $f(x)$ instead of $q_f(x)$),

$$\int_0^1 dx(u(x) - \bar{u}(x)) = \int_0^1 dx u_v(x) = 2 \ , \tag{2.52}$$

$$\int_0^1 dx(d(x) - \bar{d}(x)) = \int_0^1 dx d_v(x) = 1 \ , \tag{2.53}$$

$$\int_0^1 dx(s(x) - \bar{s}(x)) = 0 \ . \tag{2.54}$$

The distributions $u_v(x)$ and $d_v(x)$ are the valence quark distributions of the proton. By assuming isospin symmetry the distributions of the neutron can be obtained from the distributions of the proton: $u^n(x) = d(x), d^n(x) = u(x), s^n(x) = s(x)$, and analogously for the antiquarks.

2.4 Quantum Chromodynamics

The scaling of the unpolarized structure functions, predicted by the quark parton model, is only approximately valid. At small and large x it is clearly violated as can be seen in Fig. 2.2. With increasing Q^2 the structure function F_2 increases significantly at small x and slowly decreases at large x. This cannot be explained in the framework of the QPM. Another experimental result asking for an extension of the QPM is the observation that the total momentum in the nucleon is not carried by the quarks alone. Integrating their momentum distributions does not reproduce the total nucleon momentum,

$$\int_0^1 dx x \sum_f q_f(x) < 1 \ , \tag{2.55}$$

but only accounts for about half of this momentum [18].

Without having to abandon the successful quark parton model both observations can be explained if interactions among the partons are introduced. These are not accounted for in the simple version of the model. Such interactions are incorporated in the framework of Quantum Chromodynamics (QCD), the theory of the strong interaction, which is part of the Standard Model. Various introductions to QCD are available, e.g. [19, 20, 21, 22]. QCD represents a local gauge theory with an underlying non-Abelian $SU(3)_{colour}$ symmetry. The Langrangian of QCD describes three massive Dirac fields (the three colours of a given quark flavour) in interaction with eight massless vector fields (the gluons). In this theory quarks carry one of the three colour charges of the strong force, commonly denoted as red, green and blue. Accordingly antiquarks carry anticoulour. Coloured quarks interact with each other via the exchange of gluons, the field quanta of the strong force. Gluons are massless spin-1 bosons and carry colour charge as well, and therefore can couple directly to each other, either at three- or four-gluon-vertices. Every particle occurring in nature is a colour singlet. For baryons the colour state is always composed of red, green and blue, for antibaryons of antired, antigreen and antiblue. Mesons carry one unit of colour and the corresponding unit of anticolour, making them colour neutral as well.

The strength of the strong coupling is expressed by its coupling constant α_s which depends on the renormalization energy scale μ^2 (usually chosen to be equal to Q^2 in DIS). At first order (Leading Order) in perturbation theory, α_s is given by

$$\alpha_s^{(LO)}(\mu^2) = \frac{4\pi}{\beta_0 ln(\mu^2/\Lambda^2)} \ , \tag{2.56}$$

and at Next-to-Leading Order (NLO) as

$$\alpha_s^{(NLO)}(\mu^2) = \alpha_s^{(LO)}(\mu^2) \left[1 - \frac{\beta_1 ln(ln(\mu^2/\Lambda^2))}{\beta_0^2 ln(\mu^2/\Lambda^2)} \right] \ . \tag{2.57}$$

The coefficients in the above equations are given as

$$\beta_0 = 11 - \frac{2}{3} n_f , \quad \beta_1 = 102 - \frac{38}{3} n_f \ , \tag{2.58}$$

where n_f denotes the number of (energetically allowed) quark flavours with mass less than the energy scale relevant for the process. The parameter Λ, commonly known as the QCD scale parameter, represents a lower limit for the applicability of the perturbation theory. It depends on the number of active flavours n_f and the order of the perturbation calculation, resulting in a value varying between 200 and 300 MeV. Below this energy scale, i.e. in the non-perturbative domain, quarks and gluons are very strongly bound inside the hadrons due to the strong increase in α_s, a phenomenon known as *confinement*. If on the other hand the scale becomes large, α_s becomes very small and the quarks hardly interact anymore, a property called *asymptotic freedom*. In this limit the quarks can indeed be treated as non-interacting partons, as represented by the simple expressions for the various structure functions in the QPM.

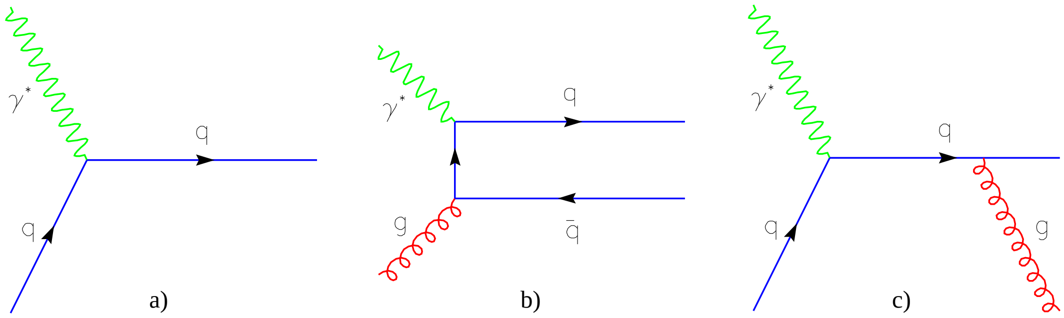

Figure 2.5: *Feynman diagrams for the leading order DIS process (a) and the two NLO processes Photon-Gluon-Fusion (b) and QCD Compton scattering (c).*

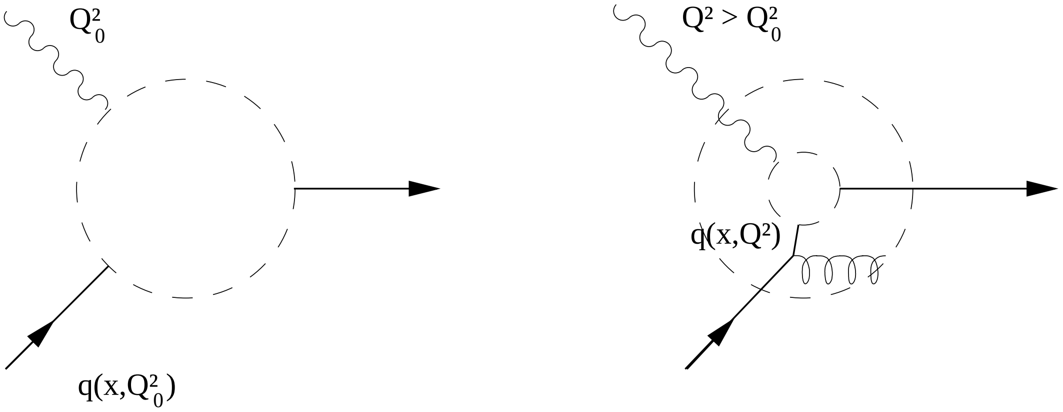

Figure 2.6: *Schematic representation of the Q^2 dependence of the parton distribution functions.*

The interactions of the quarks in the nucleon give rise to higher order corrections to the QPM. At NLO in the strong coupling ($\mathcal{O}(\alpha_s)$), photon-gluon-fusion (PGF) and QCD compton scattering (QCDC) contribute to the DIS cross section. These hard subprocesses (in this thesis often simply named processes) are depicted in Fig. 2.5. The Q^2-dependence of the (so-called running) strong coupling constant α_s also enters in the parton distribution functions. These effects lead to the observed scaling violations of the structure functions. This Q^2-dependence of the parton distribution functions can be explained graphically using the picture presented in Fig. 2.6. The quarks in the nucleon are surrounded by a cloud of gluons and quark-antiquark pairs. The value of Q^2 determines the resolution at which the nucleon structure is probed in the scattering process. For a certain value $Q^2 = Q^2_0$ the quark distribution function $q_f(x, Q^2)$ is measured. If $Q^2 > Q^2_0$ the resolution is higher and more details are resolved. In this case quarks can be resolved which carry a lower momentum fraction than before due to the emission of a gluon, or, in the same way, one can couple to a quark resulting from the splitting of a gluon into a quark-antiquark pair. Now the quark distribution function $q_f(x', Q^2)$ with momentum fraction $x' < x$ is measured. Consequently, the parton distribution functions depend on Q^2. The probability of finding a parton with large x decreases with increasing Q^2

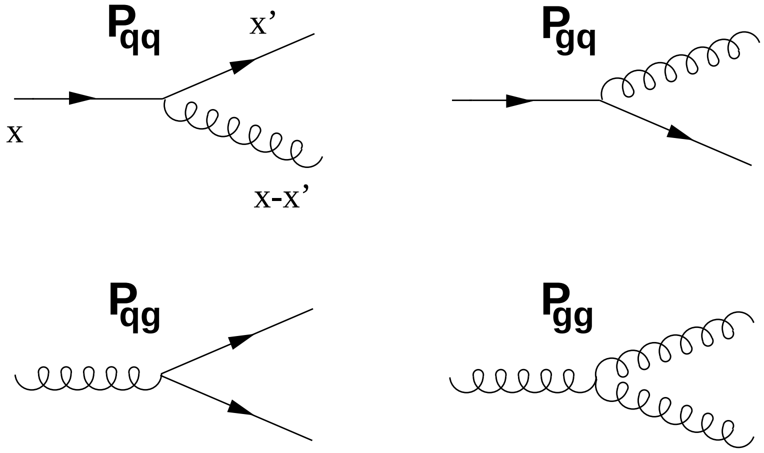

Figure 2.7: *Diagrams of the lowest order splitting functions .*

while accordingly the probability of probing partons with low x increases. This behaviour is reflected in the scaling violations, i.e. Q^2-dependence, of the unpolarized structure function F_2 which is proportional to the parton distribution functions.

The Q^2-dependence of the parton distribution functions is also named Q^2-evolution. Quantitatively, it is described by the Dokshitzer-Gribov-Lipatov-Altarelli-Parisi (DGLAP) equations

$$\frac{d}{d(lnQ^2)}q^{NS}(x,Q^2) = \frac{\alpha_s(Q^2)}{2\pi}\left[P_{qq}^{NS}\otimes q^{NS}\right](x,Q^2)\ , \tag{2.59}$$

$$\frac{d}{d(lnQ^2)}\begin{pmatrix}\Sigma(x,Q^2)\\ g(x,Q^2)\end{pmatrix} = \frac{\alpha_s(Q^2)}{2\pi}\left[\begin{pmatrix}P_{qq}^S & 2n_f P_{qg}\\ P_{gq} & P_{gg}\end{pmatrix}\otimes\begin{pmatrix}\Sigma\\ g\end{pmatrix}\right](x,Q^2)\ . \tag{2.60}$$

Here, $\otimes$ defines a convolution product

$$[f\otimes h](x,Q^2) = \int_x^1 \frac{d\xi}{\xi} f(\frac{x}{\xi},Q^2)h(\xi,Q^2)\ . \tag{2.61}$$

The functions $q^{NS}(x,Q^2)$, $\Sigma(x,Q^2)$ and $g(x,Q^2)$ are the non-singlet and singlet quark distributions, and the gluon distribution, respectively. The non-singlet and singlet quark distributions are defined as

$$q^{NS}(x,Q^2) \equiv \sum_f \left[\frac{e_f^2}{\langle e^2\rangle} - 2\right] q_f(x,Q^2)\ , \tag{2.62}$$

$$\Sigma(x,Q^2) \equiv \sum_f q_f(x,Q^2)\ , \tag{2.63}$$

where $\langle e^2\rangle = \sum_f e_f^2/n_f$. The functions $P_{ij} = P_{ij}(x'/x,Q^2)$ are called splitting functions. The probability that a parton i with momentum fraction x' originates from a parent parton j with momentum fraction x is proportional to P_{ij}. This function can be perturbatively expanded in a series in α_s. The leading order term is given by $\alpha_s(Q^2)P_{ij}^{LO}(x'/x,Q^2)$. The possible leading order splitting processes are sketched in Fig. 2.7.

The polarized parton distribution functions evolve formally in the same way as the unpolarized ones. Defining the polarized non-singlet Δq^{NS}, singlet $\Delta\Sigma$, and gluon Δg distributions and the polarized splitting functions ΔP_{ij}, in analogy to the unpolarized ones, the evolution equations for the polarized distributions follow from Eqs. (2.59) and (2.60) by replacing $q^{NS} \to \Delta q^{NS}$, $\Sigma \to \Delta\Sigma$, $g \to \Delta g$ and $P_{ij} \to \Delta P_{ij}$. The polarized gluon distribution is defined as $\Delta g = g^{\overset{\rightarrow}{\rightarrow}} - g^{\overset{\rightarrow}{\leftarrow}}$, similarly to the polarized quark distributions defined in Eq. (2.46).

The DGLAP evolution equations allow the determination of the parton distribution functions at any value of Q^2 (where perturbation theory applies), once the distributions are known at some fixed value Q_0^2. While the splitting functions are calculable in perturbative QCD, the parton distribution functions are not. They are non-perturbative objects due to singularities in collinear and soft gluon emission. Only their evolution can be calculated perturbatively. In order to obtain measurable hadronic cross sections or structure functions the parton distribution functions have to be convoluted with partonic cross sections or coefficient functions (since in this way the singularities cancel and a finite observable to all orders is constructed). The fact that this procedure is possible for every scattering process and that the PDFs involved are universal, i.e. depend only on the parton in the nucleon, but not on the hard scattering this parton enters, is called the factorization theorem of QCD.

According to the factorization theorem the unpolarized and polarized structure functions are given by

$$F_1(x,Q^2) = \frac{1}{2}\langle e^2\rangle\{C_{NS}\otimes q^{NS} + C_S\otimes\Sigma + C_g\otimes g\}(x,Q^2)\ , \tag{2.64}$$

$$g_1(x,Q^2) = \frac{1}{2}\langle e^2\rangle\{\Delta C_{NS}\otimes \Delta q^{NS} + \Delta C_S\otimes\Delta\Sigma + \Delta C_g\otimes \Delta g\}(x,Q^2)\ , \tag{2.65}$$

where $C_{NS,S,g}$ and $\Delta C_{NS,S,g}$ denote the unpolarized and polarized non-singlet, singlet and gluon coefficient functions. They describe the partonic part of the scattering and depend on the parton type, but not on the hadron involved, and are -like the splitting functions- calculable in perturbative QCD. The coefficient functions are usually expanded in α_s. The DGLAP evolution equations for the parton distributions as well as the above equations for the structure functions hold in each order of the expansion. Both coefficient and splitting functions for the unpolarized and polarized case have been calculated up to next-to-leading order. At leading order the coefficient functions are given by

$$(\Delta)C_{NS}^{(0)} = (\Delta)C_S^{(0)} = \delta\left(1 - x/\xi\right), \quad (\Delta)C_g^{(0)} = 0\ . \tag{2.66}$$

Thus, at leading order, the structure functions in the QCD framework simplify to

$$F_1(x,Q^2) = \frac{1}{2}\sum_f e_f^2 q_f(x,Q^2)\ , \tag{2.67}$$

$$g_1(x,Q^2) = \frac{1}{2}\sum_f e_f^2 \Delta q_f(x,Q^2)\ . \tag{2.68}$$

In this way one recovers the expressions of the quark parton model for the structure functions (Eqs. (2.47) and (2.49)) with the quark distributions $(\Delta)q_f(x)$ replaced by the Q^2-dependent effective distributions $(\Delta)q_f(x, Q^2)$. At this order, gluons decouple from the quarks and do not contribute to the structure functions directly, but only indirectly via the contribution to the evolution of the quark distribution functions. Only in NLO the coefficient functions $(\Delta)C_g$ are different from zero and one gets a direct contribution of the gluons to the structure functions.

2.5 Fragmentation

In the discussion so far attention has been paid only to inclusive scattering. However, the formalism described above can easily be extended to accommodate also semi-inclusive measurements in which, in addition to the scattered lepton, one or more hadrons are detected in the final state. This requires a description of the transition from the partonic to the hadronic final state (i.e. quarks and gluons to hadrons). Due to the principle of colour confinement in QCD, which allows only colour neutral states as free particles, the final state partons have to 'hadronize' into colour neutral hadrons. This hadronization process cannot be described perturbatively since in such long-range processes the energy scales are small. Instead, the hadronization is parametrized by fragmentation functions.

In describing this process, factorization is assumed, i.e. the hadronization is taken to be independent of the hard scattering process. The unpolarized (polarized) cross section for the production of a hadron h can thus be factorized into the parton distribution functions, the hard scattering cross section, and the fragmentation functions as

$$\frac{d^3(\Delta)\sigma^h}{dxdQ^2dz} = \sum_{a,b=q,\overline{q},g} (\Delta)f_a(x, Q^2) \otimes (\Delta)\hat{\sigma}_{ab}(x, Q^2) \otimes D_b^h(z, Q^2) \ , \tag{2.69}$$

where f_a is the parton distribution function of the (initial state) parton a in the nucleon, $\hat{\sigma}_{ab}$ is the partonic cross section of the process $la \rightarrow l'bX$, and D_b^h is the fragmentation function describing the transition of a (final state) parton b into a hadron h. Note that the fragmentation functions are very similar in nature to the parton distribution functions. They both encode a non-perturbative transition from a hadronic to a partonic state or vice versa.

At leading order, gluons do not contribute to the scattering, therefore the initial and the final parton are the same, namely the struck quark which then enters the hadronization, $(a = b)$. The cross section can then be written as

$$\frac{d^3(\Delta)\sigma^h}{dxdQ^2dz} = \frac{d^2(\Delta)\sigma^{incl}}{dxdQ^2} \frac{\sum_f e_f^2 (\Delta)q_f(x, Q^2) D_f^h(z, Q^2)}{\sum_f e_f^2 q_f(x, Q^2)} \ . \tag{2.70}$$

The fragmentation functions $D_f^h(z, Q^2)$ parametrize the hadronization process and can be interpreted as the probability that a quark of flavour f fragments into a hadron h with an energy fraction z of the energy of the virtual photon. The fragmentation functions are normalized to conserve energy and hadron multiplicity,

$$\sum_h \int_0^1 dz z D_f^h(z, Q^2) = 1 \ , \tag{2.71}$$

$$\sum_f \int_0^1 dz D_f^h(z, Q^2) = n_h(Q^2) \ . \tag{2.72}$$

Although the fragmentation functions are not calculable from first principles, a variety of models exists to simulate the hadronization process [23, 24], implemented in Monte Carlo programs [25, 26].

2.6 The gluon in the nucleon

As has been explained above in the framework of QCD the parton distribution functions are not calculable from first principles but need to be determined experimentally. This can be done either indirectly via the Q^2-evolution of the structure functions, or directly by considering scattering processes sensitive to a particular parton distribution. In the previous section it was explained that such a hadronic process can, according to factorization, be written as the convolution of the (calculable) partonic hard scattering with the (non-perturbative) distributions of the initial state partons inside the nucleon (and possibly the (non-perturbative) fragmentation functions accounting for the hadronization of the final state partons). This section focusses on such indirect and direct measurements of the unpolarized and polarized gluon distributions.

2.6.1 Indirect measurements through scaling violations

Scaling violations - fit formalism

As the structure functions depend on the parton distribution functions, the Q^2-evolution of the PDFs also leads to a Q^2-dependence of the structure functions, the so-called scaling violations. The gluon distribution functions are linked via the splitting functions to the quark distribution functions and thus contribute to the evolution of the structure functions. From Eqs. (2.64), (2.65) for the structure functions and the DGLAP evolution Eqs. (2.59), (2.60) for the parton distribution functions it follows that once the structure functions are measured at a fixed scale Q_0^2 they can be predicted or evaluated at any other value of Q^2. Furthermore, the DGLAP equations lead to a different Q^2-dependence for the quark and gluon distributions. These facts can be used to extract the parton distribution functions from fits to the Q^2-dependence of the structure functions.

A parametrization of the parton distribution functions at some fixed scale Q_0^2 is chosen, then evolved to another scale Q^2, and according to Eqs. (2.64), (2.65) combined to

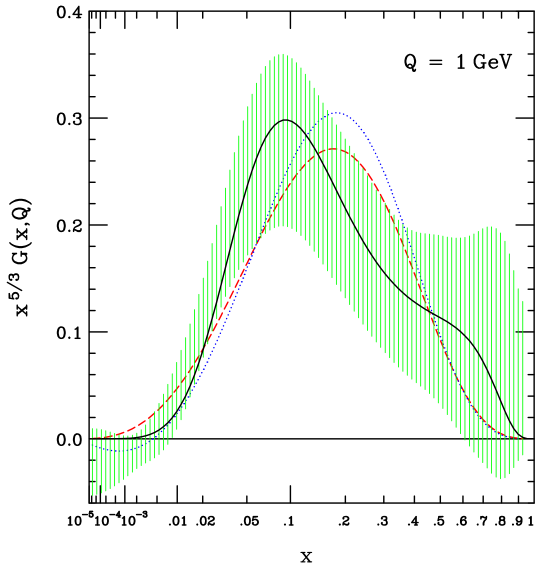

Figure 2.8: *The unpolarized gluon distribution scaled with $x^{5/3}$ as resulting from NLO QCD fits at an input scale $Q_0^2 = 1.0$ GeV ^{2}, obtained for CTEQ6 (solid line with error band) [27], compared to results obtained for CTEQ5 (dashed) [28], and MRST2001 (dotted) [29]. The plot is taken from [27].*

form the structure functions $F_2(x)$ or $g_1(x)$ at Q^2. These predictions are then compared to experimental data of $F_2(x)$ and $g_1(x)$ taken at the same scale Q^2. In this way, by fitting to the data, in addition to extracting the unpolarized and polarized quark distribution functions $q_f(x, Q^2)$ and $\Delta q_f(x, Q^2)$, the unpolarized and polarized gluon distribution functions $g(x, Q^2)$ and $\Delta g(x, Q^2)$ can be implicitly extracted from the data. The result of this procedure shows that the DGLAP evolution indeed reproduces the scaling violations of F_2 and g_1 observed in the experiments. This is considered as one of the key successes of QCD. The fits can be done to any order in which the splitting functions and coefficient functions are available. So far LO and NLO fits have been performed.

Scaling violations - unpolarized

Fig. 2.8 shows the results of several QCD fits for the unpolarized gluon distribution as a function of x. The accuracy of the gluon distribution is limited by the available precision of the data. At small Q^2 the gluon distribution has large uncertainties which decrease rapidly with Q^2, though. The quark distributions, not shown here, are determined with much better accuracy [27].

Scaling violations - polarized

Fig. 2.9 shows the results of several QCD fits for the polarized quark and gluon distribution functions. The polarized quark distributions are determined with small uncertainties. In

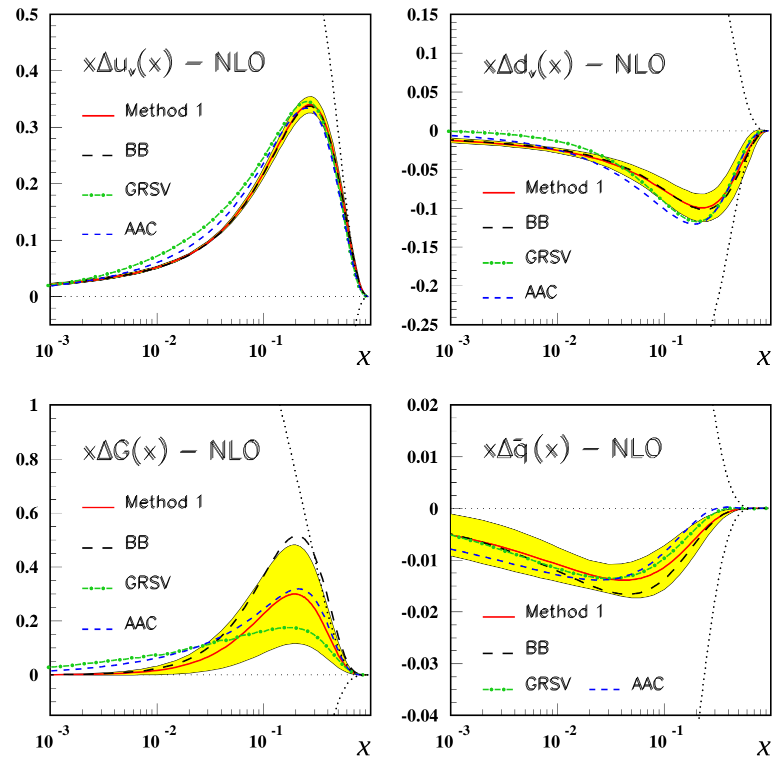

Figure 2.9: *Various polarized parton distributions as resulting from NLO QCD fits to g_1 data at an input scale $Q_0^2 = 4.0$ GeV ^{2}. The curves labelled Method 1 are obtained by HERMES using their deuteron data on g_1 (solid line with error band) [30]. Also shown are the results obtained by BB (long-dashed) [31], GRSV (dashed-dotted) [32], and AAC (dashed) [33]. The dotted lines correspond to the positivity bounds taken from unpolarized distributions. The plot is taken from [30].*

most cases, the various QCD fits are very close to each other. The polarized valence u quark distribution is large and positive, while the polarized valence d quark distribution is negative and only half as large in absolute value. The polarized distribution of the sea quarks cannot be extracted from fits to inclusive data on g_1 for the individual flavours but only for all sea quarks together, making certain assumptions when combining the flavours. For the assumption that the polarized distribution of all sea quark flavours is equal, the extracted polarized sea quark distribution is very small and negative. The polarized gluon distribution is poorly constrained from these indirect measurements. This is due to the quite limited range in x and Q^2 covered by the existing fixed target experiments. Furthermore, measurements of $A_1 \approx g_1/F_1$ have shown no significant dependence on Q^2, implying that g_1 basically evolves like F_1, which provides no constraints when trying to extract the polarized gluon distribution from such a fit. This makes it essentially impossible to determine the polarized gluon distribution from the scaling violations of g_1 alone. Either $g_1(x)$ data covering a much larger (x, Q^2) region or direct measurements are therefore required to better constrain the gluon polarization.

2.6.2 Methods for direct measurements of the gluon polarization

Direct measurements of the unpolarized and polarized gluon distributions can be performed by isolating processes with a gluon in the initial state of the scattering. Since these processes cannot be identified unambiguously in the detector, one can never completely isolate them, but always has to apply an event selection in which the contributions from scattering processes involving the gluon in the initial state (signal) are enhanced while the contributions from other processes (background) are suppressed.
In lepton-nucleon scattering the photon-gluon-fusion process is the main signal process. In such a PGF process the virtual photon interacts with a gluon from the nucleon via the exchange of a virtual quark resulting in the emission of a quark-antiquark pair back-to-back in the photon-gluon centre of mass, ($\gamma^* g \rightarrow q\overline{q}$). The quark-antiquark pair hadronizes and yields heavy (charmed) mesons if heavy (charm) quarks are involved, and jets or hadrons with large transverse momenta in the final state if light quarks are produced in the hard scattering.
In hadronic collisions, e.g pp scattering, the relevant signal processes are the inverse QCD Compton process ($qg \rightarrow \gamma q$) yielding high-p_T prompt photon production, gluon-gluon fusion resulting in heavy flavour meson production ($gg \rightarrow Q\overline{Q}$), and gluon-gluon and gluon-quark scattering leading to high-p_T jets or pions ($gg \rightarrow gg$, $qg \rightarrow gq$).
Most of these signatures have in fact already been used for measurements of the unpolarized gluon distribution. In the discussion below their applicability for measuring the polarized gluon distribution is summarized.

Prompt photon production

In polarized pp or $p\overline{p}$ collisions of sufficiently high centre-of-mass energies the gluon polarization can be accessed via prompt photon production. The signature of this channel is an isolated high-p_T photon in the detector. The underlying partonic processes are the signal process $qg \rightarrow \gamma q$ (inverse QCD Compton) and the background process $q\overline{q} \rightarrow \gamma g$ (quark-antiquark-annihilation). Theoretically, prompt photons are considered to be a very clean probe since they originate directly from the hard interaction without undergoing subsequent hadronization. This method will be pursued a the RHIC (Relativistic Heavy Ion Collider) at BNL (Brookhaven National Laboratory) in the near future. At RHIC kinematics ($\sqrt{s} = 200, 500$ GeV) the prompt photon production $pp \rightarrow \gamma X$ is dominated (at the $\sim 75\%$ level) by quark-gluon scattering $qg \rightarrow \gamma q$ whose analyzing power, i.e. hard asymmetry $\hat{a}$, is large [34, 35]. The double spin asymmetry to be measured in such experiments is approximately proportional to $\Delta g/g$ and given by

$$A_{\parallel} \sim \hat{a}(qg \rightarrow \gamma q) \cdot \frac{\Delta g}{g}(x_g) \cdot \frac{\sum_f e_f^2 \Delta q_f(x_q)}{\sum_f e_f^2 q_f(x_q)} \ , \tag{2.73}$$

providing a large sensitivity to $\Delta g/g$. Backgrounds due to photons from decaying π^0 mesons, which are produced in large numbers along with other hadrons in jets, are largely suppressed by imposing isolation cuts on the photon. Detecting a jet in coincidence with the prompt photon can provide constraints on the kinematics of the two colliding partons, and thus the gluon momentum fraction x_g can be reconstructed. This in turn allows to extract information on the x_g-dependence of the gluon polarization.

Heavy flavour meson production

In deep-inelastic lepton-nucleon scattering heavy flavour meson production is the cleanest way to access the polarized gluon distribution. Since the intrinsic heavy flavour content of the nucleon can be neglected, the dominating underlying hard process is the photon-gluon-fusion process producing a heavy flavour (charm or bottom) quark-antiquark pair ($\gamma^* g \to Q\overline{Q}$). The discussion here is limited to charm production. The charm - anticharm quark pair can either produce *hidden charm* hadrons such as the J/Ψ meson or *open charm* hadrons such as the D mesons.

In *hidden charm* production the charm - anticharm quark pair recombines to a J/Ψ-meson. The J/Ψ-meson subsequently decays, its leptonic decay products provide a clean signature by which it can be experimentally observed without much background. However, linking the double spin asymmetry in J/Ψ-meson production to the gluon distribution in the nucleon is subject to large uncertainties. First, non-negligible backgrounds might arise from the initial-state photon splitting into a $c\overline{c}$ pair resulting in the production of a J/Ψ meson. Second, the production mechanism for J/Ψ from PGF, which involves an additional gluon emitted by one of the quarks in the $c\overline{c}$ pair to form a bound state, can be described with two different models. Both predict the asymmetry to be proportional to $\Delta g/g$ but differ in their predictions of the analyzing power. First measurements of the J/Ψ double spin asymmetries at HERMES [36] showed that the difficulties mentioned above prevent the use of these data for the determination of $\Delta g/g$.

For *open charm* photoproduction, PGF is the relevant process and the double spin asymmetry can be written as

$$A_{\|}^{c\overline{c}} \sim \hat{a}(\gamma^* g \to c\overline{c}) \cdot \frac{\Delta g}{g}(x_g) \ . \tag{2.74}$$

The gluon momentum fraction x_g is determined by the photon energy, such that in principle the shape of the gluon polarization as a function of x_g can be accessed by selecting different virtual photon energies. The cross section is largest at low Q^2, i.e. in quasi-real photoproduction.
In *open charm* production, charmed mesons (such as the D and D^* mesons) are produced via the fragmentation of the charm quarks. The D-mesons can be reconstructed from their decay into $K\pi$ pairs. The background from non-resonant $K\pi$ production can be significantly reduced by requiring an additional soft pion from the decay $D^* \to D\pi$ in the event. In [37, 38, 39] D^* measurements at HERMES have been attempted, but since the HERMES energy is only just above the charm production threshold the number of identified events is too small to measure a double spin asymmetry with high enough

accuracy to extract the gluon polarization [5]. In the near future, COMPASS is expected to provide measurements of $\Delta g/g$ from charmed meson production at photon energies in the range $35 < \nu < 85$ GeV, employing scattering of a polarized muon beam off a polarized fixed target [41]. The sensitivity to $\Delta g/g$ can be further increased by selecting charmed mesons at low p_T (< 1 GeV).

Heavy flavour meson production can also be studied at hadronic colliders, i.e. in pp collisions at RHIC, in order to measure the gluon polarization [34, 35]. The heavy flavour mesons are produced predominantly by gluon-gluon fusion ($gg \to Q\overline{Q}$). In this case, the double spin asymmetry thus has a quadratic sensitivity to $\Delta g/g$ according to

$$A_{\|} \sim \hat{a}(gg \to Q\overline{Q}) \cdot \frac{\Delta g}{g}(x_{g_1}) \cdot \frac{\Delta g}{g}(x_{g_2}) \ . \tag{2.75}$$

At RHIC both *open charm* and *open bottom* mesons can be used, which are most prominently selected by observing their leptonic decays.

High-p_T jet production

Another possible approach is to measure the gluon polarization from high-p_T jet production. The idea in this approach is that the transverse momentum p_T of the jet can be related to the transverse momentum $\hat{p}_T$ of the parton (light quarks or gluons) initiating the jet, and thus can be used to distinguish different underlying processes based on their differences in $\hat{p}_T$. It has to be noted, though, that the observed transverse momentum is also partially determined by the intrinsic k_T of the parton prior to the interaction, by the transverse momentum p_T^F acquired during the fragmentation, and due to multiple soft gluon radiation of the outgoing quarks. These additional contributions to the observed transverse momentum dilute the direct correlation between observed and parton transverse momentum.

In deep-inelastic scattering, the leading order DIS process ($\gamma^* q \to q$) does not create any significant transverse momentum, but a non-zero hadron transverse momentum can still result from a non-zero intrinsic k_T of the partons in the nucleon and additional p_T^F acquired during the fragmentation. In the processes QCDC ($\gamma^* q \to qg$) and PGF ($\gamma^* g \to q\overline{q}$), the outgoing partons ((light) quark and gluon, and (light) quark-antiquark pair, respectively) are created at significant transverse momentum $\hat{p}_T$. This leads to the production of two jets with large p_T. Since jets originating from gluons or quarks develop slightly differently, the contribution from QCDC (one gluon and one quark jet) can be suppressed as compared to that from PGF (one quark and one antiquark jet) by imposing certain cuts on the jet properties. The double spin asymmetry from high-p_T dijet production is then predominantly given by the PGF process which is proportional to $\Delta g/g$. At present, no polarized ep-colliders exist at which these proposed measurements

[5] In [40] it has been attempted to use Λ_c baryon production for this purpose, but also in this case the statistics is insufficient and alternative production processes further complicate the interpretation of the data.

can be performed [42, 43], while at the existing polarized DIS fixed target experiments the centre-of-mass energies are such that no well-developed jets are produced.

Also at polarized pp colliders such as RHIC high-p_T jet production can be used for a $\Delta g/g$ measurement [34, 35]. In this case, the dominating underlying processes are gluon-gluon-scattering ($gg \to gg$) and gluon-quark-scattering ($qg \to gq$). It has been proposed to exploit both single-inclusive jet production as well as pair production of jets to determine $\Delta g/g$ where the latter channel provides in addition the possibility to reconstruct the momentum fractions of the initial state partons in the incident protons.

High-p_T hadron production

Since at current fixed target experiments the centre-of-mass energies are too low for the formation of true jets, it has been proposed to use instead high-p_T hadrons to measure the polarized gluon distribution. At these energies, the final state partons fragment into a low number of hadrons, which are not necessarily collimated around the original parton direction. Still, similar to jets, hadrons with larger p_T should be produced more often in the first order QCD processes QCDC and PGF than in the leading order DIS process. However, as for jets, the clear relation of hadron p_T to the $\hat{p}_T$ of the partonic process is again diluted by other sources of transverse momentum (intrinsic k_T, fragmentation p_T^F).

Measuring the gluon polarization via high-p_T hadron pair production was first proposed in [44]. Considering only contributions from the three processes DIS, QCDC and PGF, the (polarized) cross section for the electroproduction of high-p_T hadron pairs can be decomposed as

$$
\begin{aligned}
(\Delta)\sigma^{h_1+h_2} = \quad & \textstyle\sum_q \left\{(\Delta)q \otimes (\Delta)\hat{\sigma}^{\gamma^* q \to q} \otimes D_q^{h_1+h_2}\right\} && (2.76)\\
& + \textstyle\sum_q \left\{(\Delta)q \otimes (\Delta)\hat{\sigma}^{\gamma^* q \to qg} \otimes D_{q,g}^{h_1+h_2}\right\} && (2.77)\\
& + \textstyle\sum_q \left\{(\Delta)g \otimes (\Delta)\hat{\sigma}^{\gamma^* g \to q\overline{q}} \otimes D_{q,\overline{q}}^{h_1+h_2}\right\} \ . && (2.78)
\end{aligned}
$$

The fragmentation functions D describe the probability for a quark (q), a quark and a gluon (q, g), or a quark-antiquark pair ($q, \overline{q}$) to fragment into a hadron pair (h_1+h_2); they are spin-independent as long as one averages over the polarization of the final hadrons. Since the PGF process is the only one involving gluon polarization, large sensitivity of the double spin asymmetry (which is given by the ratio of the polarized over unpolarized cross section presented above) to the gluon polarization can, according to this superposition of processes, only be achieved if one succeeds in largely isolating the PGF process, i.e. in suppressing the background processes DIS and QCDC, in the event selection. The partonic asymmetry $\hat{a}_{LL} = \Delta\hat{\sigma}/\hat{\sigma}$ of the PGF process is negative and large in absolute value for the kinematics considered, approaching -1 in the photoproduction limit, indicating a very high sensitivity to the gluon polarization. The partonic asymmetries for the QCDC and DIS process, on the other hand, are positive. The gluon polarization is probed at a momentum fraction $x_g = x(1 + \hat{s}/Q^2)$, where $\hat{s}$ is the partonic Mandelstam variable representing the square of the sum of the initial-state four-momenta.

In [44] the following strategy for selecting high-p_T hadron pairs in electroproduction was developed for COMPASS energies, using the Monte Carlo program POLDIS [45]. The LO DIS process was shown to be largely suppressed by requiring at least one hadron with high-p_T (1.0-1.5 GeV). With this requirement the fraction of LO DIS events is already reduced to the percent level. The relative contribution of QCDC and PGF events over LO DIS could be further optimized if two hadrons with $p_T > 1.0 - 1.5$ GeV were required, an invariant mass cut of $m(h_1, h_2) > 2.5 - 3.0$ GeV was imposed, and the two hadrons were found in opposite azimuthal directions which basically corresponds to their transverse momenta cancelling each other. A further cut of $z > 0.1$ was considered to reduce fragmentation effects from the target remnant. The relative contribution of the PGF with respect to the QCDC process could be enhanced by selecting two oppositely charged hadrons or even kaons.

These last two requirements presuppose a strong relation between the final state partons and the detected hadron pair and rely on certain assumptions about the fragmentation process. First of all, the concept of favoured fragmentation is assumed, which states that a quark of flavour f preferentially fragments into a hadron containing this flavour. The final state partons of the PGF event should thus fragment preferably into oppositely charged hadrons due to their opposite flavour and opposite charge, while the final state gluon from the QCDC event should fragment with equal probability into a positive or a negative hadron. Second, strangeness suppression is assumed, i.e. the production of strange hadrons from non-strange light quarks should be disfavoured. Therefore, kaon pairs should much more likely originate from a final state $s\bar{s}$-pair produced in the PGF process than from any final state non-strange quarks or gluons produced in the other processes.

Since the total cross section, and correspondingly the event yields, are significantly increased in the limit $Q^2 \rightarrow 0$, the extension of this approach to the measurement of high-p_T hadron pairs in (quasi-real) photoproduction is profitable. In this regime however, contributions from vector meson production and resolved photon processes can no longer be neglected. The selection strategy outlined above therefore needs to be re-evaluated using the PYTHIA MC program suitable for this regime. This program also needs to be used to calculate the fractions and partonic asymmetries of the contributing processes.

HERMES has attempted an extraction of the gluon polarization from a measured negative double spin asymmetry for high-p_T hadron pairs in quasi-real photoproduction from data on a proton target taken in the years 1996-1997, using PYTHIA 5 [25, 26]. The results described in [46, 47] are based on a method which follows very closely the strategy proposed originally for COMPASS. No model dependent systematic uncertainty was quoted at that time. Nevertheless, the results must be considered to contain a significant albeit unquantified model dependence, an inevitable consequence of the extraction procedure. Further analyses were reported in [48]. In this thesis, the analysis is extended to include also the data taken on the deuteron target in the year 2000. A completely revised strategy is developed, the more recent and more comprehensive version 6 of the PYTHIA MC [49, 50] is used, and extensive studies are performed to evaluate the model dependent systematic uncertainty. The results are compared with recent first results from the SMC and COMPASS experiment [51, 52].

Since HERMES can deliver only limited statistics of high-p_T hadron pairs, it has also been considered to extract the gluon polarization requiring only one high-p_T hadron. This does increase the statistics substantially but comes at the price of reducing the PGF fraction in the sample. In this thesis, an optimization of the data selection strategy and a subsequent extraction of the gluon polarization is, in addition to the above mentioned high-p_T hadron pair photoproduction, also performed for single high-p_T hadron electroproduction. In [53] yet another alternative approach to extract the gluon polarization from HERMES data is carried out, proposed in [54, 55], namely inclusive (single) high-p_T hadron photoproduction.

Chapter 3

The HERMES experiment

The HERMES (HERa MEasurement of Spin) experiment is located at the HERA lepton-proton collider facility at the DESY (Deutsches Elektronen-Synchrotron) laboratory in Hamburg, Germany. The HERA storage rings have a circumference of 6.3 km and provide a proton beam of 920 GeV as well as a polarized positron beam [1] of 27.5 GeV. Four high energy physics experiments are performed at HERA: H1, ZEUS, HERA-B and HERMES. The HERMES set-up [56] is situated in the east section and is operated in fixed target mode. It utilizes only the positron beam whereas the proton beam passes through without interaction. The polarized positron beam (section 3.1) is scattered off a polarized gas target (section 3.2) internal to the storage ring. The achieved luminosity is measured by the luminosity monitor (section 3.3), while the HERMES forward spectrometer (section 3.4) detects the products of the positron-nucleon interactions. As part of a general upgrade project, the Lambda Wheels (section 3.5) have been designed to increase the acceptance of the spectrometer in the front region. The trigger system (section 3.6) selects relevant physics events which are then recorded and stored by the data acquisition system (section 3.7).

3.1 The polarized positron beam at HERA

A schematic view of the HERA storage rings at DESY is shown in Fig. 3.1. After injection into the HERA ring the positrons are initially unpolarized. With time they gradually build up a transverse polarization, a phenomenon referred to as the Sokolov-Ternov mechanism [57].

In the vertical field of the bending magnets, installed in the arcs of the ring, the spin of the positrons aligns either parallel or antiparallel to the magnetic field. In this process, the positrons are originally oriented in equal numbers with spins parallel or antiparallel. Emission of synchrotron radiation in the curved sections, however, can cause the positrons

[1] In 1998 electrons were used instead of positrons. Throughout this thesis the term positrons is meant to denote also electrons, except when discussing the luminosity measurement, where different physical processes are utilized for positrons and electrons.

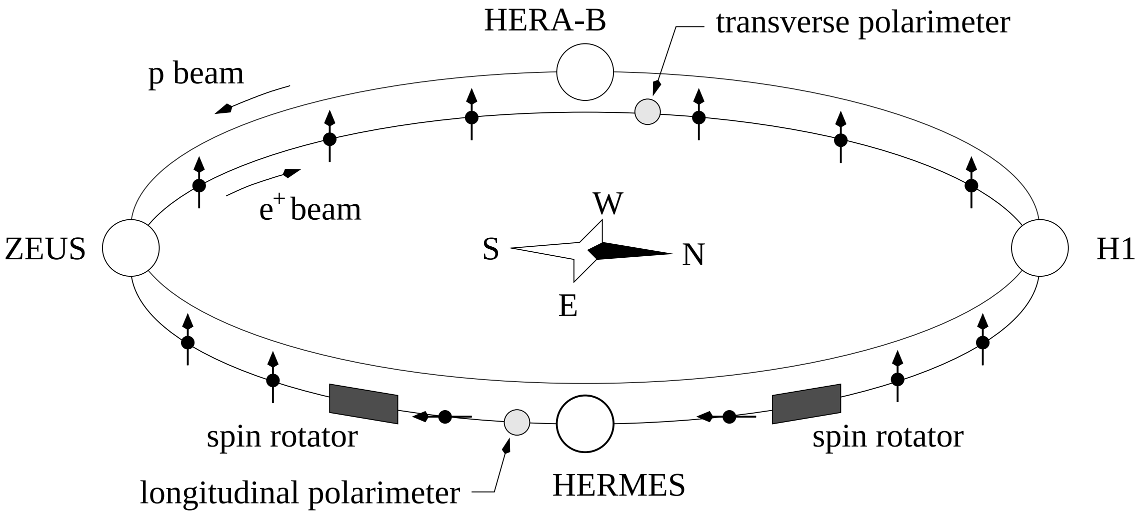

Figure 3.1: *Schematic diagram of the HERA storage rings at DESY.*

to flip their spin. A small asymmetry in the spin-flip amplitude induces self-polarization. This polarization builds up according to

$$P_{\text{beam}}(t) = P_{\text{max}}(1 - e^{-t/\tau}) \ . \tag{3.1}$$

Here P_{max} is the asymptotic polarization and τ the characteristic rise-time which depends on the beam energy and the radius of the ring. For an ideal flat ring, the maximum asymptotic polarization can be calculated to be 92.4%. In an ideal synchrotron of HERA geometry the rise-time would be 36.5 min. However, taking into account depolarization effects, the asymptotic polarization and the characteristic rise-time change significantly. At HERA maximum polarizations of about 60% are achieved, with characteristic rise-times of about 20-24 min [58, 59].

For the HERMES experiment the transverse polarization of the positron beam is changed into a longitudinal polarization by means of two spin rotators, one located up-stream and the other downstream of the experimental set-up [60]. These devices rotate the spin from transverse to longitudinal in front of the target region and back to transverse afterwards. By re-arranging the spin rotator fields, the helicity of the longitudinally polarized beam is reversed every few months in order to reduce systematic uncertainties for spin-dependent measurements.

Two polarimeters measure the positron polarization, the transverse polarimeter (TPOL) in the west straight section and the longitudinal polarimeter (LPOL) just downstream of the HERMES region. Both polarimeters are based on Compton scattering of polarized photons off polarized positrons.

The transverse polarimeter (TPOL)

The TPOL [58] determines the beam polarization by exploiting a vertical spatial asymmetry of the Compton scattering cross section. Circularly polarized light emitted continuously by a laser is backscattered off the transversely polarized positron beam and measured in a position-sensitive calorimeter. The energy and position of each photon are determined as functions of the laser beam helicity which is flipped at a rate of 90 Hz. The transverse positron beam polarization is proportional to the observed spatial asymmetry under helicity reversal. The fractional systematic uncertainty on the transverse polarization measurement is $\Delta P/P = 3.4\%$, dominated by calibration uncertainties.

The longitudinal polarimeter (LPOL)

The LPOL [61] measures the beam polarization by employing an energy asymmetry of the Compton scattering cross section. By switching the helicity of the circularly polarized laser light, the energy spectrum of the Compton photons backscattered off the longitudinally polarized positron beam is modified. The observed asymmetry of the energy deposit in the LPOL calorimeter is proportional to the longitudinal positron beam polarization. In order to reduce the influence of the high background radiation (bremsstrahlung photons from the HERMES target and synchrotron photons from the bending magnets) at its location, the LPOL is operated in multi-photon mode. In this mode it measures the total energy in the calorimeter deposited by many scattered Compton photons during one laser-positron bunch interaction. The fractional systematic uncertainty on the longitudinal polarization measurement of $\Delta P/P = 1.6\%$ is again mainly due to calibration uncertainties.

3.2 The polarized internal gas target

The HERMES experiment uses a fixed polarized gas target [62] internal to the positron beam. A gas target has several advantages over solid state targets. Due to the high purity of the target gases, contaminations are negligible. High polarization can be provided at relatively low magnetic holding fields; and the target polarization can be flipped on a time scale of a few seconds. These advantages are opposed by the disadvantage of a relatively low target density. The use of a storage cell, however, allows to increase the target density compared to conventional polarized jet targets by about two orders of magnitude. Cooling the storage cell increases the target density even further. At HERMES the cell is typically cooled to 100 K for hydrogen and to 60K for deuterium. At these temperatures, target densities of $\sim 10^{14}$ nucleons/cm^2 are obtained for polarized hydrogen and deuterium gases. Together with an average positron beam current of about 30 mA, luminosities of a few times 10^{31} cm^{-2}s^{-1} are realized.

Fig. 3.2 illustrates the setup of the HERMES polarized target. The Atomic Beam Source (ABS) injects polarized atomic gas into the storage cell. A small fraction of this gas is later analyzed by the Target Gas Analyzer (TGA) to determine the relative fractions of atoms and molecules, and by the Breit-Rabi-Polarimeter (BRP) to determine their polarizations.

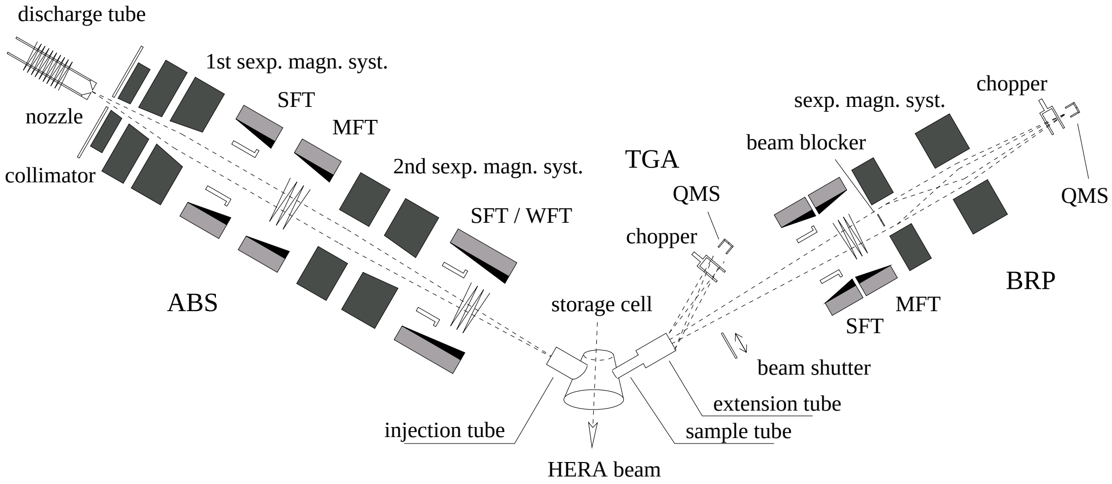

Figure 3.2: *Schematic diagram of the HERMES polarized gas target.*

The atomic beam source (ABS)

In the ABS [63], hydrogen or deuterium molecules are dissociated into atoms in a glass tube by using radio frequency discharges. The atoms escape from the tube through a cooled nozzle and their flow is shaped into an atomic beam by a skimmer and a collimator before entering a high vacuum system of sextupole magnets and RF transition units. Here certain hyperfine states of the atoms can be selected for injection into the storage cell. In an external magnetic field the atoms can be in hyperfine states $| m_I, m_s\rangle$, where m_I denotes the nuclear, and m_s the electron spin orientation, respectively. For the spin-1/2 nucleus hydrogen these hyperfine states are

$$| 1\rangle :=| +\frac{1}{2}, +\frac{1}{2}\rangle \ , \ | 2\rangle :=| -\frac{1}{2}, +\frac{1}{2}\rangle \ , \ | 3\rangle :=| -\frac{1}{2}, -\frac{1}{2}\rangle \ , \ | 4\rangle :=| +\frac{1}{2}, -\frac{1}{2}\rangle \ .$$

For deuterium which is a spin-1 nucleus there are six hyperfine states

$$\begin{aligned} &| 1\rangle :=| +1, +\frac{1}{2}\rangle \ , \ | 2\rangle :=| 0, +\frac{1}{2}\rangle \ , \ | 3\rangle :=| -1, +\frac{1}{2}\rangle \ , \\ &| 4\rangle :=| -1, -\frac{1}{2}\rangle \ , \ | 5\rangle :=| 0, -\frac{1}{2}\rangle \ , \ | 6\rangle :=| +1, -\frac{1}{2}\rangle \ . \end{aligned}$$

The first set of sextupole magnets uses the Stern-Gerlach mechanism to focus atoms of hyperfine states with electron spin orientation $m_s = +\frac{1}{2}$ (corresponding to the states $| 1\rangle$ and $| 2\rangle$ for hydrogen, and $| 1\rangle$,$| 2\rangle$, and $| 3\rangle$ for deuterium). Atoms with $m_s = -\frac{1}{2}$ (states $| 3\rangle$ and $| 4\rangle$ for hydrogen, and $| 4\rangle$,$| 5\rangle$, and $| 6\rangle$ for deuterium) are defocussed and pumped away. A second set of sextupole magnets at the end of the ABS focusses the atoms into the storage cell. RF transition units are located behind the first and second set of sextupole magnets and can induce transitions between hyperfine levels in order to select a certain nuclear polarization for injection into the storage cell. By switching on and off selected RF transitions (weak field transitions (WFT), medium field transitions (MFT), or strong field transitions (SFT)), the nuclear polarization can be reversed on a

time scale of 60 s to reduce systematic uncertainties on the asymmetry measurement.
For hydrogen, positive and negative nuclear polarizations are prepared by using the RF transitions SFT $| 2\rangle \leftrightarrow | 4\rangle$ and WFT $| 1\rangle \leftrightarrow | 3\rangle$, respectively, which interchange the occupation numbers of the involved states and therefore populate states with $| m_I\rangle = +\frac{1}{2}$ and $| m_I\rangle = -\frac{1}{2}$, respectively. This corresponds to injected states $| 1\rangle$ and $| 4\rangle$ for positive nuclear polarization and states $| 2\rangle$ and $| 3\rangle$ for negative nuclear polarization.
For deuterium, positive nuclear polarization is achieved by first applying an RF transition SFT $| 3\rangle \leftrightarrow | 5\rangle$. In the second sextupole the state $| 5\rangle$ is defocussed. Then an RF transition SFT $| 2\rangle \leftrightarrow | 6\rangle$ is induced which leaves only states $| 1\rangle$ and $| 6\rangle$, both with $| m_I\rangle = +1$, to be injected into the storage cell. Negative nuclear polarization is formed accordingly by the RF transitions SFT $| 3\rangle \leftrightarrow | 5\rangle$, WFT $| 1\rangle \leftrightarrow | 4\rangle$ & $| 2\rangle \leftrightarrow | 3\rangle$, which leaves only states $| 3\rangle$ and $| 4\rangle$ both with $| m_I\rangle = -1$ to be injected into the storage cell.

The storage cell

The storage cell [64] is an open-ended tube with a length of 400 mm along the positron beam axis and an elliptical cross section of 29 mm × 9.8 mm (which in 2000 was reduced to 21 mm × 8.9 mm). The walls are made of 75 μm thick ultra-pure aluminium, coated with "drifilm" to minimize depolarization. The polarized atomic gas provided by the ABS is injected into the centre of the cell through a tube mounted perpendicular to the beam axis. A magnetic holding field maintains the polarization of the target gas. The injected atoms are confined by the cell to a small volume around the positron beam. They perform several hundred wall collisions before leaving the cell at the open ends to be pumped away by a powerful pump system. A small fraction of the gas is extracted via a sample tube to be analyzed in the TGA and the BRP.

The target gas analyzer (TGA)

The TGA [65] is mounted at an angle of 7 degrees with respect to the axis of the sampling tube. Thus only a small fraction of the gas extracted via the sampling tube is analyzed in the TGA by a quadrupole mass analyzer (QMS). The QMS alternately measures the flux of target gas with atomic and molecular mass in order to determine the relative content of atoms and molecules. A background subtraction is made possible by a chopper in front of the QMS which also allows to measure rates from background gases permanently present in the TGA.

The Breit-Rabi polarimeter (BRP)

With the BRP [66] the relative population of the hyperfine states of the gas sampled from the storage cell is measured. Like the ABS, the BRP consists of a system of sextupole magnets and RF transition units, assembled in opposite order compared to the ABS to select atoms in certain hyperfine states, which are subsequently analyzed by a QMS.

From the measured relative occupation of the different states the polarization can be determined. A background subtraction is again facilitated by a chopper in front of the QMS.

Determination of the target polarization

The effective polarization of the target gas is calculated by combining the BRP polarization measurement with the relative fractions of atoms and molecules as determined by the TGA. This polarization is defined as the sum of the nuclear polarizations from atoms and molecules, the latter formed by recombinations in the target gas [67]. Both parts are in turn defined as the product of the fraction of atoms (molecules) in the target gas and the polarization of atoms (molecules). Hence the effective polarization in the target gas can be written as

$$P_{\text{target}} = \alpha_0 \alpha_r P^{\text{a}} + \alpha_0 (1 - \alpha_r) P^{\text{m}} \ , \tag{3.2}$$

with

$$P^{\text{a}} = c_P \cdot P^{\text{a}}_{\text{BRP}} \ , \tag{3.3}$$

and

$$\alpha_r = c_\alpha \cdot \alpha_{\text{TGA}} \ , \tag{3.4}$$

where P^{a} is the polarization of the nuclei in atoms, P^{m} the polarization of the nuclei in molecules in the target gas, α_0 is the fraction of nuclei entering the cell as atoms and α_r is the fraction of nuclei surviving recombination in the cell. P^{a} and α_r are derived from the measured polarization in the BRP ($P^{\text{a}}_{\text{BRP}}$) and the measured fraction of nuclei surviving recombination in the TGA (α_{TGA}) by applying the sampling corrections c_P and c_α, respectively. Since both $P^{\text{a}}_{\text{BRP}}$ and α_{TGA} are measured using gas samples extracted from the centre of the cell, these corrections are needed in order to account for variations along the total length of the cell. They are determined from MC simulations. The ratio of the nuclear polarization in atoms and molecules $\beta = P^{\text{m}}/P^{\text{a}}$ is taken from dedicated studies in which the target cell temperature and hence α_r is varied. One can insert $P^{\text{m}} = \beta \cdot P^{\text{a}}$ into Eq. (3.2). Note that since α_r is found to be close to unity, the second term in Eq. (3.2) is small.

Other targets

While longitudinally polarized hydrogen and deuterium was used in the years 1996-2000, HERMES ran with longitudinally polarized ^{3}He in the commissioning year 1995. From the year 2002 onwards, HERMES has operated a transversely polarized hydrogen target. In addition to the polarized gases an unpolarized gas feed system allows to inject also various unpolarized gases. Over the entire data-taking period, unpolarized H_2, D_2, ^{3}He, $^{14}N_2$, ^{20}Ne, ^{84}Kr and ^{131}Xe gases have been used.

3.3 The luminosity monitor

For fixed target experiments the luminosity is defined as the product of the flux of beam particles and the number of target particles within the beam area

$$\mathcal{L} = \Phi_{\text{beam}} \cdot N_{\text{target}} \ . \tag{3.5}$$

The measurement of this quantity with the luminosity monitor in HERMES is based on elastic scattering of the beam particles with the shell electrons of the target gas atoms. For positron beams (1996-1997,1999-now) the relevant processes are Bhabha scattering $e^+e^- \to e^+e^-$ and pair annihilation $e^+e^- \to \gamma\gamma$, while for electron beams (1998) Møller scattering $e^-e^- \to e^-e^-$ is used. The cross sections of all these processes are well known to high orders in QED. The luminosity can therefore be calculated by taking the ratio of the count rates for these processes as measured in the luminosity monitor and the cross sections integrated over the acceptance. This function can be rearranged into

$$\mathcal{L} = C_{\text{lumi}} \cdot N_{\text{lumi}} \ , \tag{3.6}$$

where N_{lumi} represents the count rate in the luminosity monitor. The luminosity constant C_{lumi} contains the integrated cross section corrected for all possible detector effects (acceptance, efficiency, dead time), and is determined in MC simulations.

The HERMES luminosity monitor [68] is located 7.2 m downstream of the target. It consists of two identical calorimeters placed symmetrically left and right close to the beam pipe. Each calorimeter is composed of 12 radiation hard $NaBi(WO_4)_2$ crystals arranged in a 3×4 matrix of total size 66 mm $\times$ 88 mm $\times$ 200 mm. Electrons, positrons and photons induce electromagnetic showers in the calorimeter crystals. The Cerenkov light produced is then detected by individual photomultipliers to determine the energy deposit. To select the appropriate processes for the luminosity measurement, two coincident signals in different calorimeter halves with energy deposits each above 4.5 GeV are required. This trigger condition suppresses background events which typically deposit significant energy in one calorimeter half only.

3.4 The spectrometer

As a fixed target experiment HERMES uses a forward spectrometer (cf. Fig. 3.3 for a schematic side view). The spectrometer [69] consists of two identical halves, symmetrically installed below and above a horizontal plane defined by the HERA storage ring. Both the positron and the proton beams pass through the gap between the two halves of the spectrometer. The origin of the HERMES coordinate system is chosen in the centre of the target with the x-axis pointing outwards with respect to the ring, the y-axis pointing upwards and the z-axis pointing in the positron beam direction, together forming a right-handed orthogonal coordinate system. The angular acceptance of the spectrometer extends from $\Theta = 40$ mrad to $\Theta = 220$ mrad which corresponds to 40 mrad $\leq |\Theta_y| \leq$

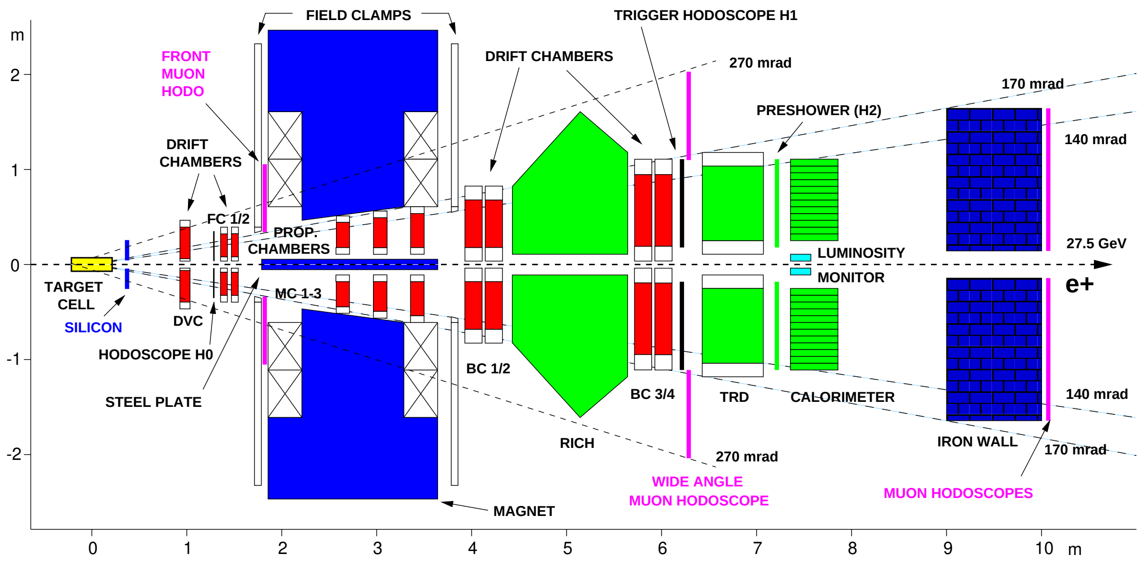

Figure 3.3: *Side view of the HERMES spectrometer.*

140 mrad in the vertical direction and $|\Theta_x| \leq 170$ mrad in the horizontal direction. The lower limit in the vertical direction is due to a steel plate in the spectrometer magnet which shields the beams from the magnetic field. The spectrometer magnet has a deflecting power of $\int B \cdot dl = 1.3$ Tm. In the vertical magnetic field charged particles are deflected in the horizontal direction, allowing a determination of the particle momenta. The trajectories of the particles are measured by tracking chambers situated in front of, inside and behind the magnet (section 3.4.1), respectively. Particle identification is accomplished by a system of detectors, including a preshower detector, a transition radiation detector and a lead-glass calorimeter. With this system a good separation of positrons and hadrons is achieved. Up to 1997 the system was complemented by a Cerenkov detector for pion identification. This detector was in 1998 replaced by a Ring-imaging Cerenkov detector for, in addition to (extended) pion, also kaon and proton identification (section 3.4.2). Besides for particle identification the calorimeter and the preshower detector also serve in the trigger, together with a system of hodoscopes (section 3.4.3).
In the following sections, individual detector systems are described, in each case showing only the component in the upper half of the spectrometer, as the one in the second half is completely identical.

3.4.1 The tracking system

The HERMES tracking detectors can be grouped into three sections, named front region, magnet region and back region, respectively.

The front region tracking system is used for the event-vertex reconstruction and the determination of the emission angles of the charged particles with respect to the beam direction. During various data-taking periods it has consisted of different combinations of tracking chambers. Two 6-plane drift chambers (FC1 and FC2) [70] were installed in the beginning and have been operational since. Two 3-plane micro-strip gas counters (VC1 and VC2) [71] had also initially been installed, but were fully operational in 1997 only. They were removed afterwards because an accidental beam loss in the vicinity of HERMES had severely damaged the read-out chips. In 1997 another 6-plane drift chamber (DVC) was added. For all datasets used in the analysis presented in this thesis the front-region tracking algorithm was based on the FCs only.

The three multi-wire proportional chambers (MC1,MC2 and MC3) [72] which are mounted in the gap of the magnet serve to reconstruct tracks of low momentum particles which are deflected by the magnetic field out of the acceptance of the back region.

The back region tracking system is employed to determine particle momenta by reconstructing tracks of deflected charged particles which do pass completely through the magnet and reach the rear of the spectrometer, and which are matched by appropriate front-tracks. Furthermore, the position information from the tracking chambers in the back region is used to match reconstructed tracks with the associated signals in the particle identification detectors. This back region tracking system comprises two sets of each two 6-plane drift chambers (BC1,BC2 and BC3,BC4) [73, 74] installed in front of and behind the Cerenkov detector, respectively.

Each tracking chamber contains several planes within which the wires are oriented either in the vertical direction (X) or tilted by $\pm$ 30 degrees with respect to the vertical direction (U and V). In some of the chambers each plane is accompanied by a second one with the same wire orientation, but a small offset of half a cell size to resolve left-right ambiguities. The DVC, the FCs and the BCs use such a configuration of six planes (XX'UU'VV' and UU'XX'VV', respectively), while the MCs have a UXV configuration with only three planes.

3.4.2 The particle identification detectors

Particle identification in the HERMES spectrometer is achieved by a system of four detectors in the back region of the spectrometer: a Cerenkov counter, a transition radiation detector (TRD), a preshower hodoscope and a lead glass calorimeter. The original threshold Cerenkov counter, which was operated until 1997, was replaced in 1998 by a ring imaging Cerenkov detector (RICH). By combining the responses of all detectors a clear separation between positrons and hadrons is provided. Additionally, the threshold Cerenkov counter can distinguish pions from other hadron types. With the RICH, pions, kaons and protons can be identified.

The threshold Cerenkov counter

The threshold Cerenkov counter is based on the principle of Cerenkov radiation. Charged particles passing through a radiator material of refractive index n with a velocity v_p

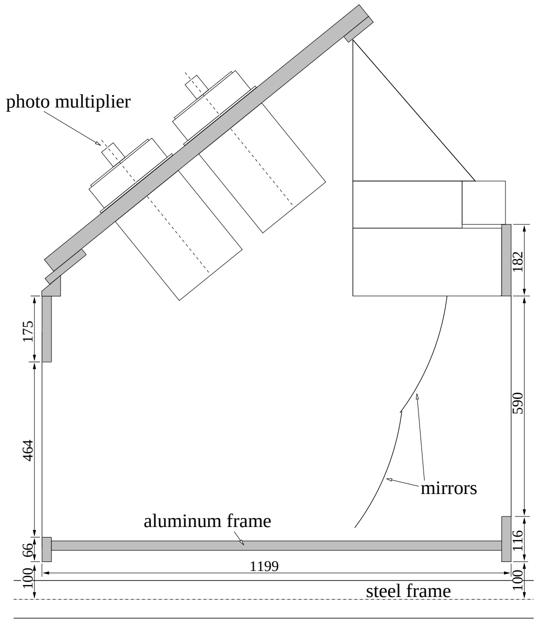

Figure 3.4: *Side view of the upper half of the threshold Cerenkov counter.*

greater than the velocity of light in that medium c_{medium} radiate Cerenkov photons at a characteristic angle

$$\cos\Theta_c = \frac{c_{\text{medium}}}{v_{\text{p}}} = \frac{c/n}{v_{\text{p}}} = \frac{1}{\beta n} \ . \tag{3.7}$$

The threshold velocity v_{thresh} of the particle in the medium is defined through

$$v_{\text{p}} > v_{\text{thresh}} = \frac{c}{n} \ . \tag{3.8}$$

From this the threshold momentum is obtained

$$p > p_{\text{thresh}} = \frac{mc}{\sqrt{n^2-1}} \ , \tag{3.9}$$

with m the mass of the particles. The dependence of the threshold momenta on the mass of the particles implies that in certain momentum ranges only certain particles will emit Cerenkov radiation. This is used in the threshold Cerenkov counter to separate particles with different masses.

Fig. 3.4 shows a schematic drawing of the upper half of the HERMES threshold Cerenkov counter. This detector consists of a gas radiator and an array of 20 spherical mirrors mounted at the rear of the detector. These mirrors focus the Cerenkov light into 20 matching photomultipliers. In 1996 and 1997 the detector was filled with a radiator gas mixture of 70% N_2 and 30% C_4F_{10}. This corresponds to below a percent of a radiation length. Hence the effect of multiple-scattering on the tracking resolution is negligible. The calculated refractive index for this gas mixture is $n = 1.00066181$. From Eq. (3.9) it follows that the threshold momenta of positrons, pions, kaons and protons are 0.014, 3.8, 13.6, 25.8 GeV, respectively. This implies that all positrons pass this

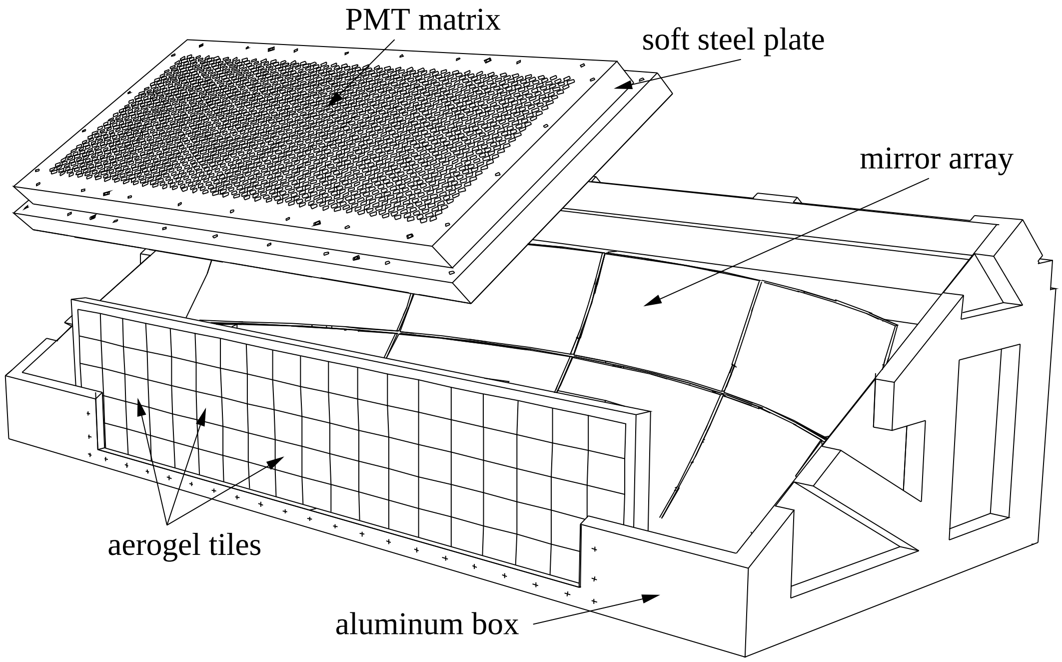

Figure 3.5: *Schematic view of the upper half of the RICH detector.*

threshold in the Cerenkov counter and consequently radiate. This is used together with the signals from the other PID detectors for the separation of positrons and hadrons. In the momentum range between 3.8 and 13.6 GeV pions are the only hadrons that produce Cerenkov radiation and can therefore be distinguished from other hadrons.

The ring-imaging Cerenkov detector (RICH)

In 1998 the threshold Cerenkov counter was replaced by a ring-imaging Cerenkov detector [75]. The RICH uses the same principle of Cerenkov radiation as described above. It measures the angular pattern of the Cerenkov photons and therefore allows the separation of pions, kaons and protons based on their different opening angles Θ_c for the same particle momentum. By employing two radiator materials with different refractive indices the identification of pions, kaons and protons is possible over a wide range of particle momenta.

A side view of the upper half of the HERMES RICH detector is shown in Fig. 3.5. A wall of silica aerogel tiles organized in 5×17 stacks of five tiles each, resulting in a total thickness of 5.5 cm, is installed directly behind the entrance window, constituting the first radiator. The same volume as previously used for the threshold Cerenkov detector is, for the RICH, filled with pure C_4F_{10} as a second radiator. The Cerenkov light emitted in the two radiators is reflected by an array of 8 spherical mirrors onto a focal plane suspended by a hexagonal matrix of 74×26 photomultipliers on which the projected cones of Cerenkov radiation appear as quasi-elliptical rings. In Tab. 3.1 the refractive indices of the two radiators as well as the resulting threshold momenta for the different

	Radiator	
	Aerogel	C_4F_{10}
n_{radiator}	1.0304	1.00137
$p^{\pi}_{\mathrm{thresh}}$ [GeV]	0.6	2.7
p^{K}_{thresh} [GeV]	2.0	9.4
p^{p}_{thresh} [GeV]	3.8	17.9

Table 3.1: *Refractive indices and threshold momenta of pions, kaons and protons for the two radiators of the HERMES RICH.*

particles are listed. The choice of radiators ensures that pions, kaons, and protons are well separated over a large part of the relevant HERMES momentum range of 1 to 15 GeV.

The transition radiation detector (TRD)

The TRD uses the phenomenon of transition radiation which occurs when a relativistic, charged particle traverses a dielectric boundary between two media with different dielectric constants. It is emitted in a forward cone with opening angle $\Theta \sim \frac{1}{\gamma}$ around the particle track, i.e. it is inversely proportional to the Lorentz factor γ. The energy of the emitted photons lies mainly in the range corresponding to X-ray radiation (several keV). The total energy is directly proportional to γ. The energy spectrum has a lower cutoff due to reabsorption and interference effects. As the emission of transition radiation from a single dielectric boundary is very small, many material interfaces are needed to build a powerful detector.

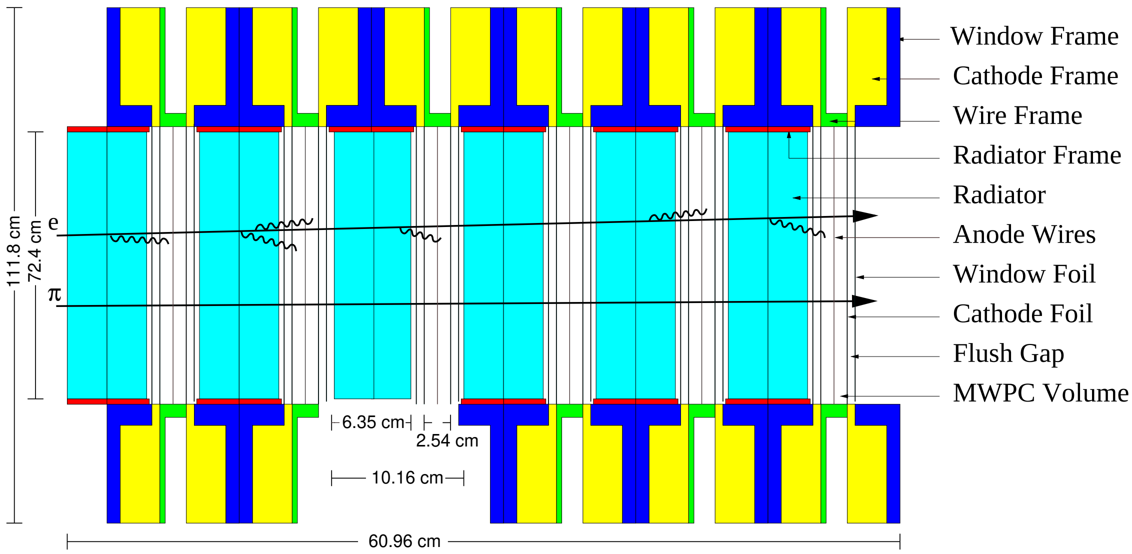

Figure 3.6: *Schematic view of the upper half of the TRD detector.*

The HERMES TRD consists of six identical modules assembled in consecutive order, as shown in Fig. 3.6. Each module contains as radiator a 6.35 cm thick two-dimensional matrix of polyethylene/polypropylene fibres corresponding to 267 dielectric layers, followed by a 2.54 cm thick multiwire-proportional chamber (MWPC) filled with a gas mixture of 10% CH_4 and 90% Xe. The transition radiation photons emitted in the radiator are measured in the MWPC. At HERMES energies scattered positrons have Lorentz factors of $\gamma > 6000$, while hadrons have $\gamma < 200$. With an effective threshold of the TRD corresponding to $\gamma \simeq 500$, only positrons emit a significant amount of transition radiation. In addition, both positrons and hadrons deposit energy in the MWPC due to ionization. At high incident energies, the transition radiation is emitted at a very small angle. Therefore it cannot be distinguished from ionization energy deposits. Thus the identification of positrons in the TRD is based solely on the larger average energy they deposit in the MWPCs, due to their additional transition radiation. The positron-hadron separation is achieved with the truncated mean average. By taking the average over the five smaller signals from the six modules, excluding the largest one, the high energy tail of the hadron response originating from δ-electrons can be reduced and the two particle classes become better separated.

The preshower detector

Particle identification with the preshower detector relies on differences in the development of electromagnetic and hadronic showers in material.

The HERMES preshower detector (cf. Fig. 3.7) consists of the hodoscope H2 with a 1 cm thick lead wall in front of it. The hodoscope comprises 42 vertically oriented plastic scintillator paddles, each 1 cm thick, 9.3 cm wide and 91 cm long, individually read-out by photomultipliers. The thickness of the lead wall corresponds to about 2 radiation lengths. Positrons create an electromagnetic shower in the radiator material and deposit much more energy in the hodoscope than hadrons which only give minimum ionizing signals. This allows to separate positrons from hadrons. The use of the preshower detector in the trigger is discussed in section 3.6.

The calorimeter

The calorimeter is positioned directly behind the preshower detector and is based on the same principle of the development of electromagnetic and hadronic showers in material.

A schematic view of the upper half of the HERMES calorimeter [76, 77] is included in Fig. 3.7. Each calorimeter half consists of 42×10 lead glass blocks of 9×9 cm^2 cross section and 50 cm length, corresponding to about 18 radiation lengths. Each column of blocks is aligned with one paddle of the preshower detector. The light produced in the lead glass by the showers is collected at the end of each block by a photomultiplier. Positrons and photons induce electromagnetic showers in the lead glass which will be up to 90% contained in one block if they enter the block in the centre at an incident angle

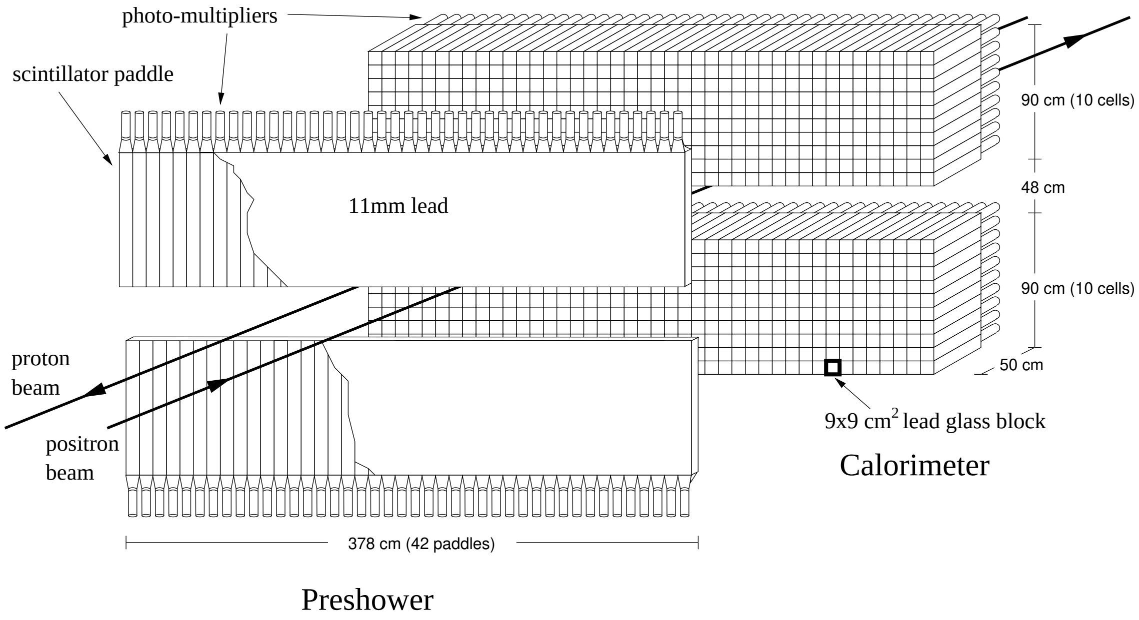

Figure 3.7: *Schematic view of the upper half of the preshower detector and calorimeter*

of 90^o with respect to the calorimeter front plane. Hadrons, on the contrary, deposit only a fraction of their energy in the calorimeter due to nuclear interactions and ionization. Thus the distribution of the ratio of the deposited energy and the momentum is $E/p \simeq 1$ for positrons, while $E/p < 1$ for hadrons. Besides for positron-hadron separation the calorimeter is also employed to measure photons (clusters in the calorimeter without any matching track in the tracking chambers) from decays of neutral particles like π^0s, and is used in the trigger as described in section 3.6.

3.4.3 The hodoscopes

The hodoscopes H0 and H1 are used for triggering purposes (cf. also section 3.6), together with the preshower hodoscope H2 and the calorimeter already described in the previous sections.

The scintillator hodoscope H1 has the same design as the preshower hodoscope H2 (apart from the non-existing lead wall in this case) and is installed between BC4 and the TRD. It consists of 42 vertical plastic-scintillator paddles each 1 cm thick and with an active area of 9.3×91 cm^2. The paddles overlap by 2-3 mm to avoid holes in the acceptance.

The hodoscope H0 is situated in the front region of the spectrometer in front of the FCs. It is made of a single sheet of plastic scintillator 3.2 cm thick, corresponding to 0.7% radiation length. The main purpose of H0 is, in combination with the rear hodoscopes, to discriminate backward going particles (originating from the proton beam) by time-of-flight considerations.

3.5 The Lambda Wheels

The Lambda Wheels are part of the HERMES silicon project [78, 79, 80] to upgrade the HERMES experiment. In 1997 a new detector system, consisting of two wheel-shaped planes of silicon counters (the Lambda Wheels) placed directly downstream of the target, and a second array of silicon counters (the recoil detector) mounted parallel to the target, was proposed. The Lambda Wheels project has been carried out by a collaboration of the University of Erlangen-Nürnberg, the PNPI in St.Petersburg, the Vrije Universiteit Amsterdam and NIKHEF in Amsterdam. In 1998 a silicon test counter was mounted and its performance investigated [81]. A prototype module of the Lambda Wheels was installed and successfully operated in the year 2000 [82]. In spring 2002 the full Lambda Wheels detector was installed and subsequently commissioned so that in autumn 2003 routine data-taking with this new detector could start. The recoil detector project was extended by a follow-up proposal in 2001 [83, 84] in which a much larger detector was proposed to replace the one originally envisaged. This project will not be discussed any further here.

Physics motivation

The purpose of the silicon project is to increase the acceptance of the spectrometer in the front region, in order to enhance especially the fractions of reconstructed strangeness and charm containing particles such as the Λ^0 hyperon and the lightest charmed baryon, the Λ_c^+. From a measurement of the Λ^0-polarization (deducible from the angular distribution of its decay products) the polarization transfer from the u-quark to the Λ^0-hyperon can be determined. If employing a transversely polarized target this method can also be used to measure the transverse spin distribution of the u-quark in the nucleon. As the new silicon detector extends the acceptance for the Λ^0-hyperons to the target fragmentation region ($x_F < 0$), a domain becomes accessible where the Λ^0-polarization is predicted to be sensitive to the polarization of the s-quarks. Reconstructing Λ_c^+ particles on the other hand, allows a study of charm production near threshold and will yield information on the open charm production mechanism [40].

Principle of operation

A charged particle traversing a semiconductor material produces electron-hole-pairs through ionization along its trajectory. The electrons are lifted into the conduction band with holes being left in the valence band. In an external electric field the produced negative and positive charges drift in opposite directions to the electrodes. In general no secondary ionizations occur in a semiconductor, in contrast to the ionization avalanches which develop in a gas. Therefore the charge collected at the electrodes is small. This requires special specifications of the semiconductor material in order to obtain a reasonable signal-to-noise ratio. The leakage currents present also in the absence of a traversing particle have to be minimized.

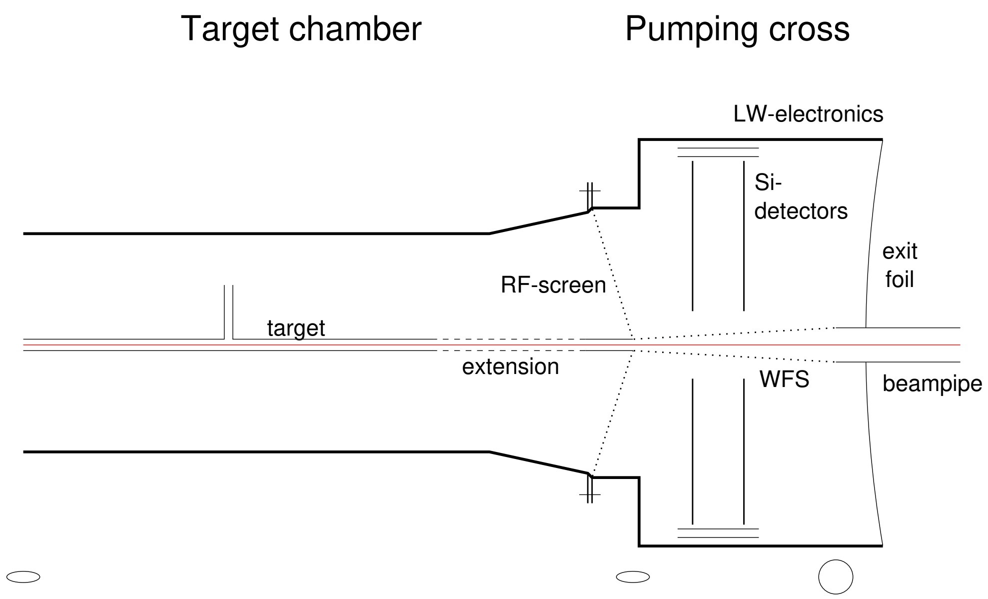

Figure 3.8: *Schematic diagram showing the position of the Lambda Wheels in the HERMES vacuum chamber. The beam is separated from the main volume by the target, the target extension-piece, the wakefield suppressor (WFS) and the beampipe. On the bottom of the figure the cross sections of the parts closest to the beam are shown.*

In the Lambda Wheels n-type silicon with p+ implants at the so-called junction side and n+ implants at the so-called ohmic side is used. The p+ implants have an excess of mobile holes while the n+ implants have extra mobile electrons. If a reverse bias voltage is applied (negative potential given to the junction side) a depletion zone free of any mobile charge carriers is formed and the leakage current is therefore minimized. Electron-hole pairs created in this zone by a traversing particle drift to opposite sides and are collected at the electrodes connected to the implants. The integrated signal of the collected charge at the two electrodes then equals the total charge generated by the traversing particle which in turn is directly proportional to its energy loss. If the two doped regions are divided into strips like in the Lambda Wheels, position information on the traversing particle trajectory can be extracted as well.

Detector description

The Lambda Wheels [85] are located inside the so-called pumping cross, which is a vacuum chamber connected directly to both the target chamber as well as to the HERA accelerator vacuum system (cf. Fig. 3.8). The two silicon layers are placed 45 cm and 50 cm from the centre of the target, a position at which about 80% of all Λ-particles have decayed. The Lambda Wheels consist of 12 identical modules mounted on a wheel-shaped frame. In this way all electronic and mechanical structures can be kept out of the acceptance of the rest of the spectrometer. The Lambda Wheels have an outer radius of 17 cm, limited by the size of the pumping cross, and an inner radius of 4.5 cm. Each

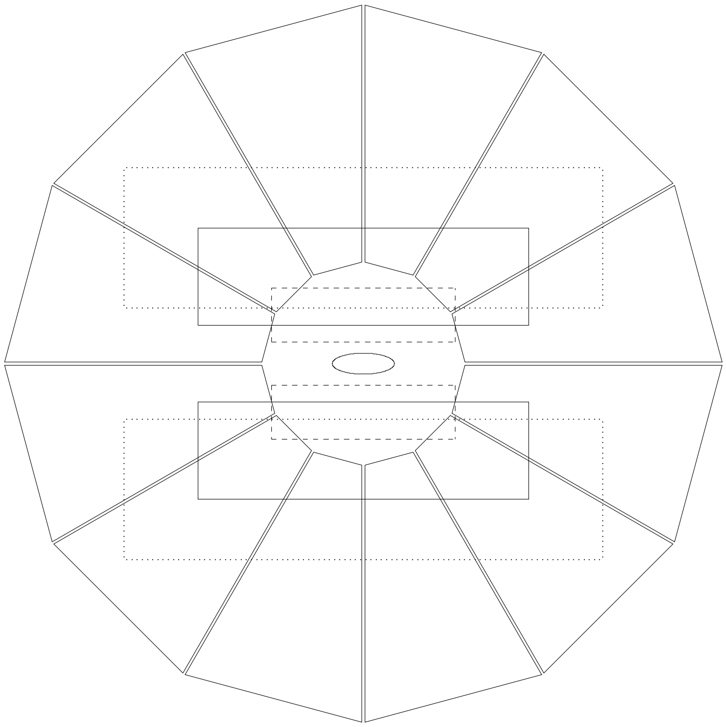

Figure 3.9: *Comparison of the size of the Lambda Wheels at $z = 45$ cm with the standard HERMES acceptance. Solid box: standard acceptance from the centre of the target ($z = 0$ cm), dotted box: acceptance from the upstream end of the target ($z = -20$ cm), dashed box: acceptance from the downstream end of the target ($z = 20$ cm). The ellipse in the centre shows the size of the target extension-piece at $z = 45$ cm.*

module comprises two double-sided silicon layers of trapezoidal shape, with a base of 85.3 mm, a top of 23.2 mm and an apex of 30^o, made of 300 μm thick n-type silicon. In Fig. 3.9 the size of the Lambda Wheels is compared with the standard HERMES acceptance, thus showing the increase in geometrical acceptance achieved by this new detector. This increase in geometrical acceptance leads to an anticipated increase of about a factor of 4 in the yield of Λ particles.

Both sides of each silicon layer contain 516 strips, each with a width of 60 μm and a pitch of 160 μm, oriented parallel to the oblique sides. As an angle of 30^o is thus formed between the strips of the two sides, two-dimensional position information on traversing minimum-ionizing particles is obtained. Of each 516 strips, 499 are read out via the front-end electronics located at the outer side of the wheel, the remaining 17 strips being too short to be connected, resulting in a total active area of 93%.

The Lambda Wheels are equipped with a cooling system, first to remove heat generated by the electronics from the vacuum, and second to reduce temperature-dependent leakage currents and radiation damage in order to achieve optimal signal-to-noise ratios. The system consists of two loops. Ultra-pure alcohol flowing in a closed internal loop, the flow being regulated by a pump, transports heat from the detector situated inside the ultra-high vacuum in the pumping cross to a set of Peltier elements situated inside a secondary vacuum in a cooling tower mounted on top of the pumping cross. These elements serve as a heat pump to transfer heat from the internal alcohol loop operated at lower temperature to an external cooling loop filled with water of about 8^oC. Their cooling power is controlled by the current passing through them. In this way up to 100 W of heat can be removed from the detector which is operated at temperatures of about 0^oC.

Radiation protection system

At the location of the Lambda Wheels in the direct vicinity of the positron beam increased radiation levels caused by beam instabilities can occur. As a high radiation dose received by a silicon detector can result in severe damage to the readout electronics and the silicon itself, a system to detect such beam instabilities early in their evolution and to trigger a controlled beam dump has been installed. This beam loss monitor (BLM) [86] consists of two sets of ionization chambers, one on either side of the beam in the horizontal plane just downstream of the Lambda Wheels. If the radiation level becomes too high and the signal from the BLM exceeds a certain threshold, a dump trigger signal is sent to the positron beam kicker. By such a controlled beam dump a possible accidental beam loss with a high radiation level at the Lambda Wheels position can be prevented. The BLM is capable of detecting and preventing most accidental beam losses; however it cannot protect the Lambda Wheels against sudden beam losses occurring in a single revolution of the beam.

3.6 The trigger

The trigger system selects relevant physics events and suppresses background events. At HERMES the trigger system comprises first level triggering only, as second level triggering is not necessary. A trigger initiates digitization and complete read-out of the detector signals. Different trigger schemes are implemented, either optimized for different physics processes, or for the purpose of detector calibration monitoring. Most of the physics events recorded have a deep-inelastic scattering or quasi-real photoproduction signature. During the time needed for the digitization and read-out of the detector components no new triggers can be accepted [2]. This dead time of the system is defined as the ratio of rejected triggers to generated triggers.

As an example of a specific physics trigger the deep-inelastic scattering trigger (trigger 21) is described here. It optimizes the probability of actually detecting a positron from a deep-inelastic scattering event. This trigger requires, in coincidence, signals from the three hodoscopes (H0,H1,H2), together with an energy deposit above a certain threshold in two adjacent calorimeter columns. Additionally, the signals are required to be in

[2] Strictly speaking, the DAQ has a double buffer structure, i.e. two triggers can be stored simultaneously, but only the third is rejected if the previous two have not yet been digitized and read out.

coincidence with the HERA bunch signal. The calorimeter threshold is set to 3.5 GeV for unpolarized running. For polarized running it is lowered to 1.4 GeV to increase the accessible kinematic range to higher values of y.

3.7 The data acquisition system

The data acquisition system (DAQ) digitizes and reads out the detector signals to store the information for offline analysis. Upon a trigger the DAQ performs the readout of all relevant detector information. First the analog and timing information of all detector components is digitized by the front-end electronics, ADC and TDC modules hosted in FastBus crates in the electronics trailer in the east hall. The digitized information is then bundled by an event builder and sent to the online cluster. Here the raw data are buffered temporarily on hard disks in EPIO (Experimental Physics Input Output) format. In addition to the detector readout initiated by the trigger, information from the luminosity monitor, the polarimeters and the detectors concerning temperatures, gas pressure, supply voltages etc. is read out by the slow control system. These slow control data are acquired independent of the triggered events on a time scale of every 10 seconds and stored together with the raw data on the hard disk of the online cluster. Between HERA fills the data are backed up on tape locally in the HERMES control room and furthermore sent from the online cluster to the DESY computer centre at the main site to be saved on disk and tape robot.

Chapter 4

Formalism for the data analysis

The combination of a polarized beam, a polarized target, and a spectrometer of large acceptance and good particle identification at HERMES facilitates the extraction of double spin asymmetries from semi-inclusive measurements. In this chapter all aspects of the procedure to determine such an asymmetry are described, starting from data reconstruction, data quality and track requirements (sections 4.1 to 4.3), via particle identification, beam and target polarization and luminosity determination (sections 4.4 to 4.6) to the final equation for the extraction of the asymmetry from these ingredients (section 4.7).

4.1 Data reconstruction

To make the recorded data usable for physics analysis an off-line data reconstruction is performed using a chain of software packages. First, the raw data written in EPIO format [87] are decoded by the HERMES decoder (HDC) and written to an ADAMO data base [1] [88]. HDC translates the recorded electronic detector signals (such as TDC or ADC signals) into hit positions, energy deposits etc. using mapping and calibration files. Next, this information is passed to the HERMES reconstruction code (HRC) [89]. HRC first finds partial straight tracks in the front and the back part of the spectrometer independently. Then front and back tracks are matched within a given tolerance at the centre of the magnet to form full tracks[2]. The reconstructed track information (stored in the so-called HRC files) is synchronized with the slow control data (stored in the so-called slowlog-files) and together stored in the so-called μDST (Data Summary Tape) files. The μDSTs contain all information concerning the recorded event and the detector status needed for physics analysis.

The level at which two still independent data streams, namely the HRC files and the slow control files, exist is called main production, while the level of μDST-files, combining all information into one data stream, is called μDST production. At both levels the data

[1] All further steps use this database.

[2] This technique is known as the *forced bridge method*.

are reconstructed several times, with each iteration refining the reconstruction. Initially data are stored in "a"-productions for each data-taking period. In this production, the detector response is determined using information from calibrations of the previous data-taking period. The "b"-productions as the next step contain more detailed calibrations based on the corresponding "a"-production of the same data-taking period. In further productions ("c" and "d") more corrections, different tracking methods etc. are included.

The μDST productions containing the latest and best knowledge of data reconstruction for the years 1996 through 2000 are 96d0, 97d1, 98d0, 99c0 and 00d0. The first two digits represent the data-taking year, the letter at the third position and the final digit identify the production version. In all years, the data with polarized targets represent the largest amount of data collected. Nevertheless, a significant amount of data was also collected with unpolarized targets. In the analysis presented in this thesis only the datasets of longitudinally polarized hydrogen from productions 96d0 and 97d0, and of longitudinally polarized deuterium from the production 00d0 have been used [3].

In the HERMES experiment, data are grouped into certain time intervals when stored in the above mentioned data productions. The shortest interval is formed by an event, containing all information on the reconstructed tracks when a single trigger occurred. Events are grouped in bursts, which represent the time scale at which the slow control information is read out, corresponding to about 10 s of data-taking. Due to the random reversal of the target polarization, a burst of 10 s can be composed of 2 or 3 parts, called records, which correspond to different target polarization states. A run is defined by an amount of EPIO data corresponding to 450 MB, which usually requires of the order of 10 min to record. Manually stopped runs can of course be shorter, which happens whenever the experimental running conditions change, for instance when switching from polarized to unpolarized data-taking. A fill represents the longest time interval, comprising all data collected during a HERA positron fill, lasting up to 10-12 hours.

4.2 Data quality

During the measurements the beam provided by HERA as well as the HERMES target density are subject to fluctuations and the response of the HERMES detector may show instabilities, due to either external influences or internal failures. To perform a precision measurement these variations need to be monitored and fluctuations beyond a pre-defined range excluded from the data used for analysis by a so-called data quality check.

To ensure optimal data taking, the status of the polarimeters, the target, and the spectrometer are monitored continuously and an online data quality analysis is performed using a fraction of the data. Detected problems are recorded and if possible immediately corrected. Using the same analysis package, but this time off-line with the full set of data, a second level of data quality checks is performed on the main productions. Finally,

[3] Since the deuterium data taken in the years 1998-2000 are overwhelmingly dominated by the data taken in 2000, it has been decided to analyze only the 00d0 production, but not 98d0, 99c0.

the μDST productions are thoroughly checked for data quality with a dedicated software package generating web pages with a large set of data quality plots and collecting all data quality information in so-called burst lists, containing data quality bit-patterns for each record [90]. The HRC, slow control and/or μDST data are reprocessed for each period with problems which can be solved by a reanalysis of the data.

Various quality criteria are applied to select data which are suitable for analysis. These include general criteria needed for any analysis of the data as well as special criteria on the beam and target polarizations if polarized cross section analyses are performed. The information whether a certain criterion is fulfilled and whether the performance of a particular part of the experiment was satisfactory for the data to be suitable for physics analysis, is encoded in a data-quality bit. The bits for all criteria are then merged into a bit-pattern for each record. As the construction of the HERMES spectrometer allows separate data quality checks for the top and the bottom detectors, two bit-patterns are filled. For the data analysis presented in this thesis a multi-track coincidence in the full detector is required, therefore the data quality criteria need to be satisfied for both detector halves simultaneously.

The data quality criteria can be divided into six groups. Data are rejected if severe problems were reported in the logbook, if the data acquisition / reconstruction system malfunctioned, if the spectrometer or the luminosity monitor showed instabilities or if the beam or target conditions were unsatisfactory.

Logbook data quality

If the shift crew reports problems in the logbook and marks certain runs as non-analyzable the records of this period are discarded.

Data acquisition and reconstruction data quality

As the DAQ performs a series of initialization and termination procedures at the beginning and end of each run, which can affect the recording of the data, the first and the last burst of each run are rejected. Furthermore, any burst for which the data acquisition or the data processing did not work properly is marked as bad. The length of a record is required to be between 0 and 11 seconds. The live time, defined as the fraction of the time that the DAQ is not busy and therefore ready to accept an event, has to exceed 50 %.

Spectrometer data quality

The proper functioning of the tracking system is assured by rejecting all records with high voltage trips in the tracking chambers. In addition, all PID detectors are required to function properly.

Bit	set/not set	condition
0	not set if	target polarization parallel or antiparallel
1	not set if	beam polarization reasonable ($0.3 < P_B < 0.8$)
2	not set if	live time reasonable (> 0.5)
3	not set if	record length reasonable (0 s $< l \leq 11$ s)
4	not set if	beam current reasonable (5 mA $\leq I_B \leq 50$ mA)
5	not set if	luminosity rate reasonable (5 Hz $\leq L \leq 80$)
6	set if	first burst in a run
7	set if	bad μDST record
8	set if	no PID computed
9	not set if	logbook: data analyzable
10	not set if	logbook: target in polarized (2- or 4-state) mode
11	set if	logbook: unpolarized data
12	set if	logbook: no data quality available
13	set if	logbook: target in special (3-state) mode
14	set if	logbook: target in Bhabha scattering mode
15	set if	unpolarized data-taking in UGFS valve setting
16	set if	target bad
17	set if	dead blocks in calorimeter
18	set if	dead blocks in preshower detector or luminosity monitor
19	set if	TRD bad
20	set if	high voltage trips in tracking chambers
21	set if	certain runs with bad calorimeter or RICH
22	set if	high voltage trips in RICH
23	empty	
24	empty	
25	set if	RICH DQ bad
26	set if	target in 4-state mode (tensor polarization)
27	empty	
28	not set if	beam polarization measured within last five minutes
29	empty	
30	not set if	live time reasonable
31	set if	more than one dead block in calorimeter

Table 4.1: *Data quality bit-pattern for the 00d0 production.*

Luminosity data quality

To guarantee a reliable measurement with the luminosity monitor, the rates measured in this detector are confined to an allowed range of 5 - 80 Hz.

Beam data quality

A stable beam current is ensured by requiring beam currents in the range of 5 - 50 mA. Also, the beam polarization measurement has to be reliable, thus a beam polarization in the range 30 - 80 % is requested.

Target data quality

Not only for the beam but also for the target a stable performance is needed. The target polarization has to be in a well-defined spin state, either parallel or antiparallel to the beam polarization.

Apart from minor differences, the data quality criteria are the same for all productions across all data-taking periods. Tab. 4.1 gives an overview of all the 32 bits making up the data quality bit-pattern (the 00d0 production is taken as an example). In an analysis of data where beam and target polarization are demanded all the listed data quality criteria have to be satisfied; this means all bits have to be 0 to ensure a good quality of the data.

4.3 Track requirements

In addition to complying with all data quality checks, in order to be selected for analysis events are required to satisfy a number of cuts concerning the individual track parameters and the overall event kinematics. Only those tracks in the detector are considered which fulfill the cuts listed in Tab. 4.2. The tracks have to originate in the target cell, which is ensured by the cut on the transverse (t_{vertex}) and longitudinal (z_{vertex}) vertex positions. Moreover, the deflection angle in the spectrometer magnet $\Delta\Theta_x$ has to lie within a certain range, which is determined by the charge and the track momentum projected onto the $x-z$ plane (p_{xz}). This cut rejects tracks which are wrongly reconstructed with HRC in such a way that assigned charge and/or momentum are not consistent with the deflection angle. Furthermore, the tracks have to cross the calorimeter within a certain volume in order for the charged particle shower energy leaking out of the edges of the calorimeter to be negligible and the particle identification with the calorimeter to be reliable. This fiducial volume cut has to be fulfilled by the projection of the track (x_{calo},y_{calo}) onto the $x-y$ plane at a depth of 18 cm into the calorimeter lead glass blocks where the electromagnetic shower starts to develop. The momentum of any track is required to be within the interval 0.5 GeV to 28 GeV. The lower cut is needed for the tracks to reach

track parameter	requirement
transverse vertex	$t_{\mathrm{vertex}} < 0.75$ cm
longitudinal vertex	$\lvert z_{\mathrm{vertex}} \rvert < 18$ cm
hrc-track bending	$-0.2998/p_{xz} \cdot 1.3\mathrm{Tm} - 0.036 < \Delta\Theta_x$
	$< -0.2998/p_{xz} \cdot 1.3\mathrm{Tm} + 0.031$ (positive particles)
	$0.2998/p_{xz} \cdot 1.3\mathrm{Tm} - 0.031 < \Delta\Theta_x$
	$< 0.2998/p_{xz} \cdot 1.3\mathrm{Tm} + 0.036$ (negative particles)
fiducial volume	$\lvert x_{\mathrm{calo}} \rvert < 175$ cm, $30 < \lvert y_{\mathrm{calo}} \rvert < 108$ cm
track momentum	0.5 GeV $< p < 28$ GeV
sum of all momenta	0 GeV $< p_{\mathrm{sum}} < 28$ GeV

Table 4.2: *Standard track requirements.*

the back region of the detector and to be subject to the full particle identification, while the upper cut represents a consistency check since the momentum of a single track can never exceed the momentum of the beam. Neither can the sum of the momenta of all tracks.

4.4 Particle identification

For the analysis of semi-inclusive deep-inelastic scattering data the separation of leptons and hadrons and the identification of different hadron types is crucial. The particle identification (PID) at HERMES relies on the combined responses of four detectors: the Cerenkov detector (until 1997)/the RICH (since 1998), the transition radiation detector, the preshower detector and the calorimeter, (for the description of these detectors cf. section 3.4.2). The aim of an optimized PID scheme is to achieve the highest possible efficiency with the lowest possible contamination in the identification of the different particle types.

4.4.1 Formalism

Particle identification with the HERMES spectrometer is based on a Bayesian probability analysis of the four PID detector responses. The formalism is described in detail in [91, 92]. Technical issues of the software are documented in [93, 94].
For each detector D a likelihood $L^i_D(p, E)$ that a particle of type i with momentum p causes a signal with an energy E in this detector is defined. These likelihoods, also called parent distributions, are an intrinsic property of each PID detector and can be extracted from data collected during normal operation of the experiment. In order to derive the likelihood distribution for one detector D, a clean sample of particle type i is selected by imposing restrictive cuts on the other three PID detectors; for this sample the response of detector D is then determined.

Furthermore, the quantity $\phi^i(p, \theta)$, also named particle flux, is defined as the probability that a track with momentum p and polar angle θ is a particle of type i. The particle fluxes are calculated from data in an iterative procedure, starting from the assumption that the fluxes of hadrons and leptons are equal, and iterating until convergence is reached, typically in less than five steps.
The parent distributions L_D^i can be combined with the particle fluxes ϕ^i to give the relevant quantity for particle identification, the probability P_D^i that a track in detector D with track momentum p, polar angle θ and energy deposit E originates from a particle of type i,

$$P_D^i = \frac{\phi^i L_D^i}{\sum_j \phi^j L_D^j} \quad , \tag{4.1}$$

where the index j runs over all particle types to be distinguished. The individual likelihoods for each PID detector are multiplied to form overall likelihoods

$$L^i = \prod_D L_D^i \quad . \tag{4.2}$$

In the same way, overall probabilities can be constructed that a track passing through all four PID detectors is caused by a particle of type i, given by

$$P^i = \frac{\phi^i L^i}{\sum_j \phi^j L^j} \quad . \tag{4.3}$$

4.4.2 Hadron-lepton separation

In the case that only two particle types (leptons e and hadrons h) have to be distinguished, the probabilities that a detected particle is a lepton and a hadron respectively, P^e and P^h, can be combined into the logarithmic ratio

$$PID' = log_{10} \frac{P^e}{P^h} \ . \tag{4.4}$$

In terms of parent distributions and particle fluxes this quantity becomes

$$PID' = log_{10} \frac{L^e}{L^h} - log_{10} \Phi \ , \tag{4.5}$$

with $\Phi = \frac{\phi^h}{\phi^e}$. The flux factor Φ is the ratio of the number of hadrons to leptons incident on the detector. The quantity PID' is larger than zero if a particle is more likely to be a lepton than a hadron and vice versa. For each PID detector the logarithmic ratio $PID_D = log_{10} \frac{L_D^e}{L_D^h}$ can be calculated. The logarithmic likelihoods for different detectors can also be combined by evaluating for instance

$$PID2 = log_{10} \frac{L^e_{\mathrm{CAL}} \cdot L^e_{\mathrm{PRE}}}{L^h_{\mathrm{CAL}} \cdot L^h_{\mathrm{PRE}}} \ . \tag{4.6}$$

PID values commonly defined for the analysis of HERMES data are

$$PID2 = PID_{\mathrm{CAL}} + PID_{\mathrm{PRE}} \quad , \tag{4.7}$$

$$PID3 = PID_{\text{CAL}} + PID_{\text{PRE}} + PID_{\text{CER}} \quad \text{(until 1997)} \;, \tag{4.8}$$

$$PID3 = PID_{\text{CAL}} + PID_{\text{PRE}} + PID_{\text{RICH}} \quad \text{(since 1998)} \;, \tag{4.9}$$

$$PID5 = PID_{\text{TRD}} \quad , \tag{4.10}$$

where the subscripts CAL, PRE and CER refer to the calorimeter, the preshower counter and the Cerenkov detector, respectively. $PID_{\text{RICH}} = \sum_i PID_{\text{RICH},i}$ is the sum over the gas and aerogel response of the RICH detector, and $PID_{\text{TRD}} = \sum_i PID_{\text{TRD},i}$ is the sum over the six TRD modules. The quantities $PID2$, $PID3$ and $PID5$ do not represent the true probabilities because they do not yet include the flux ratio. Combining all four PID detectors and applying the flux correction one gets

$$PID' = PID3 + PID5 - log_{10}\Phi \quad . \tag{4.11}$$

In the data analysis, leptons are identified by requiring $PID' \geq 1$, while hadrons are selected by requiring $PID' \leq 0$. For semi-inclusive DIS data obtained with HERMES the lepton identification efficiency is larger than 98% with contaminations smaller than 0.6%. For hadron identification, the average efficiency is 99% with contaminations smaller than 0.1% [92].

4.4.3 Hadron identification

Pion identification with the threshold Cerenkov detector

The threshold Cerenkov detector, in operation until 1998 for particle identification, employs the fact that particles radiate Cerenkov light only above the particle-specific momentum thresholds (cf. section 3.4.2). Between the pion momentum threshold of 3.8 GeV and the kaon momentum threshold of 13.6 GeV pions are the only hadrons producing Cerenkov radiation. In this momentum range pions can therefore be separated from other hadrons by requiring a signal in the Cerenkov detector (number of detected photoelectrons above noise level), in addition to being identified as a hadron by the PID of all four detectors.
The pion identification efficiency depends on the particle momentum. At a momentum of 5 GeV the efficiency is about 90% and asymptotically increases to unity with higher momenta, reaching efficiencies above 99% at momenta larger than 7.5 GeV. The contamination of the pion sample is negligible [95].

Pion, kaon and proton identification with the RICH detector

The RICH detector, which replaced the threshold Cerenkov detector in 1998, measures the angular distribution of the Cerenkov light, providing particle identification of pions, kaons and protons in the momentum range 1 GeV $< p <$ 15 GeV by making use of the differences in their Cerenkov angles. The reconstruction of the Cerenkov angles uses as input information a list of fired PMTs (with a signal exceeding a predefined threshold) and the parameters of the particle track incident on the RICH as determined by the tracking detectors. The pattern of Cerenkov photons on the PMT matrix can be associated with tracks by two different methods [96], the indirect ray tracing (IRT) and the direct ray tracing (DRT) algorithm.

The IRT algorithm [97] compares for a given track the measured average Cerenkov angles with the theoretically expected ones in the following way. For each track, the theoretical emission angle $\theta^{a,g}_{(th);h}$ is calculated for each hadron type hypothesis, i.e. $h = \pi, K, p$, and for each radiator, i.e. assuming that the photon was emitted in the aerogel (a) or in the gas (g), respectively. On the other hand, for each fired PMT the Cerenkov angle with respect to each track is calculated. The average Cerenkov angle $\langle\theta\rangle^{a,g}_{(meas);h}$ for each hadron type hypothesis and for each radiator is then determined by including only angles within $\pm 2\sigma_\theta$ of the theoretically expected value, with $\sigma_\theta \simeq 8$ mrad the single photon resolution of the RICH.
From the measured average Cerenkov angle and the theoretically expected one, the likelihood for each hadron type hypothesis and each radiator is calculated as

$$\mathcal{L}^{a,g}_h = exp\left[\frac{-(\theta^{a,g}_{(th);h} - \langle\theta\rangle^{a,g}_{(meas);h})^2}{2\sigma^2_{\langle\theta\rangle^{a,g}_{(meas);h}}}\right] . \tag{4.12}$$

The likelihoods for the two radiators are combined to obtain an overall likelihood $\mathcal{L}^{tot}_h = \mathcal{L}^a_h \cdot \mathcal{L}^g_h$. The particle type of the track is assigned to the particle hypothesis with the largest overall likelihood.
The confidence level of the hadron identification is incorporated into the quality parameter

$$rqp = log_{10}\frac{\mathcal{L}^{tot}_{h_1}}{\mathcal{L}^{tot}_{h_2}} , \tag{4.13}$$

which defines the logarithmic ratio of the particle hypothesis with the largest likelihood, $\mathcal{L}^{tot}_{h_1}$, and the one with the second largest likelihood, $\mathcal{L}^{tot}_{h_2}$. If $rqp > 0$, a hadron is considered to be identified; if $rqp = 0$, i.e. $\mathcal{L}^{tot}_{h_1} = \mathcal{L}^{tot}_{h_2}$, the particle type is considered to be undefined.

The DRT method uses Monte Carlo simulations of the path of Cerenkov photons along the particle track assuming that the emission point of the radiation and the particle momentum are known, to determine hits at the PMTs for each particle hypothesis. The probabilities for each particle hypothesis are then calculated, analogously to the IRT method, from a comparison of the simulated hits to the actual fired PMTs.

At low particle momenta the DRT method is more effective, but computationally slower as compared to the IRT method. The RICH PID scheduler (RPS) [98] assigns to each track the hadron type hypothesis as calculated by the BEST method, either IRT or DRT depending on the specific track momentum and event topology.

Efficiencies and contaminations in the RICH hadron identification have been determined using both Monte Carlo simulations and experimentally reconstructed data of pion and kaon tracks from ρ^0, Φ, K_s and Λ decays [99]. This analysis provides identification probabilities $P_{h_t}^{h_i}$ that a given hadron of true type h_t is assigned as a hadron of identified type h_i, which are arranged in the so-called P-matrix

$$P = \begin{pmatrix} P_\pi^\pi & P_K^\pi & P_p^\pi \\ P_\pi^K & P_K^K & P_p^K \\ P_\pi^p & P_K^p & P_p^p \\ P_\pi^X & P_K^X & P_p^X \end{pmatrix} . \tag{4.14}$$

The fourth row contains the probabilities that a hadron of type h_t is not identified, i.e. $rqp = 0$. The columns of the P-matrix are by definition normalized to one. Excluding the last row one gets the truncated square matrix P' whose diagonal elements represent identification efficiencies while the off-diagonal elements resemble misidentification probabilities (note that they do not describe the contamination of the sample of type h_i because the relative hadron fluxes are not included).

The flux of identified hadrons, $\vec{I} = (I_\pi, I_K, I_p, I_X)$, is related to the flux of true hadrons, $\vec{N} = (N_\pi, N_K, N_p)$, as $\vec{I} = P \cdot \vec{N}$. Analogously, the flux of true hadrons can be extracted from the flux of identified hadrons, disregarding the unidentified hadrons, by using the inverse of the truncated P-matrix as $\vec{N} = (P')^{-1} \cdot \vec{I}$ [100]. If the so-called RICH unfolding is applied, each track of identified particle type i gets a weight for each true particle type j assigned according to the inverse P-matrix. The numbers of true hadrons are then calculated as the sums of these weights, running over all hadron tracks.

The P-matrix depends on the track momentum because of the momentum dependence of the Cerenkov angles. Furthermore, it depends on the event topology, i.e. on the track multiplicities per detector half, through the topology of rings on the PMT matrix. The P-matrices are available as functions of the track momentum in 1 GeV momentum bins for one, two and three tracks per given detector half. From the numerical values of the P-matrices as given in [101] it can be seen that the identification worsens with increasing multiplicity for all hadron types. This can be explained by the fact that with increasing multiplicity the Cerenkov rings on the PMT matrix start to overlap, which makes the assignment of single photons to the rings ambiguous. The pion identification efficiency is high, for single tracks it is above 92% for momenta below 4 GeV, and above 98% for momenta larger than 4 GeV. At the same time the misidentification probability, i.e. the probability to identify a kaon or a proton as a pion, is small. For kaons, the efficiency has a stronger momentum dependence, with efficiencies above 90% for momenta below 9 GeV and track multiplicity one, decreasing down to 60% at higher momenta, with a discontinuous drop to 50% at the kaon momentum threshold for the gas radiator, between 9 and 10 GeV. Protons are identified with efficiencies above 75% over the whole momentum range for single tracks.

4.4.4 PID cuts

In Tab. 4.3 the standard PID cuts as used in the analysis presented in this thesis for the identification of leptons and hadrons are summarized. No RICH unfolding is applied. As

particle	identification
lepton	$PID' \geq 1$ & $PID' \leq 80$
hadron	$PID' \leq 0$ & $PID' \geq -100$
pion	1996/97: #photoelectrons in Cerenkov > 0.25, $4 < p_h < 13.8$ GeV
	2000: RICH-Id = pion, $rqp > 0$, $1 < p_h < 15$ GeV
kaon	2000: RICH-Id = kaon, $rqp > 0$, $2 < p_h < 15$ GeV

Table 4.3: *Standard PID cuts.*

can be concluded from the high pion identification efficiency and the small contamination of the pion sample (cf. previous section), the RICH unfolding does not have any significant effect on the pion identification. For the kaon identification on the other hand, the RICH unfolding can indeed have an effect. However, as will be shown in chapters 6 and 7, the number of detected kaons with high-p_T is too small to be used for a significant extraction of the gluon polarization. Therefore, the RICH unfolding is neglected for the analysis presented in this thesis.

4.5 Beam and target polarization

In an asymmetry measurement, information on the, experimentally limited, beam and target polarizations is needed to calculate the dilution of the asymmetry. For the effective beam polarization a calibrated value per burst is directly available in the μDST-files. But the value for the effective target polarization is not as immediately accessible from the μDST-files. In principle, the effective target polarization can be calculated per burst, according to Eq. (3.2), from the fractions and the nuclear polarizations of atoms and molecules, recorded in the μDST-files. In practice, average values per year are commonly used. For the years 1997 and 2000, offline analyses are available which provide average values of the effective target polarization calculated from Eq. (3.2) for the complete datasets [102]. For the years 1996, 1998 and 1999 however, this approach of calculating the effective target polarization from Eq. (3.2) leads to large systematic uncertainties, due to difficulties with the recording of some target parameters. Therefore, average

year	target gas	target polarization	fractional uncertainty
1996	H	$\pm 0.759 \pm 0.042$	5.5%
1997	H	$\pm 0.850 \pm 0.032$	3.8%
1998	D	$\pm 0.856 \pm 0.064$	7.5%
1999	D	$\pm 0.832 \pm 0.058$	7.0%
2000	D	$+0.851 \pm 0.031$ -0.840 ± 0.029	3.5%

Table 4.4: *Target polarizations and their systematic uncertainties.*

target polarization values were for these years determined by renormalizing the inclusive DIS cross section asymmetry to the results from the 1997 and 2000 datasets respectively, yielding smaller systematic uncertainties [103]. The effective target polarizations and their systematic uncertainties for the years 1996 to 2000, as used in the analysis presented in this thesis, are summarized in Tab. 4.4.

4.6 Luminosity determination

For normalization purposes, the value of the luminosity is required. In an asymmetry measurement the count rates for the two spin orientations are normalized by the integrated luminosities corresponding to the data taking in each of those two states. For a cross section measurement and for a comparison of the data with MC simulation results, the absolute luminosity is needed for normalization.
In general, the integrated luminosity L, calculated from the time-dependent luminosity $\mathcal{L}$, reads

$$L = \int \mathcal{L}(t) dt \quad . \tag{4.15}$$

At HERMES the luminosity monitor does not measure a continuous time-dependent luminosity function $\mathcal{L}$ but a discrete count rate per burst. For this reason the luminosity accumulated during the burst i is calculated as the product

$$L_i = r_i \ l_i \ \epsilon_{DAQ,i} \quad . \tag{4.16}$$

Here, r_i is the count rate in the luminosity monitor during burst i, l_i is the time-length of this burst, and $\epsilon_{DAQ,i}$ is the live time of the data acquisition during this burst. The integrated luminosity for each of the two different spin orientations, summing over all accepted bursts in this configuration, is given by

$$L^{\stackrel{\rightarrow}{\Leftarrow}(\stackrel{\rightarrow}{\Rightarrow})} = \sum_i L_i^{\stackrel{\rightarrow}{\Leftarrow}(\stackrel{\rightarrow}{\Rightarrow})} \quad , \tag{4.17}$$

where the superscript $\stackrel{\rightarrow}{\Leftarrow}$ denotes the configuration of anti-parallel beam and target spin polarizations and $\stackrel{\rightarrow}{\Rightarrow}$ the parallel case. These integrated luminosities, uncorrected for any detector effects, can be used as normalization for an asymmetry measurement because in this case all detector effects cancel. If on the contrary a cross section measurement is desired, an absolute luminosity is needed taking into account luminosity monitor efficiency and acceptance effects. These detector effects can be simulated in a MC study and combined into a luminosity constant C_{lumi} [104] which transforms the uncorrected luminosity L into an absolute luminosity L_{abs} according to

$$L_{abs} = C_{lumi} L \quad . \tag{4.18}$$

4.7 Double spin asymmetries

4.7.1 Extraction of double spin asymmetries

The double spin asymmetry $A_{||}$, defined in Eq. (2.28) in section 2.2.3 in terms of the polarized cross sections $\sigma^{\rightleftarrows}$ and $\sigma^{\rightrightarrows}$ as

$$A_{||} \equiv \frac{\sigma^{\rightleftarrows} - \sigma^{\rightrightarrows}}{\sigma^{\rightleftarrows} + \sigma^{\rightrightarrows}} \ ,$$

can be related to the measured count rates, the integrated luminosities, and the beam and target polarizations, in the two different spin orientations.
Defining a spin-independent cross section $\sigma_0 = \frac{1}{2}(\sigma^{\rightleftarrows} + \sigma^{\rightrightarrows})$ and a spin-dependent cross section $\Delta\sigma = \frac{1}{2}(\sigma^{\rightleftarrows} - \sigma^{\rightrightarrows})$, the asymmetry can be written as

$$A_{||} = \frac{\Delta\sigma}{\sigma_0} \ , \tag{4.19}$$

and the total cross section can be split as

$$\sigma_{total}^{\rightleftarrows(\rightrightarrows)} = \sigma_0 \pm \Delta\sigma = \sigma_0(1 \pm A_{||}) \ , \tag{4.20}$$

where the negative sign is applicable for the parallel configuration. So far, an ideal experiment without any diluting effects is assumed. In HERMES, as in any other experiment, the cross section $\sigma^{\rightleftarrows(\rightrightarrows)}$ is diminished by detector efficiency and acceptance effects, included in a factor $\mathcal{A}(t) = \mathcal{A}$ assumed constant for each data-taking period, and the spin dependent part is further diluted by beam and target polarizations, P_B and P_B, which are less than 100%. These effects are included in the expression for the observed cross section

$$\sigma_{obs}^{\rightleftarrows(\rightrightarrows)} = \mathcal{A}\ \sigma_0\ (1 \pm P_B P_T A_{||}) \ . \tag{4.21}$$

This can be rearranged into

$$A_{||} = \frac{1}{P_B P_T} \frac{\sigma_{obs}^{\rightleftarrows} - \sigma_{obs}^{\rightrightarrows}}{\sigma_{obs}^{\rightleftarrows} + \sigma_{obs}^{\rightrightarrows}} \ . \tag{4.22}$$

The observed cross sections in turn can be expressed in terms of the count rates and the integrated luminosities

$$\sigma_{obs}^{\rightleftarrows(\rightrightarrows)} = \frac{N^{\rightleftarrows(\rightrightarrows)}}{L^{\rightleftarrows(\rightrightarrows)}} \ . \tag{4.23}$$

Combining this with Eq. (4.22) the double spin asymmetry $A_{||}$ is experimentally determined as

$$A_{||} = \frac{1}{P_B P_T} \frac{N^{\rightleftarrows} L^{\rightrightarrows} - N^{\rightrightarrows} L^{\rightleftarrows}}{N^{\rightleftarrows} L^{\rightrightarrows} + N^{\rightrightarrows} L^{\rightleftarrows}} \ . \tag{4.24}$$

At this stage it is assumed that the beam and target polarizations are stable over time, which in general they are not. Therefore, they are usually included in a polarization-weighted integrated luminosity as

$$L_P^{\rightleftarrows(\rightrightarrows)} = \sum_i L_i^{\rightleftarrows(\rightrightarrows)} P_{B,i} P_{T,i} \ , \tag{4.25}$$

where $P_{B,i}$ and $P_{T,i}$ denote the beam and target polarizations, respectively, during the burst i. The formula for the double spin asymmetry then becomes

$$A_{\parallel} = \frac{N^{\rightleftarrows} L^{\rightrightarrows} - N^{\rightrightarrows} L^{\rightleftarrows}}{N^{\rightleftarrows} L_P^{\rightrightarrows} + N^{\rightrightarrows} L_P^{\rightleftarrows}} \ . \tag{4.26}$$

4.7.2 Statistical uncertainty

The statistical uncertainty $\delta A_{\parallel}$ of the measured asymmetry $A_{\parallel}$ can be calculated from the statistical uncertainties $\delta N^{\rightrightarrows(\rightleftarrows)}$ in the numbers of events $N^{\rightrightarrows(\rightleftarrows)}$ using Gaussian error propagation. For sufficiently large numbers of events, $\delta N^{\rightrightarrows(\rightleftarrows)} = \sqrt{N^{\rightrightarrows(\rightleftarrows)}}$, and

$$\begin{aligned} \delta A_{\parallel} &= \sqrt{\left(\frac{\partial A_{\parallel}}{\partial N^{\rightrightarrows}} \delta N^{\rightrightarrows}\right)^2 + \left(\frac{\partial A_{\parallel}}{\partial N^{\rightleftarrows}} \delta N^{\rightleftarrows}\right)^2} \\ &= \frac{L^{\rightrightarrows} L_P^{\rightleftarrows} + L^{\rightleftarrows} L_P^{\rightrightarrows}}{\left(N^{\rightrightarrows} L_P^{\rightleftarrows} + N^{\rightleftarrows} L_P^{\rightrightarrows}\right)^2} \sqrt{\left(N^{\rightrightarrows}\right)^2 N^{\rightleftarrows} + \left(N^{\rightleftarrows}\right)^2 N^{\rightrightarrows}} \ . \end{aligned} \tag{4.27}$$

4.7.3 Systematic uncertainties

The dominant contributions to the systematic uncertainty for $A_{\parallel}$ can be attributed to the uncertainties of the beam and target polarization measurements. A further source of systematic uncertainty arising from particle misidentification is shown to be negligible. This section summarizes the sources of systematic uncertainties on the asymmetry measurement.

Beam polarization

In the years 1996-1998 the beam polarization was measured with the transverse polarimeter (TPOL). Since 1997 time-periods in which no reliable measurement of the TPOL was available were bridged with the measurement of the longitudinal polarimeter (LPOL). For the asymmetries extracted from the datasets 1996-1998 the systematic uncertainty arising from the beam polarization was assigned to be the uncertainty of the TPOL measurement of 3.4% (cf. section 3.1).

Since 1999 the LPOL has been mainly used to measure the beam polarization as its

systematic uncertainty of 1.6% is substantially smaller (cf. section 3.1). Only if no reliable LPOL measurement was available the TPOL measurement was used instead. The systematic uncertainty on the beam polarization (combination of LPOL and TPOL systematic uncertainties) amounts to 1.8% for 1999 and 1.9% for 2000, respectively.
Since the asymmetry is inversely proportional to the beam polarization, $A_{\|} \sim 1/P_B$, the systematic uncertainty of the measured asymmetry due to the beam polarization measurement is

$$\frac{(\delta A_{\|})_{P_B}}{A_{\|}} = \left| \frac{\delta P_B}{P_B} \right| . \tag{4.28}$$

Target Polarization

The systematic uncertainty of the target polarization arises from uncertainties in the measurements of fractions and nuclear polarizations of atoms and molecules. For the years 1997 and 2000 the average target polarizations and their systematic uncertainties were calculated from Eq. (3.2). The values obtained for the systematic uncertainty on the target polarization are 3.8% and 3.5%, respectively. For the years 1996, 1998 and 1999 the average target polarizations and their systematic uncertainties were determined by a renormalization of the measured asymmetries for inclusive DIS to the corresponding asymmetries measured in 1997 and 2000, respectively. This procedure yielded a systematic uncertainty on the target polarization of 5.5% for 1996, 7.5% for 1998 and 7.0% for 1999 (cf. section 4.5).
As the asymmetry is inversely proportional also to the target polarization, $A_{\|} \sim 1/P_T$, the systematic uncertainty of the target polarization measurement propagates into the systematic uncertainty of the asymmetry in the same way as for the beam polarization

$$\frac{(\delta A_{\|})_{P_T}}{A_{\|}} = \left| \frac{\langle \delta P_T \rangle}{\langle P_T \rangle} \right| . \tag{4.29}$$

Particle Identification

As mentioned in section 4.4, the efficiencies for lepton and hadron identification are very large while the contaminations of the lepton and hadron samples are negligible for semi-inclusive events. All asymmetries obtained in this thesis were found to be very stable with respect to changes in the lepton-hadron separation, for example employing older PID schemes, omitting the flux factors, or using different cuts on the PID to identify leptons and hadrons. The systematic uncertainty on the asymmetries due to the lepton-hadron separation is therefore neglected. The uncertainties on the asymmetries due to hadron identification, using pions identified with the Cerenkov counter or pions and kaons identified with the RICH detector, are neglected for similar reasons.

Total systematic uncertainty

The total systematic uncertainty on the asymmetries is calculated as the quadratic sum of the contributions from the various sources

$$(\delta A_{\|})^{syst.}_{tot} = \sqrt{\sum_i (\delta A_{\|})^2_i} \quad . \tag{4.30}$$

For the reasons given above, for the analysis presented in this thesis the total systematic uncertainties on the asymmetries are determined as the combination of the systematic uncertainties due to the beam and the target polarization uncertainties only.

4.7.4 Weighted averages of asymmetries

Asymmetries obtained from different datasets can be merged into one asymmetry by taking the error-weighted average. This method is used when combining asymmetries from data taken in different years, for example the asymmetries from the data taken in 1996 and 1997 into one asymmetry from hydrogen target data.
For N independent measurements of an asymmetry A^i with standard deviation σ^i, the error-weighted average of the combined asymmetry A and its standard deviation σ are calculated as

$$A = \frac{\sum_{i=1}^{N} \frac{A^i}{(\sigma^i)^2}}{\sum_{i=1}^{N} \frac{1}{(\sigma^i)^2}} \ , \tag{4.31}$$

and

$$\sigma = \sqrt{\frac{1}{\sum_{i=1}^{N} \frac{1}{(\sigma^i)^2}}} \ . \tag{4.32}$$

Since the data from different years can in principle be taken under different experimental conditions, sometimes it is desirable to prove the compatibility of two datasets before combining them. This can in general be done by a so-called t-test. The quantity

$$t_j = \frac{A_j^a - A_j^b}{\sqrt{\sigma_j^a + \sigma_j^b}} \tag{4.33}$$

is calculated for every bin j in which the asymmetry is obtained. The t_j distribution should have a mean of about 0 and a standard deviation of about 1 for the datasets to be considered compatible. The χ^2 per degree of freedom (equal to the standard deviation for a mean of 0) is calculated as

$$\chi^2/ndf = \frac{1}{n}\sum_{j=1}^{n} t_j^2 \ , \tag{4.34}$$

where the number of bins n determines the number of degrees of freedom.
The compatibility of the datasets 1996 and 1997 has been shown, for example in [92] and [53], for semi-inclusive DIS-events as well as for single hadrons in electro- and in photoproduction. For the analysis presented in this thesis, the compatibility of the 1996 and 1997 datasets will in general be assumed.

Chapter 5

Formalism for the extraction of the gluon polarization

Information on the gluon polarization in the nucleon can be extracted from events in which a gluon from the nucleon is involved in the scattering process. In lepton-nucleon scattering this is the case in the photon-gluon fusion process $\gamma g \rightarrow q\overline{q}$, in which the virtual photon originating from the incident lepton interacts with a gluon in the nucleon, and in the anomalous photon processes $qg \rightarrow qg$, $gg \rightarrow q\overline{q}$ and $gg \rightarrow gg$, in which the photon first splits into partons, and one of these then interacts with a gluon in the nucleon (as to be discussed in more detail in section 5.1.4). However, not only these (signal) processes but also various background processes contribute to the measured double spin asymmetry of high-p_T hadrons. Since in the data the background processes cannot be distinguished from the signal, Monte Carlo simulations are required to obtain information on the relative contributions of the various processes to the asymmetry. With this information at hand, one can optimize the data selection and extract the gluon polarization from the measured double spin asymmetries with the highest possible significance, as will be shown in subsequent chapters.

After discussing some general principles of Monte Carlo simulations and describing two specific generators in more detail (section 5.1), the formalism to extract the gluon polarization from the measured asymmetries with the information taken from the Monte Carlo simulations is elucidated (section 5.2), and the analysis channels to be used in subsequent chapters are introduced (section 5.3).

5.1 Monte Carlo Generators

This section gives a general description of the Monte Carlo generators which are used for the extraction of the gluon polarization in the following chapters. First, the implementation of the Monte Carlo generators in the HERMES software is illustrated (section 5.1.1). It is then discussed how the generators model the fragmentation process (section 5.1.2). Finally, the two Monte Carlo generators used in this thesis are described, the LEPTO generator (section 5.1.3) and the PYTHIA generator (section 5.1.4).

5.1.1 Monte Carlo generators in Hermes software

To compare Monte Carlo simulations with data it is not sufficient to use a stand-alone MC generator, as the possible interactions of the generated particles inside the detector have to be simulated as well. Therefore, the Monte Carlo generators are embedded in the standard HERMES software chain. In separate steps, the scattering process itself and the resulting signals in the detector are simulated. At each step, the information is available in ADAMO format and can be stored if desired.

For the generation of the scattering event (including the hard process and the fragmentation) various Monte Carlo generators are available in the HERMES software, i.e. LEPTO [1] [106], PYTHIA [50] and a range of other generators for more specific applications. The generators are all implemented into a common so-called GMC frame, in which they can be combined with other generators and/or with programs that calculate radiative corrections. At this stage of simulation it is possible to vary MC model parameters, define selectors (i.e. impose restrictions on the event kinematics and topology) etc.

The generated event is passed on to either a software package called HMC or to a software package called HSG (HERMES smearing generator). HMC is a GEANT based simulation of the HERMES detector in which the particles, generated at the previous level, are tracked through the detector. Their interaction with the detector material is simulated and the information is stored in the form of simulated hits in the detectors along the particle trajectories. Those simulated hits are then fed into the track reconstruction software to give as output simulated tracks. From this stage the generated MC information is processed further in exactly the same way as the data, yielding MC-μdst-files as the final step.
For all applications used in this analysis, it is sufficient to replace the time-consuming tracking of the events with HMC by the much faster simulation with HSG. In this case, from each generated event only those particles are selected which will reach the geometrical acceptance of the detector. This is dependent on the momentum via the bending of the particles in the magnet. The selection is accomplished by using lookup tables in which the effect of the magnetic field and the geometrical parameters of the spectrometer are incorporated. The momentum of the selected particles is then altered with the help of the so-called smearing function in order to account for the interactions of the particles in the detector. In this function, which is available for every particle type, several effects are taken into account, such as the loss of particles which end up outside the acceptance due to smearing or are lost due to decays. The information from HSG is then processed into MC-μdst-files.

5.1.2 Fragmentation models in MC generators

A high-energy collision process can be split into two parts, the perturbatively calculable part of the hard interaction between the initial state partons and photons, and the non-

[1] Throughout this thesis, the modified version of LEPTO for the simulation of polarized scattering, called PEPSI [105], is used when LEPTO is mentioned.

perturbative part accounting for the fragmentation of the final state partons into hadrons. MC simulations of such collisions follow this division into two stages. The partonic processes are simulated according to their matrix elements (taken from perturbative QED and QCD calculations), while the hadronization is described by phenomenological fragmentation models. The LEPTO and PYTHIA MC generators differ in their simulation of the partonic processes (as discussed in more detail in the following two sections) but both use the same fragmentation model, namely the LUND string fragmentation model [24] as implemented in the JETSET program [25, 26].

In the LUND string model the effect of quark confinement at large distances is modelled as a string or colour flux tube. This string represents the field between two coloured objects, e.g. a $q\overline{q}$ pair, or a quark and the remnant of the nucleon after one of its quarks has been struck. The energy stored in the string increases when the two coloured objects are moved apart, according to a linearly rising potential with the so-called string constant. If the energy is large enough the string can break and split into two strings, producing a new $q\overline{q}$ pair. This procedure is repeated until the energy in a string drops below a certain threshold where the production of new $q\overline{q}$ pairs is no longer possible. Also gluons can be radiated, modelled as kinks in the strings.

The model contains a large number of parameters to describe this whole mechanism, e.g. for the distribution of transverse momenta generated at a string splitting, for the energy and longitudinal momentum sharing at such a break-up, for the relative occurrence of the different flavours, for the formation of baryons from the quarks etc. The default settings of these parameters are mostly deduced from e^+e^- collision data, but do not describe the HERMES data sufficiently well. Therefore, the parameters have been adjusted in such a way that a good account of the measured pion, kaon and proton multiplicities vs. different kinematic quantities such as x, Q^2, z, p_T etc. is obtained for HERMES. For all MC applications in this thesis the latest available adjustment of the fragmentation parameters, named tune 2004c, is used, unless otherwise stated. This tune 2004c supercedes the older tune 2004a, improving the agreement of data and MC multiplicities in general, and the reproduction of positive and negative hadron multiplicities in particular [107].

The JETSET parameters are described in detail in [26, 107]. Here, only the JETSET parameters related to the transverse momentum acquired by the hadrons in the fragmentation will be explained. This transverse momentum in the LUND string model is distributed as a Gaussian with a width $\sigma_{p_T,F}$=PARJ(21), by default set equal to 0.36 GeV. PARJ(23) and PARJ(24) determine non-Gaussians tails, modifying the Gaussian shape assumed above. A fraction PARJ(23) of the Gaussian transverse momentum distribution is taken to be a factor PARJ(24) larger than input in PARJ(21), with default values PARJ(23)=0.01 and PARJ(24)=2. At a later stage of this thesis, these fragmentation parameters will be set to other than their default values to determine their influence on the extracted gluon polarizations.

5.1.3 The LEPTO generator

First order QCD processes

The LEPTO MC generator [106] can simulate in addition to the leading order Deep-Inelastic Scattering process (DIS) the two next to leading order (or first order QCD) processes QCD Compton scattering (QCDC) and Photon-Gluon-Fusion (PGF)[2]. As LEPTO can simulate events only at $Q^2 > 0.5$ GeV^2 it is applicable to the semi-inclusive deep-inelastic scattering region covered by HERMES, but is not suitable for the (quasi-real) photoproduction domain.

The first order QCD hadronic cross sections (QCDC and PGF) are calculated by folding the parton distribution functions with the hard scattering (partonic) cross sections. The matrix elements of these partonic cross sections involve in addition to the two leptonic degrees of freedom three hadronic ones. The partonic cross sections have soft and collinear divergences which, when calculating the hadronic cross sections analytically, are partly cancelled by virtual corrections and partly absorbed by the PDFs. But to avoid such singularities in the MC simulations one imposes a cutoff which ensures that the two partons produced in the first order QCD process are resolvable. This cutoff is to a certain extent arbitrary. Its chosen value will influence the process fractions of the first order QCD processes, as resulting from the simulation.
The cutoff can be imposed using different schemes [108, 109], available through the LEPTO switch LST(20) [106]. In LEPTO the so-called W-scheme is used for fixed target experiments (which is also known as the final hadronic cms irresolvability criterion)

$$m_{ij}^2 = (p_i + p_j)^2 > y_{cut} W^2 \ . \tag{5.1}$$

The invariant mass m_{ij}^2 of any two emitted partons i and j has to be larger than a certain fraction, determined by the parameter y_{cut}, of the invariant hadronic mass squared W^2. In addition m_{ij} is not allowed to become smaller than a certain minimal value $m_{ij}^{\min}$. Those two parameters y_{cut} and $m_{ij}^{\min}$ which determine the cutoff are coded into the LEPTO parameters PARL(8) and PARL(9). Default cutoff settings tuned to EMC energies are given as $y_{cut} = 0.005$ and $m_{ij}^{\min} = 2$ GeV. For HERMES energies a lower cutoff $m_{ij}^{\min}$ might be possible [110], which is investigated in section 6.1.1.

On an event-by-event basis, LEPTO decides whether to generate one of the first order QCD processes rather than the leading order process. This decision is taken on the basis of the probabilities for each process type which are evaluated as functions of the inclusive kinematic variables (x, Q^2). The probabilities P_{qg} and $P_{q\bar{q}}$ for QCDC and PGF are calculated from the relevant matrix elements, while the probability P_q for DIS is taken as $P_q = 1 - P_{qg} - P_{q\bar{q}}$. If a first order QCD process is chosen three new hadronic variables are calculated from the matrix elements, which together with the two leptonic variables define the four-momenta of the scattered lepton and the produced partons.

[2] The simulation of the first order QCD processes is switched on with the LEPTO parameter LST(8).

The gmc_DISNG frame

The LEPTO generator is integrated in the HERMES MC frame gmc_DISNG [3]. In this frame the LEPTO generator is combined with a program that includes QED radiative corrections and a generator for elastic events, which cannot be simulated with LEPTO.

The generation of events with gmc_DISNG is performed in a series of steps, going backwards from the state observed after the actual scattering to the underlying hard process. First the kinematical variables of the virtual photon are generated, as they would be determined from the measured final state scattered lepton. These are labelled *observable kinematics*. Any two independent kinematic variables of the photon can be used at this stage (e.g. $(\log Q^2, \nu)$), which are drawn from a flat distribution. From these two variables all other kinematic quantities of the photon are derived. Furthermore, the Born cross section is determined according to the structure function F_2, either using a parametrization of the world data of F_2 or using F_2 as the sum of the charge-weighted unpolarized parton distribution functions taken from one of the PDF sets implemented in gmc_DISNG.

If no radiative corrections are simulated, the selected kinematical variables of the virtual photon are directly passed on to LEPTO to choose the process according to the process probabilities and the struck parton in the nucleon according to the unpolarized parton distributions. This information on process, struck parton and target remnant is then used by JETSET to simulate the fragmentation into a hadronic final state, using the LUND string model. A weight is assigned to every event according to the Born cross section in order to compensate for the original generation of events from a flat distribution.

If radiative corrections are simulated, the selected virtual photon kinematical variables are first handed over to RADGEN [111]. This program calculates the observable cross section taking into account the radiative corrections to the Born cross section. Depending on the type of radiative correction, RADGEN does or does not generate a real photon. If the event was classified as one in which a bremsstrahlung photon is emitted, the observable kinematical variables of the virtual photon are corrected for this extra photon emission, which occurs before the lepton is detected. In this way the virtual photon kinematical variables at the hard (virtual photon-nucleon) scattering vertex, which are labelled *true kinematics*, are calculated. Only after this step does LEPTO decide on the type of process and struck parton, whereupon JETSET simulates the fragmentation. In this case, i.e. if radiative corrections are applied in the simulation, every event is weighted according to the observable cross section.

[3] In the following analysis chapters whenever LEPTO is mentioned the full gmc_DISNG frame is actually used.

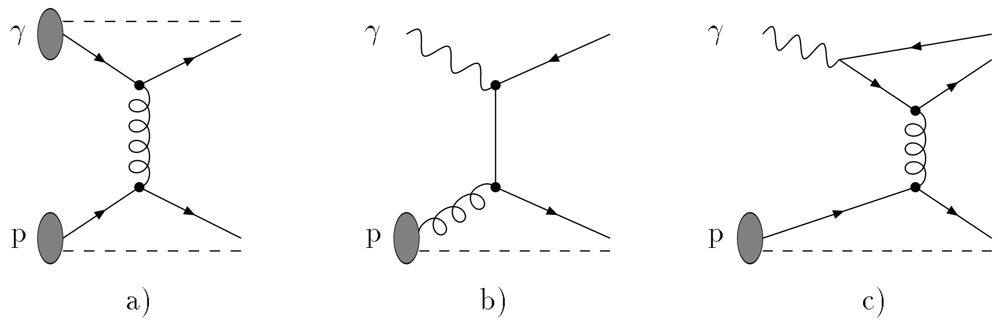

Figure 5.1: *Main event classes in γp interactions as simulated in PYTHIA: a) VMD, b) direct, and c) anomalous. The full lines represent partons that (may) give rise to high-p_T jets, the dashed lines indicate the presence of spectators. Only basic graphs are drawn.*

5.1.4 The PYTHIA generator

The PYTHIA 5 generator [25, 26], previously used in HERMES analyses, could only simulate real $\gamma p(n)$ events, i.e. it was restricted to the region of real photoproduction ($Q^2 = 0$). In order to be able to use these simulations for analysis of HERMES $ep(n)$ events, each event had to be re-weighted by the user to convert the real photoproduction cross section to a leptoproduction cross section. This was done by applying a virtual photon flux according to the Weizsaecker-William approximation to generate the virtual photon kinematic variables. It is emphasized that this conversion is not exact, as it does not involve a true simulation of the virtual photon spectrum. For the same reason, the leading order DIS process could not be simulated at all.

The new PYTHIA 6 generator [49, 50], used in the present work, incorporates the treatment of real and virtual photons, thus spanning the whole region between real photoproduction ($Q^2 = 0$) and truly deep-inelastic scattering ($Q^2 = \infty$). In this version also the leading order DIS process can be simulated. PYTHIA 6 simulates the total virtual photon-nucleon cross section and weights it with the virtual photon flux, thus obtaining the lepton-nucleon cross section.

Process classification

The events simulated with PYTHIA for $\gamma^{(*)}p$ interactions can be divided into three main event classes [112] (cf. Fig. 5.1).

1. The VMD processes: The photon turns into a vector meson before the interaction with the nucleon. In this event class all processes occurring in hadronic physics (hadron-hadron interactions) are included, namely elastic and diffractive scattering as well as hard and soft non-diffractive scattering. Non-diffractive scattering basically covers all hadronic processes which are not described by elastic or diffractive scattering and contains the hard non-diffractive VMD processes and the soft so-called low-p_T events for which no perturbative description exists.

2. The direct processes: The photon interacts with a parton from the nucleon. For real photons, this event class contains the QCD Compton scattering process (QCDC) and the Photon-Gluon-Fusion process (PGF). If the photon is virtual, also the leading order DIS process (LO DIS) is included.

3. The anomalous processes: The photon splits perturbatively into a $q\bar{q}$ pair, one quark of which (or a daughter parton thereof) interacts with a parton from the nucleon. These are QCD $2 \to 2$ processes either involving a quark/antiquark or a gluon from the nucleon. (One should note that the anomalous processes differ from the hard non-diffractive VMD processes only insofar as the former are generated according to the parton distributions in the photon but the latter according to the parton distributions in the vector meson.) [4]

For all three classes, the nucleon will always leave a remnant containing the partons that did not interact, which evolves into a 'jet'. However, the classes differ as to the possible remnant on the photon side. In the direct processes, all the photon energy is absorbed in the hard interaction leaving no remnant on the photon side, while the VMD processes (except for the elastic and single diffractive VMD) and the anomalous processes lead to a remnant on the photon side.

The different classes can only be distinguished unambiguously in certain phase space regions, but there are transition regions in which the classification of the events is not unambiguous. In a Monte Carlo simulation, however, events have to be assigned to one certain class, using sharp boundaries whereas in nature smooth transition regions exist.
In the case of a real photon interaction the Monte Carlo classification can be illustrated by introducing two transverse momentum scales, $k_\perp$ and $p_\perp$, where $k_\perp$ is the transverse momentum at the γ vertex while $p_\perp$ belongs to the hard process involving the parton from the proton (cf. Fig. 5.2). In the two-dimensional $(k_\perp, p_\perp)$-phase space the various processes correspond to distinct regions. In the region $k_\perp < k_0$, where k_0 defines the boundary, the transverse momentum at the photon vertex is small, and the process is classified as VMD. The region $k_\perp > k_0$ can be subdivided by the diagonal $k_\perp = p_\perp$. If $k_\perp > p_\perp$, the hard process, i.e. the one involving the largest momentum, is $\gamma g \to q\overline{q}$, corresponding to the upper part of Fig. 5.2(a). The lower part of the graph is included in the gluon distribution in the nucleon. The process in this case is a direct one. If on the other hand $p_\perp > k_\perp$, the hard process is $\overline{q}q' \to \overline{q}q'$, corresponding to the lower part, hence the upper part of the graph is included in the parton distribution of the photon. These processes are anomalous ones.
The distinction between VMD and anomalous processes can alternatively be replaced by the classification into VMD and Generalized VMD (GVMD) processes. In this case a region of $k_0' < k_\perp < k_0$ is defined in which the photon does split into a $q\overline{q}$ pair, but interacts just like a vector meson. This region is combined with the anomalous processes into the GVMD region, leaving the processes with $k_\perp < k_0'$ as the VMD region.
If the reaction involves a virtual photon, the photon virtuality Q^2 is introduced as a third scale, cf. Fig. 5.3. If $Q^2 > k_\perp^2 > p_\perp^2$ and $Q^2 \gg 0$ the event is identified with the

[4] The VMD and anomalous processes are often also named 'resolved' since the photon resolves in partons before interacting with the nucleon.

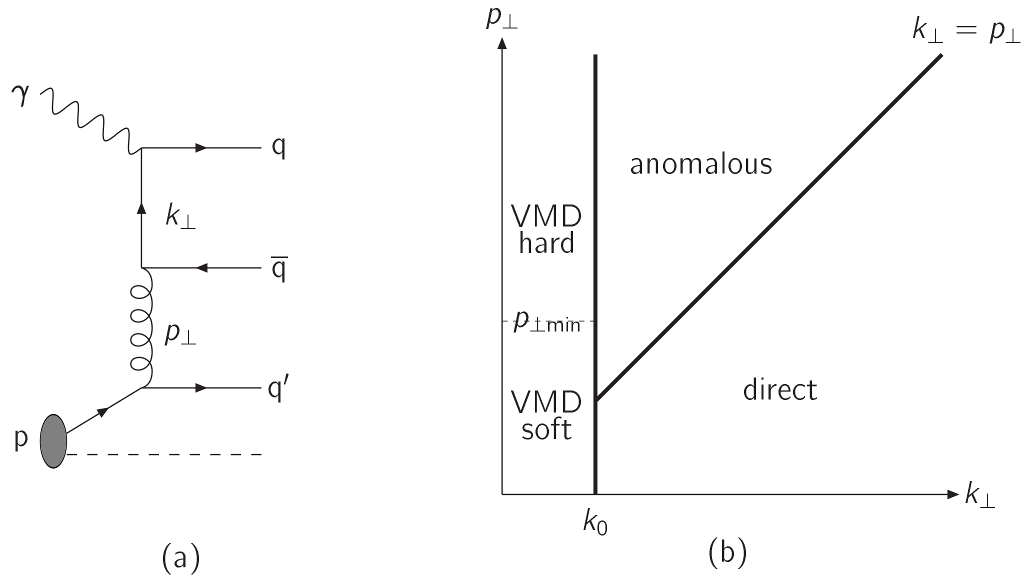

Figure 5.2: *(a) Schematic graph for a hard* γp *process, illustrating the concept of two different scales. (b) The allowed phase space for this process subdivided into event classes.*

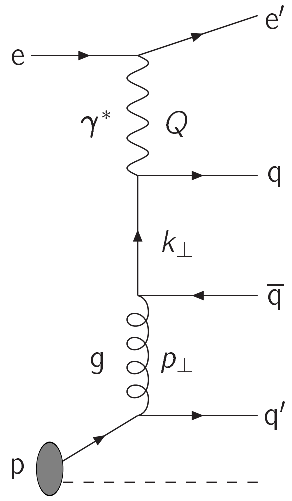

Figure 5.3: *Schematic graph for a hard* γ*p *process, illustrating the concept of three different scales.*

leading order DIS process. The region $k_\perp^2 > Q^2$ and $k_\perp^2 > p_\perp^2$ contains the first order QCD corrections to the leading order DIS process, namely QCDC and PGF. At $Q^2 \to 0$, these two processes become increasingly dominant over the leading order DIS process. The region with $p_\perp^2 > k_\perp^2 > Q^2$ can be considered as containing the anomalous processes again.
At the relatively low HERMES energies the scales Q^2, $k_\perp$ and $p_\perp$ might be close, making it difficult to classify the events unambiguously.

process	number	name	group	class
$qq \to qq$	11	QCD $2 \to 2$	anom_q	anomalous
$q\overline{q} \to q\overline{q}$	12			
$q\overline{q} \to gg$	13			
$qg \to qg$	28	QCD $2 \to 2$	anom_g	
$gg \to q\overline{q}$	53			
$gg \to gg$	68			
$Vp \to Vp$	91	elastic	VMD	VMD
$Vp \to VX$	92	proton single diffractive		
$Vp \to Xp$	93	VM single diffractive		
$Vp \to XX$	94	double diffractive		
$Vp \to X$	95	soft non-diffractive	low_pt	
$\gamma^* q \to q$	99	LO DIS	DIS	direct
$\gamma^*_T q \to qg$	131	QCDC	QCDC	
$\gamma^*_L q \to qg$	132			
$\gamma^*_T g \to q\overline{q}$	135	PGF	PGF	
$\gamma^*_L g \to q\overline{q}$	136			

Table 5.1: *The PYTHIA processes as used in the analysis presented in this thesis. V represents a vector meson, γ^*_T denotes a transverse and γ^*_L a longitudinal photon.*

In PYTHIA the processes at the partonic level are identified by process numbers. Tab. 5.1 gives an overview of the processes relevant for the analysis discussed in this thesis and the corresponding process numbers, the process name, the process group chosen for this analysis, and the event class they belong to. For all further applications in this thesis the processes are arranged into seven groups: anom_q, anom_g, VMD, low_pt, DIS, QCDC, and PGF. The processes 11-68 are, according to this, split into two groups, those with a gluon as the struck parton in the nucleon (abbreviated anom_g), and those with a quark (abbreviated anom_q) [5], and the processes 91-95 are split into the elastic and diffractive VMD (abbreviated VMD) and the soft non-diffractive VMD (abbreviated low_pt) [6]. The PGF processes together with the anom_g processes are considered signal, while all other processes are combined into background.

[5] The processes with process number 28 can involve a gluon or a quark from the nucleon and are therefore partly counted as signal (in anom_g), and partly as background (in anom_q). This could not be accounted for accurately in Tab. 5.1.

[6] Strictly speaking, events of process number 11-68 can either belong to the anomalous event class or, as hard non-diffractive VMD, belong to the VMD event class, depending on the scales involved in the scattering. This could not be depicted correctly in Tab. 5.1 either. If the term anomalous processes is used in the following parts of this thesis, the hard non-diffractive VMD processes are included.

Cross sections

Based on these different event classes [112] the total γp cross section for real photoproduction can be written as

$$\sigma_{tot}^{\gamma p} = \sigma_{VMD}^{\gamma p} + \sigma_{direct}^{\gamma p} + \sigma_{anomalous}^{\gamma p} . \tag{5.2}$$

If one extends this to virtual photons, the leading order DIS process has to be included. The direct part of the virtual photon-nucleon cross section then becomes

$$\sigma_{direct}^{\gamma^* p} \simeq \sigma_{DIS}^{\gamma^* p} = \sigma_{LODIS}^{\gamma^* p} + \sigma_{QCDC}^{\gamma^* p} + \sigma_{PGF}^{\gamma^* p} . \tag{5.3}$$

If the leading order DIS term is calculated by subtracting the QCDC and PGF terms from the total DIS cross section it can become negative at small values of Q^2. As this is not allowed, the leading order term is instead taken to decrease exponentially in PYTHIA, vanishing at $Q^2 \rightarrow 0$. This is achieved by applying a Sudakov form factor of $exp(-(\sigma_{QCDC}^{\gamma^* p} + \sigma_{PGF}^{\gamma^p})/\sigma_{DIS}^{\gamma^* p}$ to the total DIS cross section in the calculation of the leading order DIS term.
The total virtual photon-nucleon cross section is modelled by taking the sum of all processes as

$$\sigma_{tot}^{\gamma^* p} = \sigma_{LODIS}^{\gamma^* p} + \sigma_{QCDC}^{\gamma^* p} + \sigma_{PGF}^{\gamma^* p} + \epsilon(W^2, Q^2)(\sigma_{VMD}^{\gamma^* p} + \sigma_{GVMD}^{\gamma^* p}) . \tag{5.4}$$

The VMD and GVMD processes are suppressed by a factor $\epsilon(W^2, Q^2) = (W^2/Q^2 + W^2)^n$ with the tunable parameter n of the order of 3 or 4 , to avoid double counting due to an overlap between VMD and GVMD and the LO DIS process at intermediate Q^2 and small W^2.
Finally, the lepton-nucleon cross section σ^{ep} is obtained by weighting the virtual photon-nucleon cross section $\sigma^{\gamma^* p}$ with the virtual photon flux according to the Weizsaecker-Williams approximation.

PYTHIA parameters

PYTHIA contains a variety of parameters, tuning of which will, among other things, shift the relative contributions of the different processes, e.g. via one of the above mentioned suppression factors. The default PYTHIA settings were originally optimized for describing scattering processes at higher energies. Recently, the settings have been re-tuned such that PYTHIA gives a good account of the HERMES data, e.g. cross sections and other observables [53]. These adjusted parameters are used throughout this thesis. For detailed information on the parameters and the tuning to HERMES data cf. [50, 53]. At this point only one crucial parameter of the PYTHIA model shall be explained in more detail. The parameter MSTP(18) determines the lower limit of $k_\perp$ above which direct processes are generated. By default, this parameter is set to MSTP(18)=3, which calculates $k_{\perp,min}$ as a function of W^2, for HERMES kinematics $k_{\perp,min} \approx 1.4$ GeV. Setting this parameter to MSTP(18)=2 defines $k_{\perp,min}$=PARP(15), which is equal to 0.5 GeV by default. This results in a larger phase space for the generation of direct events, and consequently larger process fractions for QCDC and PGF. The effect of switching this PYTHIA model parameter from the default to MSTP(18)=2 on the results for the extracted gluon polarization will be studied in later chapters.

The PYTHIA implementation for HERMES

The PYTHIA generator is integrated in the HERMES Monte Carlo frame (GMC). The original PYTHIA code cannot handle radiative corrections, but calculates cross sections only at Born level. In PYTHIA events are generated according to a distribution reflecting the cross section, and consequently have a weight of one. This is in contrast to LEPTO where the generation is based on a flat distribution, and the events get a weight according to the cross section. First a process is selected; next, the kinematic variables of the virtual photon are determined; and subsequently the other participating partons and their kinematic variables are chosen. From a comparison to the cross section distribution it is then decided if the event is accepted or rejected. Accepted events are passed on to JETSET to simulate the fragmentation. In [53] it is described how radiative corrections are introduced into the PYTHIA MC within the HERMES Monte Carlo frame. They are implemented in a modified routine which is called to select the kinematic variables of the virtual photon. For more details on the technical implementation cf. [53].

5.2 From data and MC to gluon polarization

The double spin asymmetry measured in the production of high-p_T hadrons can be expressed as the superposition of the asymmetries $A_{||}^i$ from all subprocesses which contribute to the total asymmetry with the corresponding process fractions f_i as

$$A_{||}^{meas} = \sum_i f_i A_{||}^i = f_{sig} A_{||}^{sig} + f_{bg} A_{||}^{bg} \quad \text{with} \quad \sum_i f_i = 1 \ . \tag{5.5}$$

In order to extract the gluon polarization from the data, Monte Carlo simulations are needed to determine the relative fractions of the signal processes (f_{sig}) and those of the various processes contributing to the background (f_{bg}), and furthermore the asymmetries from these processes ($A_{||}^{bg}$), as functions of the kinematical variables involved. The asymmetry from the signal process can, on the other hand, be decomposed into the hard process asymmetry, known from perturbative calculations, and the gluon polarization, the only remaining unknown.

Two specific Monte Carlo programs, in which different processes are included (as described in section 5.1), are used for the extraction of the gluon polarization.

While the LEPTO MC can simulate events with polarized beam and target particles, the PYTHIA MC is restricted to interactions with unpolarized particles. For that reason, the formalism for the determination of the asymmetries for the various processes differs.

With the LEPTO Monte Carlo, the asymmetries are evaluated by running the MC generator in the two spin configurations (namely with target and beam spin oriented parallel and antiparallel). LEPTO simulates the count rate N for each of these two configurations by making use of the polarized parton distribution functions and the hard scattering asymmetries. Double spin asymmetries for the various processes can be calculated, analogously to the data, according to

$$A_{\parallel} = \frac{N^{\rightleftarrows} - N^{\rightrightarrows}}{N^{\rightleftarrows} + N^{\rightrightarrows}} , \tag{5.6}$$

where $N^{\rightleftarrows}$ and $N^{\rightrightarrows}$ are the number of events of a certain process type in the antiparallel and parallel spin configuration. The target and beam polarizations used in the MC are 100%. The same number of events are generated for each of the two spin configurations. These asymmetries can be calculated for each background process.

Since PYTHIA cannot be used to simulate the scattering of polarized particles, the asymmetries for the various background processes cannot be directly extracted from the simulated events. Instead, for every event j an asymmetry weight a_j is calculated on the basis of its event kinematics and the hard process involved. The asymmetry for the background processes can then be written as the normalized sum over the weights

$$f_{bg} A_{\parallel}^{bg} = \frac{1}{N_{tot}} \sum_{j=1}^{N_{bg}} a_j^{bg} . \tag{5.7}$$

Independent of the specific Monte Carlo generator used, the remaining formalism for the extraction of the gluon polarization is the same. For the signal process the asymmetry is given by

$$f_{sig} A_{\parallel}^{sig} = \frac{1}{N_{tot}} \sum_{j=1}^{N_{sig}} a_j^{sig} . \tag{5.8}$$

The asymmetry weight a_j^{sig} for every signal event can be expressed by

$$a_j^{sig} = \hat{a}_j^{sig}(y, Q^2, \hat{s}, \hat{t}, \hat{u}) \frac{\Delta g}{g}(\hat{Q}^2, x_g) . \tag{5.9}$$

Here, $\hat{a}_j$ is the hard process asymmetry as a function of the photon kinematic variables and the Mandelstam variables. The gluon polarization $\Delta g/g$ is probed at the scale of the hard process, $\hat{Q}^2$, and the fraction of the nucleon momentum carried by the struck gluon, $x_g = x(1 + \hat{s}/Q^2)$. The detailed formulae to calculate the hard process asymmetries and the asymmetry weights in LEPTO and PYTHIA can be found in appendix B.
If one restricts the p_T of the hadrons to a number of bins, the asymmetry for each of these bins can be written as

$$\frac{1}{N_{tot}} \sum_{j=1}^{N_{sig}(p_T)} a_j^{sig} = f_{sig}(p_T) \langle \hat{a}_{sig} \rangle (p_T) \left\langle \frac{\Delta g}{g} \right\rangle (p_T) , \tag{5.10}$$

where both the hard process asymmetry and the value of the gluon polarization are averaged over the bin. The expression $\langle \Delta g/g \rangle$ is in the following replaced by $\Delta G/G$ which in this thesis is used as denoting an average gluon polarization. Using this equation together with Eq. (5.5) one can calculate the average gluon polarization in a certain p_T bin as

$$\frac{\Delta G}{G}(p_T) = \frac{1}{f_{sig}(p_T)\langle \hat{a}^{sig}\rangle(p_T)}\left[A_{\parallel}^{meas}(p_T) - f_{bg}(p_T)A_{\parallel}^{bg}(p_T)\right] \ . \tag{5.11}$$

Instead of the signal and background process fractions f_{sig} and f_{bg}, the number of signal and background events N_{sig} and N_{bg} can be used, according to $f_{sig} = N_{sig}/(N_{sig} + N_{bg})$ and $f_{bg} = N_{bg}/(N_{sig} + N_{bg})$ with $N_{tot} = N_{sig} + N_{bg}$.

The statistical uncertainty of the gluon polarization depends on the statistical uncertainty of the measured asymmetry $A_{\parallel}^{meas}$ and the MC statistical uncertainties of the background asymmetry $A_{\parallel}^{bg}$, the number of signal and background events N_{sig} and N_{bg}, and the hard subprocess asymmetry of the signal $\langle \hat{a}^{sig}\rangle$. It is given by

$$\begin{aligned}\delta^2\left(\frac{\Delta G}{G}\right)^{stat.} \quad = \quad & \frac{1}{N_{sig}^2\langle \hat{a}^{sig}\rangle^2}\Big[N_{tot}^2\delta^2 A_{\parallel}^{meas} + N_{bg}^2\delta^2 A_{\parallel}^{bg} \\ & + \frac{(N_{tot}A_{\parallel}^{meas} - N_{bg}A_{\parallel}^{bg})^2}{\langle \hat{a}_{sig}\rangle^2}\delta^2\langle \hat{a}_{sig}\rangle \\ & + \frac{N_{bg}^2}{N_{sig}}(A_{\parallel}^{meas} - A_{\parallel}^{bg})^2 + N_{bg}(A_{\parallel}^{meas})^2\Big] \ .\end{aligned} \tag{5.12}$$

This formula represents the statistical uncertainty of the gluon polarization in a certain p_T bin (the explicit indication of the p_T bin is suppressed here). Details of this statistical uncertainty calculation are described in appendix C.
If the Monte Carlo is generated with large enough statistics the statistical uncertainty on the variables extracted from the MC, namely $\delta^2 A_{\parallel}^{bg}$ and $\delta^2\langle \hat{a}^{sig}\rangle$, become negligible. The statistical uncertainty of the gluon polarization is then dominated by the statistical uncertainty of the measured asymmetry $\delta^2 A_{\parallel}^{meas}$.

The experimental systematic uncertainty of the measured asymmetry, $(\delta A_{\parallel}^{meas})^{syst.}$, propagates into an experimental systematic uncertainty of $\Delta G/G$ according to Eq. (5.11) as

$$\delta\left(\frac{\Delta G}{G}\right)^{exp.syst.} = \frac{1}{f_{sig}\langle \hat{a}_{sig}\rangle}\left(\delta A_{\parallel}^{meas}\right)^{syst.} \ . \tag{5.13}$$

5.3 Selection of appropriate analysis channels

The extraction of the gluon polarization from measured double spin asymmetries as outlined in the formalism above requires an analysis channel with a significant contribution to the asymmetry from the signal processes. Hence the aim is to find appropriate selection criteria to single out a kinematic region accessible by HERMES in which these processes are enhanced while the background processes are suppressed. In this procedure a maximal signal to noise ratio together with a maximal significance is aimed for. This means that the data selection needs to be strict enough to obtain large signal process fractions but not too strict in order to not decrease the statistics in the data too much.

There are different possible channels which can be used to determine the gluon polarization by isolating the processes involving a gluon from the nucleon. Depending on the specific layout of the experiment, this can be prompt photon production, heavy flavour meson production, or the production of hadrons or jets with large transverse momenta (cf. section 2.6.2). In the following two chapters of this thesis two such analysis channels accessible for HERMES are investigated. Chapter 6 focusses on the electroproduction of single high-p_T hadrons. In this channel a high-p_T hadron is required to be detected in coincidence with the scattered lepton. In chapter 7 the (quasi-real) photoproduction of high-p_T hadron pairs is exploited. In this case events with two high-p_T hadrons detected in coincidence are analyzed while the scattered lepton is not necessarily detected. In both chapters the following steps in the analysis are performed. First, extensive MC studies are conducted to optimize the data selection criteria in such a way that the signal process fractions are maximally enhanced while a minimal amount of events is lost. Next, data asymmetries are determined using the best set of selection criteria as found from the MC studies. These data asymmetries are then interpreted as a superposition of the contributions from the various processes. Using MC information on the process fractions and asymmetries, the gluon polarization is extracted.

Chapter 6

Electroproduction of single high-p_T hadrons

The analysis presented in this chapter utilizes the electroproduction of single high-p_T hadrons to conduct an extraction of the gluon polarization. In this channel, single high-p_T hadrons are detected in coincidence with the scattered lepton[1]. Compared to the analysis of high-p_T hadron pairs in photoproduction as described in chapter 7, the single hadron electroproduction channel does not only provide higher statistics in the HERMES acceptance, but also allows the reconstruction of the full event kinematics via the detection of the scattered lepton. However, it needs to be carefully investigated if a phase space region accessible to HERMES exists in which the contribution of the photon-gluon-fusion signal is large enough for the extraction of the gluon polarization with a reasonable statistical uncertainty. Since in single high-p_T hadron electroproduction the scattered lepton is detected (which implies $Q^2 \gg 0$ GeV^2), not only PYTHIA but also LEPTO Monte Carlo simulations can be applied in the search for a suitable phase space region as well as for the extraction of the gluon polarization.
In searching for a suitable phase space region, a wide range of studies has been carried out with the LEPTO MC generator (section 6.1). For the best set of selection requirements deduced from these studies, data asymmetries are determined (section 6.2). These asymmetries are interpreted with the LEPTO MC to extract the gluon polarization (section 6.3). This extraction is repeated using the PYTHIA MC (section 6.4) which involves the simulation of a more complete set of processes, including an estimate of the model dependent systematic uncertainties. Finally, the results for the gluon polarization are summarized (section 6.5).

[1]The term 'single hadron' is used to express that in events with several hadrons, each hadron is counted separately.

6.1 LEPTO Monte Carlo studies

This section contains a collection of studies[2] carried out with the LEPTO MC generator in order to define an optimal set of cuts for the extraction of the gluon polarization in single high-p_T hadron electroproduction. A general description of the generator can be found in section 5.1.3. In the course of these studies a few special aspects of LEPTO are considered. First, the dependence of the process fractions on one general MC parameter is investigated (section 6.1.1). A data-MC comparison for semi-inclusive DIS shows very good agreement and supports the applicability of LEPTO (section 6.1.2). Acceptance studies demonstrate that no significant effects occur when going from 4π to the HERMES acceptance (section 6.1.3). To define the requirements which maximize the PGF fraction, a variety of additional MC studies are carried out (section 6.1.4).

6.1.1 Studies on cutoff parameter

In this section, the dependence of the process fractions on the LEPTO cutoff parameter PARL(9) (cf. section 5.1.3) is investigated. Semi-inclusive deep-inelastic scattering events with the standard kinematic cuts (cf. e.g. [113]) are used for this study . The scattered lepton is required to fulfill $Q^2 \geq 1$ GeV^2, $W^2 \geq 10$ GeV^2 and $0.1 \leq y \leq 0.85$, charged hadrons are considered if they meet the cuts $x_F > 0.1$ and $0.2 < z < 0.8$, all detected in the standard HERMES acceptance. The MC simulation is generated for a proton target.

Fig. 6.1 shows the fractions for the DIS, QCDC, and PGF processes versus the LEPTO cutoff parameter PARL(9). For comparison, the process fractions taken from the PYTHIA MC[3], which uses a different cutoff scheme, are also indicated. The process fraction of DIS events decreases from around 98% at PARL(9) = 2 to about 80% at PARL(9) = 0.6 and then saturates. The first order QCD processes consequently show the opposite behaviour. The process fraction of QCDC events increases from around 1% at PARL(9) = 2 to around 18% at PARL(9) = 0.6 and saturates. The process fraction of PGF events is below 1% at PARL(9) = 2 and increases to around 2% at PARL(9) = 1 before it saturates. The process fractions as obtained from the PYTHIA MC show values comparable to those from a LEPTO MC for PARL(9) = 1. From this comparison it becomes clear that the LEPTO results obtained with a lower cutoff value agree better with the results from PYTHIA. For all further studies, a cutoff parameter of PARL(9) = 1 has been chosen.

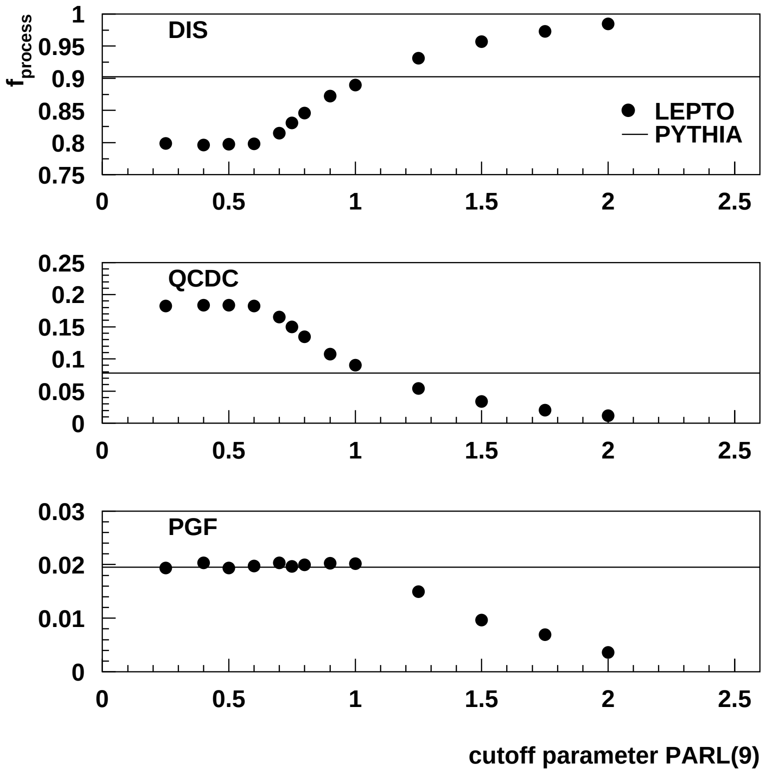

Figure 6.1: *Process fractions vs. LEPTO cutoff parameter PARL(9) for the DIS, QCDC and PGF processes obtained from LEPTO MC with a proton target, for semi-inclusive deep-inelastic scattering events with charged hadrons. For comparison, the horizontal line indicates the process fractions from PYTHIA MC.*

6.1.2 Comparison of data and MC asymmetries

In the following, a comparison of data and LEPTO MC asymmetries for semi-inclusive deep-inelastic scattering events is presented. The events are selected according to the standard cuts for this class of events in the HERMES acceptance (cf. previous section). The LEPTO MC has been generated with QED radiative corrections and detector smearing and the sets GRSV2000 for the polarized PDFs and GRV98 for the unpolarized PDFs.

Fig. 6.2 shows the process fractions of DIS, QCDC, and PGF events vs. x obtained with LEPTO on a proton target for semi-inclusive deep-inelastic events with charged hadrons. Process fractions for a deuteron target, for positive and negative charges, and for specific types of hadrons, look very similar, and are therefore not displayed here. The x bins are chosen according to the binning often used by the HERMES collaboration (cf. e.g. [114]). For smaller x the process fractions of QCDC and PGF increase. However,

[2] These studies have been carried out with a MC tune older than 2004c. Switching to 2004c does slightly alter some values of the process fractions etc., but leaves unaffected all qualitative conclusions drawn in this section.

[3] For this comparison with LEPTO only the processes DIS, QCDC and PGF are taken into account while the other processes available in PYTHIA are ignored.

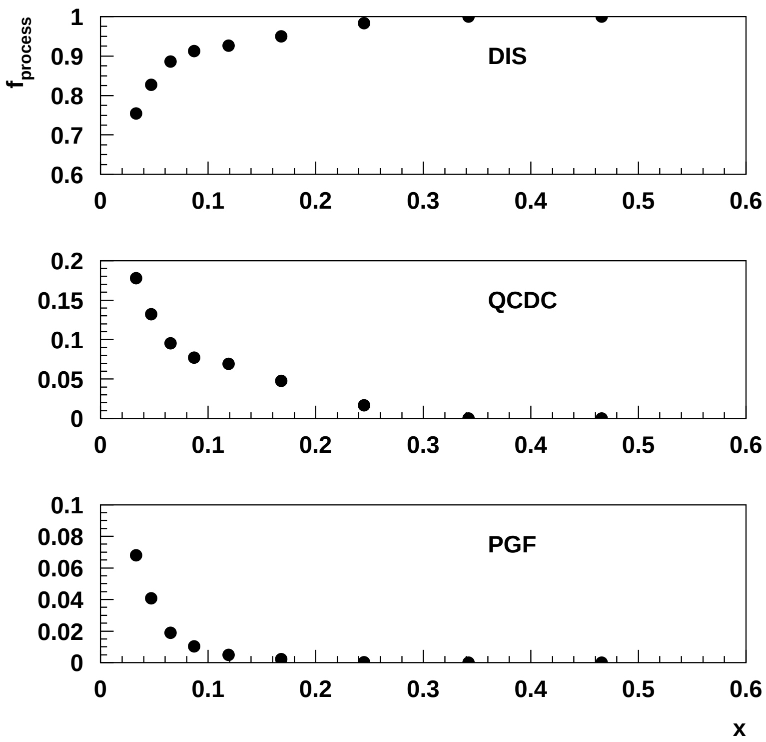

Figure 6.2: *Process fractions vs. x for the DIS, QCDC and PGF process obtained from LEPTO MC with a proton target, for semi-inclusive deep-inelastic scattering events with charged hadrons.*

the PGF process fraction never exceeds a few percent. The uncertainty in the total MC asymmetry from the poorly constrained gluon polarization, which enters into the asymmetry via the PGF events, is therefore very small. This fact makes the semi-inclusive data useful to verify the applicability of LEPTO.

The asymmetry $A_{||}$ for semi-inclusive events with positive and negative hadrons, pions, and kaons is shown in the nine standard x-bins in Fig. 6.3. The data asymmetries for the proton target (1996 and 1997 data combined) and for the deuteron target (2000 data) are taken from [92] and plotted at their average x per bin. Besides the data asymmetries, the LEPTO results are displayed, plotted at the centres of the x-bins. For both targets, very good agreement between data and MC asymmetries is observed for each hadron type. The LEPTO MC therefore proves to be very suitable for describing the data in the semi-inclusive deep-inelastic scattering region, which lends credibility to its applicability in the single high-p_T hadron electroproduction region at lower Q^2.

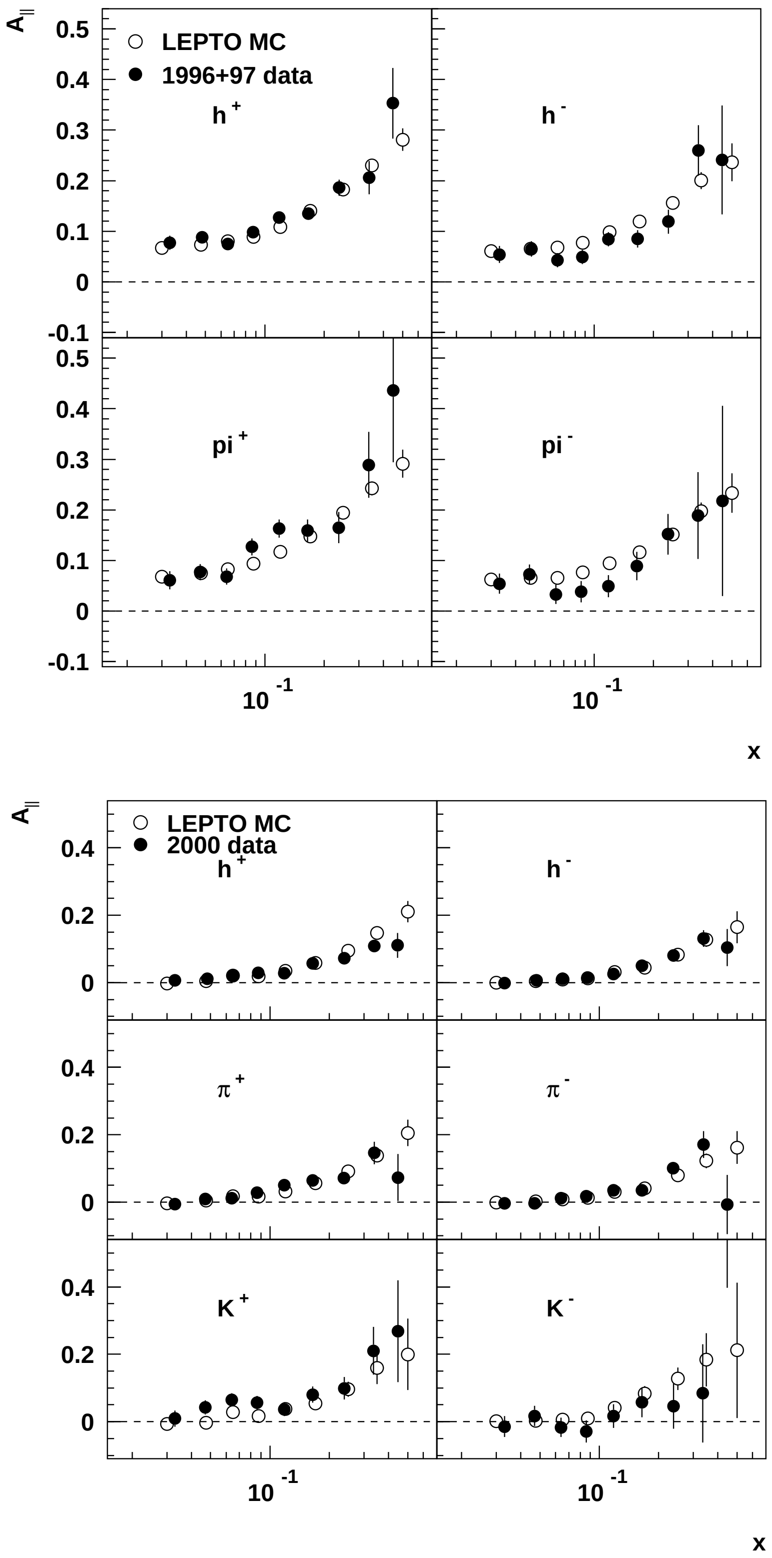

Figure 6.3: *Asymmetries $A_{\|}$ vs. x for a proton (upper panel) and a deuteron (lower panel) target for semi-inclusive deep-inelastic scattering events with positive and negative hadrons, pions and kaons. The solid symbols are the results for the LEPTO MC, the open symbols are 97c1 and 00c1 data, respectively. The systematic uncertainty on the measured asymmetry, not shown here, is of the order of a few per cent (cf. e.g. [92]).*

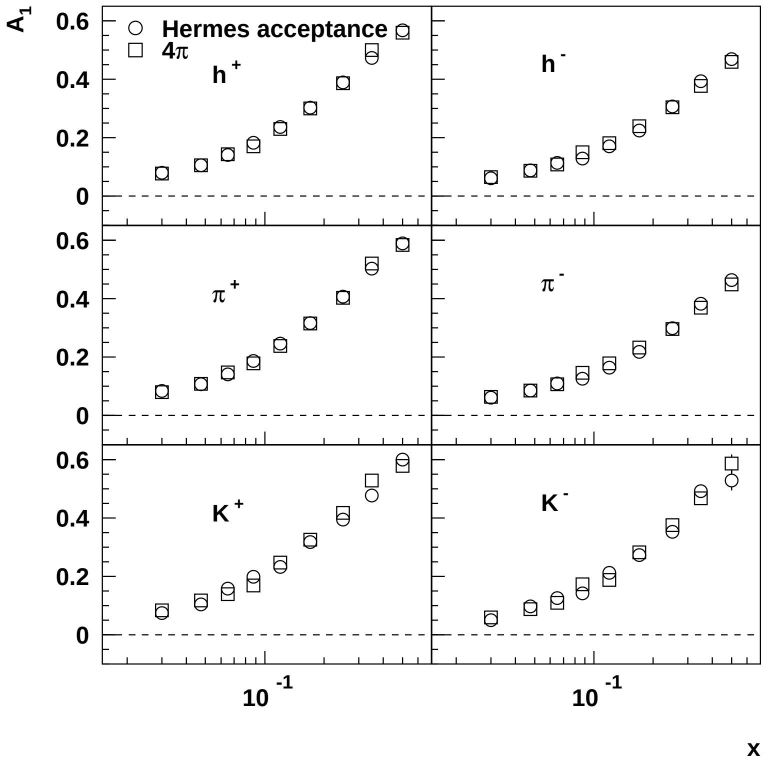

Figure 6.4: *Asymmetries A_1 vs. x as obtained from the LEPTO MC on a proton target in 4π (squares) and in the HERMES acceptance (circles), respectively, for semi-inclusive deep-inelastic scattering events with positive and negative hadrons (top), pions (middle) and kaons (bottom).*

6.1.3 Acceptance studies

Having proven the applicability of the LEPTO MC in the HERMES acceptance it remains to be studied whether the deviation of the HERMES acceptance from a full 4π coverage does not induce any detector specific acceptance effects. In order to do so, in this section a comparison is made between asymmetries calculated from the LEPTO MC generated in 4π and in the HERMES acceptance, respectively. The MC is in both cases generated without QED radiative corrections and without detector smearing. Fig. 6.4 presents the asymmetry A_1 vs. x for the semi-inclusive deep-inelastic scattering events (with the standard cuts as listed in the previous sections) in 4π- and in the HERMES acceptance on a proton target. The very good agreement between the asymmetries in 4π and in the HERMES acceptance for all hadron types and charges over the whole x-range supports the conclusion that the analysis is not influenced by acceptance effects.

6.1.4 Optimization of the selection criteria

Starting from the standard requirements for semi-inclusive deep-inelastic scattering events as described in the previous sections, the kinematic constraints on the lepton and the

Requirement	PGF process fraction
no cut	1.8%
$x < 0.1$	2.3%
$W^2 > 26$ GeV^2	3.0%
x- and W^2-cut combined	3.2%

Table 6.1: *PGF process fractions for various cuts on the lepton kinematics, for charged hadrons in electroproduction obtained from LEPTO MC with a proton target.*

hadron can now be relaxed to include also the lower Q^2 region (namely $Q^2 < 1$ GeV^2). The only remaining requirement on the scattered lepton and any single hadron is that they are detected in the HERMES acceptance. Using LEPTO MC, one can now search for a kinematic region where the PGF process fraction is maximized in order to extract the gluon polarization with the highest significance possible in this channel. All MC studies presented in this section are carried out for a proton target.

Lepton kinematics

A variety of studies on the lepton kinematic variables has been performed. Tab. 6.1 summarizes the most promising cuts and the corresponding value of the PGF process fraction. If one does not require any further cuts on the lepton except for being detected in the HERMES acceptance the PGF process fraction amounts to 1.8%. Requiring x to be smaller than 0.1, this process fraction increases to 2.3%. Requiring W^2 to be larger than 26 GeV^2, the fraction reaches 3%. Both cuts in combination yield a PGF fraction of 3.2%. This is the maximum process fraction obtainable with cuts on the lepton kinematics only.

Hadron kinematics

A second series of studies has been done on the hadron kinematic variables. The process fractions have been investigated as functions of cuts on the hadron momentum p, hadron energy fraction z, and hadron transverse momentum p_T, which is defined with respect to the virtual photon direction in the virtual photon-nucleon centre of mass system. The cut on transverse momentum has proven to be the most powerful. Fig. 6.5 shows the fractions of the DIS, QCDC, and PGF processes as functions of p_T^{min}, the lower limit imposed on the hadron p_T, for a sample of events with the scattered lepton and any single charged hadron detected in the HERMES acceptance. In this case, the PGF fraction reaches a maximum of approximately 9% at (relatively) high values of p_T^{min} ($p_T^{\text{min}} > 1.3$ GeV). If one combines this cut on the hadron p_T with those on the lepton kinematics of $x < 0.1$ and $W^2 > 26$ GeV^2, the PGF fraction still amounts to no more than 10%. There is basically no difference in the process fractions obtained for either lepton plus charged hadron, lepton plus positive hadron, or lepton plus negative hadron. Fractions for kaons

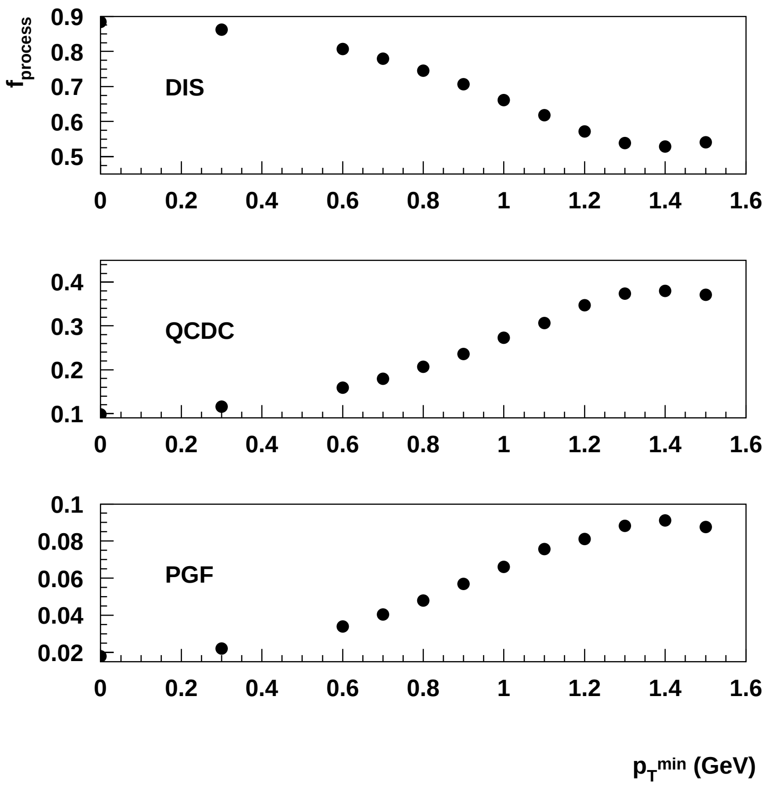

Figure 6.5: *Process fractions vs. p_T^{min}, the lower limit imposed on the hadron p_T, for the DIS, QCDC and PGF process, for charged hadrons in electroproduction obtained from LEPTO MC on a proton target,*

are slightly higher in absolute value than for other identified hadrons, but qualitatively they show an almost identical functional behaviour.

Multiplicities

As a third type of possible cut to enhance the PGF fraction, the hadron multiplicities have been studied. In Fig. 6.6 multiplicities of charged hadrons in electroproduction in 4π and in the HERMES acceptance are plotted, separately for the three processes DIS, QCDC, and PGF. Both in 4π and in the HERMES acceptance, the multiplicities for the first order QCD processes are on average slightly higher than for the DIS process. In 4π, the DIS process results on average in about three charged hadrons, while for QCDC and PGF on average about five charged hadrons are produced. In 2/3 of all DIS events none of the charged hadrons produced in 4π makes it into the HERMES acceptance. In about every fourth event one charged hadron enters the HERMES acceptance, and events with two charged hadrons in the HERMES acceptance amount to less than 10% of the sample. For QCDC and PGF, multiplicities in the HERMES acceptance are higher than for DIS. For these two processes, no charged hadron at all is detected in the HERMES acceptance for about 40% of all events, one charged hadron for about 40% and two

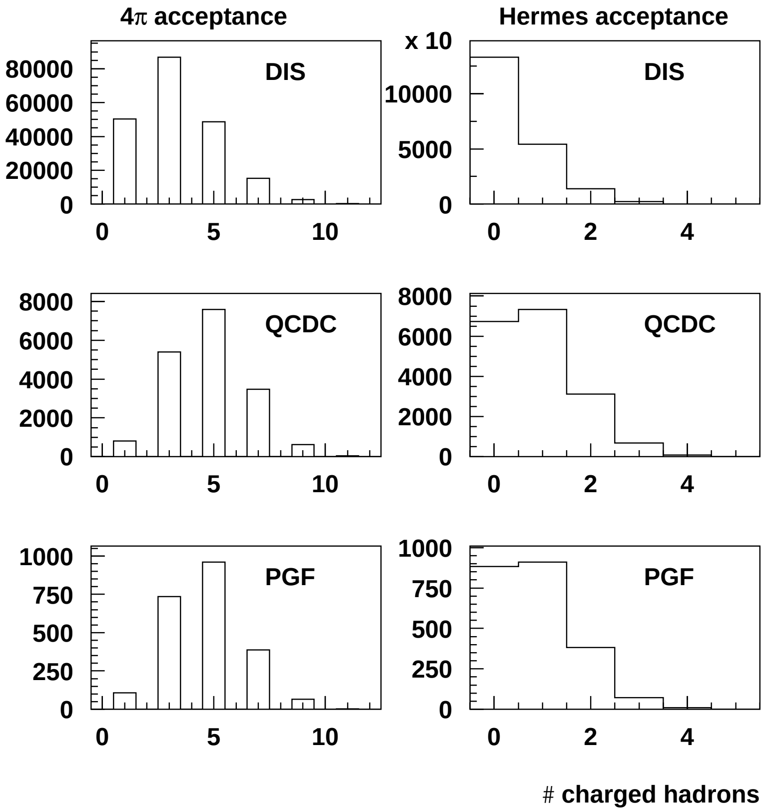

Figure 6.6: *Multiplicity distributions in 4π (left) and in the HERMES acceptance (right) for charged hadrons in electroproduction obtained from LEPTO MC with a proton target.*

charged hadrons for about 15% of the events.
From this study it becomes clear that in a PGF event the original $q\overline{q}$ pair does not necessarily fragment into only two oppositely charged hadrons as one might naively expect, but in most of the cases it does indeed fragment into a larger number of hadrons. Out of these, only one or two charged hadrons make it into the HERMES acceptance. A further MC study has shown that only about 50% of the charged hadrons in the HERMES acceptance contain one of the original quarks from the $q\overline{q}$ pair created in the hard PGF process. If one requires a transverse hadron momentum $p_T > 1$ GeV, this fractions increase to about 60%.
The effect of imposing a multiplicity cut on the process fractions has been studied by selecting events with two charged hadrons instead of one in the HERMES acceptance. The process fractions were then investigated as a function of a cut on the higher p_T of the two. PGF fractions of up to 9% could be realised, which constitutes no improvement compared to the sample with one charged hadron in the acceptance, but results in a big loss in statistics. Therefore, the idea of a possible cut on the hadron multiplicities to increase the PGF fraction was abandoned.

6.2 Data asymmetries

From the studies described in the previous section it has been concluded that a cut on the transverse hadron momentum is the most powerful to enhance the PGF fraction in the single hadron electroproduction sample, while cuts on lepton kinematics and hadron multiplicities have negligible effects. Therefore, the data are analyzed in the kinematic region defined by the detection of a scattered lepton and at least one produced charged hadron in the acceptance ($lp \to l'hX$ or $ld \to l'hX$), without imposing any additional constraint on the lepton kinematics or the hadron multiplicities. As the hadron p_T has turned out to be crucial to enhance the PGF fraction, results are presented vs. this variable.

6.2.1 Data selection

Requiring the scattered lepton in the HERMES acceptance imposes in practice $Q^2 > 0.1$ GeV^2. In order to be able to use LEPTO for the interpretation of the data asymmetries, an additional cut of $Q^2 > 0.5$ GeV^2 has been used in a second analysis; this constraint is set by the fact that the LEPTO MC generator cannot simulate events for $Q^2 < 0.5$ GeV^2. Each charged hadron observed in the acceptance in addition to the detected lepton is considered separately. The sample of hadrons is subdivided into positive and negative charges. Separate analyses are carried out for all hadrons, identified pions and kaons.
Furthermore, the standard data quality cuts for polarized scattering (cf. section 4.2), the standard track requirements (cf. section 4.3) and the standard PID cuts (cf. section 4.4) are all applied in this analysis. The productions used for this analysis are 96d0, 97d0 for the proton target and 00d0 for the deuteron target. All physics triggers are considered.

6.2.2 Measured asymmetries

The asymmetries in single high-p_T hadron electroproduction are determined in bins of the hadron transverse momentum and separately evaluated for different hadron types and charges. The hadron transverse momentum is defined with respect to the virtual photon direction in the virtual photon-nucleon centre of mass system. It is divided into nine non-equidistant bins between 0 and 2 GeV according to Tab. 6.2. The asymmetries are assigned to the centre of the bins.
Fig. 6.7 and Fig. 6.8 show the double spin asymmetries $A_{||}$ vs. p_T for the data obtained with a proton target in 1996/1997 and with a deuteron target in 2000, respectively. The asymmetries derived from the 1996 and 1997 data are merged into one asymmetry 1996/97 by taking the error-weighted average (cf. section 4.7.4). For the hydrogen data the asymmetries have been determined for positive and negative hadrons (irrespective of type) as well as for positive and negative pions as identified by the threshold Cerenkov detector in the momentum range $4 < p < 13.8$ GeV. For the deuteron data, the available

bin	p_T-range (GeV)
1	0.00-0.15
2	0.15-0.30
3	0.30-0.45
4	0.45-0.60
5	0.60-0.75
6	0.75-1.0
7	1.0-1.3
8	1.3-1.6
9	1.6-2.0

Table 6.2: *The bins in p_T used in this analysis.*

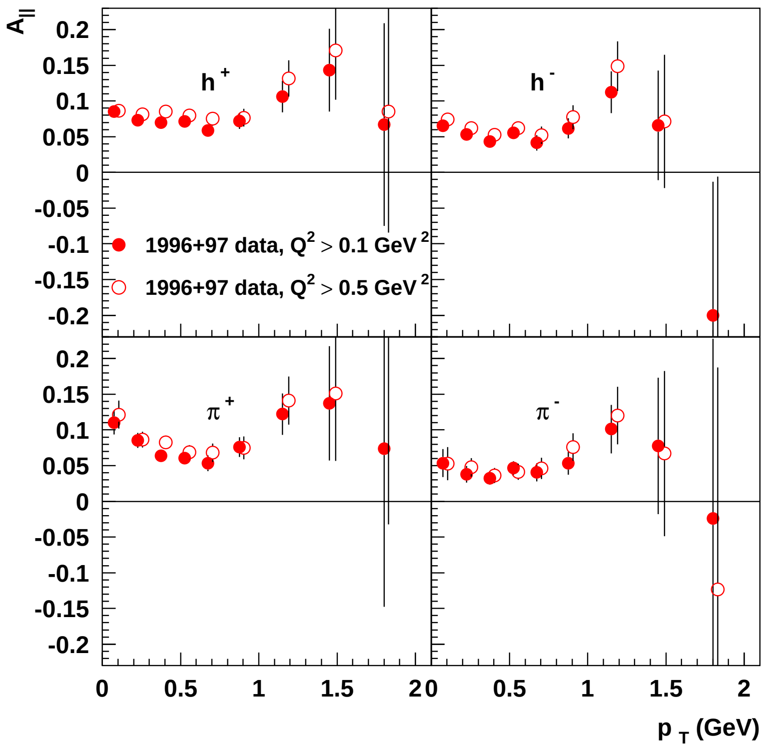

Figure 6.7: *Asymmetries $A_{||}$ vs. p_T obtained from the 1996+97 proton target data for positive and negative hadrons (top) and pions (bottom) in electroproduction with $Q^2 > 0.1$ GeV^2 (closed symbols) and $Q^2 > 0.5$ GeV^2 (open symbols), respectively. The asymmetries for $Q^2 > 0.5$ GeV^2 are shifted in p_T for presentation purposes. The systematic uncertainty on the asymmetry, evaluated according to section 4.7.3, is at most 0.008, which is too small to be indicated graphically in the plot.*

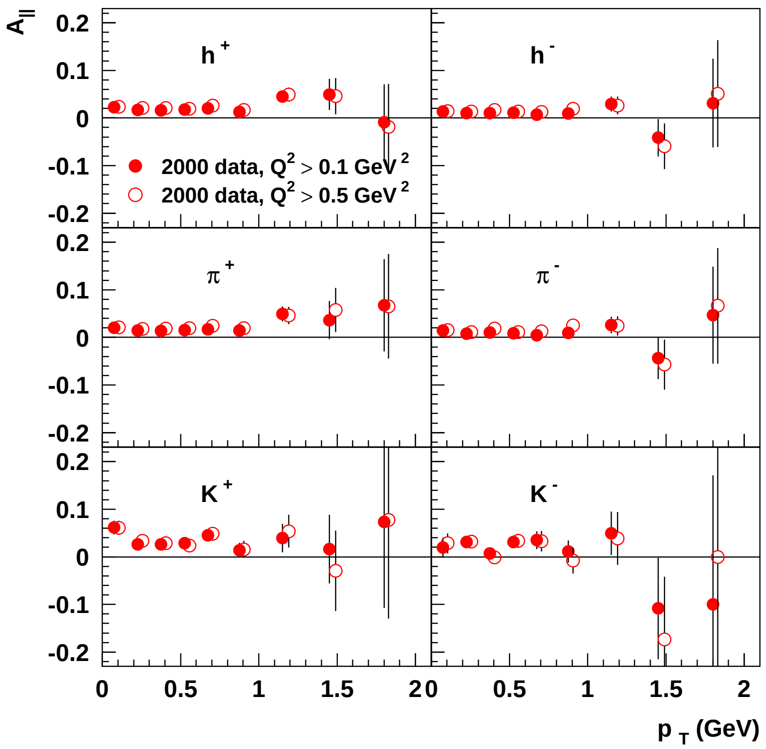

Figure 6.8: *Asymmetries $A_{||}$ vs. p_T obtained from the 2000 deuteron target data for positive and negative hadrons (top), pions (middle) and kaons (bottom) in electroproduction with $Q^2 > 0.1$ GeV ^{2} (closed symbols) and $Q^2 > 0.5$ GeV ^{2} (open symbols), respectively. The asymmetries for $Q^2 > 0.5$ GeV ^{2} are shifted in p_T for presentation purposes. The systematic uncertainty on the asymmetry, evaluated according to section 4.7.3, is well below 0.005 in all bins, which is too small to be indicated graphically in the plot.*

extra information from the RICH allows to also determine asymmetries for positive and negative kaons. In the case of the RICH, the momentum range for the identification of pions and kaons is increased as compared to the threshold Cerenkov detector, namely $1 < p < 15$ GeV and $2 < p < 15$ GeV, respectively.

6.2.3 p_T-range for the extraction of the gluon polarization

As the next step the p_T-range for the extraction of the gluon polarization needs to be defined. In section 5.2 it has been shown that the statistical uncertainty on the extracted gluon polarization is mainly determined by three variables, namely the signal fraction, the average hard process asymmetry of the signal, and the statistical uncertainty on the data asymmetries. It thus can be approximated by the first term of Eq. (5.12). The (approximated) uncertainty is proportional to the statistical uncertainty on the data asymmetries, and inversely proportional to the signal fraction and the average hard process asymmetry of the signal. As discussed in section 6.1.4 the signal process fraction is very small at small $p_T^{\rm min}$ (the lower limit imposed on the hadron p_T), and increases with $p_T^{\rm min}$, favoring's

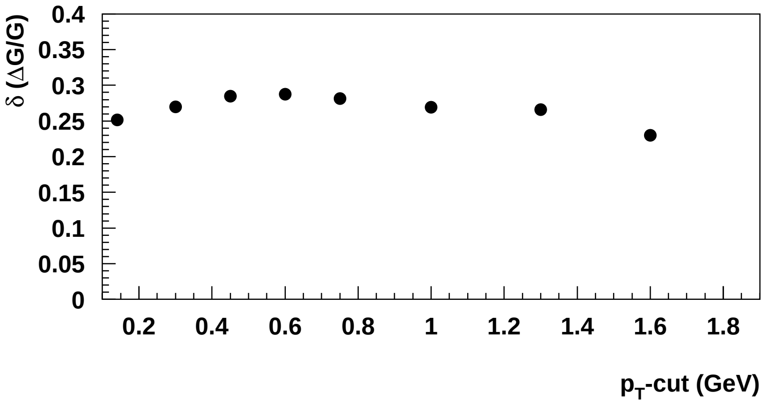

Figure 6.9: *The (approximated) statistical uncertainty of $\Delta G/G$ as a function of the $p_T^{\rm min}$ for positive hadrons as obtained from the LEPTO MC for a deuteron target.*

a large $p_T^{\rm min}$ for the extraction of the gluon polarization. At the same time, the statistics of the data decrease with p_T, consequently setting an upper limit on the possible $p_T^{\rm min}$. In Fig. 6.9 the (approximated) statistical uncertainty on the gluon polarization is given as a function of $p_T^{\rm min}$, for positive hadrons and a deuteron target, as computed using LEPTO. For a proton target (not shown here) this uncertainty is larger (because of lower statistics) but otherwise has the same functional form. No minimum for the statistical uncertainty on the gluon polarization can be found, thus no optimal $p_T^{\rm min}$ can be defined using this criterion. To decide which $p_T^{\rm min}$ to choose for an optimal extraction of the gluon polarization, some further arguments need to be introduced. In section 6.4 some additional studies with PYTHIA will show that the measured asymmetries are not sensitive to extreme variations of $\Delta G/G$ for $p_T < 0.75$ GeV due to the smallness of the signal fraction. Moreover, the average $\hat{p_T}$ of the hard PGF process as obtained from PYTHIA is only correlated with the measured p_T of the hadrons for $p_T > 1$ GeV [53]. Furthermore, for PYTHIA the statistical uncertainty of $\Delta G/G$ increases for $p_T^{\rm min}$ above 1 GeV. Combining all these arguments, the region of $p_T > 1$ GeV is chosen to extract the gluon polarization with both LEPTO and PYTHIA.

6.3 Interpretation with LEPTO MC

In this section the measured data asymmetries are interpreted using the LEPTO MC information on the process fractions (section 6.3.1), and the hard signal asymmetry and the background asymmetries (section 6.3.2), in order to extract the gluon polarization (section 6.3.3). (The detailed LEPTO MC specifications and the formula for the calculation of the hard signal asymmetry used in this analysis are given in appendix A.1 and B.2.)

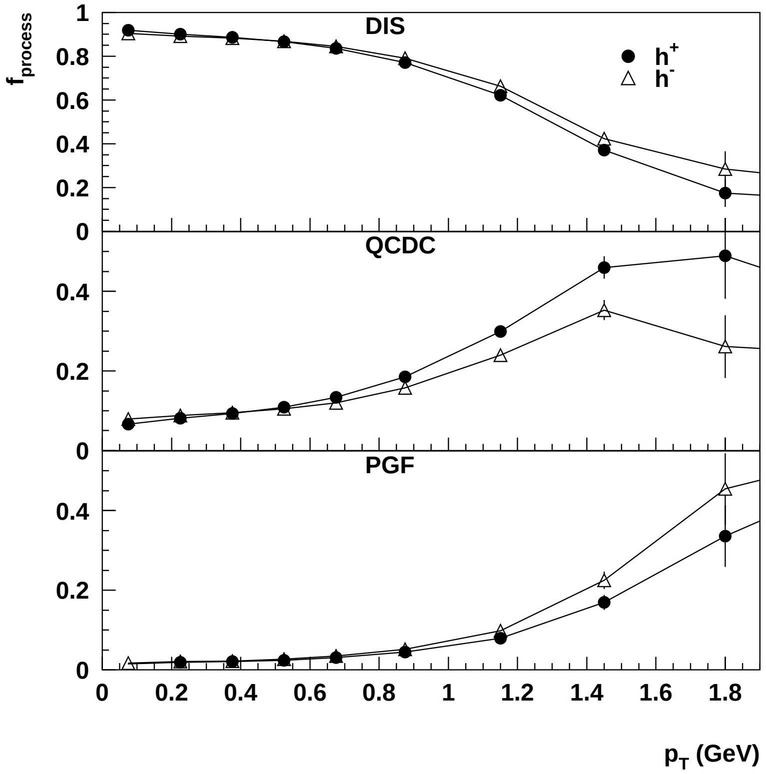

Figure 6.10: *Process fractions vs. p_T for the DIS, QCDC and PGF process for positive and negative hadrons in electroproduction obtained from LEPTO MC on a proton target. The open (closed) symbols represent the process fractions for positive (negative) hadrons. The lines in the plot do not constitute a fit but merely connect the points (applies to all plots in this and the next chapter).*

	PGF fractions	
particle	proton target	deuteron target
$h+$	8.9%	9.9%
$h-$	11.0%	12.4%
$\pi+$	8.5%	9.7%
$\pi-$	11.0 %	12.6%
$K+$	10.1%	11.1%
$K-$	12.9%	13.3%

Table 6.3: *PGF process fractions for different hadron types and targets from LEPTO MC, for single high-p_T hadron electroproduction with $p_T > 1$ GeV.*

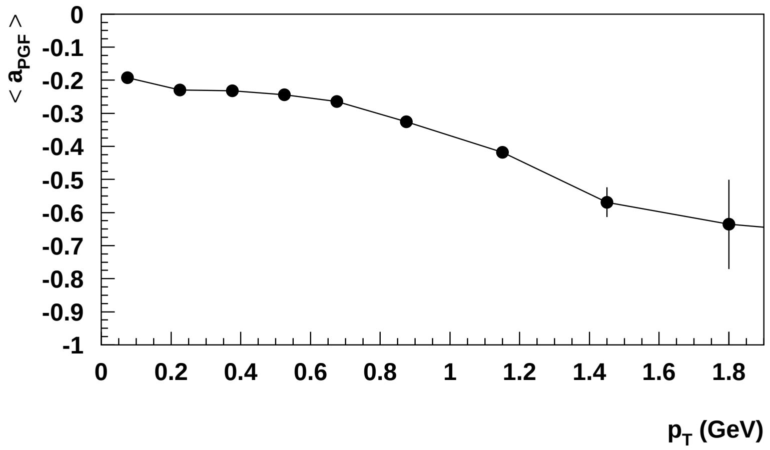

Figure 6.11: *Average hard PGF process asymmetry vs. p_T for positive hadrons in electroproduction obtained from LEPTO MC on a proton target.*

6.3.1 Process fractions

The process fractions f_i of DIS, QCDC, and PGF events as functions of p_T for positive and negative hadrons in electroproduction are shown in Fig. 6.10, as modelled with LEPTO for a proton target. The events are split into the same nine p_T bins [4] as have been used to display the data asymmetries in Fig. 6.7 and Fig. 6.8. The PGF fractions are very small for $p_T < 1$ GeV, and then rise with p_T to a maximum of about 30-40% in the highest p_T-bin. The QCDC fractions show a similar behaviour, being quite small for $p_T < 1$ GeV and then also rising with p_T to a maximum of 35-45%, while the DIS fractions decrease with p_T from 90% to about 20%. The process fractions for certain identified hadron types (pions and kaons) look very similar to these results, and are not displayed here. The same holds for the process fractions on a deuteron target. Tab. 6.3 summarizes the process fractions of PGF events for a proton and a deuteron target for positive and negative hadrons, pions and kaons with $p_T > 1$ GeV. One notices that the PGF fractions are slightly higher for negative than for positive particles, and are also slightly higher for kaons than for pions. Furthermore, they are slightly higher on a deuteron than on a proton target. The highly non-trivial fragmentation processes underlying these results prevents an exhaustive explanation of these small differences in terms of intuitive arguments alone.

6.3.2 Hard signal asymmetry and background asymmetries

In Fig. 6.11 the average hard PGF process asymmetry vs. p_T is shown for positive hadrons, as generated with LEPTO on a proton target. The asymmetries are basically identical for all hadron types and charges, and for both targets, therefore only one example representative for all is shown. A dependence of the asymmetry on p_T is observed; it is negative for all p_T, with smallest absolute values of about 0.2 in the lowest p_T bin, increasing to a

[4]Not to be confused with $p_T^{\min}$ as used in Fig. 6.5

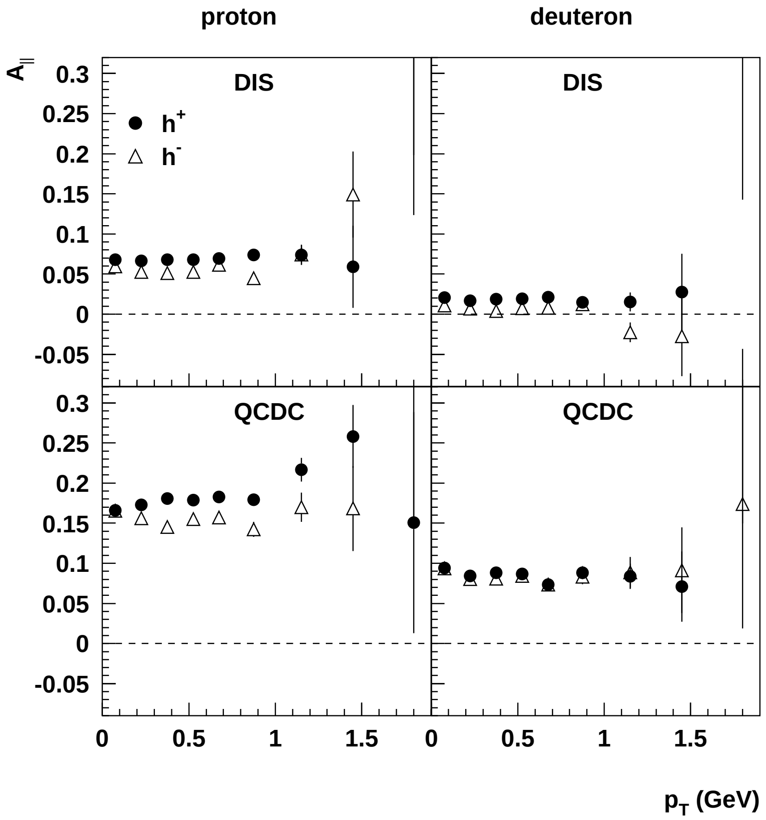

Figure 6.12: *Asymmetries $A_{||}$ vs. p_T of the two background processes DIS (top) and QCDC (bottom), for positive (closed symbols) and negative (open symbols) hadrons in electroproduction, obtained from LEPTO MC on a proton (left) and a deuteron (right) target, respectively.*

maximum of about 0.6 in the highest p_T bin. As discussed in section 5.2 the uncertainty on the extracted gluon polarization behaves inversely proportional to this hard PGF process asymmetry. Therefore, the sensitivity to the gluon polarization due to this factor, or in other words the so-called analyzing power, increases with p_T.

Fig. 6.12 displays the background (DIS and QCDC) asymmetries vs. p_T for positive and negative hadrons on a proton and a deuteron target as obtained from the LEPTO MC. The background asymmetries for pions and kaons, which are not plotted, are very similar to those shown here for hadrons. One notices that the asymmetries are positive and smaller for the deuteron than for the proton. This is qualitatively explained in the following way. The asymmetries are constructed from the hard process asymmetry and the polarized parton distributions of the struck parton in the nucleon. Whereas the hard process asymmetry is independent of the target, the polarized parton distributions depend on the target. This can be seen from the charge-weighted sums of the known polarized valence quark distributions in the proton ($8/9\ \Delta u_p + 1/9\ \Delta d_p$ with Δu_p positive and Δd_p negative), and of the isospin rotated ones for the neutron ($4/9\ \Delta u_n + 2/9\ \Delta d_n$ with $\Delta u_n = \Delta d_p$ and $\Delta d_n = \Delta u_p$). For the deuteron (proton plus neutron) a different mixture of polarized up and down quark distributions is found ($11/9\ \Delta u_p + 5/9\ \Delta d_p$). As the

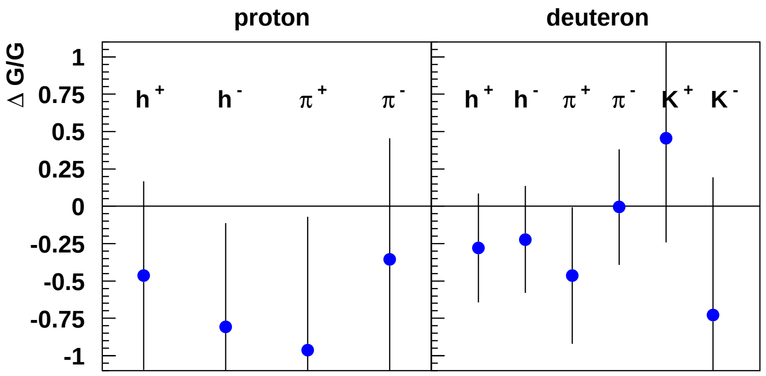

Figure 6.13: *$\Delta G/G$ extracted from the measured asymmetries and LEPTO MC for different hadron types and charges on proton (left) and deuteron (right) target respectively, for single high-p_T hadron electroproduction at $p_T > 1$ GeV.*

negative contribution of the down quarks is larger in the deuteron case, the overall size of the asymmetry decreases.

6.3.3 The gluon polarization

Taking the measured asymmetries from the data and the process fractions, the hard signal asymmetry and the background asymmetries from the LEPTO MC, the gluon polarization is now extracted for $p_T > 1$ GeV, separately for the proton and the deuteron target, for positive and negative hadrons, pions and - in the case of the deuteron target - also kaons. Fig. 6.13 displays the resulting values for $\Delta G/G$ and the corresponding statistical uncertainties. The gluon polarization is probed at an average gluon momentum fraction $\langle x_g \rangle \approx 0.23$, as calculated from the MC information. The error bars are very large for the proton target, and somewhat smaller but still large for the deuteron target. This is a direct consequence of the statistics for the proton being more limited than for the deuteron. For kaons the error bars are too large to draw reliable conclusions. Although the PGF fractions are slightly higher for kaons than for other hadrons, this advantage is overcompensated by the much poorer statistics. For both targets, and for all hadron types and charges, the values found for $\Delta G/G$ are mutually consistent and tend to be negative.

6.4 Interpretation with PYTHIA MC

As an alternative to the previous section, the extraction of the gluon polarization described in this section is performed using the PYTHIA MC. The formalism is largely similar to the extraction using LEPTO MC. (The detailed PYTHIA MC specifications and the treatment of the asymmetries used in this analysis are given in appendix A.2 and B.1.)

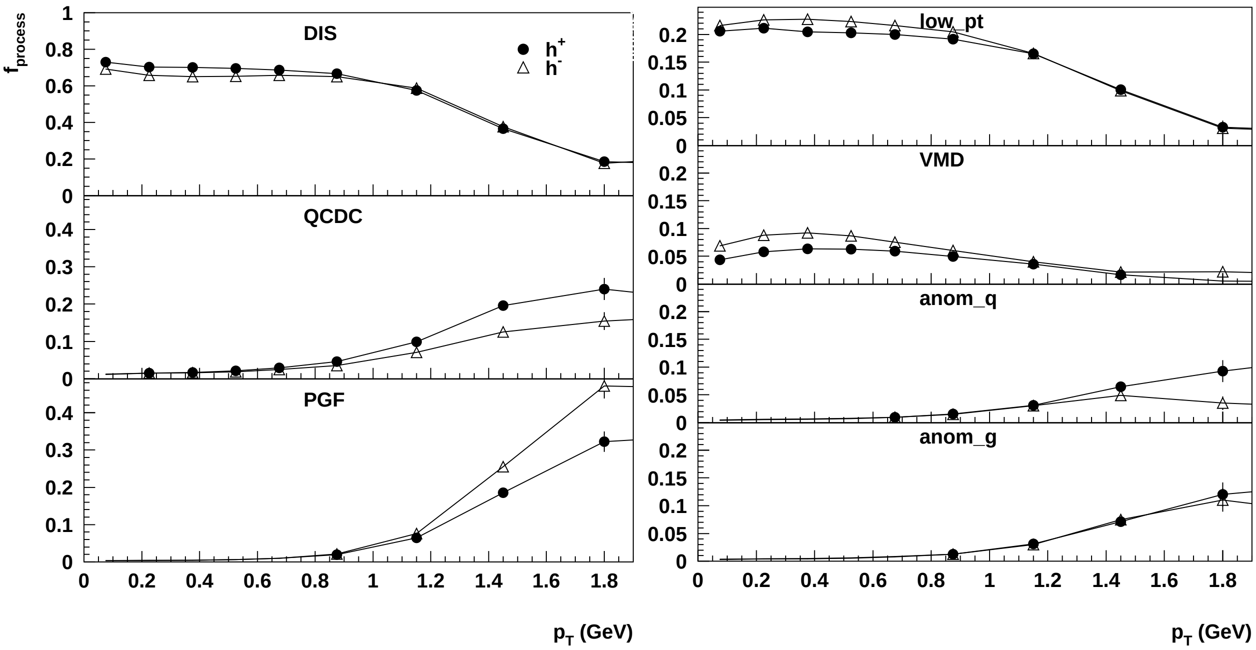

Figure 6.14: *Process fractions vs. p_T for positive (closed symbols) and negative (open symbols) hadrons in electroproduction obtained from PYTHIA MC on a proton target.*

	signal fraction	
particle	proton target	deuteron target
$h+$	11.2%	11.7%
$h-$	13.2%	14.3%
$\pi+$	10.7%	10.9%
$\pi-$	13.6 %	14.8%
$K+$	13.3%	14.8%
$K-$	13.2%	14.4%

Table 6.4: *Signal process fractions for different hadron types and targets, for single high-p_T hadron electroproduction at $p_T > 1$ GeV obtained from PYTHIA MC.*

6.4.1 Process fractions

Fig. 6.14 displays the process fractions f_i for the seven groups of processes (DIS, QCDC, PGF, low_pt, VMD, anom_q and anom_g, cf. 5.1.4) as a function of p_T for positive and negative hadrons, as calculated with PYTHIA on a proton target (other hadron types and the deuteron show similar shapes but are not displayed here). Although lower in absolute values, the shapes of the DIS and QCDC process fractions look very similar to those obtained with LEPTO. The PGF process fraction is comparable to the LEPTO result even quantitatively. In PYTHIA another four process groups, absent in LEPTO, are included. The low_pt process fraction amounts to 20% for $p_T < 1$ GeV and decreases to below 5% for larger values of p_T. The VMD process fraction shows a maximum of

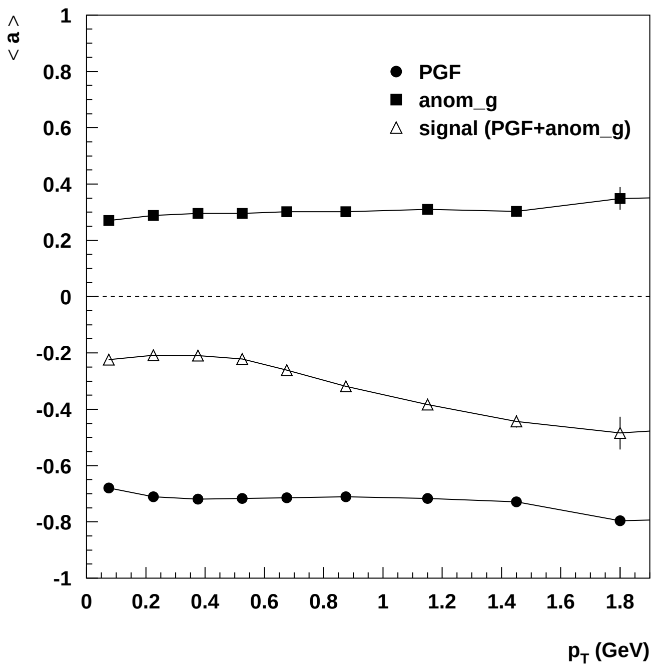

Figure 6.15: *Average hard process asymmetry vs. p_T for PGF, anom_g and both combined into one signal process for positive hadrons in electroproduction obtained from PYTHIA MC on a proton target.*

about 5% at small p_T and decreases to a few percent or less for larger p_T. The anom_q processes are negligible below $p_T = 1$ GeV and then increase to about 10%. While these three are to be considered background processes, the anom_g processes in PYTHIA are counted as signal; their fraction is very small at small p_T but increases with p_T to about 10 %.

Tab. 6.4 shows the signal fractions (PGF and anom_g processes combined) at $p_T >$ 1 GeV for the three particle types and both charges, on the proton as well as on the deuteron target. Similarly to the LEPTO results summarized in Tab. 6.3, one finds also with PYTHIA that the signal fractions on the deuteron are slightly higher than on the proton, and slightly higher for negative than for positive particles (except for kaons). In general, the combined PGF and anom_g fractions in PYTHIA are very comparable to the PGF fractions in LEPTO, albeit slightly higher.

6.4.2 Hard signal asymmetry and background asymmetries

The average hard process asymmetries vs. p_T for PGF, anom_g and both combined into one signal process, as calculated using PYTHIA, are displayed in Fig. 6.15 for positive hadrons and a proton target (results for other hadrons, charges, and the deuteron target are again very similar). One observes very little dependence on p_T. The average hard PGF process asymmetry is about -0.7 in the complete p_T-range. The anom_g processes contribute positively with about +0.35 to the average hard signal process asymmetry, in

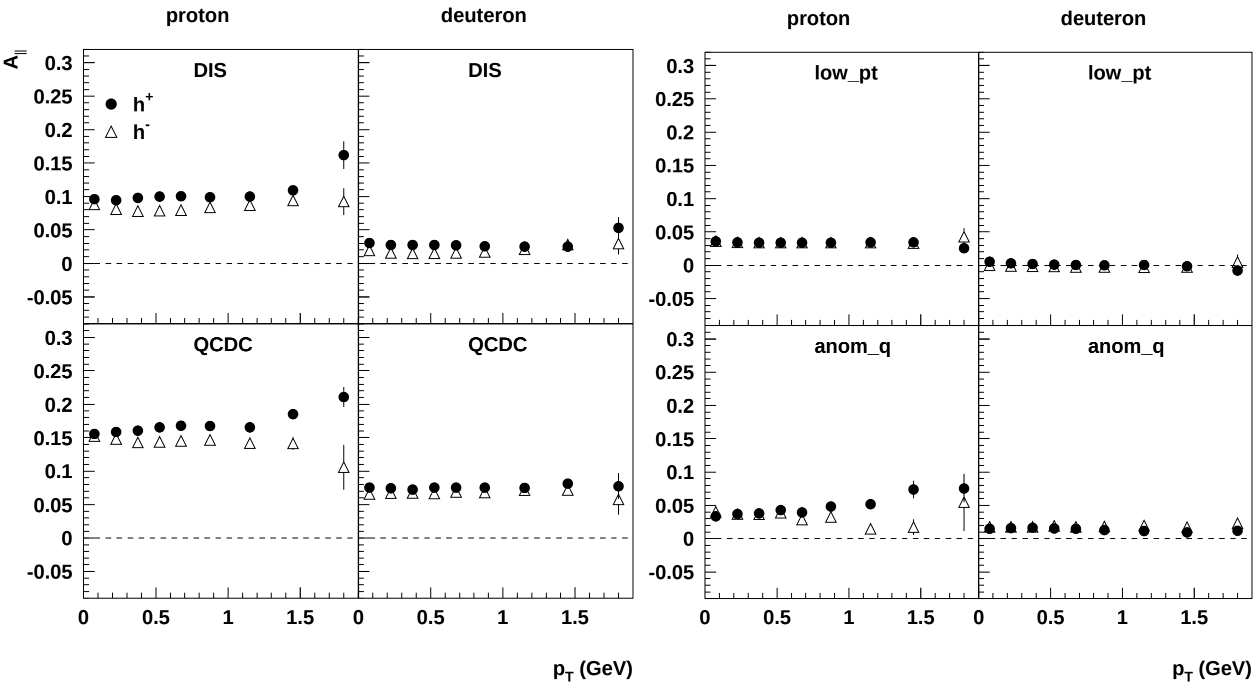

Figure 6.16: *Asymmetries $A_{||}$ vs. p_T of the background processes from PYTHIA MC on a proton (left) and a deuteron (right) target respectively, for positive and negative hadrons in electroproduction.*

consequence reducing the overall analyzing power to about -0.2 to -0.5 across the p_T-range. The average hard PGF process asymmetry obtained with PYTHIA shows larger absolute values than the corresponding LEPTO results. This can be understood as a consequence of its Q^2-dependence (cf. appendix B.1) and the fact that the PYTHIA MC has been generated with $Q^2 > 0.1$ GeV^2, whereas LEPTO is limited to $Q^2 > 0.5$ GeV^2. The hard PGF process asymmetry is close to -1 for $Q^2 \approx 0$ GeV^2 and decreases in absolute value with increasing Q^2.

In Fig. 6.16 the background (DIS, QCDC, low_pt and anom_q) asymmetries vs. p_T as obtained using PYTHIA are plotted for positive and negative hadrons on the proton and the deuteron target (pions and kaons show a similar behaviour). Remember that the VMD processes are treated as a dilution with a background asymmetry set equal to zero. For DIS and QCDC, the results found are very similar to those of LEPTO. The asymmetries from low_pt and anom_q are small, reaching values of a few percent at most. They are, analogously to the DIS and QCDC asymmetries, smaller for the deuteron than for the proton.

6.4.3 The gluon polarization

Before the gluon polarization is extracted from the measured asymmetries (using the process fractions, the hard signal asymmetry, and the background asymmetries from the

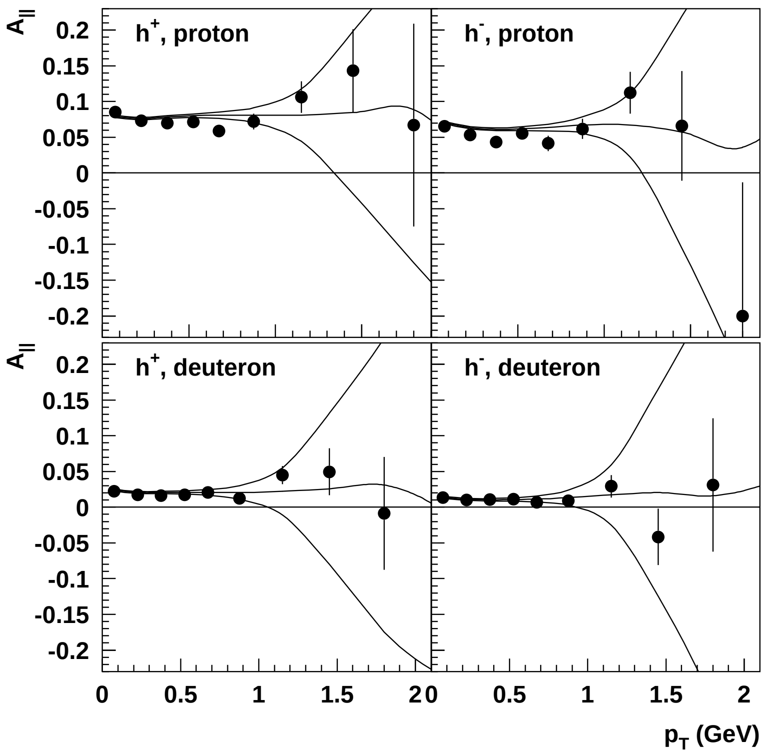

Figure 6.17: *The measured asymmetries $A_{||}$ vs. p_T for positive (left) and negative (right) hadrons in electroproduction on the proton (top) and the deuteron (bottom) target overlaid with the PYTHIA MC asymmetries determined for three different assumptions of the gluon polarization, $\Delta G/G$=-1 (upper line), $\Delta G/G$=0 (middle line), and $\Delta G/G$=+1 (lower line).*

PYTHIA MC given above), the sensitivity of the asymmetries vs. p_T to different values of the gluon polarization is investigated. At the same time, the suitability of the PYTHIA model (with the externally built-in asymmetry weights) to describe the measured asymmetries can be verified. As the gluon polarization $\Delta G/G$ is so far hardly constrained, different assumptions for $\Delta G/G$ are used to calculate the overall MC asymmetries. Fig. 6.17 shows the measured asymmetries for positive and negative hadrons on the proton and the deuteron target vs. p_T together with the asymmetries obtained from the PYTHIA MC for three different assumptions on the gluon polarization, namely $\Delta G/G = -1, 0, +1$.

At small p_T, the signal process fraction is so small that the overall asymmetry is dominated by the background. Consequently, the various assumptions for $\Delta G/G$, which determine the size of the asymmetries from the signal processes, hardly influence the overall MC asymmetry. Hence, in this region the unknown gluon polarization plays virtually no role and the asymmetry is dominated by the background processes (especially about 60% DIS, 20% low_pt, 10% VMD). As the MC asymmetries agree very well with those measured it is demonstrated that the PYTHIA model is in general well suited to describe the asymmetries measured by HERMES.

At larger p_T, especially at $p_T > 1$ GeV, the signal process fraction becomes sufficiently

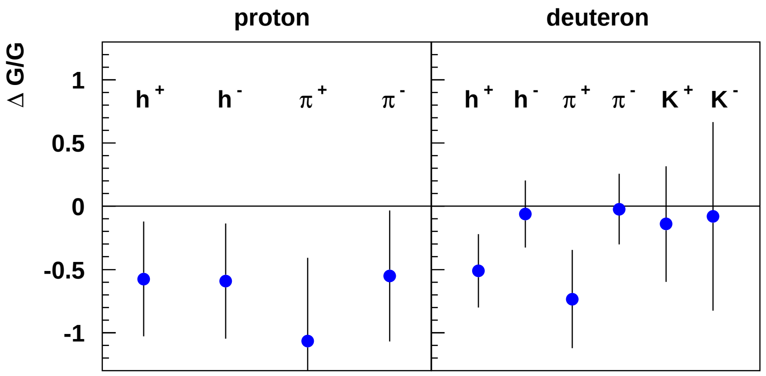

Figure 6.18: $\Delta G/G$ *extracted from the measured asymmetries and the PYTHIA MC for different hadron types and charges on proton (left) and deuteron (right) target respectively, for single high-p_T hadron electroproduction at $p_T > 1$ GeV.*

large to cause significant differences in the overall MC asymmetries for the different $\Delta G/G$ assumptions. In this region, the data asymmetries are measured with an accuracy high enough to distinguish between the three entirely different gluon polarization scenarios. Hence, it is in this region that a value for the gluon polarization is extracted from the measured asymmetries.

Fig. 6.18 displays the values of $\Delta G/G$, including the statistical uncertainties, extracted from the measured asymmetries at $p_T > 1$ GeV using PYTHIA, in the way described in section 5.2. The results are presented separately for the proton and the deuteron and for the different hadron types and charges. As for the extraction performed with LEPTO, the gluon polarization is extracted at an average gluon momentum fraction $\langle x_g \rangle \approx 0.23$. The x_g-distributions cover a range from 0.07 to 0.65, with a half maximum width given by the range 0.1 to 0.25.

Again, due to statistics, the uncertainties are larger for the proton than for the deuteron. Furthermore, the uncertainties for kaons are larger than for the other hadrons, which is caused by the limited statistics despite slightly increased signal fractions. In general, the uncertainties on the gluon polarization extracted with PYTHIA are slightly smaller than those extracted with LEPTO. This is directly related to the small differences in the signal process fraction and the hard signal asymmetry. The values obtained with PYTHIA for $\Delta G/G$ tend to be negative or consistent with zero for all hadron types, charges, and both targets considered. This is entirely consistent with the results extracted using LEPTO.

6.4.4 Systematic studies

In this section it is investigated how the obtained results for the gluon polarization depend on the different choices made in the extraction procedure with PYTHIA. These choices can be made at two stages in the extraction procedure, either in the calculation of the asymmetries, and/or in the generation of the unpolarized events. In the calculation of the asymmetries the largest uncertainties arise from the not well-defined low_pt process, the unknown polarized parton distribution functions of the photon and the differences between various sets of polarized parton distribution functions of the nucleon (cf. section 5.1.4 and appendix B.1 for details). In the generation of the unpolarized events the different choices made for the PYTHIA model itself and the fragmentation parameters influence the results (cf. section 5.1.4 and 5.1.2 for details). In the following, the effect of different treatments of the low_pt processes, different polarized parton distribution functions in the photon and in the nucleon, and different choices for the PYTHIA model parameters as well as different fragmentation tunes will be investigated.

Treatment of low_pt processes

According to the PYTHIA MC calculations for single high-p_T hadron electroproduction, the low_pt process fraction is only about 10-15% at $p_T > 1$ GeV (cf. Fig. 6.14). Hence, the effect on the extracted gluon polarization of treating these processes in alternative ways is probably small, but not necessarily negligible. It therefore needs to be studied. Three different treatments are considered in this study (cf. appendix B.1 for details), namely modelling the MC background asymmetry arising from low_pt processes

- as a dilution ($A_1^{low\_pt} = 0$),
- as the charge weighted sum of the polarized over unpolarized PDFs in the x and Q^2 range where the PDFs are available ($A_1^{low\_pt} = g_1/F_1$ for $x > x_{min}$ and $Q^2 > Q^2_{min}$ with $x_{min} = 10^{-5}$ and $Q^2_{min} = 0.22$ GeV^2, $A_1^{low\_pt} = 0$ otherwise); this method has been used in the standard extraction of the gluon polarization presented above,
- as the parametrization of the experimental data for A_1 in the whole x and Q^2 range ($A_1^{low\_pt} = A_1^{exp}$ for all x and Q^2 values).

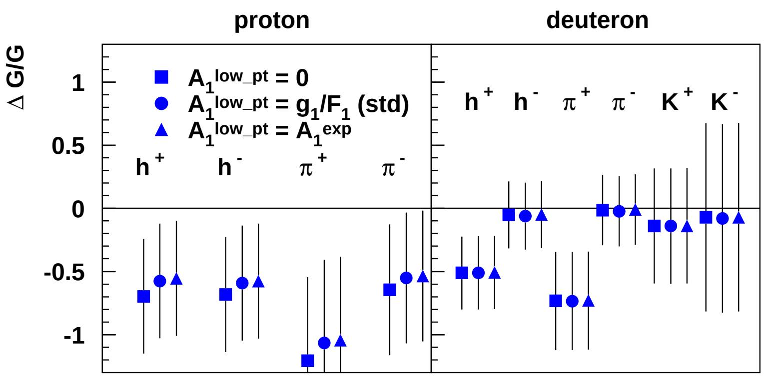

Figure 6.19: *$\Delta G/G$ extracted with the three different treatments of the MC background asymmetry from low_pt processes, for different hadron types and charges on proton (left) and deuteron (right) target respectively, for single high-p_T hadron electroproduction at $p_T > 1$ GeV.*

Fig. 6.19 shows the extracted gluon polarization obtained for the three options used in calculating the asymmetries from the low_pt processes. For the proton target the three methods yield differences of up to 20%, showing the same behaviour for positive and negative hadrons and pions. In this case, treating the low_pt events as a dilution rather than assigning a small positive asymmetry to them results in a slightly more negative gluon polarization. For the deuteron target, the three different methods have virtually no influence on the result. This can be explained by the much smaller values of A_1 for the deuteron in comparison to its values for the proton, in combination with the small contribution of the low_pt processes.

Polarized PDFs of the photon

The anomalous processes contribute to the signal as well as to the background; the contribution of the anomalous gluon processes, considered as signal, and the contribution of the anomalous quark processes, consequently considered as background, is a few % each at $p_T > 1$ GeV. It has been studied how different assumptions made for the polarized photon parton distribution functions, entering in the calculation of the asymmetries for these anomalous processes, influence the results for the extracted gluon polarization. These different assumptions alter the hard signal asymmetry for the anom_g processes and the background asymmetry for the anom_q processes. Two different assumptions are considered, i.e. no polarization of partons in the photon ($\Delta q^\gamma = \Delta g^\gamma = 0$) which means treating the anomalous processes as a dilution both to the signal and the background, or 'maximal' polarization ($\Delta q^\gamma = \Delta g^\gamma = +1$, as used in the standard extraction of the gluon polarization presented above) which implies adding a positive asymmetry from anom_g processes to the negative asymmetry from PGF processes and adding a positive asymmetry from the anom_g processes to the asymmetry of the other background processes (cf. appendix B.1 for details). In Fig. 6.20 the results for these two different methods are presented. The effect on the extracted gluon polarization is of the order of 10%.

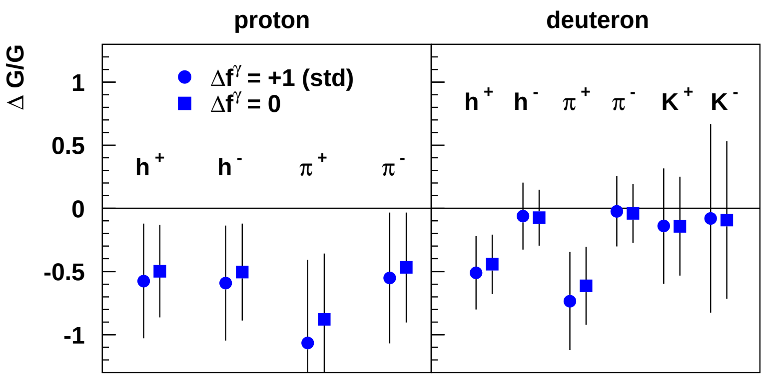

Figure 6.20: *$\Delta G/G$ extracted with two different assumptions for the polarized photon PDFs for the asymmetries from anomalous processes, for different hadron types and charges on proton (left) and deuteron (right) target respectively, for single high-p_T hadron electroproduction at $p_T > 1$ GeV.*

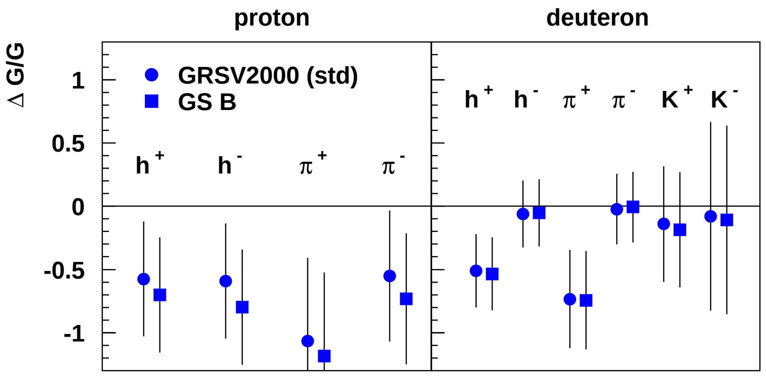

Figure 6.21: *$\Delta G/G$ extracted with two different sets of polarized nucleon PDFs for all background asymmetries, for different hadron types and charges on proton (left) and deuteron (right) target respectively, for single high-p_T hadron electroproduction at $p_T >$ 1 GeV.*

Polarized PDFs of the nucleon

The polarized parton distribution functions of the nucleon are used in the calculation of the asymmetry for all background processes. Their choice determines the size of the background asymmetries, and as a consequence can have an impact on the extracted gluon polarization. This effect is investigated in this section. Two different polarized PDF sets are applied, namely the leading order GRSV 2000 valence scenario [32] (as used in the standard extraction of the gluon polarization presented above), and as an alternative the leading order GS set B [115]. In Fig. 6.21 the results for the gluon polarization are plotted when using these two different PDF sets in the calculation of the background asymmetries. For the proton target relatively small deviations of up to 20% are observed. For the deuteron target, the effect is negligible, which might be due to the effects for the polarized PDFs of the proton and the neutron (partially) cancelling each other in a deuteron target.

PYTHIA model parameters

It is beyond the scope of this thesis to present an exhaustive study on the dependence of the extracted gluon polarization on a range of different settings for various PYTHIA model parameters. The discussion here is limited to only one parameter. As explained in section 5.1.4, the process fractions obtained with the PYTHIA MC depend crucially on the PYTHIA model parameter MSTP(18). Using different settings of this parameter therefore causes variations of the extracted gluon polarization, to be studied in this section. The parameter MSTP(18) defines the lower cutoff $k_{\perp,min}$ for the generation of direct processes (PGF and QCDC). When changing this parameter from the default value MSTP(18)=3 (as used for the standard extraction of the gluon polarization presented above) to MSTP(18)=2 (which means going from $k_{\perp,min} \approx 1.4$ GeV to

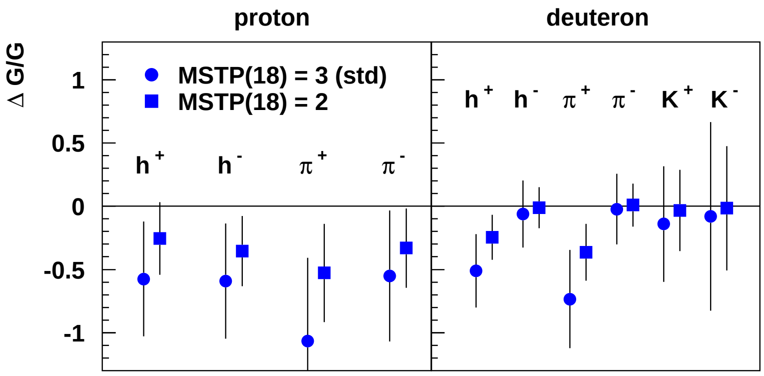

Figure 6.22: *$\Delta G/G$ extracted with two PYTHIA parameter sets, for different hadron types and charges on a proton (left) and a deuteron (right) target respectively, for single high-p_T hadron electroproduction at $p_T > 1$ GeV.*

$k_{\perp,min}$ = 0.5 GeV), the process fractions for PGF and QCDC increase while the process fractions for the anomalous processes decrease. The effect on the extracted gluon polarization shown in Fig. 6.22 is sizable. Since data-MC cross section comparisons for different PYTHIA parameter settings do not show a distinctively better agreement for either one of the two settings [116], this difference in the extracted gluon polarization is considered as a systematic uncertainty.

Fragmentation tunes

As the last part of the systematic studies the dependence of the extracted gluon polarization on the description of the fragmentation is investigated. The final state partons of the hard process, generated according to the PYTHIA model parameters, hadronize according to the JETSET fragmentation parameters. It is especially important for the analysis presented in this thesis to study how the final state particles acquire transverse momentum in the fragmentation. This is determined by the parameters PARJ(21)-PARJ(24) (cf. section 5.1.2). Here, the latest tune 2004c (as used for the standard extraction of the gluon polarization presented above) which uses the default setting for PARJ(23)=0.01 and PARJ(24)=2.0 is compared with the older tune 2004a with PARJ(23)=0.03 and PARJ(24)=2.5. Note that the two tunes differ in more than just these two parameters. A third tune, tune 2004d[5], uses the same parameter settings as tune 2004c, except for PARJ(23) and PARJ(24) which are set to the values of tune 2004a. Increasing the values for these two parameters, as has been done in tune 2004a and 2004d, results in the hadrons acquiring on average more transverse momentum $p_{T,F}$ in the fragmentation in addition to the contribution from the intrinsic k_T of the partons participating in the hard process. This influences the hadron p_T distribution significantly, but differently for the various processes, and therefore changes the process fractions vs. p_T. The process fractions for DIS increase significantly while the process fractions for QCDC, PGF and

[5]MC simulations generated with tune 2004d are only available for the proton at the time of writing.

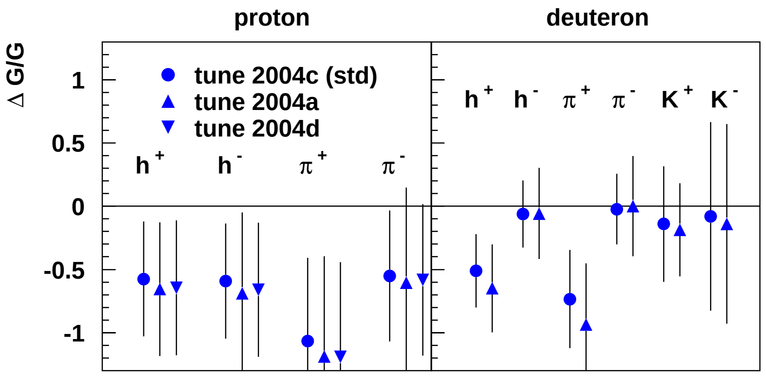

Figure 6.23: *$\Delta G/G$ extracted using different fragmentation tunes, for different hadron types and charges on a proton (left) and a deuteron (right) target respectively, for single high-p_T hadron electroproduction at $p_T > 1$ GeV.*

the anomalous process decrease. Fig. 6.23 shows the extracted gluon polarization for these different fragmentation tunes. The differences between the results for tune 2004c and 2004a are of the order of 20-30%. Comparing the results for tune 2004a and 2004d, which have in common the settings for the parameters PARJ(23) and PARJ(24) but differ in the settings for the other fragmentation parameters, one observes virtually no difference. From this it is concluded that PARJ(23) and PARJ(24) are crucial for the value of the extracted gluon polarization. Although in general tune 2004c agrees better with the data than tune 2004a [117], this argument cannot be applied for tune 2004d. Therefore, the difference in the extracted gluon polarization has to be treated as a systematic uncertainty.

6.5 Summary of results

The extracted gluon polarizations and their uncertainties discussed in detail in the previous sections are summarized here. The various results are checked for consistency, and averaged where appropriate.

All results presented in this chapter show that the extracted gluon polarization in the single high-p_T hadron electroproduction at $p_T > 1$ GeV is consistent when comparing positive and negative particles. This was to be expected since the measured asymmetries for positive and negative particles are consistent, and the MC simulations do not show any significant differences between the two charges either. Hence, at this stage the results for positive and negative particles can be averaged. The combined results for the gluon polarization and the corresponding statistical uncertainties for charged particles are presented in Tab. 6.5 (taking the error-weighted average).

From Tab. 6.5 it is concluded that the results for pions and kaons are consistent with the results obtained for all hadrons. Since the statistical uncertainties of the extracted gluon polarization are about a factor of two larger for kaons than for all hadrons and there

target	hadron type	MC	$\Delta G/G$
proton	h	LEPTO	-0.62 ± 0.47
		PYTHIA	-0.53 ± 0.28
	π	LEPTO	-0.63 ± 0.60
		PYTHIA	-0.67 ± 0.35
deuteron	h	LEPTO	-0.25 ± 0.26
		PYTHIA	-0.24 ± 0.17
	π	LEPTO	-0.20 ± 0.29
		PYTHIA	-0.24 ± 0.20
	K	LEPTO	0.02 ± 0.56
		PYTHIA	-0.12 ± 0.34

Table 6.5: *Averaged $\Delta G/G$ values for charged hadrons, pions and kaons as obtained on a proton and a deuteron target using either LEPTO or PYTHIA MC. The error-weighted average is taken from the separate results for positive and negative particles, for single high-p_T hadron electroproduction at $p_T > 1$ GeV.*

is no evidence that the systematic uncertainties for kaons are any different than for all hadrons, kaons are not considered any further. The pions are not considered separately any further either since also in this case the statistical uncertainties are larger than for all hadrons (by about a factor 1.2) without any apparent differences in the systematic uncertainties. Since the (all) hadron results are dominated by the pion contribution, the results for well-identified pions are very similar to those obtained for all hadrons.

Moreover, it can be inferred that the results obtained using the LEPTO MC and the PYTHIA MC are consistent. Since PYTHIA includes a more complete description of the involved processes, and extends down to smaller Q^2 values, the results extracted with the PYTHIA MC are to be preferred.

Hence, the $\Delta G/G$ results obtained for charged hadrons from the proton and the deuteron target with the PYTHIA MC are taken as the final results for single high-p_T hadron electroproduction at $p_T > 1$ GeV. In Tab. 6.6 and Tab. 6.7 these results for the gluon polarization are summarized together with the statistical, experimental systematic, and model dependent systematic uncertainties. The statistical uncertainty is calculated according to Eq. (5.12), and the experimental systematic uncertainty according to Eq. (5.13). The model dependent systematic uncertainties associated with each of the studies presented in section 6.4.4 are determined as the differences between the gluon polarizations from the varied and the standard extraction.

In chapter 8 the present $\Delta G/G$ results for single high-p_T hadron electroproduction are compared with the results presented in chapter 7 for high-p_T hadron pairs photoproduction, including a final discussion of the total model dependent systematic uncertainties and a consistency check.

	proton	deuteron
$\Delta G/G$	-0.583	-0.266
$\delta(\Delta G/G)^{stat.}$	0.322	0.195
$\delta(\Delta G/G)^{exp.syst.}$	0.114	0.031

Table 6.6: *Results for $\Delta G/G$ including statistical and experimental systematic uncertainties for charged high-p_T hadrons in electroproduction on the proton and the deuteron target using the PYTHIA MC.*

$\delta(\Delta G/G)^{\text{mod.dep.syst.}}$	proton	deuteron
$A_1^{low\_pt} = 0$	-0.106	+0.005
$A_1^{low\_pt} = A_1^{exp}$	+0.018	+0.008
$\Delta f^{\gamma} = 0$	+0.083	+0.019
GS B	-0.166	-0.005
MSTP(18)=2	+0.277	+0.148
tune 2004a	-0.085	-0.097

Table 6.7: *List of model dependent systematic uncertainties, for charged high-p_T hadrons in electroproduction on the proton and the deuteron target using the PYTHIA MC.*

Chapter 7

Photoproduction of high-p_T hadron pairs

In this chapter the analysis performed to extract the gluon polarization from high-p_T hadron pairs in photoproduction is discussed. For this analysis events containing two or more hadrons with large transverse momenta are considered. Detection of the scattered lepton is not required. This reaction channel is expected to be powerful for tagging the photon-gluon fusion process. However, the statistical accuracy for hadron pair detection at high-p_T turns out to be quite limited in the HERMES acceptance. This necessitates extra diligence in the identification (through extensive Monte Carlo studies) of a phase space region providing optimal conditions for the extraction of the gluon polarization. The high-p_T hadron pairs are produced mostly at very small photon virtuality, i.e. the lepton is scattered at such a small angle that it escapes detection. This kinematic region is only covered by the PYTHIA Monte Carlo package, while LEPTO is not applicable.

A series of PYTHIA MC studies (section 7.1) is conducted to optimize the event selection in such a way that the signal process fraction is large while the number of selected events is still reasonable. Subsequently, data asymmetries are derived for this optimized event selection (section 7.2). Information from PYTHIA MC simulations is used for the extraction of the gluon polarization from the data asymmetries including an estimate of the model dependent systematic uncertainties (section 7.3). Finally, a summary of results for the extracted gluon polarization is presented (section 7.4)

7.1 PYTHIA Monte Carlo studies

In order to provide the basis for the extraction of the gluon polarization with highest attainable significance in the subsequent sections, the aim of this section is to optimize the cuts for the channel of high-p_T hadron pairs in photoproduction. Relevant parameters for the optimization are the lepton detection or veto, respectively, the hadron charges, types, multiplicities, and the two transverse hadron momenta, the latter either considered separately or in combination. All PYTHIA MC simulations for these studies have been

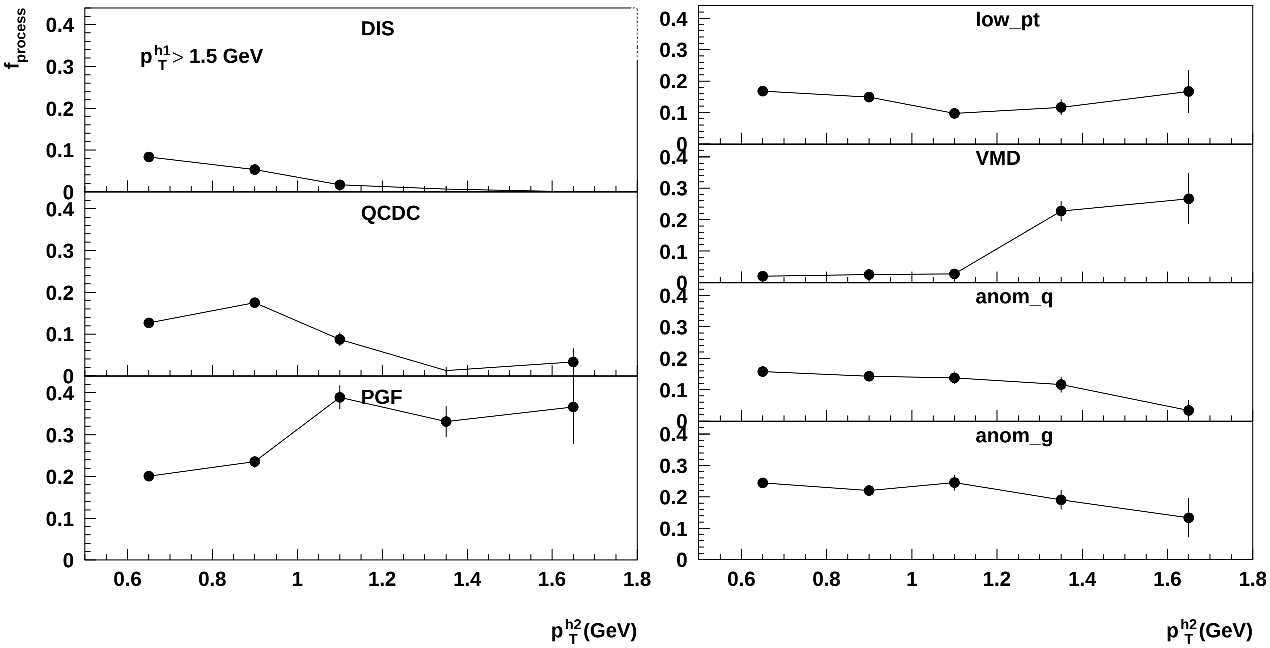

Figure 7.1: *Process fractions vs. p_T^{h2} for $p_T^{h1} > 1.5$ GeV for the two signal processes PGF and anom_g and the five background processes DIS, QCDC, low_pt, VMD and anom_q for oppositely charged hadron pairs with the lepton vetoed as obtained from PYTHIA MC on a proton target.*

generated for a proton target, using the fragmentation tune 2004c, neglecting QED radiative corrections, but applying detector smearing.

7.1.1 Initial set of selection criteria for optimization studies

The initial selection criteria, used as a starting point for further optimization studies, are chosen in analogy to a previous analysis of high-p_T hadron pairs by the HERMES collaboration [46, 47]. The scattered lepton is vetoed, i.e. events containing leptons with beam charge are rejected, two hadrons with opposite charge are required, the p_T of one of these has to be greater than 1.5 GeV, while the other p_T is divided into five bins (0.5-0.8, 0.8-1.0, 1.0-1.2, 1.2-1.5, and > 1.5 GeV). The hadron p_T is calculated with respect to the z-axis of the HERMES coordinate system, since the p_T with respect to the virtual photon is not available as the lepton is not detected. For these selection criteria, Fig. 7.1 displays the process fractions of the seven relevant process groups (cf. 5.1.4) simulated in PYTHIA. The PGF fraction is about 20% for smaller values of p_T^{h2}, the transverse momentum of the second hadron, and amounts to about 35-40% at $p_T^{h2} > 1.0$ GeV, while the anom_g processes contribute less than 25-15% across the range of p_T^{h2}; both are combined in the signal. The composition of the background (DIS, QCDC, low_pt, VMD, anom_q) also varies with p_T^{h2}. The contribution of the DIS process is very small, with less than 10% at any p_T^{h2}. The QCDC process fraction amounts to at most 20% at smaller p_T^{h2} and then decreases to a few percent at larger p_T^{h2}. The low_pt process fraction shows a value of 10-15% largely independent of p_T^{h2}. The VMD process fraction is only a few percent at $p_T^{h2} < 1$ GeV, and increases with p_T^{h2} to a maximum of about 30%. The anom_q process fraction decreases from about 15% to a few % at large p_T^{h2}. Combining the last three p_T^{h2}-bins (as done in the previous analysis for the extraction of the gluon polarization), i.e. asking for one hadron with $p_T > 1.5$ GeV and a second, oppositely charged, hadron with $p_T > 1.0$ GeV, PYTHIA gives, for PGF and anom_g processes taken together, a signal fraction of about 59 %. In the following sections, it is investigated to which extent the combination of a large signal process fraction and small statistical uncertainties on the data asymmetries can be optimized. This is accomplished in an iterative procedure as follows: From the initial set of criteria, all are left unaltered with the exception of a single one chosen for optimization. The result of this optimization (which may or may not be identical to the original choice) is in the following kept fixed. In the next step, the procedure is repeated with a different criterion, until all criteria from the set have been considered.

7.1.2 Studies on the lepton

To optimize the cuts on the scattered lepton, three possible treatments have to be considered. In coincidence with the hadron pair, the lepton can be

- required NOT to be in the HERMES acceptance, i.e. vetoed as in the initial set of criteria discussed in the previous section,
- required to be detected in the HERMES acceptance, or
- not constrained at all, which combines the two above samples.

Lepton in acceptance

Only in less than 10% of the MC signal events which meet the requirements as defined in the previous section, the scattered lepton is detected in the HERMES acceptance. Requiring the scattered lepton in the HERMES acceptance in coincidence with a high-p_T hadron pair would therefore reduce the number of accepted events so significantly that any extraction of the asymmetry becomes impossible. Independently of any statement on the signal fraction the conclusion can be drawn that cuts on the lepton kinematics are not feasible.

No constraints on lepton

When vetoing the scattered lepton in the acceptance, about 9% of the MC signal events are discarded, while of the background more than 50% of the DIS events, but only less than 5% of the other background processes are rejected. This means that the DIS events are suppressed while the other background events are favoured with respect to the signal events, compared to not putting any constraints on the lepton. In effect, the signal to background ratio remains unaffected. This leads to the conclusion that optimal conditions are obtained if no constraints on the scattered lepton are imposed, thus combining the statistics of the events with and without the scattered lepton in the acceptance, at no loss in signal process fraction. For all further studies, this is adopted.

7.1.3 Studies on the hadron charges

Next it is checked if the restriction to oppositely charged hadron pairs can be removed. If hadron pairs with any charge combination are included, the signal sample increases by about 35%. The background sample contains 50% more events of the anom_q group, no extra VMD events are included, and the number of events of all the other background processes increases by about 20%. In other words, the process fraction of anom_q events is slightly larger, the fractions of the other background processes slightly smaller, but the signal process fraction remains essentially unchanged if instead of only oppositely charged hadron pairs any charge combination is accepted. The conclusion from this study is that optimal results are obtained if the statistics of hadron pairs with opposite and like charges are combined, as it leaves the signal process fraction virtually unchanged. Hence in all further studies, hadrons pairs of any charge combination are considered.

7.1.4 Studies on the hadron types

While the method in the two previous studies was to relax certain conditions to improve the statistics at no loss of signal process fraction, one can now also apply the opposite approach. Here it is investigated if one can restrict the hadrons to certain types, which will surely decrease the number of events, but might increase the signal process fraction. If one demands that the hadron pairs are two identified pions, about 65% of the signal events are left. For the low_pt and the VMD events slightly more than 80% of the hadron pairs are both pions, while for the other background processes (DIS, QCDC and anom_q) only 50-60% are both pions. In total, the signal process fraction is not affected. Requiring two kaons in the hadron pair decreases the number of events drastically. This by itself is reason enough to abandon the idea of analyzing kaon pairs. But the MC study has also shown that the signal process fraction even decreases. Since constraints on the hadron types only decrease the number of events without improving the signal process fraction, for all further studies hadron pairs of any type are included.

7.1.5 Studies on the hadron multiplicities

Analogously to the studies on the hadron types it is also investigated if imposing constraints on the hadron multiplicities can increase the signal process fraction. About 75%

of the signal events discussed in the previous section have exactly two hadrons in the acceptance. For the background events this fraction is the same. This implies that constraints on hadron multiplicities only severely decrease the number of events without any improvement on the signal process fraction. Therefore, the idea of a possible cut on hadron multiplicities is abandoned.

7.1.6 Studies on separate hadron p_T

Having exploited constraints on the lepton, the hadron charges, types and multiplicities, the dependence of the process fractions on the transverse momenta, p_T^{h1} and p_T^{h2}, of the hadron pairs is further studied. At this stage, the transverse momenta of the two hadrons are still treated as two separate quantities. The process fractions have been studied when relaxing the cut on the hadron with higher p_T, while the other hadron p_T is still required to be above 1.0 GeV. When relaxing the higher $p_T^{\min}$ from 1.5 GeV down to 1.0 GeV, the signal process fraction decreases from about 60% to about 40%. But at the same time, the number of events increases by about an order of magnitude. This overcompensates the loss in signal process fraction and in essence even decreases the uncertainty on the extracted gluon polarization. Therefore, a relaxed $p_T^{\min}$ is also considered for the extraction of the gluon polarization in the following sections.

7.1.7 Studies on combinations of the p_T of the two hadrons

Going one step further in the studies on p_T, the separate p_T of the two hadrons are now combined into a single quantity. In this study, the process fractions have been investigated as functions of the following four quantities:

- the p_T of the vector sum of the two hadron momenta,
- the relative p_T of the two hadrons, resulting from the projection of one hadron momentum onto the other,
- the sum of the two p_T, and
- the sum of the squares of the two p_T.

For all cases, in addition to the thresholds on the above mentioned quantities, the p_T of the two individual hadrons is required to be larger than 0.5 GeV.

The signal process fraction increases with increasing p_T of the vector sum as well as with increasing relative p_T, but does not exceed 20% and 25%, respectively, in the region accessible to HERMES. Therefore, these quantities are not considered any further.

On the contrary, cuts on the sum of the two p_T and on the sum of the squares of the two p_T are much more efficient in enhancing the signal process fraction. In both cases,

Initial selection criteria	
lepton	no lepton with charge of beam allowed in acceptance
hadrons	at least two hadrons of opposite charge in acceptance
	one of which with $p_T^{h1} > 1.5$ GeV, the other one in p_T^{h2} bins
New selection criteria	
lepton	no constraints
hadrons	at least two hadrons of any charge in acceptance
	with two different options for p_T^{h1} and p_T^{h2}:
	1. $p_T^{h1} > 1.0$ GeV, p_T^{h2} >threshold
	2. $(p_T^{h1})^2 + (p_T^{h2})^2 >$ threshold, and p_T^{h1}, $p_T^{h2} > 0.5$ GeV

Table 7.1: *Selection criteria for high-p_T hadron pairs in photoproduction as used in the initial set and as optimized from PYTHIA studies.*

signal process fractions of about 60% are achievable with increasing cuts, making them competitive to the cuts on separate hadron p_T. As the second quantity delivers the same signal process fractions at higher statistics, it is utilized for an extraction of the gluon polarization in the following sections.

7.1.8 Conclusion from MC studies

Tab. 7.1 summarizes the conclusions from the various studies described in the previous sections in comparison to the initial set of conditions for high-p_T hadron pairs in photoproduction. With these new selection criteria more events are included at a comparable signal process fraction, which leads to an improved significance for the extraction of the gluon polarization. The process fractions for these new selection criteria are shown in section 7.3.1. The lower limit imposed on the p_T of the second hadron is in the following abbreviated $(p_T^{h2})^{\min}$, the lower limit imposed on the sum of the squares of the two hadron p_T is in the following abbreviated $(\sum p_T^2)^{\min}$.

At this stage, it should be pointed out that the two different methods for cutting on the p_T of the two hadrons cover different parts of phase space. The events selected when requiring the two p_T separately above a certain threshold (method 1) are always a subset of those events selected when requiring the combined p_T quantity above a corresponding threshold (method 2). The second method includes additional (more asymmetric) events, namely with larger spreads between the transverse momenta of the two hadrons. To exclude events in which one of the hadrons has a very small p_T (for which the signal fractions are too drastically reduced while the background is enhanced), in addition a lower threshold of 0.5 GeV is imposed for the two separate p_T in method 2.

7.2 Data asymmetries

The studies presented in the previous section have shown that both methods of selecting on hadron p_T, namely setting thresholds on the p_T of each hadron separately or on a specific combination of the p_T of the two hadrons, can lead to a comparable precision in the extraction of the gluon polarization. Therefore, two alternative data analyses are conducted in this section, corresponding to these two choices of p_T cuts.

7.2.1 Data selection

For the data analysis, events are selected with at least two charged hadrons in the HERMES acceptance. There is no constraint placed on the scattered lepton. All hadrons are considered, independent of type and charge. In an event with more than two hadrons, each combination of hadrons is analyzed and counted if it fulfills the p_T requirements.
Two different treatments for the thresholds set on the hadron p_T[1] are performed. In the first analysis, thresholds are imposed separately on the p_T of the two hadrons. One hadron p_T is required to be above 1.0 GeV, and the second is required to be above a certain threshold, which is varied in five steps from 1.0 GeV to 1.5 GeV. The results are presented as a function of this lower limit on the second hadron p_T, i.e. $(p_T^{h2})^{\mathrm{min}}$.
In the second analysis, a cut on a combination of the two hadron p_T is used. The sum of the squares of the two hadron p_T is required to be above a threshold which is varied in non-equidistant steps from 1.0 to 4.0 GeV^2. In addition, both p_T are required to be above 0.5 GeV. The results are presented as a function of this lower limit on the sum of transverse momenta squared, i.e. $(\sum p_T^2)^{\mathrm{min}}$.
As in the analysis of single high-p_T hadrons in electroproduction, the standard data quality cuts for polarized scattering (see section 4.2), the standard track requirements (see section 4.3), and the standard PID cuts (see section 4.4) are all applied in this analysis of high-p_T hadron pairs as well. As usual the productions 96d0, 97d0 for the proton target and 00d0 for the deuteron target are used and all physics triggers are considered.

7.2.2 Measured asymmetries

In this section the measured asymmetries are presented for high-p_T hadron pairs, according to the data selection criteria described above, following the two different methods to cut on hadron p_T.
In Fig. 7.2 the asymmetries $A_{||}$ determined from data taken in 1996/97 with a proton target and from data taken in 2000 with a deuteron target are plotted as functions of the p_T^{min} for the hadron with the higher transverse momentum, while the p_T of the hadron

[1] Recall that the hadron p_T is calculated with respect to the z-axis of the HERMES coordinate system

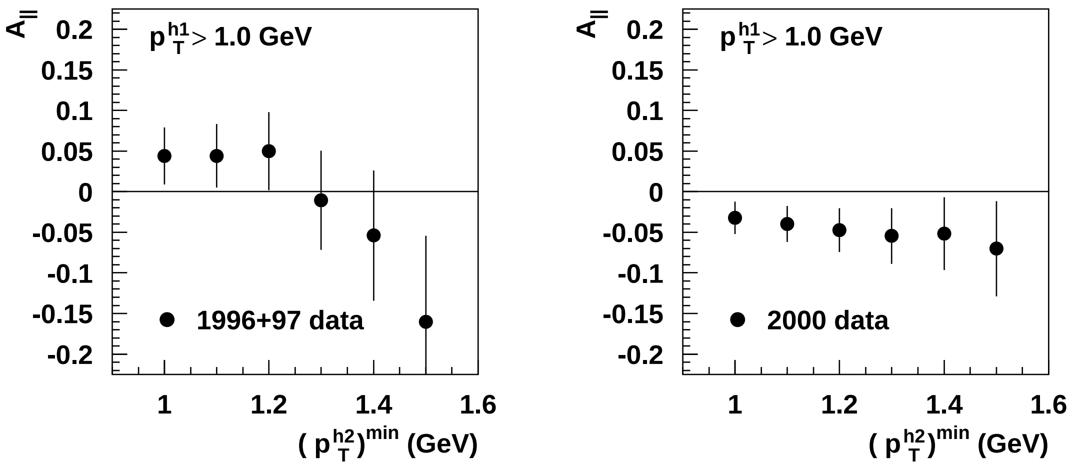

Figure 7.2: *Asymmetries $A_{\|}$ vs. $(p_T^{h2})^{\min}$ with $p_T^{h1} > 1.0$ GeV obtained from the 1996+97 proton target data (left) and the 2000 deuteron target data (right) for hadron pairs of any charge and any type in photoproduction. The systematic uncertainty of the asymmetry, evaluated according to section 4.7.3, which is at most 0.008, is not indicated in the figure.*

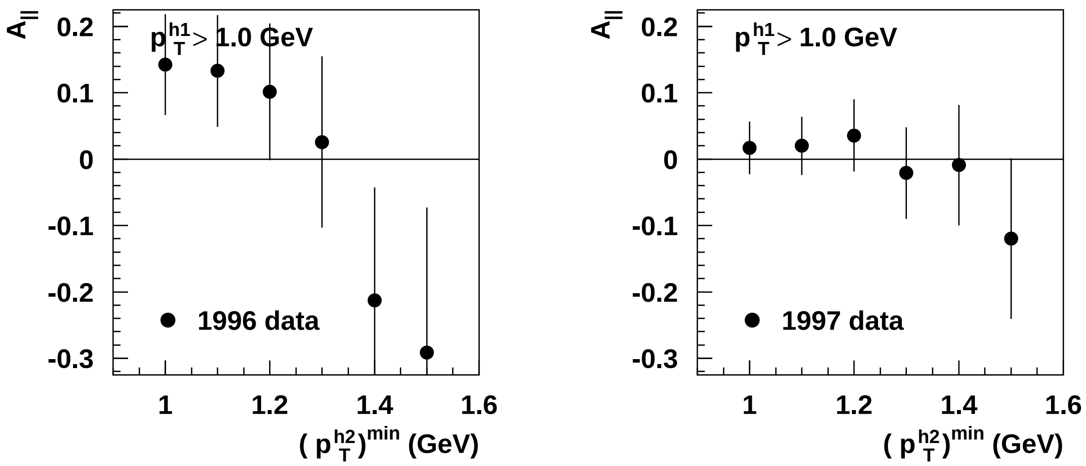

Figure 7.3: *Asymmetries $A_{\|}$ vs. $(p_T^{h2})^{\min}$ with $p_T^{h1} > 1.0$ GeV obtained from the 1996 proton target data (left) and the 1997 proton target data (right) for hadron pairs of any charge and any type in photoproduction. The systematic uncertainty of the asymmetry, evaluated according to section 4.7.3, which is at most 0.018 for 1996 and 0.006 for 1997 is not indicated in the figure.*

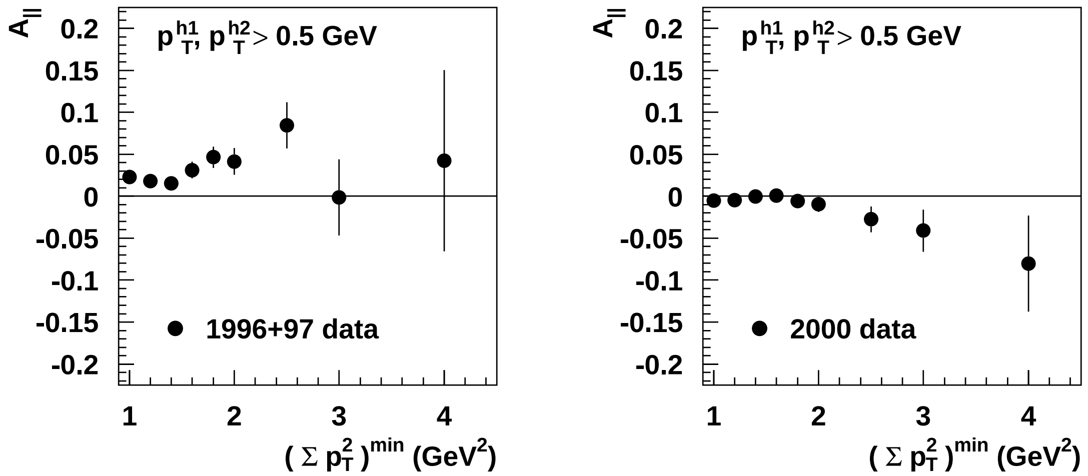

Figure 7.4: *Asymmetries $A_{\|}$ vs. $(\sum p_T^2)^{\mathrm{min}}$ with $p_T^{h1}, p_T^{h2} > 0.5$ GeV obtained from the 1996+97 proton target data (left) and the 2000 deuteron target data (right) for hadron pairs of any charge and any type in photoproduction. The systematic uncertainty on the asymmetry, evaluated according to section 4.7.3, is well below 0.005 in all bins, and not indicated in the plot.*

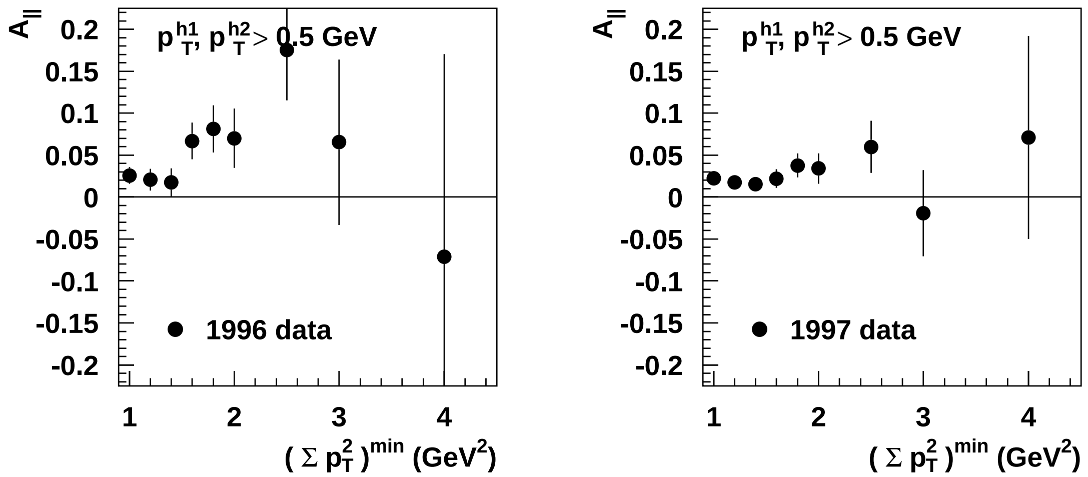

Figure 7.5: *Asymmetries $A_{\|}$ vs. $(\sum p_T^2)^{\mathrm{min}}$ with $p_T^{h1}, p_T^{h2} > 0.5$ GeV obtained from the 1996 proton target data (left) and the 1997 proton target data (right) for hadron pairs of any charge and any type in photoproduction. The systematic uncertainty on the asymmetry, evaluated according to section 4.7.3, is below 0.012 for 1996 and below 0.005 for 1997 in all bins, and not indicated in the plot.*

with lower transverse momentum is required to be above 1.0 GeV. The threshold on the higher p_T is varied in the range between 1.0 and 1.5 GeV. Fig. 7.3 displays the asymmetries separately for the data sets obtained in 1996 and 1997 [2].

Fig. 7.4 shows the asymmetries $A_{\|}$ determined from data taken in 1996/97 with a proton target and from data taken in 2000 with a deuteron target as functions of $(\sum p_T^2)^{\mathrm{min}}$, with the additional condition that both hadron p_T values are above 0.5 GeV. The threshold on this sum of the squares of the hadron p_T is varied in the range from 1.0 to 4.0 GeV^2. In Fig. 7.5 again these asymmetries are displayed for the data sets obtained in 1996 and 1997 separately.

In both cases, the two asymmetries based on the 1996 and 1997 data, respectively, are merged into a single asymmetry 1996/97 according to the error-weighted average (cf. section 4.7.4), as has been previously done in chapter 6.

The statistical uncertainties for the proton are significantly larger than for the deuteron, which as a consequence of the differences (by about a factor of 3) in statistics was to be expected. There appears to be a trend towards negative values of the asymmetry at large p_T cuts for both methods, at least for the more significant deuteron data. Note that the data points in these plots are not uncorrelated in the sense that they represent successive subsets.

7.3 Interpretation with PYTHIA MC

In this section, the process fractions (sections 7.3.1), the hard signal asymmetry and the background asymmetries (section 7.3.2) as extracted from the PYTHIA MC are presented. This information is then used to extract the gluon polarization from the data asymmetries (section 7.3.3). Finally, various systematic studies done on the extraction of the gluon polarization are summarized (section 7.3.4). (A detailed list of PYTHIA MC specifications and a discussion of the treatment of the asymmetries are given in appendix A.2 and B.1)

7.3.1 Process fractions

In Fig. 7.6 the process fractions, as obtained from the PYTHIA MC simulations for a proton target, are plotted. The upper half of the plots shows the results for the five background processes (DIS, QCDC, low_pt, VMD and anom_q, cf. 5.1.4), while in the lower half those for the two signal processes (PGF, anom_g, cf. 5.1.4) are presented. The process fractions are displayed against $(p_T^{h2})^{\mathrm{min}}$ for method 1 on the left, and against $(\sum p_T^2)^{\mathrm{min}}$ for method 2 on the right. The process fractions for a deuteron target are essentially the same and not shown here.

The PGF fractions rise with increasing p_T cut, reaching up to 35% and 30%, respectively, for the two methods. The anom_g fractions show a similar behaviour, reaching up to 20%

[2] The data for the years 1996 and 1997 are presented separately in order to investigate possible systematic differences for the extraction of the gluon polarization in section 7.3.4.

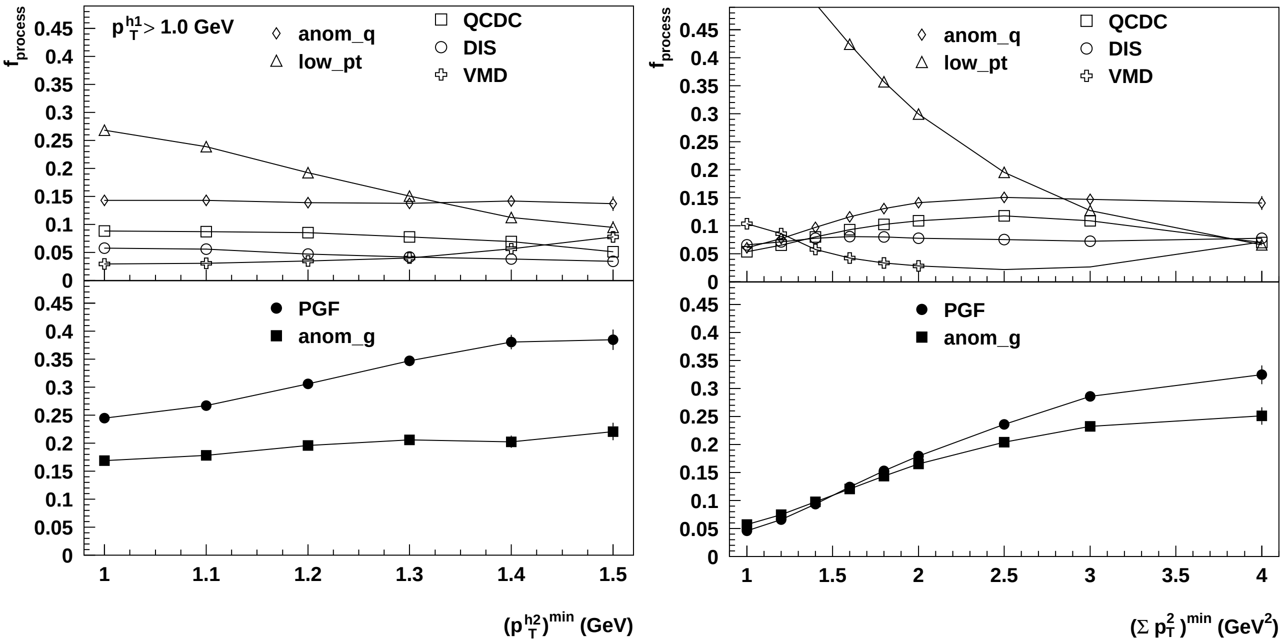

Figure 7.6: *Process fractions vs. $(p_T^{h2})^{\min}$ (left) and $(\sum p_T^2)^{\min}$ (right) for the five background processes DIS, QCDC, low_pt, VMD and anom_q (upper part) and for the two signal processes PGF and anom_g (lower part) for any charge hadron pairs in photoproduction obtained from PYTHIA MC on a proton target.*

and 25%, respectively. The three background processes DIS, QCDC and VMD do not exceed 10% for either method, while the two background processes anom_q and low_pt show considerably higher fractions in certain regions. The anom_q process fractions are about 15% across the whole range of $(p_T^{h2})^{\min}$ for method 1, and increase with increasing $(\sum p_T^2)^{\min}$ from values of about 5% to a maximum of about 15% for method 2, while the low_pt process fractions decrease with increasing p_T cut from values of above 25% and 50%, respectively, down to below 10%.

7.3.2 Hard signal asymmetry and background asymmetries

Fig. 7.7 shows the average hard process asymmetries for PGF and anom_g processes, both individually and combined into one signal process, as functions of $(p_T^{h2})^{\min}$ for method 1 on the left and of $(\sum p_T^2)^{\min}$ for method 2 on the right, as determined from the PYTHIA MC simulations for a proton target. Again, the results obtained from the PYTHIA MC on a deuteron target are not displayed as they are essentially identical.
The dependence of the average hard process asymmetry on the p_T-cut is negligible for the separate PGF and anom_g processes. The average hard PGF process asymmetry amounts to about -0.9, while the average hard anom_g process asymmetry is about 0.4. For the combined average hard signal asymmetry this adds up to about -0.4 across the whole range of $(p_T^{h2})^{\min}$ for method 1, and to about -0.2 to -0.4 with increasing $(\sum p_T^2)^{\min}$ for method 2. Due to its Q^2-dependence (with a minimum of -1 at $Q^2 \approx 0$ and increasing

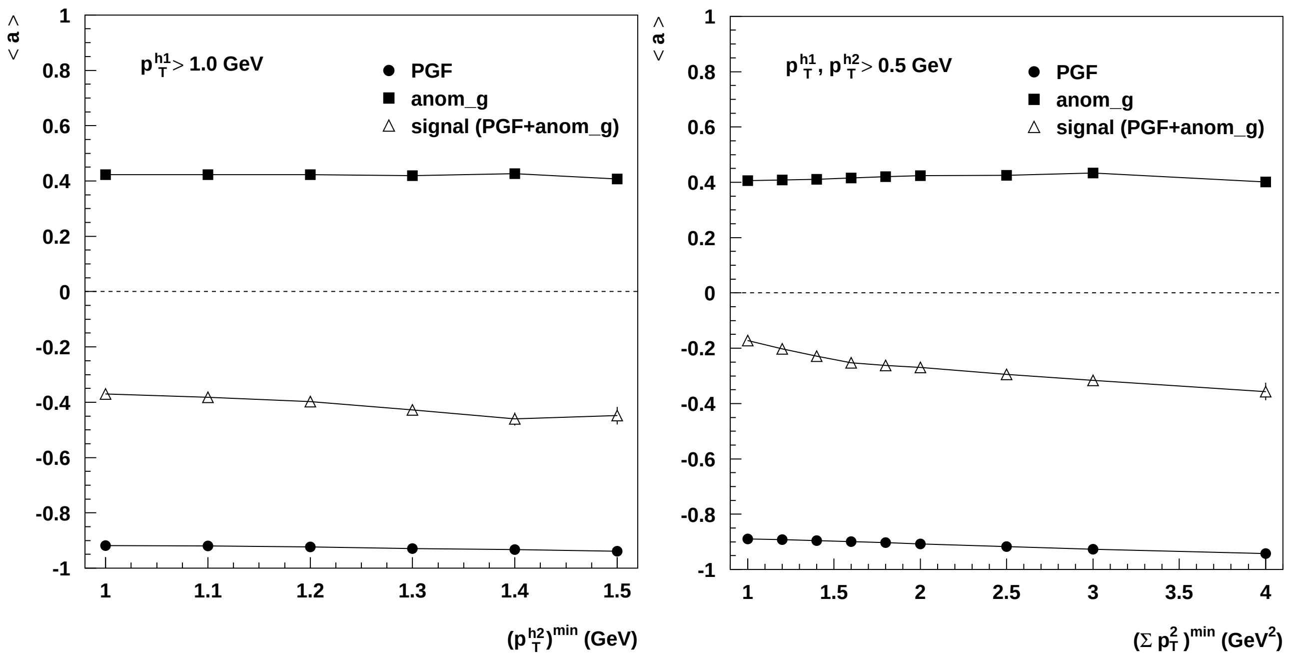

Figure 7.7: *Average hard process asymmetry vs.* $(p_T^{h2})^{\min}$ *(left) and* $(\sum p_T^2)^{\min}$ *(right), for PGF, anom_g and both combined for any charge hadron pairs in photoproduction obtained from PYTHIA MC on a proton target.*

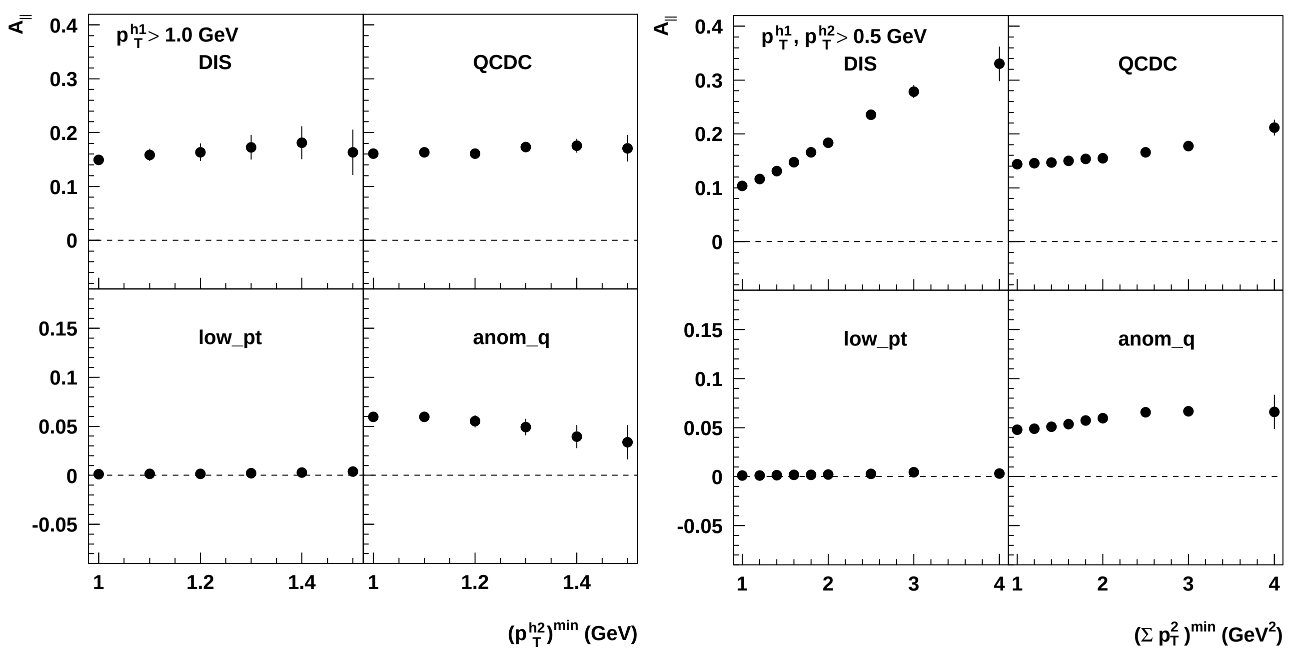

Figure 7.8: *Asymmetries* $A_\parallel$ *vs.* $(p_T^{h2})^{\min}$ *(left) and* $(\sum p_T^2)^{\min}$ *(right), for the background processes DIS, QCDC, low_pt and anom_q for any charge hadron pairs in photoproduction obtained from PYTHIA MC on a proton target.*

values for increasing Q^2), the hard PGF process asymmetry thus expectedly turns out to be more negative for the high-p_T hadron pairs photoproduction as compared to the single high-p_T hadron electroproduction (which is measured at a higher average Q^2).

The asymmetries of the background processes DIS, QCDC, low_pt and anom_q, as extracted from the PYTHIA MC on a proton target, are displayed in Fig. 7.8, again as functions of $(p_T^{h2})^{\min}$ for method 1 on the left, and of $(\sum p_T^2)^{\min}$ for method 2 on the right. Once again, the asymmetry from the VMD processes is set equal to zero, and is therefore not shown here. The DIS and QCDC asymmetries are positive and rise with $(\sum p_T^2)^{\min}$ for method 2, while the low_pt asymmetries are basically zero across the whole range independently of the method. The anom_q asymmetries are positive and not very dependent on the p_T cut. The results for the deuteron target MC are not shown here, but as expected the background asymmetries are smaller in that case.

7.3.3 The gluon polarization

From the measured asymmetries and the PYTHIA MC simulations presented in the previous sections, the gluon polarization can now be extracted. Before this is done, the sensitivity of the asymmetries to different values of the gluon polarization is studied. The applicability of the PYTHIA model, augmented with external asymmetry weights, to describe the measured asymmetries is investigated. In particular, PYTHIA asymmetries are calculated with three different assumptions for the gluon polarization, $\Delta G/G = -1, 0, +1$. In Fig. 7.9, these MC results are compared with the measured asymmetries vs. $(\sum p_T^2)^{\min}$ for high-p_T hadron pairs on a proton and a deuteron target. With increasing values of $(\sum p_T^2)^{\min}$ the MC asymmetries for the various $\Delta G/G$ assumptions become more clearly

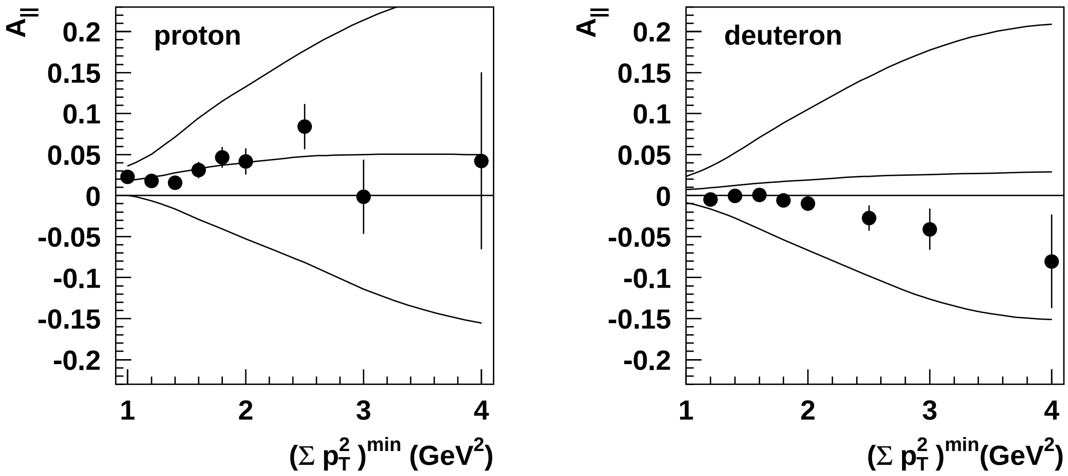

Figure 7.9: *The measured asymmetries vs. $(\sum p_T^2)^{\min}$ for hadron pairs in photoproduction on the proton (left) and the deuteron (right) target overlaid with the MC asymmetries determined for three different assumptions of the gluon polarization, $\Delta G/G$=-1 (upper line), $\Delta G/G$=0 (middle line), $\Delta G/G$=+1 (lower line).*

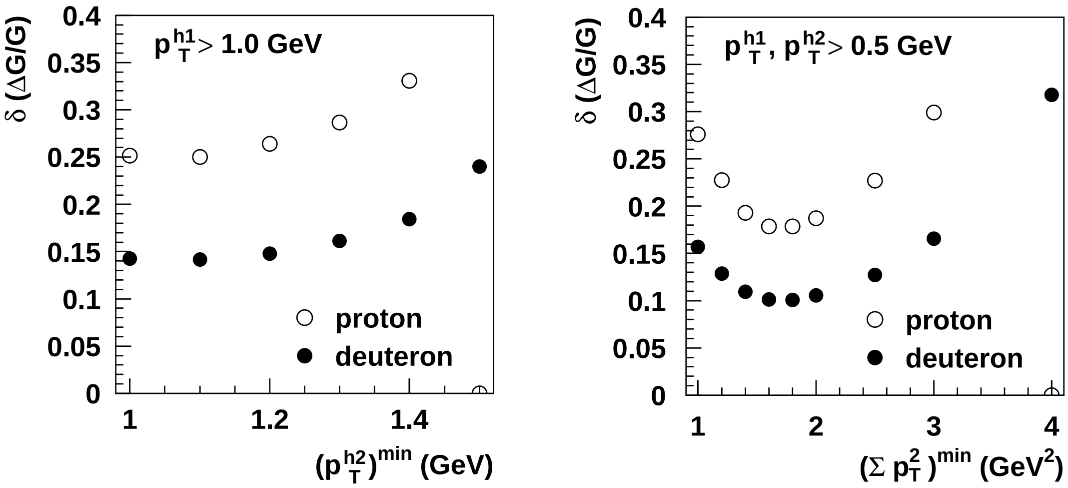

Figure 7.10: *The (approximated) statistical uncertainty on $\Delta G/G$ extracted from hadron pairs in photoproduction as a function of the $(p_T^{h2})^{\min}$ (left) and the $(\sum p_T^2)^{\min}$ (right) for the proton (open symbols) and the deuteron (closed symbols) target.*

separated, as a direct consequence of the signal fractions increasing from about 10% to 60%. Across the whole range of $(\sum p_T^2)^{\min}$ from 1 to 4 GeV^2 the measured asymmetries lie well inside the band of values spanned by the MC asymmetries for the two extreme values of the gluon polarization. This proves once again that the PYTHIA model with the externally built-in asymmetry weights is convincingly applicable. Furthermore, at any value of $(\sum p_T^2)^{\min}$ in this range, the statistical uncertainties on the measured asymmetries are significantly smaller than the spread of MC asymmetries for the different gluon polarization assumptions. It is therefore concluded that the gluon polarization can in principle be extracted at any $(\sum p_T^2)^{\min}$ between 1 and 4 GeV^2. Fig. 7.9 qualitatively suggests that the (statistically less significant) proton data could be compatible with a zero value for the gluon polarization, whereas the deuteron data appear to favour positive values.

To extract the gluon polarization with maximal significance, the optimum value for the threshold on p_T which yields the smallest statistical uncertainty has to be determined. According to section 5.2 this uncertainty can be approximated by the first term of Eq. (5.12), which is determined by the signal fraction, the average hard signal asymmetry, and the statistical uncertainty on the data asymmetry. Fig. 7.10 displays the (approximated) statistical uncertainty on the gluon polarization as a function of the p_T-cut for the two methods. In both cases the function displays a minimum. For method 1 (two separate p_T-cuts on the two hadrons), the statistical uncertainty on the extracted gluon polarization is minimized if the p_T of each hadron is required to be larger than 1.0 GeV. For method 2 (combined p_T-cut on the two hadrons), a minimum of the statistical uncertainty on the extracted gluon polarization is achieved for $(\sum p_T^2)^{\min} = 1.6$ GeV^2. One should keep in mind that the optimization for the gluon polarization extraction is at this stage exclusively based on the statistical uncertainty. Studies in the following section provide an estimate also of the systematic uncertainties. Only then can the combined

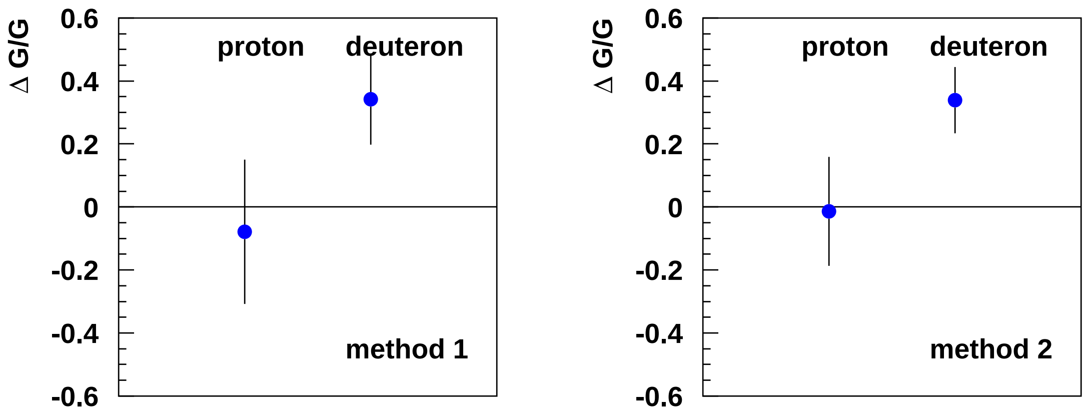

Figure 7.11: *$\Delta G/G$ extracted from the measured asymmetries and PYTHIA MC on the proton and the deuteron target for any charge hadron pairs in photoproduction at $p_T^{h1}, p_T^{h2} > 1.0$ GeV (left) and at $(p_T^{h1})^2 + (p_T^{h2})^2 > 2.0$ GeV^2, $p_T^{h1}, p_T^{h2} > 0.5$ GeV (right).*

statistical and systematic uncertainties be minimized. These studies show that some of the systematic uncertainties decrease with increasing $(\sum p_T^2)^{\min}$. While the minimum of the statistical uncertainty is rather flat, i.e. the statistical uncertainty increases only by about 1% upon shifting the $(\sum p_T^2)^{\min}$ value by some 0.1 GeV with respect to the minimum, the systematic uncertainty decreases significantly upon this shift. Therefore, the final choice for the optimized value for method 2 is $(\sum p_T^2)^{\min} = 2.0$ GeV^2.

In the following, the gluon polarization is extracted from the data at these minima for either method. Note that at their respective minima, the second method yields a statistical uncertainty slightly smaller than the first.

In Fig. 7.11 the values of $\Delta G/G$ and their statistical uncertainties as extracted from the measured asymmetries and the PYTHIA MC information on the proton and the deuteron target are shown. The left panel gives the results when cutting separately on the two hadron p_T, namely p_T^{h1} and $p_T^{h2} > 1.0$ GeV. The right panel represents the results when using a combined p_T-cut, namely $(p_T^{h1})^2 + (p_T^{h2})^2 > 2.0$ GeV^2 and in addition $p_T^{h1}, p_T^{h2} > 0.5$ GeV. The average gluon momentum fraction at which the gluon polarization is extracted according to PYTHIA is $\langle x_g \rangle \approx 0.20$ for both methods and both targets. The x_g-distributions cover a range from 0.08 to 0.6, with a half maximum width given by the range 0.1 to 0.23. The uncertainties for the proton are larger than for the deuteron due to statistics. The values for $\Delta G/G$ for the proton are slightly negative and consistent with zero for both methods, while the values for $\Delta G/G$ for the deuteron are positive. The results obtained with the two methods are entirely consistent, with a smaller statistical uncertainty on $\Delta G/G$ if the threshold is imposed on the combined p_T, i.e. method 2.

7.3.4 Systematic studies

The effects on the extracted gluon polarization of the various choices made for the parameters used in the extraction procedure are studied in this section. First, the dependence of the extracted gluon polarization on the values of the p_T-cuts, and the effect of splitting the proton data into two separate sets is investigated. Furthermore, the same series of systematic studies as carried out for the single high-p_T hadrons in electroproduction, discussed in the previous chapter, is performed for the high-p_T hadron pairs in photoproduction, i.e. different treatments of the low_pt background asymmetries, different polarized parton distribution functions and different PYTHIA model parameters and fragmentation tunes are considered.

Variation of p_T-cuts

In the following, the gluon polarization is extracted at different values of the lower thresholds on p_T. As observed in Fig. 7.6 in section 7.3.1, the process fractions vary with this threshold. This implies not only that the (total) signal and (total) background fractions vary, but also that the composition of the background changes significantly with p_T. Studying the dependence of the extracted gluon polarization on the p_T-cut therefore provides information on the stability of the extracted gluon polarization values with varying process fractions. This is done for both methods, namely separate lower thresholds on p_T for both hadrons (method 1), and a combined lower threshold on $(p_T^{h1})^2 + (p_T^{h2})^2$ (method 2). For method 1 in the range of 1.0 to 1.5 GeV for $(p_T^{h2})^{\text{min}}$, the signal fraction varies from about 40% to about 60% while especially the low_pt background process fraction decreases from about 25% to about 10%. For method 2 the range in $(\sum p_T^2)^{\text{min}}$ has been chosen as 1.4 to 3.0 GeV^2, i.e. as a subset of the previously used range (from 1.0 to 4.0 GeV^2), in order to exclude regions with either too low a signal process fraction or too low statistics of the data. In this restricted range the signal fraction increases from about 20% to about 50% while the low_pt process fraction decreases from about 50% to about 10%. This constitutes sizable variations in the process fractions, especially of the not well-defined low_pt process. The average gluon momentum fraction for the extraction of the gluon polarization hardly varies across the whole range of p_T-cuts for either method and either target ($\langle x_g \rangle \approx 0.19$ to 0.22).

Fig. 7.12 and Fig. 7.13 display the extracted gluon polarization vs. the p_T cuts for method 1 and method 2, respectively. The left panels show the results for the proton target, and the right ones those for the deuteron target. The extracted gluon polarization for the deuteron target shows hardly any dependence on the p_T cut for method 1, and very little dependence for method 2. This represents a convincing stability of the extracted value of the gluon polarization over a wide range of p_T cut in which the signal process fractions as well as the low_pt process fractions change significantly. The results obtained for the proton, on the other hand, change more drastically when varying the p_T cut. Part or all of this behaviour can probably be attributed to statistical fluctuations [3] which due

[3] It should be explicitly mentioned that in Fig. 7.12 and Fig. 7.13 the data points are highly correlated

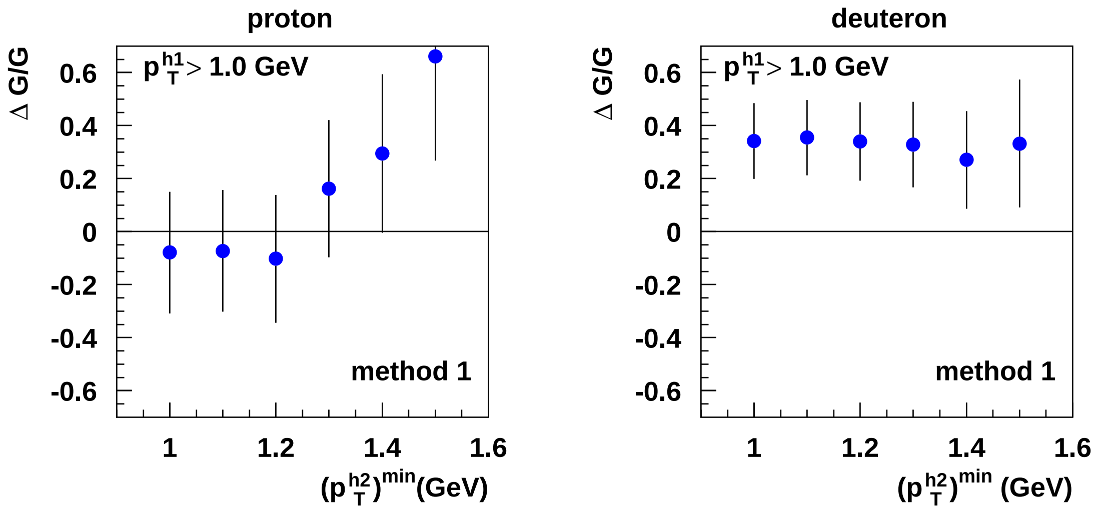

Figure 7.12: $\Delta G/G$ *extracted from the measured asymmetries and the PYTHIA MC on the proton (left) and the deuteron (right) target for hadron pairs in photoproduction at* $p_T^{h1} > 1.0$ *GeV as a function of* $(p_T^{h2})^{\min}$ *(method 1).*

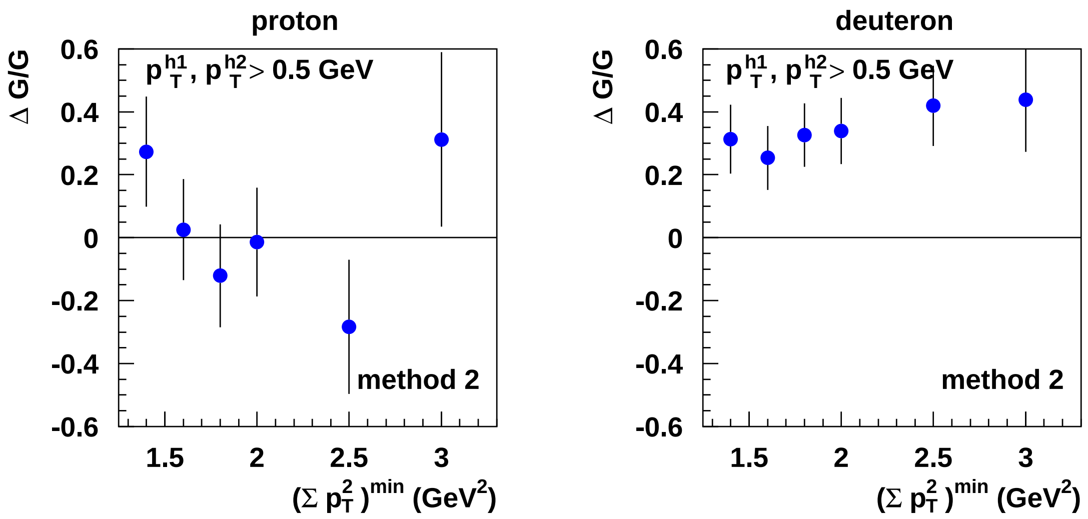

Figure 7.13: $\Delta G/G$ *extracted from the measured asymmetries and the PYTHIA MC on the proton (left) and the deuteron (right) target for hadron pairs in photoproduction at* $p_T^{h1}, p_T^{h2} > 0.5$ *GeV as a function of* $(\sum p_T^2)^{\min}$ *(method 2).*

to the much lower statistics of the proton data are expected to be higher. It still remains to be investigated whether other reasons can be found for the less smooth behaviour of the proton results.

(data represent subsequent subsets from left to right). Hence they will not show a statistical spreading typically expected from uncorrelated data.

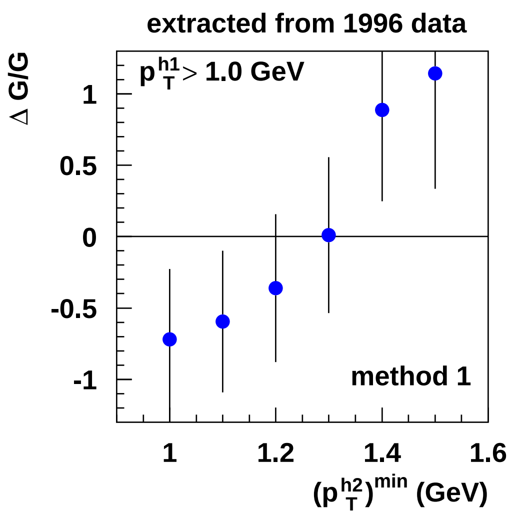

Figure 7.14: $\Delta G/G$ *extracted from the measured 1996 (left) and 1997 (right) asymmetries and the PYTHIA MC on the proton target for hadron pairs in photoproduction at* $p_T^{h1} > 1.0$ *GeV as a function of* $(p_T^{h2})^{\min}$ *(method 1).*

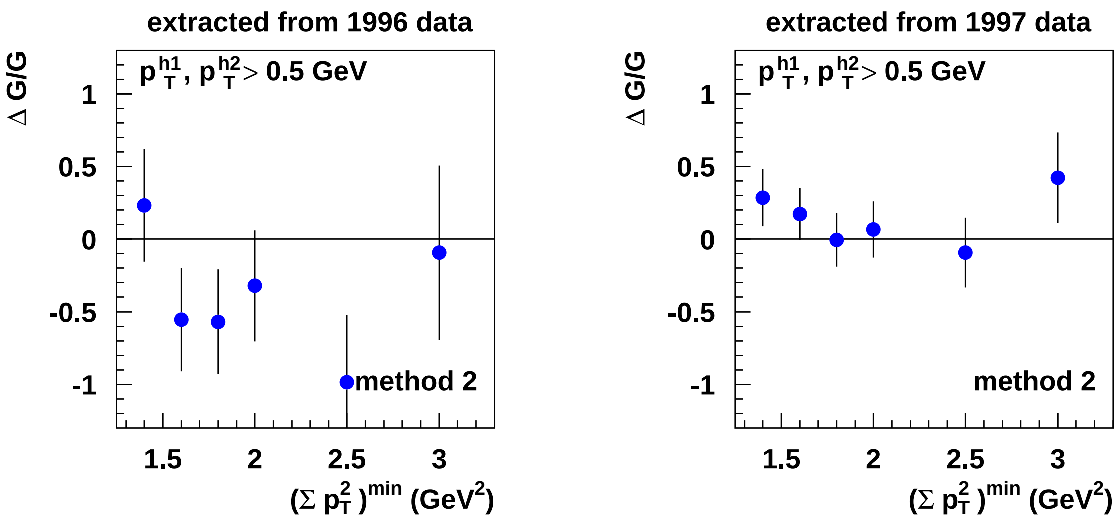

Figure 7.15: $\Delta G/G$ *extracted from the measured 1996 (left) and 1997 (right) asymmetries and the PYTHIA MC on the proton target for hadron pairs in photoproduction at* $p_T^{h1}, p_T^{h2} > 0.5$ *GeV as a function of* $(\sum p_T^2)^{\min}$ *(method 1).*

Split of the proton data into two independent sets

Fig. 7.14 and Fig. 7.15 show the results for the gluon polarization extracted separately for the datasets of 1996 and 1997. The behaviour of the results versus p_T-cut is clearly different for these two years. The variation of the extracted gluon polarization with p_T-cut is larger for the year 1996 than for the combined data set, while it is small for the year 1997. This suggests that the 1996 dataset might contain a hitherto unidentified effect. However, investigating these differences has not produced any compelling reasons to exclude the 1996 dataset from the proton data. The statistical limitations of the data (cf. appendix Tab. D.4 and Tab. D.6) preclude further investigations (e.g. further subdividing the data into separate data taking periods, separate detector halves etc.). Therefore, it was decided to use the combined 1996+1997 dataset. Nevertheless, this study suggests that the deuteron data are, not only for their higher statistical significance, more trustworthy than the proton data.

Treatment of low_pt processes

Since the low_pt process fractions are considerably larger for the high-p_T hadron pairs in photoproduction than for the single high-p_T hadrons in electroproduction (which was systematically studied in the previous chapter), the effect of different treatments of the low_pt processes on the extracted gluon polarization might be expected to be more sizable as well. Again, three different treatments are considered (cf. appendix B.1 for details), namely modelling the low_pt background asymmetry as

- $A_1^{low\_pt} = 0$ (dilution),
- as the charge weighted sum of the polarized over unpolarized PDFs in the x and Q^2 range where the PDFs are available ($A_1^{low\_pt} = g_1/F_1$ for $x > x_{min}$ and $Q^2 > Q^2_{min}$ with $x_{min} = 10^{-5}$ and $Q^2_{min} = 0.22$ GeV^2, $A_1^{low\_pt} = 0$ otherwise); this method has been used in the standard extraction of the gluon polarization presented above,
- as the parametrization of the experimental data for A_1 in the whole x and Q^2 range.

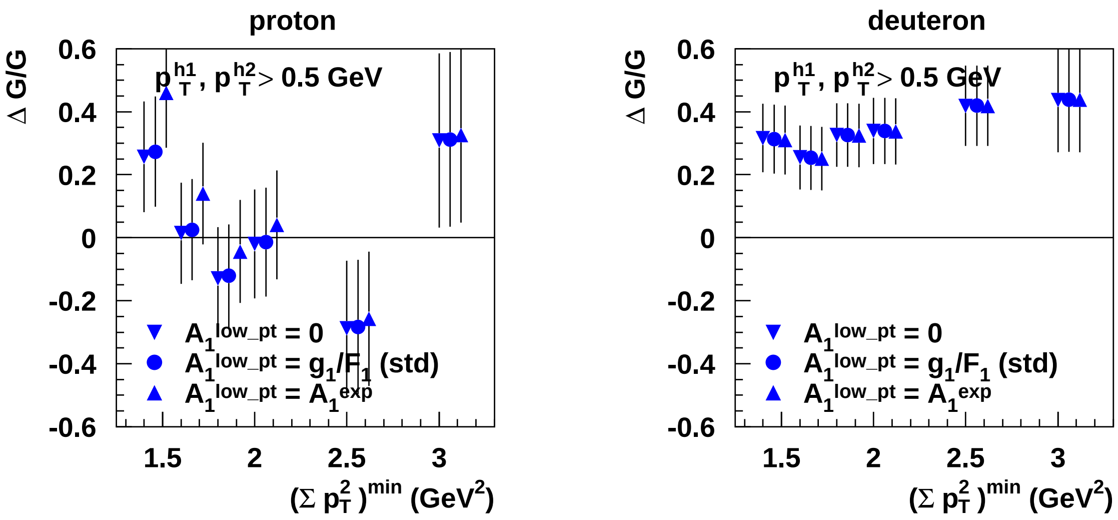

Figure 7.16: *$\Delta G/G$ extracted with three different treatments of the MC background asymmetry from low_pt processes, on the proton (left) and the deuteron (right) target for hadron pairs in photoproduction at $p_T^{h1}, p_T^{h2} > 0.5$ GeV as a function of $(\sum p_T^2)^{min}$.*

In Fig. 7.16 the results for the gluon polarization are plotted for these three alternatives in calculating the low_pt background asymmetry. Only the results for method 2 (cut on the combined p_T) are displayed. Varying $(\sum p_T^2)^{\rm min}$ spans a wider variation of process fractions, and therefore shows more evidently the differences in effects for different p_T cuts. The effects versus $(p_T^{h2})^{\rm min}$ for method 1 (two separate p_T cuts) are basically within the range of effects shown for the three largest values of $(\sum p_T^2)^{\rm min}$ of method 2. All further studies are conducted for method 2 only.

The results for the first two treatments of the low_pt background essentially do not differ. This is due to the fact that for the second treatment only in less than 10% of the low_pt events Q^2 exceeds the minimum where the asymmetry is determined by the non-zero PDFs rather than set to zero. Hence, for more than 90% of the events the asymmetry is set to zero, corresponding to a dilution. The difference between the results of treating low_pt as a dilution or as A_1^{exp} for the whole (x,Q^2) range on the other hand is more pronounced for the proton target, especially at small $(\sum p_T^2)^{\rm min}$. But this difference decreases with increasing $(\sum p_T^2)^{\rm min}$, which is related to the decreasing low_pt fraction. For the deuteron target the effect is again negligible which is due to the smaller size of the corresponding A_1-parametrization.

Polarized PDFs of the photon

Similarly to the low_pt process fractions, also the fractions of the anomalous processes are much higher for the high-p_T hadron pairs in photoproduction (where they can reach up to 40%) than for the single high-p_T hadrons in electroproduction (where they are

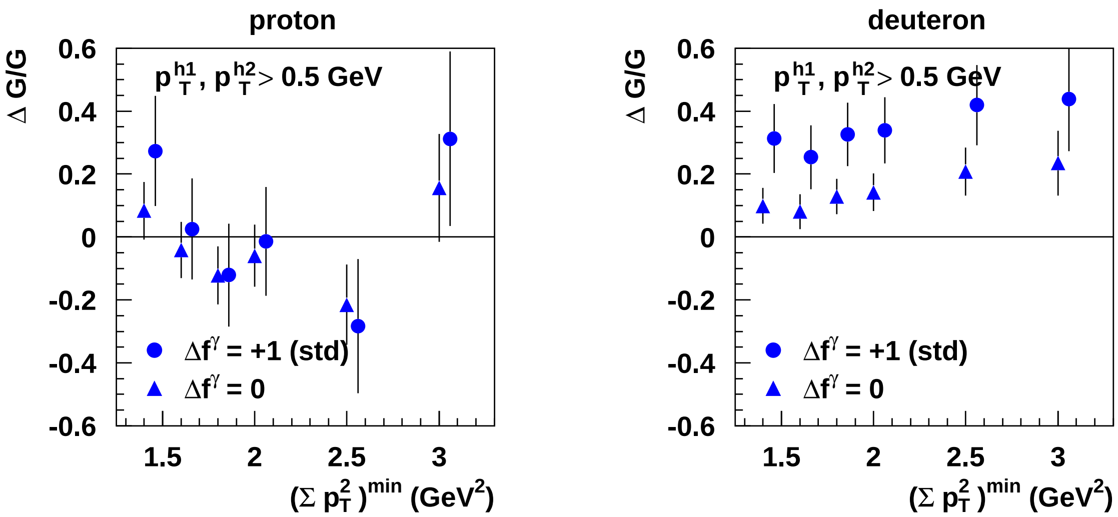

Figure 7.17: *$\Delta G/G$ extracted with two different assumptions for the polarized photon PDFs for the MC asymmetries from anomalous processes on the proton (left) and the deuteron (right) target for hadron pairs in photoproduction at $p_T^{h1}, p_T^{h2} > 0.5$ GeV as a function of $(\sum p_T^2)^{\rm min}$.*

below 20%) (cf. Fig. 7.6 and Fig. 6.14). Therefore, the effect of different assumptions for the polarized photon parton distribution functions on the extracted gluon polarization is expected to be non-negligible in this case. The two different assumptions considered are again $\Delta q^\gamma = \Delta g^\gamma = 0$ (no polarization of partons in the photon, i.e. the anomalous processes are treated as a dilution both to the signal and the background), and $\Delta q^\gamma = \Delta g^\gamma = +1$ ('maximal' polarization, implying a positive contribution of the anom_g processes to the hard signal asymmetry as well as a positive contribution of the anom_q processes to the background asymmetry, as used in the standard extraction of the gluon polarization presented above) (cf. appendix B.1 for details). The results for the gluon polarization obtained for these two assumptions are shown in Fig. 7.17, again only for method 2. The effect is sizable, both for the proton and the deuteron target; one should bear in mind that it depends strongly on the absolute value of $\Delta G/G$.

Polarized PDFs of the nucleon

Next, the effect of different polarized PDFs of the nucleon is studied. These enter the calculation of the asymmetry weights for the background processes and can consequently influence the extracted gluon polarization. As in the previous chapter, two sets of polarized PDFs are used, namely the leading order GRSV 2000 valence scenario (as used for the standard extraction of the gluon polarization presented above) and the leading order GS set B. Fig. 7.18 displays the results for the extracted gluon polarization using these two different sets; again only results for method 2 are shown. The effect is small and of comparable size for the proton and the deuteron. The difference between the extracted gluon polarization for the two different PDF sets decreases very slightly with increasing $(\sum p_T^2)^{\min}$, which can be explained by the decrease of the total background contribution,

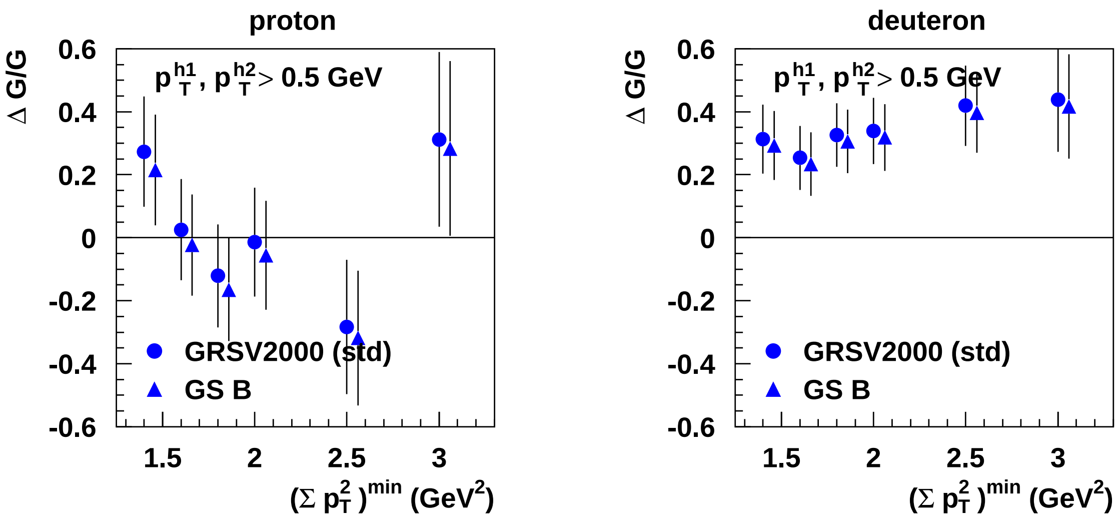

Figure 7.18: *$\Delta G/G$ extracted with two different sets of polarized PDFs for all background processes, on the proton (left) and the deuteron (right) target for hadron pairs in photoproduction at $p_T^{h1}, p_T^{h2} > 0.5$ GeV as a function of $(\sum p_T^2)^{\min}$.*

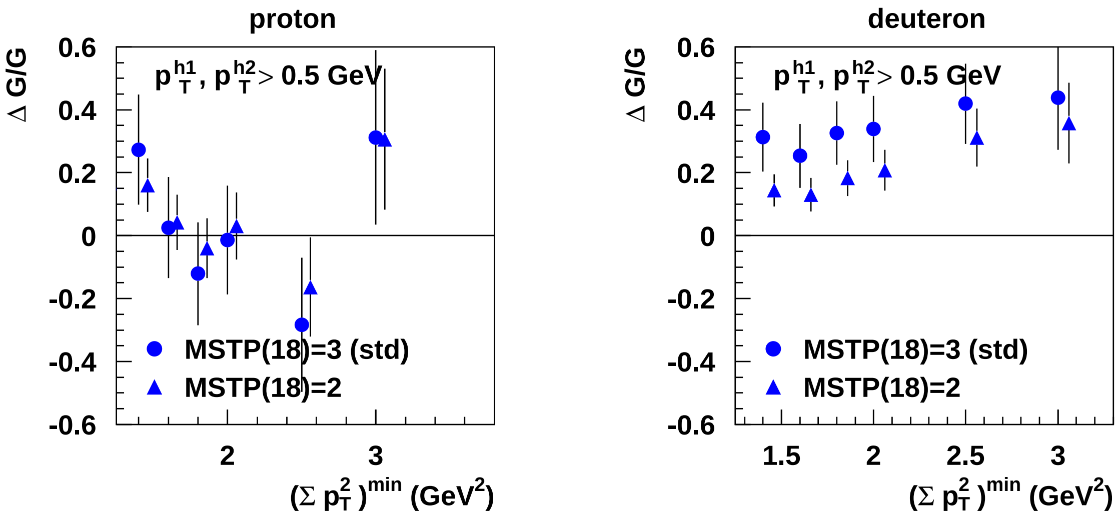

Figure 7.19: *$\Delta G/G$ extracted with two different settings of the PYTHIA parameter MSTP(18), on the proton (left) and the deuteron (right) target for hadron pairs in photoproduction at $p_T^{h1}, p_T^{h2} > 0.5$ GeV as a function of $(\sum p_T^2)^{\min}$.*

implying a decreasing sensitivity to the PDFs.

PYTHIA model parameters

As for single high-p_T hadron electroproduction, also for high-p_T hadron pairs photoproduction only one PYTHIA model parameter is varied to study its effect on the gluon polarization. It should be recalled that the parameter MSTP(18) (described in detail in section 5.1.4) determines the cutoff scale for the direct processes. For the default choice MSTP(18)=3 (as used for the standard extraction of the gluon polarization presented above), where the lower cutoff $k_{\perp,min} \approx 1.4$ GeV, the process fractions for PGF and QCDC are smaller while the fractions for the anomalous processes are larger than for MSTP(18)=2, where $k_{\perp,min} = 0.5$ GeV. The comparison of the results for the gluon polarization obtained with these two settings of the PYTHIA parameter MSTP(18) is presented in Fig. 7.19. Similar to the results for single high-p_T hadron electroproduction, the effect is again sizable. However, it decreases slightly with increasing $(\sum p_T^2)^{\min}$. At larger $(\sum p_T^2)^{\min}$, the signal process fractions are larger and therefore slight changes in these fractions have a smaller impact on the extracted gluon polarization.

Fragmentation tunes

As a last systematic study the influence of different fragmentation tunes on the extracted gluon polarization is investigated. As described in detail in sections 5.1.2 and 6.4.4 some of the most influential parameters for the extracted gluon polarization are the ones which define how much transverse momentum the hadrons acquire in the fragmentation. In the fragmentation tune 2004c these parameters are set to PARJ(23)=0.01 and

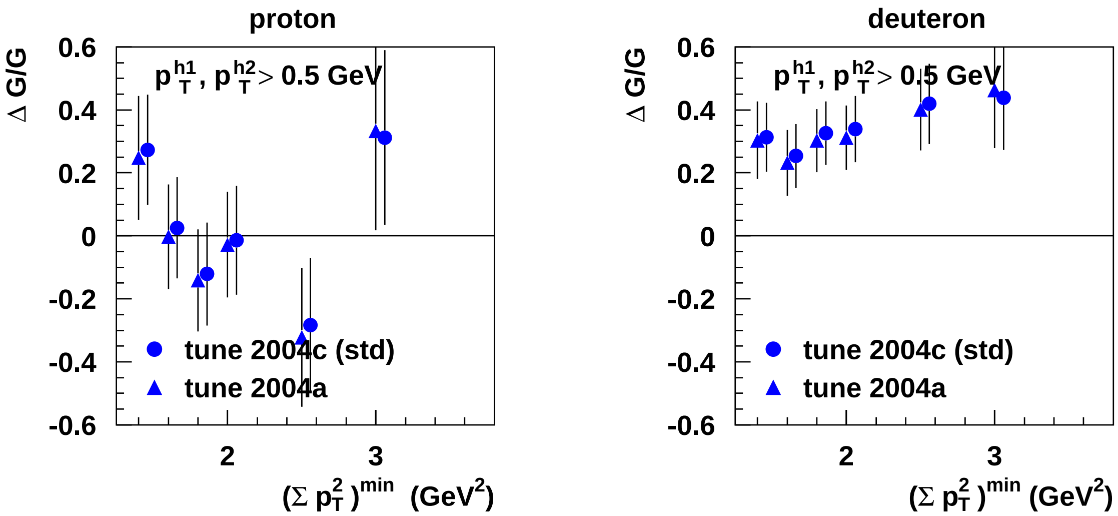

Figure 7.20: $\Delta G/G$ *extracted for different fragmentation tunes, on the proton (left) and the deuteron (right) target for hadron pairs in photoproduction at* $p_T^{h1}, p_T^{h2} > 0.5$ *GeV as a function of* $(\sum p_T^2)^{\min}$.

PARJ(24)=2.0, while in tune 2004a they are set to PARJ(23)=0.03 and PARJ(24)=2.5. In the latter case on average a larger transverse momentum $p_{T,F}$ is acquired by the hadrons in the fragmentation which consequently influences the process fractions (DIS and low_pt fractions increase, PGF, QCDC and anomalous fractions decrease). In Fig. 7.20 the results for the gluon polarization using the tune 2004c (as used for the standard extraction of the gluon polarization presented above) and the tune 2004a are compared. Since it is very time-consuming to generate sufficient MC statistics for high-p_T hadron pairs in photoproduction for many settings of MC parameters, due to time-constraints no PYTHIA MC simulation is available yet for the fragmentation tune 2004d, as was available for the single high-p_T hadron electroproduction. The effect of different fragmentation tunes on the extracted gluon polarization is very small. One notices that it is smaller than for single high-p_T hadron electroproduction which is due to the fact that in the latter case the DIS process plays a much bigger role, hence the changes in the DIS process fraction are larger, and thus the results are influenced more strongly.

7.4 Summary of results

To conclude this chapter, a final value of the p_T-cut is chosen for an optimized extraction of the gluon polarization. The results for the extracted gluon polarization and their uncertainties are summarized.

The two different methods for cutting on the transverse momenta of the hadrons, either requiring the two p_T values separately above a certain threshold (method 1) or requiring the combination $(p_T^{h1})^2 + (p_T^{h2})^2$ to exceed a certain threshold together with each p_T individually above 0.5 GeV (method 2), have yielded consistent results for all

	proton	deuteron
$\Delta G/G$	-0.014	0.339
$\delta(\Delta G/G)^{stat.}$	0.173	0.106
$\delta(\Delta G/G)^{exp.syst.}$	0.025	0.004

Table 7.2: *Results for $\Delta G/G$ including statistical and experimental systematic uncertainties, for high-p_T hadron pairs in photoproduction on the proton and the deuteron target using the PYTHIA MC.*

$\delta(\Delta G/G)^{mod.dep.syst.}$	proton	deuteron
$A_1^{low\_pt} = 0$	-0.006	-0.0001
$A_1^{low\_pt} = A_1^{exp}$	+0.055	-0.001
$\Delta f^{\gamma} = 0$	-0.046	-0.197
GS B	-0.041	-0.021
MSTP(18)=2	+0.045	-0.131
tune 2004a	-0.014	-0.027

Table 7.3: *List of model dependent systematic uncertainties, for high-p_T hadron pairs in photoproduction on the proton and the deuteron target using the PYTHIA MC.*

studies performed. Since the resulting statistical uncertainties on the gluon polarization are smaller for method 2 than for method 1 (cf. Fig. 7.10), only the results of method 2 are further considered.

Tab. 7.2 and Tab. 7.3 summarize the final results for the extracted gluon polarization together with the statistical, experimental systematic, and model dependent systematic uncertainties. These results are obtained for high-p_T hadron pairs in photoproduction at $(p_T^{h1})^2 + (p_T^{h2})^2 > 2.0$ GeV^2 and $p_T^{h1}, p_T^{h2} > 0.5$ GeV for the proton and the deuteron target. As in the previous chapter, the statistical uncertainty is calculated according to Eq. (5.12), the experimental systematic uncertainty according to Eq. (5.13), and the model dependent systematic uncertainties are determined as the differences between the gluon polarizations from the varied and the standard extraction for each of the studies discussed in section 7.3.4.

A final discussion of the total model dependent systematic uncertainties and comparisons with the results for the single high-p_T hadrons in electroproduction from the previous chapter and the results from other experiments and theoretical calculations will be presented in the following chapter.

Chapter 8

Conclusions and outlook

In this final chapter of the thesis the results for the gluon polarization presented in the previous two chapters are compared and used for obtaining a best estimate for $\Delta G/G$ (section 8.1). This is supplemented by a comparison to existing data (section 8.2) and a discussion of the possible importance of higher-order theoretical calculations (section 8.3).

8.1 Results on the gluon polarization

The evaluation of the total model dependent systematic uncertainty requires a detailed discussion (section 8.1.1) before the results on the gluon polarization including all uncertainties can be presented (section 8.1.2), followed by suggestions for possible future improvements in assessing the model dependence (section 8.1.3).

8.1.1 The total model dependent systematic uncertainty

In order to carry out a complete evaluation of the total model dependence one has to compare the values of the gluon polarization extracted with different, independent MC models. This is clearly beyond the scope of the work presented in this thesis. For the photoproduction region, the PYTHIA MC is the only available Monte Carlo program able to simulate events at such low Q^2-values. There is no alternative available providing a comparably complete description of different processes, especially including non-perturbative ones. In the electroproduction region, the LEPTO MC could be considered as an alternative, but as discussed above it is limited to $Q^2 > 0.5$ GeV^2 and contains only the leading order DIS and the first order QCD processes QCDC and PGF. Ignoring these limitations, a comparison of the gluon polarization extracted with LEPTO and with PYTHIA for single high-p_T hadrons in electroproduction has shown that the results are consistent (cf. section 6.5). The differences between the values for the gluon polarization are mostly of the order of a few %, up to a maximum of 20% (in absolute values 0.01-0.10), depending on the targets and hadrons considered (cf. Tab. 6.5).

$\delta(\Delta G/G)^{mod.dep.syst.}$	electroproduction		photoproduction	
	proton	deuteron	proton	deuteron
linear sum	+0.378	+0.180	+0.100	+0.0
	-0.357	-0.102	-0.107	-0.377
quadratic sum	+0.290	+0.150	+0.071	+0.0
	-0.214	-0.097	-0.064	-0.239

Table 8.1: *Total model dependent systematic uncertainty on $\Delta G/G$, calculated as the linear and quadratic sum of the individual contributions, respectively, for single high-p_T hadron electroproduction and high-p_T hadron pair photoproduction, for both the proton and the deuteron target.*

Because of the above mentioned limitations of the LEPTO MC and since an alternative MC is only available for the electroproduction but not for the photoproduction regime, a different approach to estimating the model dependent systematic uncertainty is chosen in this thesis. Instead of comparing different MC models, the model dependent systematic uncertainties are estimated by successively varying a set of parameters within the single available model (PYTHIA augmented with external asymmetry weights).
As described in section 6.4.4 for single high-p_T hadron electroproduction and in section 7.3.4 for high-p_T hadron pair photoproduction, various systematic studies have been performed to estimate the effect on the extracted gluon polarization of varying certain parameters in the extraction procedure. For each of these studies, the model dependent systematic uncertainties are taken as the differences between the values of the gluon polarization from the varied and the standard extraction. As listed in Tab. 6.7 and Tab. 7.3, (in parts large) model dependent systematic uncertainties are seen to arise from the PYTHIA model and fragmentation parameters and from the assumptions on the asymmetries used in the extraction. The uncertainties listed represent a selection of systematic studies, incorporating what is feasible and what is thought to cause the largest variations, but this list is not proven to be exhaustive. These uncertainties are known to be (at least partially) correlated (e.g. varying PYTHIA model parameters alters the process fractions, but with altered process fractions the effect of varying the assumptions on the asymmetries is changed as well). To completely evaluate these correlations requires a full "parameter scan". However, it is very time-consuming to generate sufficient MC statistics, especially for high p_T hadron pairs in photoproduction, and a full correlation matrix can therefore not be evaluated within the scope of this thesis. The calculation of the total model dependent systematic uncertainty is therefore not unambiguous.
Two possible methods to address this problem are considered here, namely separately taking the linear sums over all positive and negative deviations, respectively (i.e. assuming all individual uncertainties to be correlated, possibly overestimating the total uncertainty), or separately taking the quadratic sum over all positive and negative deviations, respectively (i.e. assuming the individual uncertainties to be completely uncorrelated and given by Gaussian-distributions, definitely underestimating the total uncertainty[1]). Tab. 8.1 gives

[1]If the error distributions were truly Gaussian, one would, strictly speaking, have to take the quadratic

the values of the total model dependent systematic uncertainties calculated according to these two approaches for the single high-p_T hadron electroproduction and the high-p_T hadron pair photoproduction[2]. To provide a conservative estimate, the linear sum of the individual contributions is chosen as the total model dependent systematic uncertainty. This choice is made because the individual uncertainties are partially correlated and since some of them are definitely not given by Gaussian-distributions (e.g. the PYTHIA model parameter MSTP(18) represents a switch and can thus take only discrete values, making the uncertainty distribution clearly non-Gaussian). Once again it should be emphasized that the total model dependent systematic uncertainty is not derived by applying different MC models, but could only be estimated by varying a set of parameters within the PYTHIA MC and the extraction procedure.

8.1.2 Overall results and consistency

In this section the results for the gluon polarization $\Delta G/G$ derived from single high-p_T hadrons in electroproduction are compared to those from the high-p_T hadron pairs in photoproduction, the consistency of the results is investigated, and the averages of the results for the proton and the deuteron target are calculated.

The results for the gluon polarization from single high-p_T hadrons in electroproduction, as summarized in Tab. 6.6, are for the proton given by

$$\Delta G/G = -0.583 \pm 0.322(\text{stat.}) \pm 0.114(\text{exp.syst.})^{+0.378}_{-0.357}(\text{mod.dep.syst.}) \ , \tag{8.1}$$

and for the deuteron by

$$\Delta G/G = -0.266 \pm 0.195(\text{stat.}) \pm 0.031(\text{exp.syst.})^{+0.180}_{-0.102}(\text{mod.dep.syst.}) \ . \tag{8.2}$$

These results have been obtained at an average gluon momentum fraction $\langle x_g \rangle \approx 0.23$, and an average scale $\langle \hat{Q}^2 \rangle \approx 1.8$ GeV^2.
The results from high-p_T hadron pairs in photoproduction, as summarized in Tab. 7.2, are for the proton given by

$$\Delta G/G = -0.014 \pm 0.173(\text{stat.}) \pm 0.025(\text{exp.syst.})^{+0.100}_{-0.107}(\text{mod.dep.syst.}) \ , \tag{8.3}$$

and for the deuteron by

$$\Delta G/G = \ 0.339 \pm 0.106(\text{stat.}) \pm 0.004(\text{exp.syst.})^{+0.0}_{-0.377}(\text{mod.dep.syst.}) \ . \tag{8.4}$$

In this case, the results have been obtained at an average gluon momentum fraction $\langle x_g \rangle \approx 0.20$, and an average scale $\langle \hat{Q}^2 \rangle \approx 1.4$ GeV^2.

---

sum over all contributions irrespective of sign. However, as the individual contributions are seen to be asymmetric, positive and negative distributions have separately been added to provide an optimistic estimate of the total uncertainty, to be compared with the conservative estimate based on the linear sum.

[2]The fact that for high-p_T hadron pair photoproduction on the deuteron all systematic deviations happen to be negative is an incidental consequence of the choices made for the standard extraction.

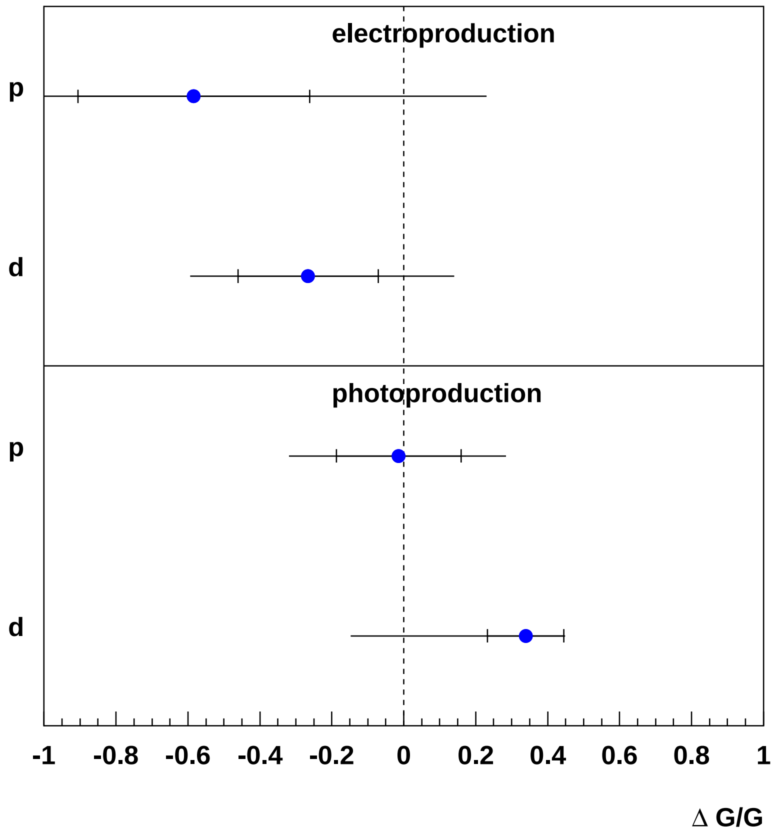

Figure 8.1: *$\Delta G/G$ extracted for single high-p_T hadron electroproduction (top) and high-p_T hadron pair photoproduction (bottom), each for the proton and the deuteron target. The systematic uncertainty is added linearly to the statistical uncertainty, separated by marks.*

In Fig. 8.1 the final results for the gluon polarization extracted for the single high-p_T hadron electroproduction and the high-p_T hadron pair photoproduction, for both the proton and the deuteron target, are presented. The total model dependent systematic and experimental systematic uncertainties are added linearly to the statistical uncertainty, separated by marks. This linear sum is again chosen to provide a conservative estimate (without further detailed studies, the total model dependent systematic uncertainty cannot be assumed to be Gaussian-distributed, therefore one cannot by default simply take their quadratic sum).

The results obtained separately for the proton and the deuteron target are for both analyses (electroproduction and photoproduction) consistent within the (large) uncertainties. The results for the proton and the deuteron target are combined using the error-weighted average, where the dominating weight is given by the deuteron, yielding an average for the gluon polarization from single high-p_T hadron electroproduction of

$$\Delta G/G = -0.35 \pm 0.17(\text{stat.}) \pm 0.05(\text{exp.syst.})^{+0.23}_{-0.17}(\text{mod.dep.syst.}) \,, \tag{8.5}$$

and from high-p_T hadron pair photoproduction of

$$\Delta G/G = \ 0.24 \pm 0.09(\text{stat.}) \pm 0.01(\text{exp.syst.})^{+0.01}_{-0.30}(\text{mod.dep.syst.}) \,. \tag{8.6}$$

Within the (large) uncertainties the results for single high-p_T hadron electroproduction and high-p_T hadron pair photoproduction are consistent. For single high-p_T hadron electroproduction the various uncertainties are considerably larger, therefore the measurement of the gluon polarization in this analysis channel is less significant than for the high-p_T hadron pair photoproduction. In this case, the extraction of the gluon polarization is limited by the very small signal process fraction of about 13%. (Recall that the statistical uncertainty is inversely proportional to the signal process fraction.) This limitation cannot simply be overcome by taking more data, but is inherent to the kinematic constraints of the HERMES experiment, which does not reach out to higher transverse momenta where the signal process fractions would be larger.

For high-p_T hadron pair photoproduction the result for the extracted gluon polarization is more significant. Here the signal process fractions is of the order of 35%, resulting in smaller statistical uncertainties. However, the systematic uncertainties are still large, reflecting a strong model dependence of the extraction method.

8.1.3 Possible future improvements in assessing the model dependence

The total model dependent systematic uncertainties stated in this thesis represent, according to present knowledge, the best (first) estimate of the model dependence of the extracted gluon polarization. It is beyond the scope of this thesis to investigate these uncertainties (including correlations etc.) in more detail. However, some improvements for future analyses can be suggested.

First of all, some of the individual contributions to the model dependent systematic uncertainty might be reducible, e.g. the systematic uncertainty arising from different assumptions for the polarized photon PDFs. Instead of assuming constant maximal values of $\Delta f^\gamma = 0$ or $+1$ over the whole x-range for the partons in the photon, a parametrization vs. x from [118, 119], which has recently become available, could be applied. Furthermore, the correlations between the individual systematic uncertainties could be investigated in more detail and might be estimated and represented in a correlation matrix. This might allow to replace the linear sum of the individual contributions by the sum of the contributions according to their covariances in order to arrive at a more precise estimate of the total model dependent systematic uncertainty. Finally, one could consider to treat the different systematic uncertainties listed above not on an equal footing. It could be argued that e.g. the uncertainty arising from different settings of the PYTHIA model parameter MSTP(18) (which can only be switched between two settings but not varied continuously) is more fundamental than the uncertainties arising from different treatments of the asymmetries in the extraction. One might therefore decide to separately state the gluon polarization extracted for both settings and combine only the remaining systematic uncertainties into a total systematic uncertainty for each setting.

8.2 Comparison with existing data

In [53], the gluon polarization is extracted from the same HERMES data utilizing inclusive high-p_T hadron photoproduction. This leads to a value of the gluon polarization of

$$\Delta G/G = 0.10 \pm 0.04(\text{stat.}) \pm 0.01(\text{exp.syst.})^{+0.07}_{-0.14}(\text{mod.dep.syst.}) \ ,$$

at $\langle x_g \rangle = 0.15$ and $\langle \hat{Q}^2 \rangle = 1.3$ GeV^2. This result is based on the same extraction procedure as used in this thesis, utilizing in principle the same PYTHIA MC program augmented with external asymmetry weights, but with somewhat different choices for the parameters in the standard extraction and also slight differences in the systematic studies. Keeping in mind these differences, the value for $\Delta G/G$ from [53] can be compared with the two values found in this work for single high-p_T hadron electroproduction and high-p_T hadron pair photoproduction; the three values are consistent within the uncertainties stated.

In a previous analysis of high-p_T hadron pair photoproduction published by the HERMES collaboration [46], a value of

$$\Delta G/G = 0.41 \pm 0.18(\text{stat.}) \pm 0.03(\text{exp.syst.}) \ ,$$

at $\langle x_g \rangle = 0.17$ and $\langle \hat{p}_T^2 \rangle = 2.1$ GeV^2 was extracted from the measured asymmetries on the proton target, using PYTHIA 5, a previous version of the MC generator. In that analysis, only the PGF, QCDC, and VMD processes were taken into account. No estimate of the model dependent systematic uncertainty was given at that time.

The gluon polarization extracted from high-p_T hadron pair photoproduction presented in this thesis supercedes the former analysis for the following reasons. In addition to the data taken with the proton target, also the data for the deuteron target are analyzed. The selection of high-p_T hadron pairs is optimized by replacing two separate p_T thresholds with one combined threshold for the sum of the squares of p_T. A more appropriate PYTHIA model and a much more elaborate method for extracting $\Delta G/G$ is used, which includes a more complete set of processes and a more sophisticated treatment of the asymmetries. Finally, a first estimate is made of the model dependent systematic uncertainty.

Recently, other measurements of $\Delta G/G$ also extracted from high-p_T hadron pairs have been reported by the SMC and the COMPASS experiment. From the SMC data, collected during the years 1993-1996 with a muon beam of 190 GeV and longitudinally polarized proton and deuteron targets, the gluon polarization has been evaluated as

$$\Delta G/G = -0.20 \pm 0.28(\text{stat.}) \pm 0.20(\text{syst.}) \ ,$$

at $\langle x_g \rangle = 0.07$ [51]. The analysis is limited to the region $Q^2 > 1$ GeV^2, and high-p_T hadron pairs are selected with a neural network at a PGF fraction of about 30%. The extraction of $\Delta G/G$ is done using the LEPTO MC.

From the COMPASS data, obtained during the years 2002 and 2003 using a 160 GeV polarized muon beam scattered off a polarized ^{6}LiD target, the extracted gluon polarization reads

$$\Delta G/G = 0.024 \pm 0.089(\text{stat.}) \pm 0.057(\text{syst.}) \ ,$$

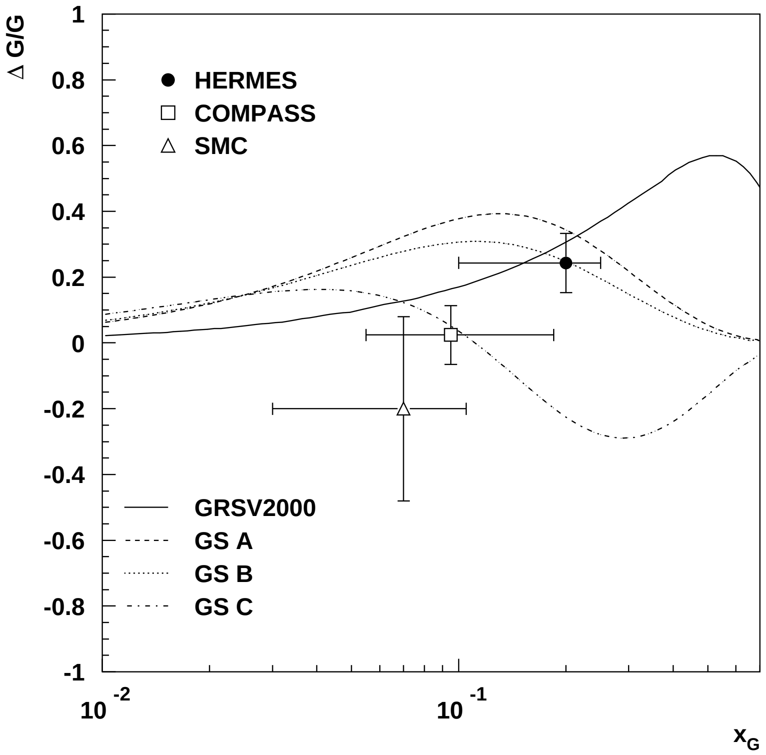

Figure 8.2: *$\Delta G/G$ vs. x_G extracted from HERMES, SMC and COMPASS data for high-p_T hadron pair photoproduction, compared to theoretical leading order fits for the gluon polarization as functions of the gluon momentum fraction at a scale $\hat{Q}^2 = 1.4$ GeV^2. The theoretical curves are taken from [32] and [115]. The SMC and COMPASS results are taken from [51] and [52]. The data are plotted at their average gluon momentum fraction x_G, the uncertainty in x_G corresponds to the width at the half maximum of the gluon momentum fraction distribution for the HERMES result, and is taken from [120] for the SMC and COMPASS results.*

at $\langle x_g \rangle = 0.095$ and $\langle \hat{p}_T^2 \rangle = 3$ GeV^2 [52]. Only events with $Q^2 < 1$ GeV^2 and containing two high-p_T hadrons with $p_T^{h1}, p_T^{h2} > 0.7$ GeV and $(p_T^{h1})^2 + (p_T^{h2})^2 > 2.5$ GeV^2 are considered. For this extraction of $\Delta G/G$, PYTHIA MC is used, but the contributions from DIS and low_pt processes are neglected.

The extraction of the gluon polarization and especially the evaluation of the systematic uncertainty are done quite differently by each the SMC collaboration, the COMPASS collaboration, and in the analysis presented in this thesis. Taking the results at face value, the extracted values for $\Delta G/G$ and the statistical uncertainties can be compared, but no attempt is made to compare the systematic uncertainties [3]. Fig. 8.2 shows the values of $\Delta G/G$ extracted in these three analyses at their average gluon momentum fractions. Note that besides at different values of $x_G = \langle x_g \rangle$, the results are also obtained

[3]Note that it is particularly difficult to compare the (seemingly rather large) model dependent systematic uncertainty based on the thorough systematic MC studies presented in this thesis with the uncertainties quoted in [51] and [52], which do not include systematic MC studies at the level of detail presented here.

at different average scales. The experimental results are in Fig. 8.2 also compared to theoretical curves for the gluon polarization as functions of the gluon momentum fraction which are taken at a scale $\hat{Q}^2 = 1.4$ GeV^2, corresponding to the average scale at which the result of this thesis is obtained.

The results for $\Delta G/G$ seem to disfavour very large absolute values for the gluon polarization. However, to convincingly distinguish between different theoretical curves, the statistical significance is still insufficient and the gluon momentum fraction range covered too small. Furthermore, large model dependent systematic uncertainties remain. Considerably more precision and analysis channels in kinematic regions with in particular smaller model dependent systematic uncertainties are therefore needed.

In the near future, more precise results on $\Delta G/G$ are expected from the RHIC-spin experiments STAR and PHENIX [34]. They are planning to measure the gluon polarization with high statistical precision in the x_g range from about 0.02 to 0.2, using prompt photon production, heavy flavour meson production and jet production in pp-collisions. These experiments are supposed to provide more information not only on the size of the gluon polarization at a certain average gluon momentum fraction $\langle x_g \rangle$, but also on the shape of the gluon polarization vs. x_g.

8.3 Next-to-leading order considerations

In all direct measurements of the gluon polarization so far, leading order (LO) Monte Carlo simulations have been used for the extraction of $\Delta G/G$. Full next-to-leading (NLO) MC programs are not available yet and will most probably not become available in the near future. To make possible a full NLO extraction of $\Delta G/G$ the polarized and unpolarized cross sections of all contributing hard processes have to be known at sufficient order, which is not the case at present.

However, there exist NLO calculations of cross sections for certain processes, evaluated at COMPASS and HERMES kinematics. In [121, 122, 123] unpolarized and polarized cross sections are calculated at NLO for the direct (QCDC, PGF) and resolved (anomalous, hard VMD) processes for photoproduction of inclusive high-p_T hadrons. At the p_T values accessible to HERMES the correction from LO to NLO (commonly referred to as the K-factor) for unpolarized (polarized) cross sections for these processes is found to be large, namely of the order of 4 (2). Furthermore, the scale dependence (i.e. the uncertainties due to the choice of renormalization and factorization scales) which is sizable at LO, is only slightly reduced at NLO. This highlights the importance of NLO calculations at HERMES energies.
For high-p_T hadron pair photoproduction the same calculations are under way [124]. Again, the scale dependence at LO is found to be sizable. The NLO calculations have not yet been completed, hence the K-factor is not yet available.

From the results available so far, it is concluded that the large scale dependence and the large K-factors obtained at HERMES energies ($\sqrt{s} = 7.5$ GeV) are only slightly

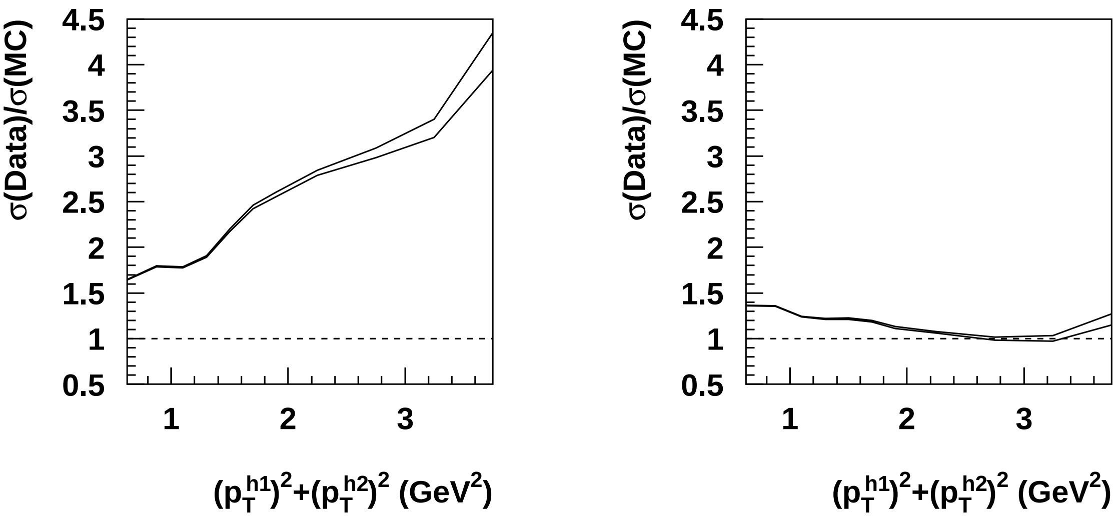

Figure 8.3: *Ratio of measurements and MC simulations for the unpolarized cross section* $\sigma(\mathrm{Data})/\sigma(\mathrm{MC})$ *for hadron pairs in photoproduction with* $p_T^{h1}, p_T^{h2} > 0.5$ *GeV as a function of* $(p_T^{h1})^2 + (p_T^{h2})^2$. *The lines in the plot do not constitute a fit but merely connect individual points; the band indicates the statistical uncertainty. The cross sections for the data are calculated from the 1996+1997 polarized proton data. The MC cross sections are obtained from PYTHIA with the parameters as used for the standard extraction of* $\Delta G/G$ *(left), and with a fudge factor of 4 applied to the direct and resolved processes (right).*

reduced at COMPASS energies ($\sqrt{s} = 18$ GeV).
The authors of [121] conclude: "All this indicates that the pQCD framework in the COMPASS and HERMES kinematic regimes is delicate, and calls for a 'reference measurement' of the unpolarized photoproduction cross section before the spin asymmetry can be analyzed in terms of ΔG". [4]

Comparing unpolarized cross sections from experiment and from theory at different orders can therefore provide a valuable first estimate of the importance of higher order corrections on the extraction of the gluon polarization. In Fig. 8.3 (left panel) the ratio of unpolarized cross sections from HERMES data and (LO) PYTHIA MC, $\sigma(\mathrm{Data})/\sigma(\mathrm{MC})$, is plotted vs. $(p_T^{h1})^2+(p_T^{h2})^2$ for high-p_T hadron pair photoproduction. The (LO) PYTHIA MC underestimates the cross section by a factor of about 1.5 to 4.5, increasing with p_T. In some of the systematic studies described in previous chapters, alternative choices for certain MC parameters, namely the PYTHIA model parameter MSTP(18) and the fragmentation tune, can make this deviation decrease. The resultant differences in the extracted gluon polarization have consequently been taken into account in the model dependent systematic uncertainty. However, the question now arises if the deviation is automatically reduced upon going to NLO. Since no full NLO calculation is available yet, its potential effects can only be estimated. One could make the assumption that the K-factor for the direct and resolved processes in high p_T hadron pair photoproduction

[4] To comply with this thesis, the notation of the authors of [121] has been modified from δg to ΔG.

is comparable to the one calculated for inclusive high-p_T hadron photoproduction cited above. A very crude first estimate of potential NLO effects can be obtained if one applies a constant (*fudge*) K-factor of 4 to the unpolarized cross sections of the direct and resolved processes in the MC. Since the contribution of these processes (QCDC, PGF, anom_q, and anom_g) increases with p_T (as can be inferred from Fig. 7.6), multiplying them by an extra factor can be expected to affect the MC cross section to a larger extent at higher p_T. This should be reflected in a changing shape of the ratio $\sigma(\mathrm{Data})/\sigma(\mathrm{MC})$ vs. $(p_T^{h1})^2 + (p_T^{h2})^2$. The resulting $\sigma(\mathrm{Data})/\sigma(\mathrm{MC})$ is plotted in Fig. 8.3 (right panel). This ratio is seen to be surprisingly close to 1 across the relevant range of p_T. Despite all its limitations, this result can be understood as an indication that future analyses of $\Delta G/G$ in the HERMES and COMPASS kinematic regime might profit from taking NLO effects into account.

Summary

The composition of the nucleon spin from its constituent partons represents one of the important unresolved issues in the physics of the strong interaction. Much insight into the nucleon's internal structure has been provided by deep-inelastic lepton nucleon scattering (DIS). While initially only unpolarized DIS could be studied, it is now possible to probe also the spin structure of the nucleon by polarized DIS. In this thesis, polarized DIS has been used to investigate the extent to which gluons contribute to the total spin of the nucleon.

The strong interaction between the partonic constituents of the nucleon, the quarks and gluons, is described by Quantum Chromodynamics (QCD). In its high energy regime, QCD is very successful in quantitatively explaining the scattering of (almost) free partons, i.e. the processes underlying DIS. However, the distributions of partons inside the nucleon are not calculable from first principles, but need to be determined experimentally.

Collider as well as fixed-target experiments have measured the unpolarized quark and gluon distributions to impressively high accuracies over large kinematic ranges. The polarized parton distributions, in particular the until recently only indirectly accessed polarized gluon distribution, are still much less well known. HERMES, a fixed-target polarized DIS experiment at DESY, has made significant contributions to further constraining the polarized quark distributions, investigating e.g. the quark flavour decomposition of the nucleon spin.

In this thesis, HERMES data have been used to extract information on the gluon polarization in the nucleon. The present analysis has been based on two channels, namely single high-p_T hadron electroproduction and high-p_T hadron pair photoproduction. The double spin asymmetries measured for these channels receive contributions not only from the processes sensitive to the gluon polarization but also from various background processes. Since the individual processes cannot be distinguished in the data, Monte Carlo simulations are required to determine their relative contributions and to extract the gluon polarization, thus inevitably introducing a model dependence into the results.

For each analysis channel, extensive MC studies have been conducted to optimize the data selection criteria in order to maximally enhance the significance of the extracted value for the gluon polarization. Data asymmetries have been determined for the best set of selection criteria found. Using information on the process fractions and their individual asymmetries from MC simulations, the gluon polarization has been extracted

from the data asymmetries. The model dependence of the extraction procedure has been thoroughly investigated.

The final results on the gluon polarization presented in this thesis are given below. For single high-p_T hadron electroproduction the result is

$$\Delta G/G = -0.35 \pm 0.17(\text{stat.}) \pm 0.05(\text{exp.syst.})^{+0.23}_{-0.17}(\text{mod.dep.syst.})\ ,$$

and for high-p_T hadron pair photoproduction

$$\Delta G/G = 0.24 \pm 0.09(\text{stat.}) \pm 0.01(\text{exp.syst.})^{+0.01}_{-0.30}(\text{mod.dep.syst.})\ .$$

Each of these results represents an average over proton and deuteron data, dominated by the latter. The total model dependent systematic uncertainties constitute the best (first) estimate of the model dependence of the extracted gluon polarization.
Within their (sizable) uncertainties, the results obtained for each of the two analysis channels studied are mutually consistent and compare well with other measurements. The data suggest that the gluon polarization in this kinematic region is small.

While the current analysis is based on Monte Carlo simulations utilizing leading order QCD calculations, first theoretical results and preliminary cross checks with experimental data point to the potential importance of next-to-leading order terms. Unfortunately, a full next-to-leading order extraction is, due to the absence of a MC to this order, currently not possible. In the future, more precise information on the gluon polarization is expected to be provided by more precise data covering a wider kinematic range and making use also of other analysis channels, together with theoretical input in the form of complete next-to-leading order calculations.

Samenvatting

De oorsprong van de spin van het proton (of neutron) representeert één van de belangrijkste onopgeloste vraagstukken van de fysica van de sterke wisselwerking. Meer in het bijzonder moet de vraag beantwoord worden hoe de spin van het nucleon (een verzamelnaam voor het proton en het neutron) voortkomt uit de spin van de bouwstenen van het nucleon, de quarks en gluonen. Veel inzicht in de interne structuur van het nucleon is verkregen door middel van diep-inelastische lepton-nucleon verstrooiing (ofwel "deep-inelastic scattering", DIS). Hoewel aanvankelijk alleen ongepolariseerde DIS kon worden bestudeerd, is het nu mogelijk om door gepolariseerde DIS experimenten ook de spinstructuur van het nucleon te onderzoeken. In dit proefschrift is gepolariseerde DIS gebruikt om te bepalen in hoeverre gluonen bijdragen aan de totale spin van het nucleon.

De sterke wisselwerking tussen de bouwstenen van het nucleon (ook wel "partonen" genoemd), wordt beschreven door de Quantum Chromodynamica (QCD). In het hoge-energiedomein slaagt QCD er uitermate goed in om de verstrooiing aan (bijna) vrije partonen (d.w.z. het proces dat ten grondslag ligt aan DIS) kwantitatief te beschrijven. Hierbij zijn de partonverdelingen binnen het nucleon echter niet berekenbaar uit de basisprincipes, maar moeten experimenteel worden gemeten.

De ongepolariseerde quark- en gluonverdelingen zijn met indrukwekkend hoge nauwkeurigheid over een groot kinematisch gebied gemeten in experimenten die ofwel van botsende bundels, ofwel van gefixeerde trefplaten gebruik maken. De gepolariseerde partonverdelingen, in het bijzonder de tot kort geleden alleen indirect toegankelijke gepolariseerde gluonverdeling, zijn nog steeds in veel mindere mate bekend. HERMES, een gepolariseerd DIS experiment met gefixeerde trefplaat op DESY, heeft belangrijke bijdrages geleverd aan de nadere bepaling van de gepolariseerde quarkverdelingen, bijvoorbeeld met betrekking tot de smaakdecompositie van de nucleonspin.

In dit proefschrift zijn HERMES data gebruikt om informatie over de gluonpolarisatie in het nucleon te verkrijgen. De analyse is gebaseerd op twee reactiekanalen, met name enkelvoudige elektroproductie van een hadron met grote transversale impuls p_T, en fotoproductie van een tweetal hadronen met grote transversale impuls in de eindtoestand. De in deze kanalen gemeten asymmetrieën van het aantal verstrooide deeltjes ten opzichte van de spinoriëntatie van het lepton en het nucleon ontvangen niet alleen bijdrages van processen die gevoelig zijn voor de gluonpolarisatie, maar ook van verschillende achtergrondprocessen. Omdat individuele processen in de data niet kunnen worden onderscheiden zijn Monte Carlo simulaties nodig om hun relatieve bijdrages te bepalen en - zodoende - de gluonpolarisatie te extraheren. Dit introduceert onvermijdelijk een model-afhankelijkheid van de resultaten.

Voor elk analysekanaal zijn omvangrijke MC simulaties uitgevoerd om de data selectiecriteria te optimaliseren en de betrouwbaarheid van de voor de gluonpolarisatie geëxtraheerde waarde te vergroten. De asymmetrieën van het aantal meetgegevens ten opzichte van de relatieve oriëntatie van de spin van de bundel en de trefplaat zijn bepaald met behulp van de geoptimaliseerde selectiecriteria. Gebruik makend van de in MC simulaties verkregen informatie over de procesbijdrages en hun individuele asymmetrieën, is de gluonpolarisatie geëxtraheerd uit de gemeten asymmetrieën. De modelafhankelijkheid van de gebruikte procedure is grondig onderzocht.

De eindresultaten voor de gluonpolarisatie, zoals gepresenteerd in dit proefschrift, worden hieronder weergegeven. Voor enkelvoudige elektroproductie van een hadron met grote transversale impuls luidt het resultaat

$$\Delta G/G = -0.35 \pm 0.17(\text{stat.}) \pm 0.05(\text{exp.syst.})^{+0.23}_{-0.17}(\text{mod.dep.syst.}) \ ,$$

en voor fotoproductie van een tweetal hadronen met grote transversale impuls in de eindtoestand

$$\Delta G/G = 0.24 \pm 0.09(\text{stat.}) \pm 0.01(\text{exp.syst.})^{+0.01}_{-0.30}(\text{mod.dep.syst.}) \ .$$

Elk resultaat stelt een gemiddelde over proton en deuteron data voor, maar wordt gedomineerd door de laatste. De totale model afhankelijke systematische onzekerheid is de beste (en eerste) schatting van de modelafhankelijkheid van de geëxtraheerde gluonpolarisatie. Binnen de (aanzienlijke) onzekerheden zijn de verkregen resultaten onderling consistent en sluiten goed aan bij andere metingen. Uit de meetgegevens blijkt dat de gluonpolarisatie in dit kinematisch domein klein is.

Hoewel de huidige analyse gebaseerd is op Monte Carlo simulaties welke van eerste-orde QCD berekeningen gebruik maken, wijzen eerste theoretische resultaten en voorlopige vergelijkingen met experimentele data erop dat hogere orde termen mogelijkerwijs belangrijk zijn. Helaas is een volledige hogere-orde extractie op dit moment niet mogelijk, als gevolg van het ontbreken van een MC programma dat gebaseerd is op hogere orde QCD berekeningen. Het is te verwachten dat in de toekomst nauwkeurigere informatie over de gluonpolarisatie beschikbaar zal komen door meer precieze metingen die een groter kinematisch domein bestrijken, en door het gebruik maken van andere analysekanalen, in samenspel met theoretische input in de vorm van volledige hogere orde QCD berekeningen.

Appendix A

Monte Carlo specifications

A.1 LEPTO MC specifications used for the $\Delta G/G$ extraction

The LEPTO MC specifications used for the analysis presented in this thesis are:

- LEPTO 6.5 incorporated in the gmc_DISNG frame for polarized scattering,
- including QED radiative corrections and detector smearing,
- cutoff parameter for first order QCD processes PARL(9)=1,
- LUND fragmentation parameters tuned to the HERMES data as in tune 2004c [107],
- polarized and unpolarized PDFs as in GRSV2000 (LO valence scenario) and GRV98, and
- 10^7 events generated in the HERMES acceptance each for parallel and antiparallel spin orientation for both a proton and a deuteron target.

A.2 PYTHIA MC specifications used for the $\Delta G/G$ extraction

The PYTHIA MC specifications used for the analysis presented in this thesis are:

- PYTHIA 6.2 with QED radiative corrections incorporated,
- QED radiative corrections turned on for single high-p_T hadrons in electroproduction and turned off for high-p_T hadron pairs in photoproduction,

- including detector smearing,
- PYTHIA parameters tuned to the HERMES data as described in [53], in particular MSTP(18)=3 was taken,
- LUND fragmentation parameters tuned to the HERMES data as in tune 2004c [107],
- unpolarized PDFs as in GRV98, and
- $5 \cdot 10^7$ events generated in the HERMES acceptance for a proton target, and combining $2.5 \cdot 10^7$ events for a proton target with $2.5 \cdot 10^7$ events for a neutron target to simulate a deuteron target.

Appendix B

Formalism for evaluating Monte Carlo asymmetries

B.1 Asymmetry weights with PYTHIA MC

Formalism

As has been discussed already in section 2.2.3 the lepton-nucleon cross sections can be split into the flux of virtual photons from leptons and the virtual photon-nucleon cross sections. For the double spin asymmetry $A_{||}$ this yields

$$A_{||} = \frac{\Delta\sigma^{ep}}{\sigma^{ep}} = \frac{\Delta\Gamma_T \Delta\sigma_T^{\gamma^* p}}{\Gamma_T \sigma_T^{\gamma^* p} + \Gamma_L \sigma_L^{\gamma^* p}} \ , \tag{B.1}$$

with

$$\Delta\Gamma_T = \frac{1}{2}\left[1-(1-y)^2 - y^3\frac{2m_e^2}{Q^2} + \frac{1}{2}\gamma^2 y^2 (2-y)\right] \ , \tag{B.2}$$

$$\Gamma_T = \frac{1}{2}\left[1+(1-y)^2 - y^2\frac{2m_e^2}{Q^2}(1+\gamma^2) + \frac{1}{2}\gamma^2 y^2\right] \ , \tag{B.3}$$

$$\Gamma_L = 1 - y - \frac{1}{4}\gamma^2 y^2 \ . \tag{B.4}$$

The equations for the fluxes are modified from those given in [45] by adding those terms proportional to m_e^2 (lepton mass squared) and $\gamma^2 = Q^2/\nu^2$ as in [125]. These terms cannot be neglected in the region $Q^2 \to 0$, as applicable in the analysis of quasi-real photoproduction.

Due to factorization, the cross sections can be written as a convolution of the partonic cross sections with the parton distribution functions

$$(\Delta)\sigma_{T(L)}^{\gamma^* p} = (\Delta)\hat{\sigma}_{T(L)} \otimes (\Delta) f \ . \tag{B.5}$$

The convolution integrals are performed by summing these quantities over all events in the generated sample. For the asymmetries one then obtains

$$A_{\parallel} = \frac{1}{N} \sum_{j=1}^{N} a_j \ , \tag{B.6}$$

with the asymmetry weights constructed as

$$a_j = \hat{a}(y, Q^2, \hat{s}, \hat{t}, \hat{u}) \frac{\Delta f(x, Q^2)}{f(x, Q^2)} \ , \tag{B.7}$$

where the partonic asymmetry $\hat{a}$ is a function of the virtual photon kinematics and the Mandelstam variables. The depolarization of the virtual photon with respect to the lepton is included in $\hat{a}$. It can be expressed as

$$\hat{a} = \frac{\Delta \Gamma_T \Delta \hat{\sigma}_T}{\Gamma_T \hat{\sigma}_T + \Gamma_L \hat{\sigma}_L} \ . \tag{B.8}$$

Asymmetry weights for different processes

For the calculation of the partonic asymmetry weights of the different processes the following expressions for the cross sections are used. In each case the relevant x and Q^2 used for the evaluation of the parton distribution functions are also described. (The expressions for LO DIS, QCDC, and PGF are taken from [45], but a common factor $4\pi\alpha^2 e_q^2 / xQ^2$ has been omitted for the cross sections.)

- LO DIS

$$\Delta \hat{\sigma}_T = 1 \tag{B.9}$$

$$\hat{\sigma}_T = 1 \tag{B.10}$$

$$\hat{\sigma}_L = 0 \tag{B.11}$$

  The cross section σ_L for the absorption of longitudinal virtual photons vanishes in LO DIS, leaving the asymmetry just equal to $\Delta\Gamma_T / \Gamma_T$. The parton distribution functions are evaluated at the (true) x and Q^2 of the event.

- QCDC

$$\Delta \hat{\sigma}_T = \frac{2\alpha_s}{3\pi} \frac{1}{(\hat{s} + Q^2)^2} \left[\frac{2(Q^2 - \hat{u})}{\hat{s} + Q^2} - \frac{Q^4 + \hat{u}^2}{\hat{s}\hat{t}} \right] \tag{B.12}$$

$$\hat{\sigma}_T = \frac{2\alpha_s}{3\pi} \frac{1}{(\hat{s} + Q^2)^2} \left[2 - \frac{2\hat{u}Q^2}{(\hat{s} + Q^2)^2} - \frac{Q^4 + \hat{u}^2}{\hat{s}\hat{t}} \right] \tag{B.13}$$

$$\hat{\sigma}_L = -\frac{2\alpha_s}{3\pi} \frac{1}{(\hat{s} + Q^2)^2} \frac{4Q^2 \hat{u}}{(\hat{s} + Q^2)^2} \tag{B.14}$$

Technically, PYTHIA generates the longitudinal and transverse photon cross sections in two separate processes, but in this analysis they are both combined into one process, with regard to the process fractions and the asymmetries, applying the above equations to calculate the partonic asymmetry for this combined process. The parton distribution functions are evaluated at the parton momentum fraction $x_P = x(1 + \hat{s}/Q^2)$, and the PYTHIA scale $\hat{Q}^2$ (usually a combination of $\hat{p}_T$ and Q^2 where $\hat{p}_T$ is the transverse momentum at the vertex with the parton from the nucleon).

- PGF

$$\Delta\hat{\sigma}_T = \frac{\alpha_s}{4\pi}\frac{1}{(\hat{s}+Q^2)^2}\frac{Q^2-\hat{s}}{\hat{s}+Q^2}\frac{\hat{u}^2+\hat{t}^2}{\hat{u}\hat{t}} \tag{B.15}$$

$$\hat{\sigma}_T = \frac{\alpha_s}{4\pi}\frac{1}{(\hat{s}+Q^2)^2}\frac{Q^4+\hat{s}^2}{(\hat{s}+Q^2)^2}\frac{\hat{u}^2+\hat{t}^2}{\hat{u}\hat{t}} \tag{B.16}$$

$$\hat{\sigma}_L = \frac{\alpha_s}{4\pi}\frac{1}{(\hat{s}+Q^2)^2}\frac{8Q^2\hat{s}}{(\hat{s}+Q^2)^2} \tag{B.17}$$

Again, the contributions from longitudinal and transverse photons, technically separated in PYTHIA, are combined into one process. And the parton distribution functions are evaluated again at x_P and $\hat{Q}^2$.

- Anomalous
The processes considered here are $qq \to qq$, $q\overline{q} \to q\overline{q}$, $q\overline{q} \to gg$, $qg \to qg$, $gg \to q\overline{q}$ and $gg \to gg$. Their transverse cross sections in leading order are taken from [126] [1]. The longitudinal cross section is parametrized as $\hat{\sigma}_L = R\hat{\sigma}_T$ with R given in [128]. The parton distribution functions (in the nucleon) are evaluated at x_P and $\hat{Q}^2$, as for the direct QCDC and PGF processes. In the asymmetry weight for the anomalous processes also the parton distribution functions in the photon $(\Delta)f_{a/\gamma}$ need to be taken into account like

$$a_j = \hat{a}^{ab\to cd}(y, Q^2, \hat{s}, \hat{t}, \hat{u})\frac{\Delta f_{a/\gamma}(x,Q^2)}{f_{a/\gamma}(x,Q^2)}\frac{\Delta f_{b/N}(x,Q^2)}{f_{b/N}(x,Q^2)}\ , \tag{B.18}$$

with $f = q, \overline{q}, g$.

So far no measurements but only estimates of the possible range for the polarized photon parton distribution functions exist. In [118, 119] the positivity constraint on the presently unknown polarized structure function of the photon g_1^γ, namely $|g_1^\gamma|/F_1^\gamma \leq 1$, is used to determine a minimal and maximal scenario for the polarized photon parton distributions as functions of x and Q^2 (cf. Fig. B.1).

The two extremes, i.e. the maximum value of the maximal scenario and the minimum value of the minimal scenario, are about +1 and -0.5 for the polarized quark and about +1 and -0.1 for the polarized gluon photon PDF.

[1] Their hard asymmetries have recently become available also in next-to-leading order [127] but these will not be considered here

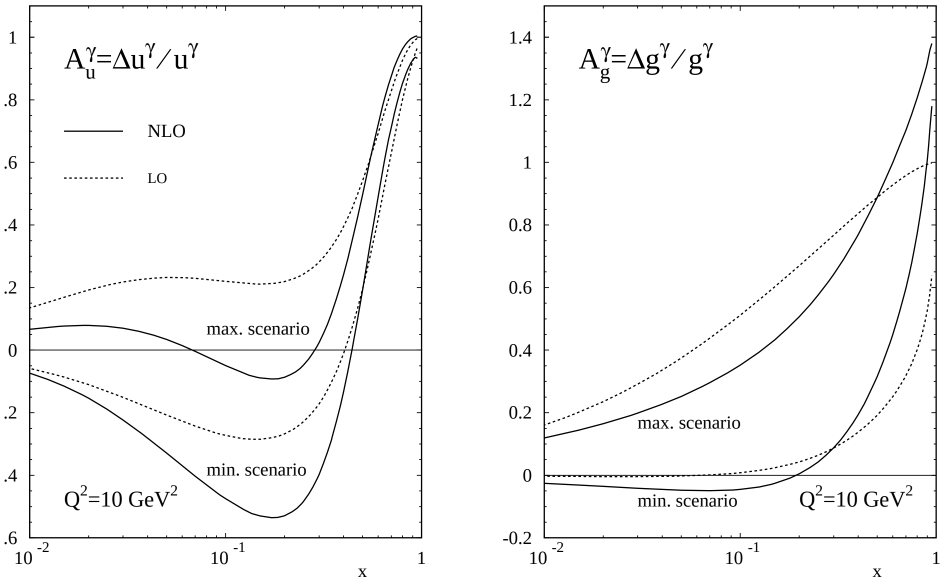

Figure B.1: *The polarized photon parton distribution functions $\Delta u^\gamma/u^\gamma$ and $\Delta g^\gamma/g^\gamma$ for the maximal and minimal scenario at $Q^2 = 10$ GeV^2 in LO and NLO as presented in [118]. These distribution functions do not change much with Q^2 [119].*

In order to find a reasonable assumption for the polarized photon PDFs in between these two extremes to be used in the description of the anomalous processes in this thesis, the x-distributions are plotted in Fig. B.2 for the anomalous processes involving a quark in the photon on the left and for those involving a gluon in the photon on the right, respectively. These distributions have been obtained with PYTHIA on a proton target for single hadrons in electroproduction. In this case, x can be understood as the momentum fraction of the parton in the photon. The distributions look basically the same for hadron pairs in photoproduction, not shown here. One observes a $\langle x \rangle$ of about 0.4 - 0.6, and a range of $0.1 < x < 0.9$. The values of $\langle x \rangle$ therefore correspond to those regions in the graphs of Fig. B.1 where both in the maximal and in the minimal scenario the polarized photon PDFs are positive. This justifies to restrict the polarized photon PDFs to positive values in this analysis. A constant value for the polarized photon parton distribution functions is assumed over the whole kinematic range, namely $\Delta q^\gamma/q^\gamma = 1$, $\Delta g^\gamma/g^\gamma = 1$ for the maximal scenario , and $\Delta q^\gamma/q^\gamma = 0$, $\Delta g^\gamma/g^\gamma = 0$ for a scenario with no polarization of the partons in the photon. The maximal scenario, which implies adding a positive anom_g asymmetry to the negative PGF asymmetry and adding a positive anom_q asymmetry to the background asymmetry, is used for the standard extraction of $\Delta G/G$. The zero scenario, which implies treating the anom_g and anom_q processes as a dilution to the signal and the background respectively, is used in the systematic studies.

- elastic and single/double diffractive VMD
  These VMD processes are considered as a dilution to the asymmetry, i.e. $\Delta\hat{\sigma}^{VMD} \equiv 0$. This is motivated by the results on the asymmetries for exclusive ρ^0- and ϕ-

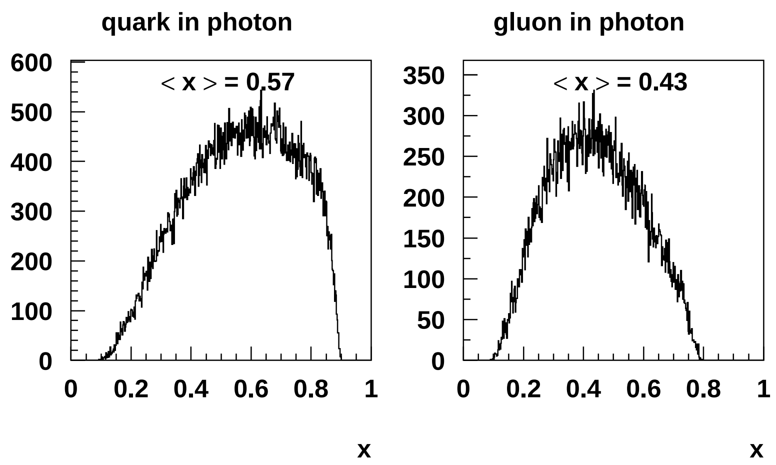

Figure B.2: *x-distributions for the anomalous processes involving a quark in the photon on the left and for those involving a gluon in the photon on the right, respectively, obtained with PYTHIA on a proton target for single hadrons in electroproduction.*

electro- and quasi-real photoproduction measured by HERMES [128]. All these asymmetries were found to be consistent with zero (except for a very small positive asymmetry for exclusive ρ^0-electroproduction from the proton target, but in this case statistical evidence was weak).

- <u>low_pt (soft non-diffractive VMD)</u>
  To the so-called low_pt processes no hard process kinematics or asymmetry can be assigned. These processes are generated in PYTHIA as a soft gluon exchange between the partons of the photon and the partons of the nucleons if neither scale involved in the scattering is hard enough for a perturbative QCD calculation of the process (cf. Fig. 5.3). This means that the low_pt processes do not represent a well defined process but rather a PYTHIA tool for occupying this soft region in order to reproduce the total cross section. Different treatments for the asymmetry from these low_pt processes can now be considered. One can either argue that soft processes as such should not show any asymmetry, and therefore treat them as a dilution to the asymmetry, i.e. $\Delta\hat{\sigma}^{low\_pt} \equiv 0$. On the other hand, one could reason as follows. As mentioned above the low_pt processes are generated if neither scale is hard enough for a perturbative treatment. But the distinction between the different scales, and the associated classification of the low_pt processes as soft, is to a certain extent arbitrary. One can now, alternatively, assume that even though classified as soft the low_pt processes might exhibit an asymmetry which must then be contained in the measured overall A_1-asymmetry. As a maximally extreme assumption one can then take $\Delta\hat{\sigma} = A_1 = g_1/F_1$ and $\hat{\sigma}_T = 1$, $\hat{\sigma}_L = R\hat{\sigma}_T$. In this case, g_1 and F_1 can be calculated in the QPM as the charge-weighted sum of the polarized and unpolarized parton distribution functions, or A_1 can be taken from a parametrization of the data. As both the parton distribution functions and the measured A_1 data only extend down to certain minimum values for Q^2 and x, a further assumption needs to be made for the photoproduction region

with values of x and Q^2 below these limits. One can either assume that $A_1 = 0$ or $A_1 = A_1(x_{min}, Q^2_{min})$ or extend the A_1 parametrization, for all $x < x_{min}$ and $Q^2 < Q^2_{min}$.

Using different assumptions for the low_pt asymmetry in the MC simulations, in [53] a data-MC comparison was performed for the asymmetries vs. x of charged hadrons in electroproduction and the asymmetries vs. p_T of charged hadrons in photoproduction. At small x and small p_T, respectively, the contribution from low_pt processes is very large (about 70% and above 50%, respectively). In these regions it can therefore be tested how well the MC and data asymmetries compare for the different low_pt assumptions. For charged hadrons in electroproduction at small x it was found that the data are not well described for $\Delta\hat{\sigma}^{low\_pt} \equiv 0$ as the MC asymmetries lie below the data asymmetries, while $\Delta\hat{\sigma}^{low\_pt} \equiv A_1^{exp}$ results in MC asymmetries much more comparable with the data asymmetries. For charged hadrons in photoproduction at small p_T the picture is not that clear because of the larger statistical fluctuations of the data. Here, it cannot be distinguished unambiguously which of the assumptions for low_pt gives a better agreement of the MC asymmetries with the data. The same type of comparison of data and MC asymmetries using theses various assumptions for the low_pt asymmetry is shown vs. p_T in Fig. B.3 for positive and negative hadrons in electroproduction on the proton target. At small p_T, where the MC asymmetries are not sensitive to the gluon polarization, the contribution from low_pt processes is about 20%. The MC asymmetries when treating the low_pt process as a dilution (dashed lines in Fig. B.3) lie below those determined for the two other treatments and are somewhat closer to the data. From this comparison one may argue that treating the low_pt process as a dilution gives the best agreement between data and MC asymmetries at small p_T.

It is concluded from these studies in [53] and from the plots discussed above, that for the evaluation of the systematic uncertainties due to the low_pt processes, three different treatments of the low_pt asymmetry are considered, namely

- as a dilution ($A_1^{low\_pt} = 0$),
- as the charge weighted sum of the polarized over unpolarized PDFs in the x and Q^2 range where the PDFs are available ($A_1^{low\_pt} = g_1/F_1$ for $x > x_{min}$ and $Q^2 > Q^2_{min}$, $A_1^{low\_pt} = 0$ otherwise), or
- as the experimental A_1-parametrization in the whole x and Q^2 range ($A_1^{low\_pt} = A_1^{exp}$ for all x and Q^2).

x and Q^2 are taken as the (true) x and Q^2 of the event like for the DIS processes, since their is no hard scattering kinematics assigned to the soft low_pt events. The second treatment of the low_pt asymmetry is used in the standard extraction of the gluon polarization; it basically represents treating the low_pt asymmetry as a dilution in the photoproduction and similar to A_1 in the electroproduction channel, because of the different kinematic regions of those two analyses. The other two alternatives are used in the systematic studies.

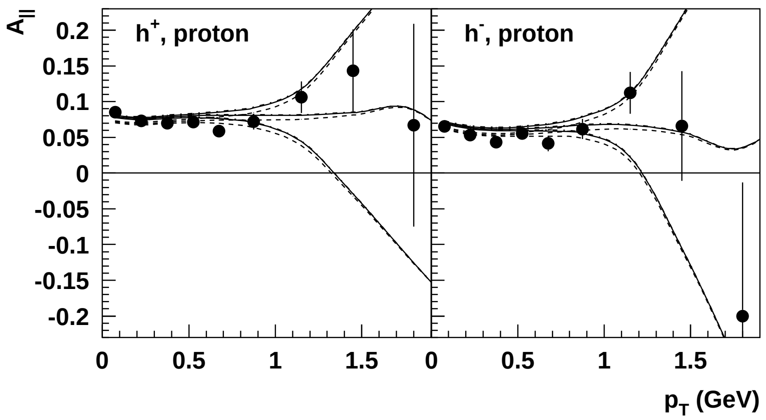

Figure B.3: *The measured asymmetries $A_{||}$ vs. p_T for positive (left) and negative (right) hadrons in electroproduction on the proton target overlaid with the PYTHIA MC asymmetries determined for different treatments of the low_pt processes, $\Delta\hat{\sigma}^{low\_pt} = g_1/F_1$(solid), $\Delta\hat{\sigma}^{low\_pt} = 0$(dashed), $\Delta\hat{\sigma}^{low\_pt} = A_1^{exp}$(dashed-dotted, almost coinciding with the solid line, and therefore hardly distinguishable). In each case the MC asymmetries are shown for three different assumptions of the gluon polarization, $\Delta G/G$=-1 (upper lines), $\Delta G/G$=0 (middle lines), $\Delta G/G$=+1 (lower lines).*

Asymmetry weights for the deuteron target

In PYTHIA, a deuteron target cannot be simulated directly, but only by mixing an equal number of events on a proton and a neutron target. In the deuteron, the proton and the neutron mostly occupy S states where their spins are aligned parallel to the spin of the nucleus. At a small probability $\omega_D = 0.05 \pm 0.01$ however the deuteron is in a D state in which the spins of the nucleons are aligned antiparallel to the spin of the nucleus, yielding an effective nucleon polarization of 92.5% compared to the deuteron polarization. Thus the deuteron asymmetry is diluted with respect to an effective proton-neutron asymmetry,

$$A_{||}^{d} = A_{||}^{pn}(1 - \frac{3}{2}\omega_D) \ , \tag{B.19}$$

with

$$A_{||}^{pn} = \frac{\sigma_p A_{||}^{p} + \sigma_n A_{||}^{n}}{\sigma_p + \sigma_n} \ , \tag{B.20}$$

where σ_p and σ_n are the cross sections on the proton and the neutron, and $A_{||}^{pn}$ is the asymmetry of a proton-neutron configuration with its spins 100% aligned.
To simulate a deuteron target with PYTHIA, equal amounts of events on a proton and a neutron target are generated, with each event on the neutron target getting an extra weight of σ_n/σ_p (≈ 0.9 in electroproduction and ≈ 0.98 (neglected) in photoproduction). To all events the factor $(1 - 3/2\omega_D)$ is applied in addition. With the events weighted like this, asymmetries and process fractions on the deuteron can be constructed.

Choices for the standard extraction

The different processes are treated and the corresponding asymmetry weights are calculated as follows in the extraction of $\Delta G/G$ referred to as *standard*:

- In the asymmetry weight of the anomalous processes the polarizations of the partons in the photon are taken as $+1$ (according to the maximal scenario).
- Elastic and diffractive VMD events are treated as a dilution, they do not show any asymmetry, i.e. $A_{\parallel}^{VMD} = 0$.
- The asymmetry weight for the low_pt process is calculated with the charged-weighted sums of the polarized and unpolarized PDFs in the range where they are available and set to zero below these limits.
- The polarized and unpolarized PDFs are taken from GRSV2000 (LO valence scenario) and GRV98 via a call to PDFLIB for $x > x_{min} = 10^{-5}$ and $Q^2 > Q^2_{min} = 0.22$ GeV^2 where the PDFs are available. For x and/or Q^2 values below these limits, the PDFs are called at x_{min} and/or Q^2_{min} (except for the low_pt process for which the PDFs are set to zero in this case).

B.2 Hard PGF asymmetry with LEPTO MC

Since LEPTO is a generator for polarized lepton-nucleon scattering, the asymmetries of the background processes can be directly accessed by running the generator in two opposite configurations for the target and beam spin. Only the hard PGF asymmetry needs to be calculated separately in order to obtain all ingredients necessary for the extraction of the gluon polarization from the data asymmetries. It can be written as the ratio of the polarized over the unpolarized cross sections

$$\hat{a} = \frac{\Delta\hat{\sigma}}{\hat{\sigma}} , \tag{B.21}$$

where the cross sections represent the product of the virtual photon-nucleon cross section and the flux of virtual photons from the leptons. In LEPTO instead of the Mandelstam variables, the following three variables are used to characterize the first order QCD processes,

$$x_p = \frac{x}{\xi} , \; z_q = \frac{p \cdot p_q}{p \cdot q} , \; \phi = \frac{(\vec{p} \times \vec{l}) \cdot (\vec{p} \times \vec{p_q})}{|\vec{p} \times \vec{l}||\vec{p} \times \vec{p_q}|} , \tag{B.22}$$

where ξ is the momentum fraction of the incoming parton, p and l are the momenta of the incoming proton and lepton, and p_q is the momentum of one of the final quarks. The cross sections can then be written as

$$\hat{\sigma} = \hat{\sigma_0} + cos(\phi)\hat{\sigma_1} + cos(2\phi)\hat{\sigma_2} \tag{B.23}$$

$$\Delta\hat{\sigma} = \Delta\hat{\sigma_0} + cos(\phi)\Delta\hat{\sigma_1} \tag{B.24}$$

with

$$\hat{\sigma_0} = \frac{\alpha_s}{4\pi}\left\{\frac{1+(1-y)^2}{2}\frac{\left[x_p^2+(1-x_p)^2\right]\left[z_q^2+(1-z_q)^2\right]}{z_q(1-z_q)} + (1-y)8x_p(1-x_p)\right\} \tag{B.25}$$

$$\hat{\sigma_1} = \frac{\alpha_s}{2\pi}(y-2)\sqrt{1-y}\sqrt{\frac{x_p(1-x_p)}{z_q(1-z_q)}}(1-2x_p)(1-2z_q) \tag{B.26}$$

$$\hat{\sigma_2} = \frac{\alpha_s}{\pi}(1-y)x_p(1-x_p) \tag{B.27}$$

$$\Delta\hat{\sigma}_0 = \frac{\alpha_s}{4\pi}\frac{1-(1-y)^2}{2}\frac{(2x_p-1)\left[z_q^2+(1-z_q)^2\right]}{z_q(1-z_q)} \tag{B.28}$$

$$\Delta\hat{\sigma}_1 = \frac{\alpha_s}{2\pi}y\sqrt{1-y}\sqrt{\frac{x_p(1-x_p)}{z_q(1-z_q)}}(1-2z_q) \tag{B.29}$$

The above formulae have been taken from [45]. A common factor $2\alpha^2 e_q^2/xQ^2$ has been omitted.

Appendix C

Statistical uncertainty of $\Delta G/G$

In section 5.2 is was derived that the average gluon polarization in a certain p_T-bin is

$$\frac{\Delta G}{G} = \frac{1}{N_{sig}\langle \hat{a}^{sig}\rangle}\left[(N_{sig}+N_{bg})A_{\parallel}^{meas} - N_{bg}A_{\parallel}^{bg}\right] \ . \tag{C.1}$$

The explicit indication of the p_T-dependence is omitted in this section.
The statistical uncertainty of the average gluon polarization therefore depends on the statistical uncertainty of the measured asymmetry $A_{\parallel}^{meas}$ and the MC statistical uncertainties of the background asymmetry $A_{\parallel}^{bg}$, the hard process asymmetry of the signal $\langle \hat{a}^{sig}\rangle$, and the number of signal and background events N_{sig} and N_{bg}. It can be calculated via Gaussian error propagation of i independent variables x_i according to

$$\delta^2\left(\frac{\Delta G}{G}\right) = \sum_i \left[\frac{\partial}{\partial x_i}\left(\frac{\Delta G}{G}\right)\right]^2 \delta^2 x_i \ . \tag{C.2}$$

Keeping in mind that

$$A_{\parallel}^{bg} = \frac{1}{N_{bg}}\sum_{j=1}^{N_{bg}} a_j^{bg} \ , \ \frac{\partial}{\partial N_{bg}}A_{\parallel}^{bg} = \frac{-\sum_{j=1}^{N_{bg}} a_j^{bg}}{N_{bg}^2} \ , \tag{C.3}$$

the partial derivatives are

$$\frac{\partial}{\partial A_{\parallel}^{meas}}\left(\frac{\Delta G}{G}\right) = \frac{(N_{sig}+N_{bg})}{N_{sig}\langle \hat{a}^{sig}\rangle} \ , \tag{C.4}$$

$$\frac{\partial}{\partial A_{\parallel}^{bg}}\left(\frac{\Delta G}{G}\right) = \frac{-N_{bg}}{N_{sig}\langle \hat{a}^{sig}\rangle} \ , \tag{C.5}$$

$$\frac{\partial}{\partial \langle \hat{a}^{sig}\rangle}\left(\frac{\Delta G}{G}\right) = -\frac{N_{sig}\left[(N_{sig}+N_{bg})A_{\parallel}^{meas} - N_{bg}A_{\parallel}^{bg}\right]}{(N_{sig}\langle \hat{a}^{sig}\rangle)^2} \ , \tag{C.6}$$

$$\frac{\partial}{\partial N_{sig}}\left(\frac{\Delta G}{G}\right) = \frac{-\langle \hat{a}^{sig}\rangle N_{bg}(A_{\parallel}^{meas} - A_{\parallel}^{bg})}{(N_{sig}\langle \hat{a}^{sig}\rangle)^2} \ , \tag{C.7}$$

$$\frac{\partial}{\partial N_{bg}}\left(\frac{\Delta G}{G}\right) = \frac{A_{\parallel}^{meas}}{N_{sig}\langle \hat{a}^{sig}\rangle} \ . \tag{C.8}$$

Using these partial derivatives and the uncertainties $\delta^2 N_{sig} = N_{sig}$ and $\delta^2 N_{sig} = N_{sig}$ in Eq. (C.2) the statistical uncertainty of the average gluon polarization becomes

$$\begin{aligned} \delta^2\left(\frac{\Delta G}{G}\right) \quad = \quad & \frac{1}{N_{sig}^2\langle \hat{a}^{sig}\rangle^2}\Big[N_{tot}^2\delta^2 A_{\parallel}^{meas} + N_{bg}^2\delta^2 A_{\parallel}^{bg} \\ & + \frac{(N_{tot}A_{\parallel}^{meas} - N_{bg}A_{\parallel}^{bg})^2}{\langle \hat{a}_{sig}\rangle^2}\delta^2\langle \hat{a}_{sig}\rangle \\ & + \frac{N_{bg}^2}{N_{sig}}(A_{\parallel}^{meas} - A_{\parallel}^{bg})^2 + N_{bg}(A_{\parallel}^{meas})^2\Big] \end{aligned} \tag{C.9}$$

The uncertainty on the average hard process asymmetry is calculated as the standard deviation for the average of the distribution of the weights according to the central limit theorem. For the uncertainty on the background asymmetry in PYTHIA the same holds, while for the uncertainty on the background asymmetry in LEPTO an Gaussian error propagation for the formula in Eq. (5.6) is taken.

Appendix D

Tables of results

Electroproduction of single high-p_T hadrons

Asymmetry for h^+ on proton	
p_T-bin	$A_{\parallel} \pm \sigma_{\text{stat}} \pm \sigma_{\text{syst}}$
0.00-0.15	0.085 ± 0.006 ± 0.005
0.15-0.30	0.073 ± 0.004 ± 0.004
0.30-0.45	0.070 ± 0.004 ± 0.004
0.45-0.60	0.071 ± 0.006 ± 0.004
0.60-0.75	0.059 ± 0.008 ± 0.003
0.75-1.0	0.072 ± 0.011 ± 0.004
1.0-1.3	0.106 ± 0.022 ± 0.006
1.3-1.6	0.143 ± 0.058 ±0.008
1.6-2.0	0.067 ± 0.142 ±0.003

Asymmetry for h^- on proton	
p_T-bin	$A_{\parallel} \pm \sigma_{\text{stat}} \pm \sigma_{\text{syst}}$
0.00-0.15	0.065 ± 0.007 ± 0.004
0.15-0.30	0.053 ± 0.005 ± 0.003
0.30-0.45	0.043 ± 0.005 ± 0.002
0.45-0.60	0.055 ± 0.007 ± 0.003
0.60-0.75	0.041 ± 0.011 ± 0.002
0.75-1.0	0.062 ± 0.014 ± 0.003
1.0-1.3	0.112 ± 0.029 ± 0.006
1.3-1.6	0.066 ± 0.077 ± 0.004
1.6-2.0	-0.200 ± 0.187 ± 0.011

Asymmetry for π^+ on proton	
p_T-bin	$A_{\parallel} \pm \sigma_{\text{stat}} \pm \sigma_{\text{syst}}$
0.00-0.15	0.110 ± 0.016 ± 0.006
0.15-0.30	0.085 ± 0.010 ± 0.005
0.30-0.45	0.064 ± 0.008 ± 0.004
0.45-0.60	0.060 ± 0.009 ± 0.003
0.60-0.75	0.053 ± 0.011 ± 0.003
0.75-1.0	0.076 ± 0.014 ± 0.004
1.0-1.3	0.122 ± 0.029 ± 0.006
1.3-1.6	0.137 ± 0.080 ± 0.008
1.6-2.0	0.074 ± 0.221 ± 0.003

Asymmetry for π^- on proton	
p_T-bin	$A_{\parallel} \pm \sigma_{\text{stat}} \pm \sigma_{\text{syst}}$
0.00-0.15	0.054 ± 0.019 ± 0.003
0.15-0.30	0.038 ± 0.012 ± 0.002
0.30-0.45	0.032 ± 0.009 ± 0.002
0.45-0.60	0.047 ± 0.010 ± 0.002
0.60-0.75	0.040 ± 0.013 ± 0.002
0.75-1.0	0.053 ± 0.016 ± 0.003
1.0-1.3	0.101 ± 0.034 ± 0.005
1.3-1.6	0.078 ± 0.095 ± 0.004
1.6-2.0	-0.024 ± 0.252 ± 0.002

Table D.1: *Measured Asymmetries $A_{\parallel}$ and their statistical and experimental systematic uncertainties in each p_T-bin for positive and negative hadrons and pions on the proton target (combined 1996 and 1997 data), for electroproduction of single high-p_T hadrons.*

Asymmetry for h^+ on deuteron	
p_T-bin	$A_{\parallel} \pm \sigma_{\text{stat}} \pm \sigma_{\text{syst}}$
0.00-0.15	0.022 ±0.004 ± 0.001
0.15-0.30	0.017 ± 0.002 ± 0.001
0.30-0.45	0.016 ± 0.003 ± 0.001
0.45-0.60	0.017 ± 0.003 ± 0.001
0.60-0.75	0.020 ± 0.005 ± 0.001
0.75-1.0	0.012 ± 0.006 ± 0.001
1.0-1.3	0.045 ± 0.019 ± 0.002
1.3-1.6	0.049 ± 0.033 ± 0.002
1.6-2.0	-0.009 ± 0.079 ± 0.000

Asymmetry for h^- on deuteron	
p_T-bin	$A_{\parallel} \pm \sigma_{\text{stat}} \pm \sigma_{\text{syst}}$
0.00-0.15	0.014 ± 0.005 ± 0.001
0.15-0.30	0.010 ± 0.003 ± 0.000
0.30-0.45	0.011 ± 0.003 ± 0.000
0.45-0.60	0.011 ± 0.004 ± 0.000
0.60-0.75	0.007 ± 0.006 ± 0.000
0.75-1.0	0.009 ± 0.008 ± 0.000
1.0-1.3	0.029 ± 0.016 ± 0.001
1.3-1.6	-0.042 ± 0.040 ± 0.002
1.6-2.0	0.031 ± 0.093 ± 0.001

Asymmetry for π^+ on deuteron	
p_T-bin	$A_{\parallel} \pm \sigma_{\text{stat}} \pm \sigma_{\text{syst}}$
0.00-0.15	0.020 ± 0.004 ± 0.001
0.15-0.30	0.014 ± 0.003 ± 0.001
0.30-0.45	0.014 ± 0.003 ± 0.001
0.45-0.60	0.015 ± 0.004 ± 0.001
0.60-0.75	0.017 ± 0.006 ± 0.001
0.75-1.0	0.014 ± 0.008 ± 0.001
1.0-1.3	0.049 ± 0.015 ± 0.002
1.3-1.6	0.036 ± 0.040 ± 0.001
1.6-2.0	0.067 ± 0.097 ± 0.003

Asymmetry for π^- on deuteron	
p_T-bin	$A_{\parallel} \pm \sigma_{\text{stat}} \pm \sigma_{\text{syst}}$
0.00-0.15	0.015 ± 0.005 ± 0.001
0.15-0.30	0.007 ±0.003 ± 0.000
0.30-0.45	0.010 ± 0.00 ± 0.000
0.45-0.60	0.008 ± 0.004 ± 0.000
0.60-0.75	0.004 ± 0.006 ± 0.000
0.75-1.0	0.009 ± 0.008 ± 0.000
1.0-1.3	0.026 ± 0.017 ± 0.001
1.3-1.6	-0.044 ± 0.044 ± 0.002
1.6-2.0	0.0478 ±0.102 ± 0.002

Asymmetry for K^+ on deuteron	
p_T-bin	$A_{\parallel} \pm \sigma_{\text{stat}} \pm \sigma_{\text{syst}}$
0.00-0.15	0.062 ± 0.015 ± 0.002
0.15-0.30	0.026 ± 0.008 ± 0.001
0.30-0.45	0.026 ± 0.008 ± 0.001
0.45-0.60	0.029 ± 0.009 ± 0.001
0.60-0.75	0.045 ± 0.013 ± 0.002
0.75-1.0	0.014 ± 0.016 ± 0.001
1.0-1.3	0.040 ± 0.030 ± 0.002
1.3-1.6	0.016 ± 0.072 ± 0.001
1.6-2.0	0.073 ± 0.180 ± 0.003

Asymmetry for K$^-$ on deuteron	
p_T-bin	$A_{\parallel} \pm \sigma_{\text{stat}} \pm \sigma_{\text{syst}}$
0.00-0.15	0.020 ± 0.021 ± 0.001
0.15-0.30	0.031 ± 0.011 ± 0.001
0.30-0.45	0.007 ± 0.010 ± 0.000
0.45-0.60	0.031 ± 0.013 ± 0.001
0.60-0.75	0.035 ± 0.019 ±0.001
0.75-1.0	0.011 ± 0.023 ±0.000
1.0-1.3	0.049 ± 0.045 ± 0.002
1.3-1.6	-0.108 ± 0.107 ± 0.004
1.6-2.0	-0.100 ± 0.270 ± 0.004

Table D.2: *Measured Asymmetries $A_{\parallel}$ and their statistical and experimental systematic uncertainties in each p_T-bin for positive and negative hadrons, pions and kaons on the deuteron target (2000 data), for electroproduction of single high-p_T hadrons.*

Photoproduction of high-p_T hadron pairs

Asymmetry for h_1h_2 on proton	
$(p_T^{h2})^{\min}$	$A_{\parallel} \pm \sigma_{\rm stat} \pm \sigma_{\rm syst}$
1.0	0.044 ± 0.035 ± 0.003
1.1	0.044 ± 0.039 ± 0.003
1.2	0.050 ± 0.048 ± 0.003
1.3	-0.011 ± 0.061 ± 0.001
1.4	-0.054 ± 0.080 ± 0.003
1.5	-0.160 ± 0.106 ± 0.009

Asymmetry for h_1h_2 on deuteron	
$(p_T^{h2})^{\min}$	$A_{\parallel} \pm \sigma_{\rm stat} \pm \sigma_{\rm syst}$
1.0	-0.032 ± 0.020 ± 0.001
1.1	-0.040 ± 0.022 ± 0.002
1.2	-0.047 ± 0.027 ± 0.002
1.3	-0.055 ± 0.034 ± 0.002
1.4	-0.052 ± 0.045 ± 0.002
1.5	-0.070 ± 0.059 ± 0.003

Asymmetry for h_1h_2 from 1996 data	
$(p_T^{h2})^{\min}$	$A_{\parallel} \pm \sigma_{\rm stat} \pm \sigma_{\rm syst}$
1.0	0.142 ± 0.076 ± 0.009
1.1	0.133 ± 0.084 ± 0.009
1.2	0.101 ± 0.103 ± 0.007
1.3	0.026 ± 0.129 ± 0.002
1.4	-0.213 ± 0.171 ± 0.014
1.5	-0.291 ± 0.218 ± 0.019

Asymmetry for h_1h_2 from 1997 data	
$(p_T^{h2})^{\min}$	$A_{\parallel} \pm \sigma_{\rm stat} \pm \sigma_{\rm syst}$
1.0	0.015 ± 0.040 ± 0.001
1.1	0.020 ± 0.044 ± 0.001
1.2	0.036 ± 0.054 ± 0.002
1.3	-0.021 ± 0.069 ± 0.001
1.4	-0.009 ± 0.091 ± 0.000
1.5	-0.120 ± 0.121 ± 0.006

Table D.3: *Measured Asymmetries $A_{\parallel}$ and their statistical and experimental systematic uncertainties for each $(p_T^{h2})^{\min}$ for hadron pairs of any charge on proton target (combined 1996 and 1997 data), deuteron target (2000 data), and from 1997 and 1997 data separately, for photoproduction of high-p_T hadron pairs.*

Statistics for h_1h_2						
	1996		1997		2000	
$(p_T^{h2})^{\min}$	$\overrightarrow{\Rightarrow}$	$\overrightarrow{\Leftarrow}$	$\overrightarrow{\Rightarrow}$	$\overrightarrow{\Leftarrow}$	$\overrightarrow{\Rightarrow}$	$\overrightarrow{\Leftarrow}$
1.0	509	571	1558	1584	6269	6090
1.1	414	461	1268	1293	5155	4975
1.2	280	304	823	851	3464	3320
1.3	185	189	520	511	2136	2034
1.4	115	97	300	298	1256	1199
1.5	72	57	178	160	736	691

Table D.4: *Statistics for hadron pairs for each $(p_T^{h2})^{\min}$ per year and spin orientation.*

Asymmetry for $h_1 h_2$ on proton	
$(\sum p_T^2)^{\rm min}$	$A_\parallel \pm \sigma_{\rm stat} \pm \sigma_{\rm syst}$
1.0	0.023 ± 0.004 ± 0.001
1.2	0.018 ± 0.006 ± 0.001
1.4	0.016 ± 0.008 ± 0.001
1.6	0.031 ± 0.010 ± 0.002
1.8	0.047 ± 0.013 ± 0.003
2.0	0.041 ± 0.016 ± 0.002
2.5	0.084 ± 0.028 ± 0.005
3.0	-0.001 ± 0.045 ± 0.000
4.0	0.042 ± 0.108 ± 0.002

Asymmetry for $h_1 h_2$ on deuteron	
$(\sum p_T^2)^{\rm min}$	$A_\parallel \pm \sigma_{\rm stat} \pm \sigma_{\rm syst}$
1.0	-0.005 ± 0.003 ± 0.000
1.2	-0.005 ± 0.003 ± 0.000
1.4	-0.000 ± 0.004 ± 0.000
1.6	0.001 ± 0.006 ± 0.000
1.8	-0.006 ± 0.007 ± 0.000
2.0	-0.010 ± 0.009 ± 0.000
2.5	-0.028 ± 0.015 ± 0.001
3.0	-0.041 ± 0.025 ± 0.002
4.0	-0.080 ± 0.057 ± 0.003

Asymmetry for $h_1 h_2$ from 1996 data	
$(\sum p_T^2)^{\rm min}$	$A_\parallel \pm \sigma_{\rm stat} \pm \sigma_{\rm syst}$
1.0	0.026 ± 0.010 ± 0.002
1.2	0.021 ± 0.013 ± 0.001
1.4	0.017 ± 0.017 ± 0.001
1.6	0.067 ± 0.022 ± 0.004
1.8	0.081 ± 0.028 ± 0.005
2.0	0.070 ±0.035 ± 0.005
2.5	0.175 ± 0.060 ± 0.011
3.0	0.065 ±0.099 ± 0.004
4.0	-0.071 ± 0.241 ± 0.005

Asymmetry for $h_1 h_2$ from 1997 data	
$(\sum p_T^2)^{\rm min}$	$A_\parallel \pm \sigma_{\rm stat} \pm \sigma_{\rm syst}$
1.0	0.022 ± 0.005 ± 0.001
1.2	0.017 ± 0.007 ± 0.001
1.4	0.015 ± 0.009 ± 0.001
1.6	0.022 ± 0.011 ± 0.001
1.8	0.038 ± 0.014 ± 0.002
2.0	0.034 ± 0.018 ± 0.002
2.5	0.060 ± 0.031 ± 0.003
3.0	-0.019 ± 0.051 ± 0.001
4.0	0.071 ± 0.121 ± 0.004

Table D.5: *Measured Asymmetries $A_\parallel$ and their statistical and experimental systematic uncertainties for each $(\sum p_T^2)^{\rm min}$ for hadron pairs of any charge on proton target (combined 1996 and 1997 data), deuteron target (2000 data), and from 1996 and 1997 data separately, for photoproduction of high-p_T hadron pairs.*

Statistics for $h_1 h_2$						
	1996		1997		2000	
$(\sum p_T^2)^{\rm min}$	$\stackrel{\rightarrow}{\Rightarrow}$	$\stackrel{\rightarrow}{\Leftarrow}$	$\stackrel{\rightarrow}{\Rightarrow}$	$\stackrel{\rightarrow}{\Leftarrow}$	$\stackrel{\rightarrow}{\Rightarrow}$	$\stackrel{\rightarrow}{\Leftarrow}$
1.0	31051	31729	97904	100020	383148	381518
1.2	18167	18490	56739	57713	222859	221959
1.4	10755	10916	33108	33609	130439	130450
1.6	6248	6598	19702	20124	77398	77480
1.8	3801	4061	11925	12353	47710	47473
2.0	2421	2563	7513	7758	30120	29863
2.5	802	924	2483	2624	10389	10137
3.0	311	328	951	936	3959	3816
4.0	55	52	163	174	776	722

Table D.6: *Statistics for hadron pairs for each $(\sum p_T^2)^{\rm min}$ per year and spin orientation.*

List of Figures

Photoproduction of high-p_T hadron pairs

Conclusions and outlook

Appendix

List of Tables

Bibliography

[1] D. H. Perkins, "Introduction to High Energy Physics", *Reading, USA: Addison-Wesley (1982) 437p.*

[2] D. J. Griffiths, "INTRODUCTION TO ELEMENTARY PARTICLES", *New York, USA: Wiley (1987) 392p.*

[3] F. Halzen and A. D. Martin, "QUARKS & LEPTONS: An Introductory Course in Modern Particle Physics", *New York, USA: Wiley (1984) 396p.*

[4] E. Leader, "Spin in Particle Physics", *Camb. Monogr. Part. Phys. Nucl. Phys. Cosmol.* **15** (2001) 1.

[5] M. Anselmino, A. Efremov, and E. Leader, "THE THEORY AND PHENOMENOLOGY OF POLARIZED DEEP INELASTIC SCATTERING", *Phys. Rept.* **261** (1995) 1–124, `hep-ph/9501369`. Erratum-ibid.281:399-400,1997.

[6] R. L. Jaffe, "SPIN, TWIST AND HADRON STRUCTURE IN DEEP INELASTIC PROCESSES", `hep-ph/9602236`.

[7] B. W. Filippone and X.-D. Ji, "THE SPIN STRUCTURE OF THE NUCLEON", *Adv. Nucl. Phys.* **26** (2001) 1, `hep-ph/0101224`.

[8] B. Lampe and E. Reya, "Spin Physics and Polarized Structure Functions", *Phys. Rept.* **332** (2000) 1–163, `hep-ph/9810270`.

[9] A. V. Manohar, "AN INTRODUCTION TO SPIN DEPENDENT DEEP INELASTIC SCATTERING", `hep-ph/9204208`.

[10] L. N. Hand, "Experimental investigation of pion electroproduction", *Phys. Rev.* **129** (1963) 1834–1846.

[11] V. Tvaskis, "Longitudinal-transverse separation of deep-inelastic scattering at low Q^2 on nucleons and nuclei", *PhD thesis, Vrije Universiteit Amsterdam* (2004).

[12] Particle Data Group Collaboration, K. Hagiwara *et al.*, "Review of particle physics", *Phys. Rev.* **D66** (2002) 010001.

[13] J. I. Friedman and H. W. Kendall, “Deep inelastic electron scattering”, *Ann. Rev. Nucl. Part. Sci.* **22** (1972) 203–254.

[14] J. D. Bjørken, “ASYMPTOTIC SUM RULES AT INFINITE MOMENTUM”, *Phys. Rev.* **179** (1969) 1547–1553.

[15] J. D. Bjørken and E. A. Paschos, “INELASTIC ELECTRON-PROTON AND γ-PROTON SCATTERING, AND THE STRUCTURE OF THE NUCLEON”, *Phys. Rev.* **185** (1969) 1975–1982.

[16] R. P. Feynman, “Very high-energy collisions of hadrons”, *Phys. Rev. Lett.* **23** (1969) 1415–1417.

[17] C. G. Callan and D. J. Gross, “High-energy electroproduction and the constitution of the electric current”, *Phys. Rev. Lett.* **22** (1969) 156–159.

[18] T. Sloan, R. Voss, and G. Smadja, “THE QUARK STRUCTURE OF THE NUCLEON FROM THE CERN MUON EXPERIMENTS”, *Phys. Rept.* **162** (1988) 45–167.

[19] R. D. Field, “APPLICATIONS OF PERTURBATIVE QCD”, *Redwood City, USA: Addison-Wesley (1989) 366 p. (Frontiers in physics, 77)*.

[20] CTEQ Collaboration, R. Brock *et al.*, “Handbook of perturbative QCD: Version 1.0”, *Rev. Mod. Phys.* **67** (1995) 157–248.

[21] G. Sterman, “AN INTRODUCTION TO QUAMTUM FIELD THEORY”, *Cambridge, UK: Univ. Pr. (1993) 572 p.*

[22] M. E. Peskin and D. V. Schroeder, “An Introduction to Quantum Field Theory”, *Reading, USA: Addison-Wesley (1995) 842 p.*

[23] R. D. Field and R. P. Feynman, “A parametrization of the Properties of Quark Jets”, *Nucl.Phys* **B136** (1978) 1.

[24] B. Andersson *et al.*, “Parton Fragmentation and String Dynamics”, *Phys.Rept* **97** (1983) 31.

[25] T. Sjöstrand, “High-energy physics event generation with PYTHIA 5.7 and JETSET 7.4”, *Comput. Phys. Commun.* **82** (1994) 74–90.

[26] T. Sjöstrand, “PYTHIA 5.7 and JETSET 7.4: Physics and manual”, `hep-ph/9508391`.

[27] J. Pumplin *et al.*, “New generation of parton distributions with uncertainties from global QCD analysis”, *JHEP* **07** (2002) 012, `hep-ph/0201195`.

[28] CTEQ Collaboration, H. L. Lai *et al.*, “Global QCD analysis of parton structure of the nucleon: CTEQ5 parton distributions”, *Eur. Phys. J.* **C12** (2000) 375–392, `hep-ph/9903282`.

[29] A. D. Martin, R. G. Roberts, W. J. Stirling, and R. S. Thorne, "MRST2001: partons and α_s from precise deep inelastic scattering and Tevatron jet data", *Eur. Phys. J.* **C23** (2002) 73–87, `hep-ph/0110215`.

[30] HERMES Collaboration, H. Böttcher, "NLO QCD Analysis of the Spin Structure Function g_1", *Nucl. Phys. Proc. Suppl.* **133** (2004) 69–72.

[31] J. Blümlein and H. Böttcher, "QCD analysis of polarized deep inelastic scattering data and parton distributions", *Nucl. Phys.* **B636** (2002) 225–263, `hep-ph/0203155`.

[32] M. Glück, E. Reya, M. Stratmann, and W. Vogelsang, "Models for the Polarized Parton Distributions of the Nucleon", *Phys. Rev.* **D63** (2001) 094005, `hep-ph/0011215`.

[33] Asymmetry Analysis Collaboration, Y. Goto *et al.*, "Polarized parton distribution functions in the nucleon", *Phys. Rev.* **D62** (2000) 034017, `hep-ph/0001046`.

[34] C. Aidala *et al.*, "Research Plan for Spin Physics at RHIC", *RHIC* (2005).

[35] G. Bunce, N. Saito, J. Soffer, and W. Vogelsang, "Prospects for spin physics at RHIC", *Ann. Rev. Nucl. Part. Sci.* **50** (2000) 525–575, `hep-ph/0007218`.

[36] F. Meissner, "Measurement of the J/Ψ-Cross Section and Double-Spin Asymmetries in Vector Meson Production in Polarized Lepton-Nucleon Scattering at HERMES", *PhD thesis, Humboldt Universität Berlin* (2000).

[37] E. Volk, "Measurement of the $D^{*\pm}$ Cross-section at HERMES", *PhD thesis, Universität Heidelberg* (2001).

[38] M. Ehrenfried, "Eine Studie zur Nachweisbarkeit von open charm Ereignissen bei HERMES", *Diploma thesis, Universität Münster* (2001).

[39] A. Laziev, "Quasi-Real Photo-Production and Semi-Leptonic Decay of D^{*-} Mesons", *PhD thesis, Vrije Universiteit Amsterdam* (2005).

[40] D. Heesbeen, "Quasi-real photo-production of hyperons on polarized ^{1,2}H targets", *PhD thesis, Rijksuniversiteit Groningen* (2003).

[41] COMPASS Collaboration, G. Baum *et al.*, "COMPASS: A Proposal for a Common Muon and Proton Apparatus for Structure and Spectroscopy", *CERN-SPSLC-96-14*.

[42] J. Feltesse, F. Kunne, and E. Mirkes, "Prospects for measuring Δg from jets at HERA with polarized protons", *Phys. Lett.* **B388** (1996) 832–836, `hep-ph/9607336`.

[43] M. Stratmann and W. Vogelsang, "Photoproduction of jets and heavy flavors at future polarized ep colliders", *Z. Phys.* **C74** (1997) 641–650, `hep-ph/9605330`.

[44] A. Bravar, D. von Harrach, and A. Kotzinian, "Large gluon polarization from correlated high-p_T hadron pairs in polarized electro-production", *Phys. Lett.* **B421** (1998) 349–359, `hep-ph/9710266`.

[45] A. Bravar, K. Kurek, and R. Windmolders, "POLDIS: A Monte Carlo for POLarized (semi-inclusive) Deep Inelastic Scattering", *Comput. Phys. Commun.* **105** (1997) 42–61, `hep-ph/9704313`.

[46] HERMES Collaboration, A. Airapetian *et al.*, "Measurement of the Spin Asymmetry in the Photoproduction of Pairs of High-p_T hadrons at HERMES", *Phys. Rev. Lett.* **84** (2000) 2584–2588, `hep-ex/9907020`.

[47] J. Martin, "Measurement of the Spin Asymmetry $A_{||}$ in the Photoproduction of High-p_T Hadron Pairs", *PhD thesis, Massachusetts Institute of Technology* (2000).

[48] F. Menden, "Determination of the Gluon Polarization in the Nucleon", *PhD thesis, Albert-Ludwigs-Universität Freiburg* (2001).

[49] T. Sjöstrand *et al.*, "High-energy-physics event generation with PYTHIA 6.1", *Comput. Phys. Commun.* **135** (2001) 238–259, `hep-ph/0010017`.

[50] T. Sjöstrand, L. Lonnblad, and S. Mrenna, "PYTHIA 6.2: Physics and manual", `hep-ph/0108264`.

[51] Spin Muon (SMC) Collaboration, B. Adeva *et al.*, "Spin asymmetries for events with high p_T hadrons in DIS and an evaluation of the gluon polarization", *Phys. Rev.* **D70** (2004) 012002, `hep-ex/0402010`.

[52] COMPASS Collaboration, C. Bernet, "Recent measurement of $\Delta G/G$ at COMPASS", `hep-ex/0507049`.

[53] P. Liebing, "Can the Gluon Polarization in the Nucleon be Extracted from HERMES Data on Single High-p_T Hadrons?", *PhD thesis, Universität Hamburg* (2004).

[54] A. Afanasev, C. E. Carlson, and C. Wahlquist, "Measuring polarized gluon and quark distributions with meson photoproduction", *Phys. Rev.* **D58** (1998) 054007, `hep-ph/9706522`.

[55] A. Afanasev, C. E. Carlson, and C. Wahlquist, "Soft contributions to hard pion photoproduction", *Phys. Rev.* **D61** (2000) 034014, `hep-ph/9903493`.

[56] HERMES Collaboration, "Hermes Technical Design Report", *DESY-PRC-93-06* (1993).

[57] A. A. Sokolov and I. M. Ternov, "On polarization and spin effects in the theory of synchrotron radiation", *Sov.Phys.Dokladi* **8** (1964) 1203.

[58] D. P. Barber *et al.*, “The HERA polarimeter and the first observation of electron spin polarization at HERA”, *Nucl. Instrum. Meth.* **A329** (1993) 79–111.

[59] D. P. Barber *et al.*, “High spin polarization at the HERA Electron Storage Ring”, *Nucl. Instrum. Meth.* **A338** (1994) 166–184.

[60] D. P. Barber *et al.*, “The first achievement of longitudinal spin polarization in a high-energy electron storage ring”, *Phys. Lett.* **B343** (1995) 436–443.

[61] M. Beckmann *et al.*, “The longitudinal polarimeter at HERA”, *Nucl. Instrum. Meth.* **A479** (2002) 334–348, `physics/0009047`.

[62] HERMES Collaboration, A. Airapetian *et al.*, “The HERMES polarized hydrogen and deuterium gas target in the HERA electron storage ring”, *Nucl. Instrum. Meth.* **A540** (2005) 68–101.

[63] A. Nass *et al.*, “The HERMES polarized atomic beam source”, *Nucl. Instrum. Meth.* **A505** (2003) 633–644.

[64] C. Baumgarten *et al.*, “The storage cell of the polarized H/D internal gas target of the HERMES experiment at HERA”, *Nucl. Instrum. Meth.* **A496** (2003) 277–285.

[65] C. Baumgarten *et al.*, “A gas analyzer for the internal polarized target of the HERMES experiment”, *Nucl. Instrum. Meth.* **A508** (2003) 268–275.

[66] C. Baumgarten *et al.*, “An atomic beam polarimeter to measure the nuclear polarization in the HERMES gaseous polarized hydrogen and deuterium target”, *Nucl. Instrum. Meth.* **A482** (2002) 606–618.

[67] C. Baumgarten *et al.*, “Measurements of atomic recombination in the HERMES polarized hydrogen and deuterium storage cell target”, *Nucl. Instrum. Meth.* **A496** (2003) 263–276.

[68] T. Benisch *et al.*, “The luminosity monitor of the HERMES experiment at DESY”, *Nucl. Instrum. Meth.* **A471** (2001) 314–324.

[69] HERMES Collaboration, K. Ackerstaff *et al.*, “HERMES spectrometer”, *Nucl. Instrum. Meth.* **A417** (1998) 230–265, `hep-ex/9806008`.

[70] J. T. Brack *et al.*, “The HERMES forward tracking chambers: Construction, operation, and aging effects”, *Nucl. Instrum. Meth.* **A469** (2001) 47–54.

[71] J. Blouw *et al.*, “Design and performance of a large microstrip gas tracker for HERMES”, *Nucl. Instrum. Meth.* **A434** (1999) 227–243.

[72] A. Andreev *et al.*, “Multiwire proportional chambers in the HERMES experiment”, *Nucl. Instrum. Meth.* **A465** (2001) 482–497.

[73] S. Bernreuther *et al.*, "Design and performance of the large HERMES drift chambers", *Nucl. Instrum. Meth.* **A367** (1995) 96–99.

[74] S. Bernreuther *et al.*, "The HERMES back drift chambers", *Nucl. Instrum. Meth.* **A416** (1998) 45–58, `hep-ex/9803005`.

[75] N. Akopov *et al.*, "The HERMES dual-radiator ring imaging Cerenkov detector", *Nucl. Instrum. Meth.* **A479** (2002) 511–530, `physics/0104033`.

[76] H. Avakian *et al.*, "Performance of F101 radiation resistant lead glass shower counters", *Nucl. Instrum. Meth.* **A378** (1996) 155–161.

[77] H. Avakian *et al.*, "Performance of the electromagnetic calorimeter of the HERMES experiment", *Nucl. Instrum. Meth.* **A417** (1998) 69–78, `hep-ex/9810004`.

[78] HERMES Collaboration, "New silicon detector systems for the HERMES front region", *DESY-HERMES-97-32*.

[79] HERMES Collaboration, M. G. van Beuzekom *et al.*, "Technical Design Report of the new Silicon-Detector System", *Hermes Internal Note 98-014* (1998).

[80] J. J. M. Steijger, "The HERMES silicon project", *Nucl. Instrum. Meth.* **A447** (2000) 55–60.

[81] J. Visser *et al.*, "Design and performance of a silicon test counter for HERMES", *Nucl. Instrum. Meth.* **A521** (2004) 430–440.

[82] M. G. van Beuzekom, E. Garutti, D. Heesbeen, J. J. M. Steijger, and J. Visser, "First experience with the HERMES silicon detector", *Nucl. Instrum. Meth.* **A461** (2001) 247–250.

[83] HERMES Collaboration, "A large acceptance recoil detector for HERMES", *DESY-PRC-01-01*.

[84] HERMES Collaboration, "The HERMES recoil detector", *DESY-PRC-02-01*.

[85] J. J. M. Steijger, "The lambda wheels, a silicon vertex detector for HERMES", *Nucl. Instrum. Meth.* **A453** (2000) 98–102.

[86] M. G. van Beuzekom *et al.*, "The HERMES silicon project: The radiation protection system", *Nucl. Instrum. Meth.* **A512** (2003) 44–51.

[87] CERN-CN Division, "EPIO-Experimental Physics Input Output Package", *CERN Program Library Long Writeup* **I101** (1993).

[88] CERN Programming Techniques Group, "ADAMO-Entity-Relationship Programming System, Users Guide, Version 3.3", *CERN* (1994).

[89] W. Wander, "Rekonstruktion hochenergetischer Streuereignisse im HERMES Experiment", *PhD thesis, Friedrich-Alexander-Universität Erlangen-Nürnberg* (1996).

[90] HERMES Data Quality Website *http://www-hermes.desy.de/groups/daqlgrp/*.

[91] J. Wendland, "Improved Particle Identification at HERMES and Polarised Valence Quark Distributions in the Proton", *Master's thesis, Simon Fraser University* (1999).

[92] J. Wendland, "Polarized Parton Distributions Measured At The Hermes Experiment", *PhD thesis, Simon Fraser University* (2003).

[93] J. Wendland, "Particle Identification for HERMES Run I", *Hermes Internal Note 01-067* (2001).

[94] HERMES Particle Identification Website *http://www-hermes.desy.de/PID/*.

[95] D. de Schepper et al., "The HERMES Cerenkov detector", *Hermes Internal Note 00-021* (2000).

[96] R. K. D. de Schepper and E. Cisbani, "Particle Identification with the HERMES RICH Detector: Description of the Different Approaches", *Hermes Internal Note 98-008* (1998).

[97] R. Kaiser, "Likelihood analysis for the RICH IRT method", *Hermes Internal Note 00-021* (2000).

[98] A. Maas, "Particle identification with RICH detectors: algorithms and their optimization", *PhD thesis, GSI Darmstadt, DESY Zeuthen* (2000).

[99] K. Negodeva, "The PID efficiency of the Hermes RICH detector for the IRT method", *Hermes Internal Note 00-028* (2000).

[100] R. Kaiser and B. Hommez, "Using the RICH detector for physics analysis", *Hermes Internal Note 00-003* (2000).

[101] HERMES RICH Website, "http://www-hermes.desy.de/groups/richgrp/",.

[102] HERMES target group, "The polarization of HERMES target and its error for the deuterium running in 2000", *Hermes Internal Note 02-010* (2002).

[103] M. Beckmann, "Target polarization values and their uncertainties used by the Δq analysis group for the 1996 to 2000 running periods", *Hermes Internal Note 03-005* (2003).

[104] U. Elschenbroich, "Analysis of Luminosity Monitor Data for Different Years", *Hermes Internal Note 02-013* (2002).

[105] L. Mankiewicz, A. Schäfer, and M. Veltri, "PEPSI: A Monte Carlo generator for polarized leptoproduction", *Comput. Phys. Commun.* **71** (1992) 305–318.

[106] G. Ingelman, A. Edin, and J. Rathsman, "LEPTO 6.5 - A Monte Carlo Generator for Deep Inelastic Lepton-Nucleon Scattering", *Comput. Phys. Commun.* **101** (1997) 108–134, `hep-ph/9605286`.

[107] A. Hillenbrand, "Measurement and Simulation of the Fragmentation Process at HERMES", *PhD thesis, Friedrich-Alexander-Universität Erlangen* (2005).

[108] J. G. Korner, E. Mirkes, and G. A. Schuler, "QCD JETS AT HERA. 1. O(α_s) RADIATIVE CORRECTIONS TO ELECTROWEAK CROSS SECTIONS AND JET RATES", *Int. J. Mod. Phys.* **A4** (1989) 1781.

[109] A. Edin, G. Ingelman, and J. Rathsman, "Unified Description of Rapidity Gaps and Energy Flows in DIS Final States", *Z. Phys.* **C75** (1997) 57–70, `hep-ph/9605281`.

[110] G. Ingelman *private communication* (2002).

[111] I. Akushevich, H. Böttcher, and D. Ryckbosch, "RADGEN 1.0: Monte Carlo generator for radiative events in DIS on polarized and unpolarized targets", `hep-ph/9906408`.

[112] C. Friberg and T. Sjöstrand, "Total cross sections and event properties from real to virtual photons", *JHEP* **09** (2000) 010, `hep-ph/0007314`.

[113] HERMES Collaboration, A. Airapetian *et al.*, "Flavor decomposition of the sea quark helicity distributions in the nucleon from semi-inclusive deep- inelastic scattering", *Phys. Rev. Lett.* **92** (2004) 012005, `hep-ex/0307064`.

[114] HERMES Collaboration, A. Airapetian *et al.*, "Quark helicity distributions in the nucleon for up, down, and strange quarks from semi-inclusive deep-inelastic scattering", *Phys. Rev.* **D71** (2005) 012003, `hep-ex/0407032`.

[115] T. Gehrmann and W. J. Stirling, "Polarized Parton Distributions in the Nucleon", *Phys. Rev.* **D53** (1996) 6100–6109, `hep-ph/9512406`.

[116] P. Liebing *private communication* (2005).

[117] E. Aschenauer *private communication* (2005).

[118] M. Glück, E. Reya, and C. Sieg, "Spin-Dependent Structure Functions of the Photon", *Phys. Lett.* **B503** (2001) 285–291, `hep-ph/0102014`.

[119] M. Glück, E. Reya, and C. Sieg, "Spin-Dependent Structure Functions of Real and Virtual Photons", *Eur. Phys. J.* **C20** (2001) 271–281, `hep-ph/0103137`.

[120] COMPASS Collaboration, C. Bernet, "Recent measurement of $\Delta G/G$ at COMPASS", *Talk given at DIS05.*

[121] B. Jäger, M. Stratmann, and W. Vogelsang, "Longitudinally Polarized Photoproduction of Inclusive Hadrons at Fixed-Target Experiments", `hep-ph/0505157`.

[122] B. Jäger, M. Stratmann, and W. Vogelsang, "Longitudinally Polarized Photoproduction of Inclusive Hadrons Beyond the Leading Order", *Phys. Rev.* **D68** (2003) 114018, `hep-ph/0309051`.

[123] B. Jäger, "Studies of Hadronic Spin Structure in Hard Scattering Processes at the Next-to-Leading Order of QCD", *PhD thesis, Universität Regensburg* (2004).

[124] C. Hendlmeier, "Two Hadron Production in Longitudinally Polarized Lepton-Nucleon Collisions", *Diploma thesis, Universität Regensburg* (2005).

[125] Spin Muon Collaboration, B. Adeva *et al.*, "Spin Asymmetries A_1 of the Proton and the Deuteron in the low x and low Q^2 Region from Polarized High Energy Muon Scattering", *Phys. Rev.* **D60** (1999) 072004. Erratum-ibid.D62:079902,2000.

[126] J. Babcock, E. Monsay, and D. W. Sivers, "Quantum Chromodynamic Predictions for Inclusive Spin-Spin Asymmetries at Large Transverse Momentum", *Phys. Rev.* **D19** (1979) 1483.

[127] B. Jäger, A. Schäfer, M. Stratmann, and W. Vogelsang, "Next-to-leading order QCD corrections to high-p_T pion production in longitudinally polarized pp collisions", *Phys. Rev.* **D67** (2003) 054005, `hep-ph/0211007`.

[128] HERMES Collaboration, K. Ackerstaff *et al.*, "Measurement of angular distributions and $R = \sigma_L/\sigma_T$ in diffractive electroproduction of ρ^0 mesons", *Eur. Phys. J.* **C18** (2000) 303–316, `hep-ex/0002016`.

Acknowledgements

FINISHED! What a feeling to reach this stage, to finally get to write these last (most enjoyable) pages of my thesis! From my first day at NIKHEF up to now it has been quite a journey, with ups and downs (naturally), but at this point paying off for all the effort I guess. Looking back, it seems like it has in fact been quite a major learning process. In the past five years (plus some months to be honest) I have learned even the most unexpected things, and not only about physics, that's for sure.
Fortunately, doing a PhD (as a high-energy experimentalist at least) is not a lonesome expedition, but rather a sociable international adventure. I am very grateful that I have had all of you to accompany me during these years, helping in one way or the other, directly or indirectly. You kept telling me that I would manage, even when I myself couldn't see the light at the end of the tunnel. Your continuous support, advice and guidance, your optimism and everything else, I have appreciated enormously. This thesis wouldn't have materialized without you. Time to say thank you so much.
Of course, no list of acknowledgements will ever be exhaustive, can ever give appropriate credit to every person for every contribution. For the risk of being incomplete, I would like to thank the following indispensable crew:

- my promoter who has given me the opportunity for this adventure and who has supported me with unbeatable enthusiasm for ΔG throughout the years,

- my co-promoter who has carefully looked at every plot and every sentence of this thesis, helping to increase its internal consistency and to reduce the amount of jargon used,

- my adviser in every aspect of the analysis and beyond who even as busy HERMES spokeswoman has always made time for me, to discuss the probably more than a thousand plots I have produced over the years (well, I lost count at some point), and to help in every other respect, knowing HERMES inside out,

- my fellow ΔG analyst who with her pioneering work has paved the way and who has always been willing to share: experience, ideas, code, insider information,...

- my fellow NIKHEF HERMES PhD students and our postdocs who have been an extremely nice bunch of people to work and to have fun with, during and after working hours,

- my officemate at NIKHEF who was always up for a chat, an explanation or whatever was needed and who kindly left her poster, jungle and (wooden) parrot to keep me company when she moved on to sunny San Francisco,

- the HERMES crew at DESY who I could really ask any kind of question and would still get a patient answer, and with whom meetings on site have always been fruitful, and offsite meetings always a good laugh,

- my fellow datacops and MC simulators who I got my initiation to HERMES data and MC analysis from, and who I have greatly enjoyed working with,

- all the people involved and interested in the ΔG hunt who I have had many intriguing discussions with,

- my officemate at DESY who, when not busy talking Swiss German to his computer, would always help me out with any kind of programming problem,

- the NIKHEF HERMES staff who have come up with many helpful questions and suggestions when listening to my progress reports and who have particularly been a source for error calculation support,

- my many proofreaders who have suggested quite a few improvements and who have tracked down typos so well hidden that even the spell check wouldn't find them, (I am curious if I will nevertheless see another demonstration of that well known law of nature, finding a typo on the first page I open when the thesis is still hot from the press),

- all my fellow NIKHEF oios (in varying cast with all this coming and going) who I have enjoyed so many coffee breaks and other social events at NIKHEF with (although I still don't get the culinary pleasure of a haringfeestje...),

- my physio-consultants who talked some (physical) sense into me when my body was complaining heavily about all this strenuous computer work,

- my yoga teacher and mental coach who has helped me incredibly to find my balance even in the most stressful phases of this thesis, her lessons I will never forget,

- my friends, who, in Amsterdam, Hamburg, Düsseldorf, or via phone and internet from all over the place, have always found the right words, doubling the joy and halving the pain of this journey, making sure that I wouldn't neglect the other (really important) things in life,

- my family who all these years has been there for me, in fact unconditionally, no matter which (difficult) mood I would be in when calling or visiting home,

- and my husband who has not only performed as my invaluable personal motivator, but who to me is simply everything.

GerardWillemElkePatty

ChiaraJanJohanErikaAndreas

RiccardoDavidArmenVladasPaulMichielJeroen

UliThoreJürgenIngridAchimBinoFelixBeni

MarcMauriceLarryJimNaomiMatthiasWolf-Dieter

JosLoukHenkKeithMariekeMirandaFrancien

NinaSvenKlausPiaSaschaAndreaMarkNinaPeter

SimonBettinaOliverLukasJohannaAlessandro

JoanaDaniëlSandraJordAndreaAlexTino

MamaPapaLydiaPatrick

PlusManyMore

AndAboveAll

Tim

THANK YOU

FOR EVERYTHING